

63-3-2

4 14.00

(5) 518 700

91

401031

MASSACHUSETTS INSTITUTE OF TECHNOLOGY
LINCOLN LABORATORY

(11) G-0052

AD NC
COPY

A Magneto-Optic Apparatus for the Dynamic
Study of Ferromagnetic Surface Domains

(12) AF19(604)74

(13) NA

(8) Frederick Williams Sarles, Jr.

(9) 23 December 1960

(10) 200 p. metallog. tables, refs.

ASTIA
RECEIVED
APR 15 1963
JISIA

The research reported in this document was performed at the Computer Components and Systems Group, Department of Electrical Engineering, M.I.T. under contract with the Department of the Navy, and at Lincoln Laboratory, a center for research operated by the Massachusetts Institute of Technology, with the joint support of the U.S. Army, Navy, and Air Force under Air Force Contract AF 19(604)-7400.

LEXINGTON

MASSACHUSETTS

plf-1330a

14.00

A MAGNETO-OPTIC APPARATUS FOR THE DYNAMIC STUDY OF FERROMAGNETIC SURFACE DOMAINS

by

FREDERICK WILLIAMS SARLES, JR.

Submitted to the Department of Electrical
Engineering on January 9, 1961, in partial
fulfillment of the requirements for the de-
gree of Doctor of Science.

ABSTRACT

↓
A magneto-optic apparatus which incorporates a Kerr electro-optical shutter, a high-intensity flash lamp source, and fast-risetime pulsed magnetic fields ^{which} ~~has been~~ constructed. This apparatus was designed for the dynamic study of ferromagnetic surface domains, and, in particular, for the study of thin permalloy films. Photographs of 10 ^{milli-microseconds} ~~microseconds~~ exposure duration can be taken at any time point over a 4.5 ^{microsecond} ~~microsecond~~ range; pulsed magnetic fields up to 13 oersteds are available for switching the specimen.

The magneto-optic transmission of the system is analyzed for the two magnetically saturated states of a specimen. Conditions are derived for optimum operation of the system in terms of the transmissions of these states and the ratio of the transmission. Analysis is carried out for the effect of a thin dielectric layer upon the amplitude reflection coefficients. A tentative explanation of color effects observed visually with a dielectric coated specimen is given.

The geometric optical design of the system is discussed with special attention being given to image positioning, image distortion, and aperture limitations. A new brightness theorem is derived; this theorem is particularly useful for determining the illuminance at any point in a lossless optical system.

Optical performance estimates of the system, based upon the analysis results, agree within an order of magnitude of actual system performance.

Photographs are presented illustrating reversal of a thin permalloy film. Visual observations of static domain configurations following the application of a short duration magnetic pulse to the specimen are discussed.

Thesis Supervisor: _____ David J. Epstein

Title: _____ Associate Professor of Electrical Engineering

↑
(A)

ACKNOWLEDGMENTS

The author would like to express his appreciation to Professor D. J. Epstein for his supervision of this thesis and to thank Dr. D. O. Smith of Lincoln Laboratory who brought the topic to the author's attention. Discussions with Professor A. L. Loeb on optical and magnetic phenomena were quite helpful during the course of this project.

Appreciation is also due to Thomas Milligan, George Klonizchii, Allen Pacela, and Al Johnson for their technical assistance in various phases of the work. Carol Schupbach, Sandra Jean Bergstrom, and Mrs. Minna Lowe contributed to the typing of the thesis.

The switching coefficient curves in Chapter I are taken from Reference 3 of Chapter I in the bibliography and are reproduced from the Journal of Applied Physics with the kind permission of the American Institute of Physics.

Finally, the author wishes to thank his wife Valerie who typed the major portion of this thesis and who also spent many long hours assisting in taking and developing photographs during the final phases of this thesis.

TABLE OF CONTENTS

Abstract	ii
Acknowledgments	iii
Index of Illustrations	vii
 Chapter I: PURPOSE AND BACKGROUND OF OPTICAL SWITCHING STUDIES	 1
1.1 Switching Modes	2
1.2 Previous Magneto-Optical Studies	6
1.3 Utilization of the Magneto-Optic Photographic Apparatus	7
1.4 System Specifications	
 Chapter II: THE USE OF THE LONGITUDINAL KERR EFFECT FOR OBSERVING SURFACE MAGNETIZATION	 11
2.1 Reflection Coefficients	13
2.2 Monochromatic Analysis	19
2.3 Analysis for a White Light Source	41
2.4 Dielectric Layer on a Ferromagnetic Film	50
 Chapter III: SYSTEM DESIGN	 78
3.1 The Magneto-Optic Photographic System	79
3.2 Choice of System	84
3.3 Light Source	85
3.4 Shutter	87
3.5 Photographic Film Sensitivity	88
3.6 Pulsed Magnetic Field	90
3.7 Estimated Operating Limits	93

Chapter IV: OPTICAL APPARATUS	98
4.1 Requirements of Optical System	98
4.2 Initial Optical Experimentation	101
4.3 Single Lens Analysis	103
4.4 Two-Lens Analysis	106
4.5 Brightness	118
4.6 Aperture and Field of View	123
 Chapter V: THE ELECTRO-OPTICAL SHUTTER	 127
5.1 Nitrobenzene Characteristics	128
5.2 Kerr Cell Design	129
5.3 High Voltage Pulse Generator	132
 Chapter VI: ELECTRONIC INSTRUMENTATION	 144
6.1 Pulsed Magnetic Field Apparatus	144
6.2 Flash Lamp Circuitry	147
6.3 Synchronization Circuitry	153
6.4 Static Field Circuitry	162
6.5 Miscellaneous Circuitry	166
 Chapter VII: EXPERIMENTAL RESULTS	 169
7.1 High Speed Photographs	169
7.2 Experimental Problems	178
7.3 Visual Observations with Short Pulses	180
7.4 Apparatus Improvements	182
7.5 Summary and Conclusions	183
 Appendix A: ALTERNATIVE TRANSMISSION DERIVATION	 185
 Appendix B: KERR CELL TRANSMISSION	 189

Appendix C: HYDROGEN THYRATRON CONSIDERATIONS	192
Bibliography	195
Biographical Note	201

INDEX OF ILLUSTRATIONS

Figure 1-1	Switching Coefficient Data	3
1-2	Switching Coefficient Data	4
Figure 2-1	Reference Angle for Magnetization Vector	12
2-2	Simplified Magneto-Optic Photographic System	14
2-3	Optical Data for Permalloy Film	16
2-4	Optical Reference Axes	17
2-5	Magnitude of Permalloy Reflection Coefficients	20
2-6	Phase of Permalloy Reflection Coefficients	21
2-7	Polarizer Transmission	23
2-8	Amplitude Vectors After First Polarizer	25
2-9	Amplitude Vectors After Reflection	25
2-10	Rotation of Reference Axes	26
2-11	Amplitude Vectors After Second Polarizer	26
2-12	Loci of Constant Contrast	30
2-13	Variation of P-Vectors	31
2-14	Contrast Ratio and Normalized Transmission	34
2-15	Maximum Contrast Ratio (Monochromatic)	36
2-16	Normalized Monochromatic Transmission vs. Contrast Ratio	38
2-17	Transmission Characteristics of Polarizers	40
2-18	Transmission Variation	49
2-19	Interference Rays in Dielectric Layers	52
2-20	Amplitude Reflection Coefficients	61
2-21	Reflection Coefficient Products	62
2-22	Normalized Magnitude and Phase of R_x	63
2-23	Variation of Reflection Coefficients -- $n_1 = 1.065$	65
2-24	Variation of Reflection Coefficients -- $n_1 = 1.123$	66

Figure 2-25	Variation of Reflection Coefficients -- $n_1 = 1.66$	67
2-26	Variation of Reflection Coefficients -- $n_1 = 2.4$	68
2-27	Variation of Reflection Coefficients -- $n_1 = 3.14$	69
2-28	R_{kx} of Permalloy Film with Dielectric Layer -- $n_1 = 2.66$	70
2-29	R_{kx} of Permalloy Film with Dielectric Layer -- $n_1 = 2.4$	71
2-30	Example of Transmission Factors Which Yield Color Effects	74
Figure 3-1a	Completed Magneto-Optic Photographic Apparatus	80
3-1b	Completed Magneto-Optic Photographic Apparatus	80a
3-2	Optical Schematic	81
3-3	Electronic Instrumentation Block Diagram	82
3-4	Specimen Holder and Field Coils	83
3-5	Remanent States	86
3-6	10 μ sec Exposure -- Royal-X Pan Film	89
3-7	10 μ sec Exposure -- Double-X Film	89
3-8	Inductance and Field Curves for Single-Turn Helmholtz Pairs	92
Figure 4-1	Single Lens Analysis	104
4-2	Image Area Distortion	107
4-3	Two Lens Analysis	108
4-4	Variation in Area Magnification	114
4-5	Specimen Photograph Showing Area Distortion and Intensity Variation	116
4-6	Variation of Image Angle	117
4-7	Brightness Derivation	119
4-8	Aperture Limitation of Source Image	122
4-9	Aperture Analysis	124
4-10a	Variation of ω_r	126
4-10b		

Figure 5-1	Nitrobenzene Cell Design	131
5-2	Simplified Pulse Generator	133
5-3	Zero Potential Distributions and Pulse Waveforms	135
5-4	Electro-Optical Shutter Unit	137
5-5	Kerr Cell Module	138
5-6	10 nanosecond Delay Line Assembly	139
5-7	High Voltage Pulse Generator Circuit	141
5-8	Voltage Pulse and Light Transmission Waveforms	142
Figure 6-1	Artificial Delay Lines	146
6-2	Field Pulse Generator Circuit	148
6-3	Pulse Generator Circuit Waveforms	149
6-4	Flash Lamp Circuitry	152
6-5	Flash Lamp Output	154
6-6	Pulse Distribution Circuit	155
6-7	Pulse Generator Circuit	156
6-8	Four-Layer Diode Characteristic	157
6-9	Clock Circuit	160
6-10	Restoring Pulse Generator to Relay Driver	162
6-11	Surge Field Supply	164
6-12	Fast Angle Panel	165
6-13	Regulated High Voltage Power Supply	167
6-14	Thyatron Heated Power Panel	168
Figure 7-1	Switching Sequence 1	171
7-2	Switching Sequence 2	172
7-3	Switching Sequence 3	173
7-4	Switching Sequence 4	174
7-5	Switching Sequence 5	175

7-6	Sketch of Switching Sequence 1	176
7-7	Test Photographs	179
Figure B-1	Kerr Cell Transmission	191
Figure C-1	4C35 Rise Time Constant and Anode Delay	194

CHAPTER I

PURPOSE AND BACKGROUND OF OPTICAL SWITCHING STUDIES

During the past few years thin film magnetic technology has developed to the extent where functional systems, such as computer memories, have been built. Such films are fabricated primarily through vacuum evaporation or electrodeposition techniques; the fabrication usually takes place in the presence of a magnetic field which causes a preferred orientation of the magnetic vector in the film². This preferred orientation is treated as an internal anisotropy field of magnitude H_K . The field is not necessarily uniform either in magnitude or direction.

Since films in device applications are usually switched from one permanent state to the other, the process by which this reversal takes place is of considerable interest. The purpose of this thesis is to investigate a photographic technique for studying the reversal process; the basis for this investigation is the longitudinal Kerr magneto-optic effect in combination with ultra-high speed photographic techniques. For this work a magneto-optic apparatus has been constructed. This apparatus is capable of taking pictures of the magnetic configuration of a film during reversal, the exposures having a duration as short as 10 μsec and a time resolution of about 5 μsec .

In this chapter we present a discussion of the switching modes which occur in thin ferromagnetic films, some comment on previous switching study research, a brief summary of the various ways in which such an apparatus can be employed for research on thin films, and a short statement of the desired system specification.

Chapter II deals with the use of the longitudinal Kerr magneto-optic effect for observation of surface magnetic configuration. The transmission of light through the system is discussed for a monochromatic and a white light source. It is shown that for two domains

of opposite magnetization, the contrast between light reflected from the two domains can be maximized, although other system considerations may mean that optimum results are not obtained at maximum contrast operation. This chapter concludes with the analysis of optical effects of a thin dielectric layer on top of the ferromagnetic film.

Design of the system is discussed in Chapter III. Reasons are given for and against the use of various components, and computer calculations are made for the estimated operating limits of the system.

Chapter IV contains an analysis of the geometrical effects in the system. Distortion of and distortion in the image to be photographed are determined, and the system is designed to give a high resolution. The system is designed to give a high resolution, and the system is designed to give a high resolution. The system is designed to give a high resolution, and the system is designed to give a high resolution.

The wave effects that are involved in the design and construction of the electro-optical shutter are discussed. This is presented in Chapter V. The electro-optical shutter is discussed in Chapter VI. Experimental results and recommendations to improve the system are presented in Chapter VII.

2.1. Switching Modes

The existence of three different modes of switching in thin ferromagnetic films has been fairly soundly established experimentally^{3, 4, 5, 6, 7, 8}. These modes can be seen fairly clearly as regions of different slope in switching coefficient data for two specimens as measured by Olsen and Pohm³ (shown in Figs. 1-1 and 1-2). The three modes are as follows:

- I. Domain wall switching, sometimes referred to as the "creep" mode. Reversal takes place by propagation of domain walls through the specimen. The threshold applied field is denoted as H_c ; usually H_c is less than H_k . Nucleation of domains usually occurs at the edge of the specimen, although nucleation has also been observed at other places in the specimen⁹.

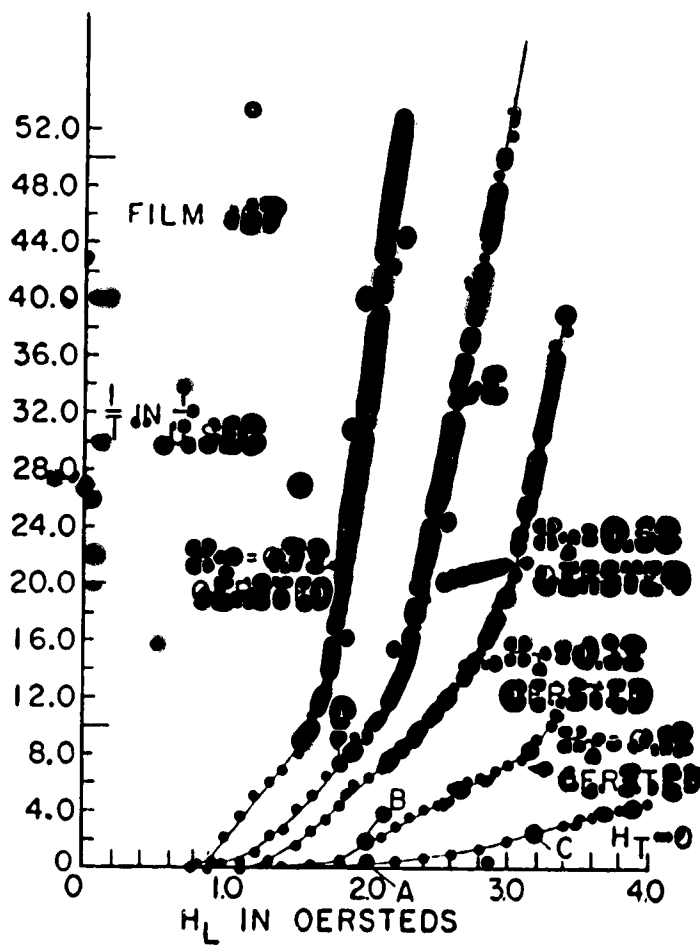


FIG. 1-1 SWITCHING COEFFICIENT DATA

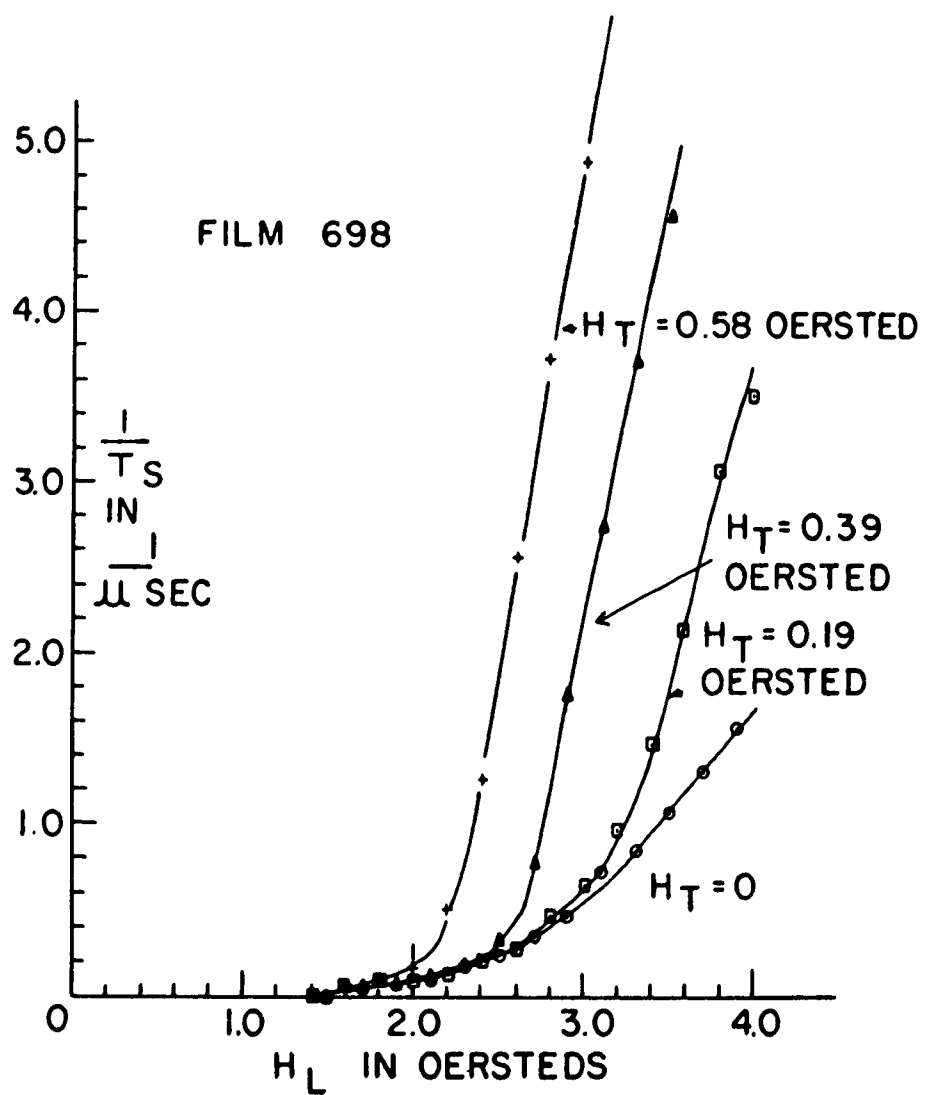


FIG. 1-2 SWITCHING COEFFICIENT DATA

Conger and Essig¹⁰ have postulated that the curvature of the switching coefficient curve in this region results from an increase in the number of nucleation sites as the magnitude of the applied field is increased. The writer's observations bear out this postulate.

II. Nonhomogeneous Rotational Switching. The mechanism for this process is the least understood of the switching modes. The reversal is presumed to take place partially or completely by rotation of the magnetic vector in various regions of the specimen, but with no phase relationship between these various regions. The writer is of the opinion that this is his own observation and upon the basis of the writer's own nonhomogeneous rotational switching from a single magnetic disc. This will be discussed in Chapter IV.

Coherent Rotational Switching. This is the most rapid reversal mode. Reversal has been observed for a minimum of about 100 gauss for this process. The observed switching times as shown in Fig. 1-1 are the lowest when the applied field is greater than H_k . Switching times are developed on the magnetic vector in the film so that the film behaves as a single domain in the reversal process. To insure that the magnetic vector develops in the same sense throughout the entire film, either a transverse bias must be applied or the reversal field must be applied at a slight angle with respect to the anisotropy axis. The effect of applying the reversal field along the anisotropy axis with no transverse bias can be seen in Fig. 1-1 in the curve for which $H_1=0$. Under these conditions the angular dispersion of H_k is sufficient so that some areas of the film rotate in a clockwise sense while others rotate in a counter-clockwise sense, resulting in a Mode II reversal (nonhomogeneous rotation).

1.2 Previous Magneto-Optical Studies

The initial application of the longitudinal Kerr effect for observing magnetic configurations was conducted in 1951 by Williams, Foster and Wood¹⁴ in observations on single crystals of silicon iron. Following this, Fowler and Fryer^{15, 16} demonstrated the use of this effect for observing domains on thin films of nickel-iron and showed that, in a sufficiently thin ferromagnetic film (approximately 1000 Å), the domain pattern was the same on both surfaces of the specimen, indicating that the domain configuration as seen from one surface extends through the specimen to the other surface. They have also shown¹⁷ that the Faraday effect can be used for domain observations of thin nickel-iron films which are not optically opaque. In a further refinement of the application of the longitudinal Kerr effect, Fowler, Fryer and Treves¹⁸ have observed domain structure in an iron whisker at a magnification of 100X. Olmen and Mitchell¹⁹ have observed slow propagation (on the order of minutes) of domains on a ferromagnetic film when a constant magnetic field is applied. Callaby²⁰ has used the transverse Kerr effect to study directions of magnetization in polycrystalline Ferrites.

Some investigation has also been conducted toward developing components and display techniques using magneto-optic phenomena. In 1954, Roberts and Bean²¹ demonstrated the large optical rotations for normally reflected (or transmitted) light from (or through) thin films of MnBi. Following this work, Williams, et al.²² have developed a technique for writing magnetically on those films and subsequently detecting the writing by magneto-optic methods. Kleinrock²³ has discussed possibilities of using thin ferromagnetic films in a magneto-optic setup as computer logical components. Following the work of Heinrich²⁴, he has also studied the increase in longitudinal Kerr rotation resulting from the evaporation of thin layers of various dielectrics onto the ferromagnetic films.

Thus far, the investigations described have dealt with static or quasistatic observations. There are a few reports in the literature on dynamic studies which have been conducted, all employing the

Conger and Essig¹⁰ have postulated that the curvature of the switching coefficient curve in this region results from an increase in the number of nucleation sites as the magnitude of the applied field is increased. The writer's observations bear out this postulate.

II. Nonhomogeneous Rotational Switching. The mechanism for this process is the least understood of the switching modes. The reversal process takes place partially or completely by rotational reversal in various regions of the specimen with the consequence between these various regions. The writer's opinion, based on his own observations and those of Smith¹¹, that non-homogeneous rotation is characterized by angular and magnitude dispersion. This will be discussed further in Chapter VII.

III. Coherent Rotational Switching. This is the high speed reversal mode. Kikuchi¹² has calculated a reversal time minimum of about 10 nsec for this process; Smith¹³ has observed switching times as short as 3 μ sec. In this mode, the applied field is greater than H_k . Sufficient torque is developed on the magnetic vector throughout the film so that the film behaves as a single domain during the entire reversal process. To insure that this torque is developed in the same sense throughout the entire film, either a transverse bias must be applied or the reversal field must be applied at a slight angle with respect to the anisotropy axis. The effect of applying the reversal field along the anisotropy axis with no transverse bias can be seen in Fig. 1-1 in the curve for which $H_1=0$. Under these conditions the angular dispersion of H_k is sufficient so that some areas of the film rotate in a clockwise sense while others rotate in a counterclockwise sense, resulting in a Mode II reversal (nonhomogeneous rotation).

1.2 Previous Magneto-Optical Studies

The initial application of the longitudinal Kerr effect for observing magnetic configurations was conducted in 1951 by Williams, Foster and Wood¹⁴ in observations on single crystals of silicon iron. Following this, Fowler and Fryer^{15, 16} demonstrated the use of this effect for observing domains on thin films of nickel-iron and showed that, in a sufficiently thin ferromagnetic film (approximately 1000 Å), the domain pattern was the same on both surfaces of the specimen, indicating that the domain configuration as seen from one surface extends through the specimen to the other surface. They have also shown¹⁷ that the Faraday effect can be used for domain observations of thin nickel-iron films which are not optically opaque. In a further refinement of the application of the longitudinal Kerr effect, Fowler, Fryer and Treves¹⁸ have observed domain structure in amorphous wires as a magnification of 100X. Olmen and Mitchell¹⁹ have observed slow propagation (on the order of minutes) of domains on a ferromagnetic film when a constant magnetic field is applied. Callaby²⁰ has used the transverse Kerr effect to study directions of magnetization in polycrystalline Ferrites.

Some investigation has also been conducted toward developing components and display techniques using magneto-optic phenomena. In 1954, Roberts and Bean²¹ demonstrated the large optical rotations for normally reflected (or transmitted) light from (or through) thin films of MnBi. Following this work, Williams, et al.²² have developed a technique for writing magnetically on those films and subsequently detecting the writing by magneto-optic methods. Kleinrock²³ has discussed possibilities of using thin ferromagnetic films in a magneto-optic setup as computer logical components. Following the work of Heinrich²⁴, he has also studied the increase in longitudinal Kerr rotation resulting from the evaporation of thin layers of various dielectrics onto the ferromagnetic films.

Thus far, the investigations described have dealt with static or quasistatic observations. There are a few reports in the literature on dynamic studies which have been conducted, all employing the

longitudinal Kerr magneto-optic effect. Using a small light beam as a probe, Lee²⁵ has been able to study the velocities and oscillations of domain walls. Moore²⁶ reports a magneto-optic apparatus incorporating a television camera. With this equipment, he has observed dynamic domain configurations, including nucleation and erratic jumps of domain walls (apparently Barkhausen effect), under the influence of a varying magnetic field. He suggests stroboscopic techniques to allow observations at high reversal rates. Conger, et al.⁹ have reported operation of a magneto-optic apparatus which uses a photo cell to sense the change in light reflection from any one of 64 sampling areas in a square specimen. With this they can determine the time at which a given sampling area switches and thereby reconstruct an approximate configuration of the magnetization at various times during reversal. They report on switching times of a few microseconds duration.

1.3 Utilization of the Magneto-Optic Photographic Apparatus

The apparatus described in this report can be used in a variety of ways to investigate the magnetic characteristics of this ferromagnetic. Not all of these techniques have been explored during the present work. Nonetheless, the writer believes that a summary of the potential applications of such an apparatus is germane to this report.

1. Ultra high speed photographing (10 msec duration) of the magnetic configuration parallel to the easy axis* during film reversal. This is the type of photography for which the apparatus was fundamentally designed. The longitudinal Kerr effect is sensitive only to that portion of the magnetization vector which is parallel to the plane of incidence of light (see Chapter II); In this application the film is positioned so that the easy axis is parallel to the plane of incidence. The pulsed magnetic field is applied parallel to the easy axis.

2. Ultra high speed photographing of the magnetic configur-

*The easy axis is the axis of the ferromagnetic film which displays a rectangular hysteresis loop. See Olsen and Pohn³ for further discussion.

ation perpendicular to the easy axis. The procedure in this technique is identical to that of Technique 1, except that the easy axis of the film and the pulsed field are perpendicular to the plane of incidence.

3. Integrated time photographing of the flux perpendicular to the easy axis during any sort of rotational flux reversal. In this case the specimen and the pulsed magnetic field are oriented as in Technique 2. The shutter is opened for part or all of the specimen reversal. A localized area rotating in one sense will reflect more light while one rotating in the opposite sense will tend to reflect less light. Since the system can be adjusted so that the reflected light intensity is proportional to the square of the magnetic vector component parallel to the plane of incidence, the density of the photographic negative at various points in the image will be a record of the squared magnetic vector component integrated over time during which the shutter was opened.

4. Repetitive photographs. If the magnetic configurations of the specimen are repeatable from cycle to cycle, repetitive photographing can be done to increase the image density and hence gain resolution by enabling the use of a larger image magnification. If the configuration is not exactly repeatable, information may still be obtained on a statistical basis.

5. Visual pulsed observations:

- a. Slow motion domain switching. Very short magnetic field pulses (50 to 100 musec long) can be used to observe a slowed down domain wall reversed by pulsing the film at repetition rates on the order of 100 cps.
- b. Threshold studies. The onset of nonhomogeneous rotation switching can be observed by pulsing the specimen with a single short pulse. Data can be

taken on the magnitude of this field as a function of transverse bias and pulse duration. Correlation with angular and magnitude dispersion of H_k could lead to a possible explanation of the origin of the non-homogeneous rotational switching mode.

- c. Nucleation studies. Nucleation at locations in specimens other than at the edge have been observed by the writer and by others.²⁷ The magnetic field magnitude and/or duration required to cause nucleation can be determined through causing nucleation by application of a single pulse of some short duration. The nucleated domain may be too small to be observed at this point, but it can be enlarged by application of a series of pulses of much lower amplitude which are incapable of causing further nucleation but which are sufficient to move an existing domain wall.

As stated at the beginning of this section, all of these techniques have not been explored. Those which have are discussed in Chapter VII.

1.4 System Specifications

Although a number of techniques for using the magneto-optic photographic apparatus have been described, the primary design objective was a system capable of photographing domain wall and nonhomogeneous rotational switching modes described as Technique 1 in Section 1.3. With this objective in mind, the following design specifications were set up on the basis of preliminary computations and considerations.

1. Exposure duration -- 10 musc.
2. Time resolution -- 10 musc or better.
3. Flash source peak brightness -- 10^7 candles/cm².
4. Specimen diameter -- One centimeter.
5. Photographic resolution -- best obtainable.
6. Switching field magnitude -- 10 oerstads.
7. Switching field risetime -- 25 musc.
8. Switching field uniformity -- 5 per cent.

9. Static field available -- 30 oerstads.
10. Static field angular orientation -- variable.
11. Repetition rate of apparatus -- 100 cps (for short periods).
12. Steady source and telescope for visual observations.

All specifications were met or exceeded with two exceptions. The field of view will only cover a specimen area of 0.6 cm by 1 cm. The repetition rate is extremely slow because of triggering electrode problems in the flash lamp circuitry. Examination of these problems revealed that both could probably be brought up to the stated specifications, but lack of time has prevented the accomplishment of this in the immediate project.

CHAPTER II

THE USE OF THE LONGITUDINAL KERR EFFECT FOR OBSERVING SURFACE MAGNETIZATION

In a thin ferromagnetic film, the magnetization vector \vec{M} lies primarily in the plane of the film. The longitudinal Kerr magneto-optic amplitude reflection coefficient \hat{r}_k^* is proportional to the magnitude of the component of \vec{M} which is parallel to the plane of incidence, i.e., if we write \hat{r}_k as

$$\hat{r}_k = r_k \exp[j\delta_k] \quad (\text{II-1})$$

then

$$r_k \sim M \cos \alpha$$

or

$$r_k = r_{km} \cos \alpha \quad (\text{II-2})$$

where

r_k = amplitude of \hat{r}_k

r_{km} = maximum value of r_k

δ_k = phase lag of \hat{r}_k

α is taken with reference to the plane of incidence as shown in Fig. 2-1.

The magnitude of \vec{M} is constant at any point in a given specimen (except for the extremely small region in a domain wall), and hence the amplitude of r_k for a given specimen at a given wavelength is dependent wholly upon α . We see, then, that r_k has two extreme values, $-r_{km}$ and $+r_{km}$, one

*In these analyses, a carat over amplitude reflection coefficient indicates that the coefficient is complex. The coefficient written without the carat indicates the magnitude of the coefficient. We will assume it understood that the electric vectors can be complex and will not use any special sign to so indicate. An arrow over a quantity means that the quantity is a space vector.

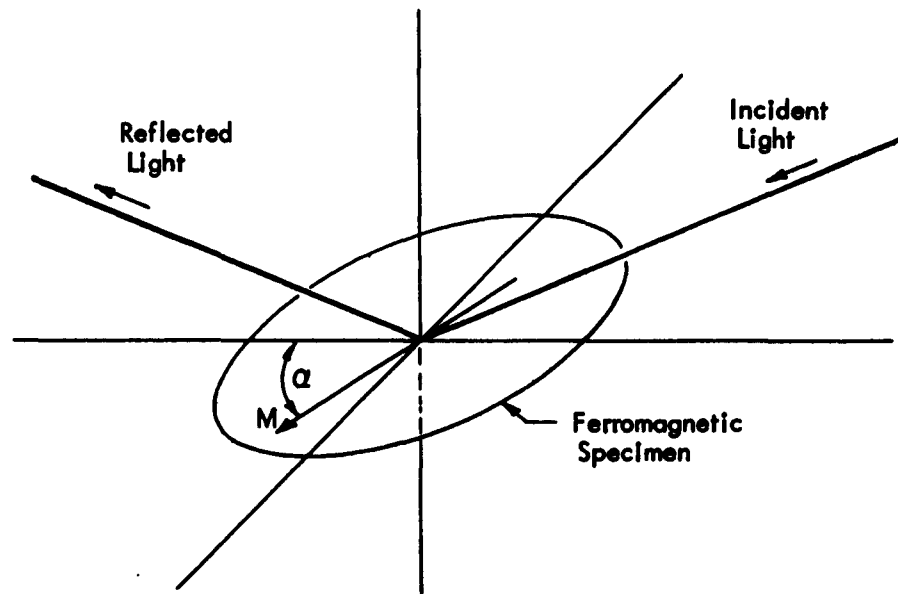


FIG. 2-1 REFERENCE ANGLE FOR MAGNETIZATION VECTOR

occurring when $\alpha = 180^\circ$, the other when $\alpha = 0^\circ$. We shall refer to these two extremes respectively as State I and State II.

Since r_{km} is quite small (on the order of 5×10^{-3} as we shall see later), a detailed analysis of the use of the longitudinal Kerr effect as an observation technique is desirable in order that optimum results can be achieved. A simplified schematic of the optical apparatus used in this project is shown in Fig. 2-2. The analyses in this chapter deal with the passage of light from the light source to the point preceding the shutter. The primary results desired from these analyses are:

1. The light transmission factor over the optical path mentioned above, taking into account the adjustments of the polarizers, the characteristics of the specimen, and the state of magnetization of the specimen.
2. The ratio between the transmission factor in State II and the transmission factor in State I.
3. The effects of the polarizer quality on the transmission factor and on the ratio mentioned above.
4. Determination of the optimum operating condition of the apparatus for a given specimen.
5. The effect of a thin dielectric layer on top of the specimen.

Any exact numerical correlation between the results of these analyses and the data obtained from the experimental apparatus would require instrumentation which has not been included in this project. Nonetheless, the writer believes the analyses to be significant in that the results indicate some limitations of the techniques being used and serve as a guide for achieving optimum results with the apparatus.

2.1 Reflection Coefficients

Before we undertake the transmission analyses, it is desirable to know something about the complex reflection coefficients involved. All numerical computations for these coefficients are based on Robinson's data for

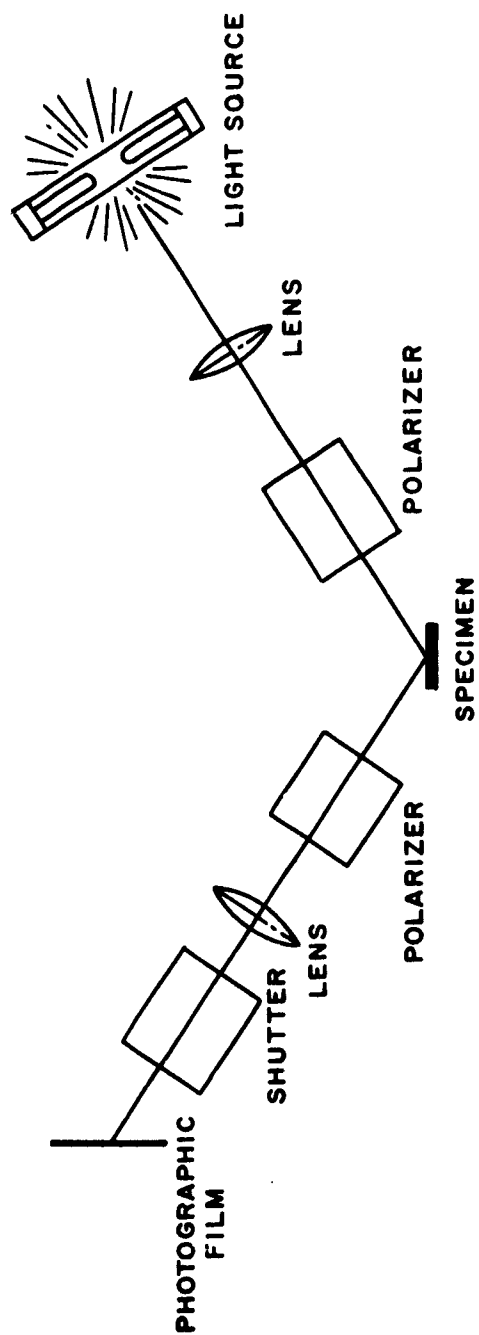


FIG. 2-2 SIMPLIFIED MAGNETO-OPTIC PHOTOGRAPHIC SYSTEM

permalloy films¹ (see Fig. 2-3), since this is the material under immediate investigation in this project.

The reference axes used in all analyses are shown in Fig. 2-4. Note that the positive z direction is always the same as the direction of light propagation. The x direction is always perpendicular to the plane of incidence. In all vector diagrams shown in this chapter, the positive z direction is to be taken as coming out of the page. The positive x direction is then to the right and the positive y direction is upward.

The amplitude reflection of light from a magnetized specimen is given by the matrix equation

$$\begin{bmatrix} \hat{r}_x & \hat{r}_k \\ -\hat{r}_k & \hat{r}_y \end{bmatrix} \begin{bmatrix} E_{ox} \\ E_{oy} \end{bmatrix} = \begin{bmatrix} E_{rx} \\ E_{ry} \end{bmatrix} \quad (\text{II-3})$$

\hat{r}_x and \hat{r}_y are the ordinary amplitude reflection coefficients given by the Fresnel equations

$$\hat{r}_x = \frac{n_o \cos \theta_o - n_2 \cos \theta_2}{n_o \cos \theta_o + n_2 \cos \theta_2} = r_x \exp[j\delta_x] \quad (\text{II-4a})$$

$$\hat{r}_y = \frac{n_2 \cos \theta_o - n_o \cos \theta_2}{n_2 \cos \theta_o + n_o \cos \theta_2} = r_y \exp[j\delta_y] \quad (\text{II-4b})$$

\hat{r}_k is the Kerr magneto-optic amplitude reflection coefficient given by Robinson's equation²

$$\hat{r}_k = \frac{-jQ \cos \theta_o \sin \theta_o}{(\cos \theta_o + N \cos \theta_2)(N \cos \theta_o + \cos \theta_2)} \quad (\text{II-4c})$$

In Eqs. (II-4a) through (II-4c),

n_o = index of refraction of air

n_2 = index of refraction of specimen

N = relative index of refraction of specimen with respect to adjacent medium

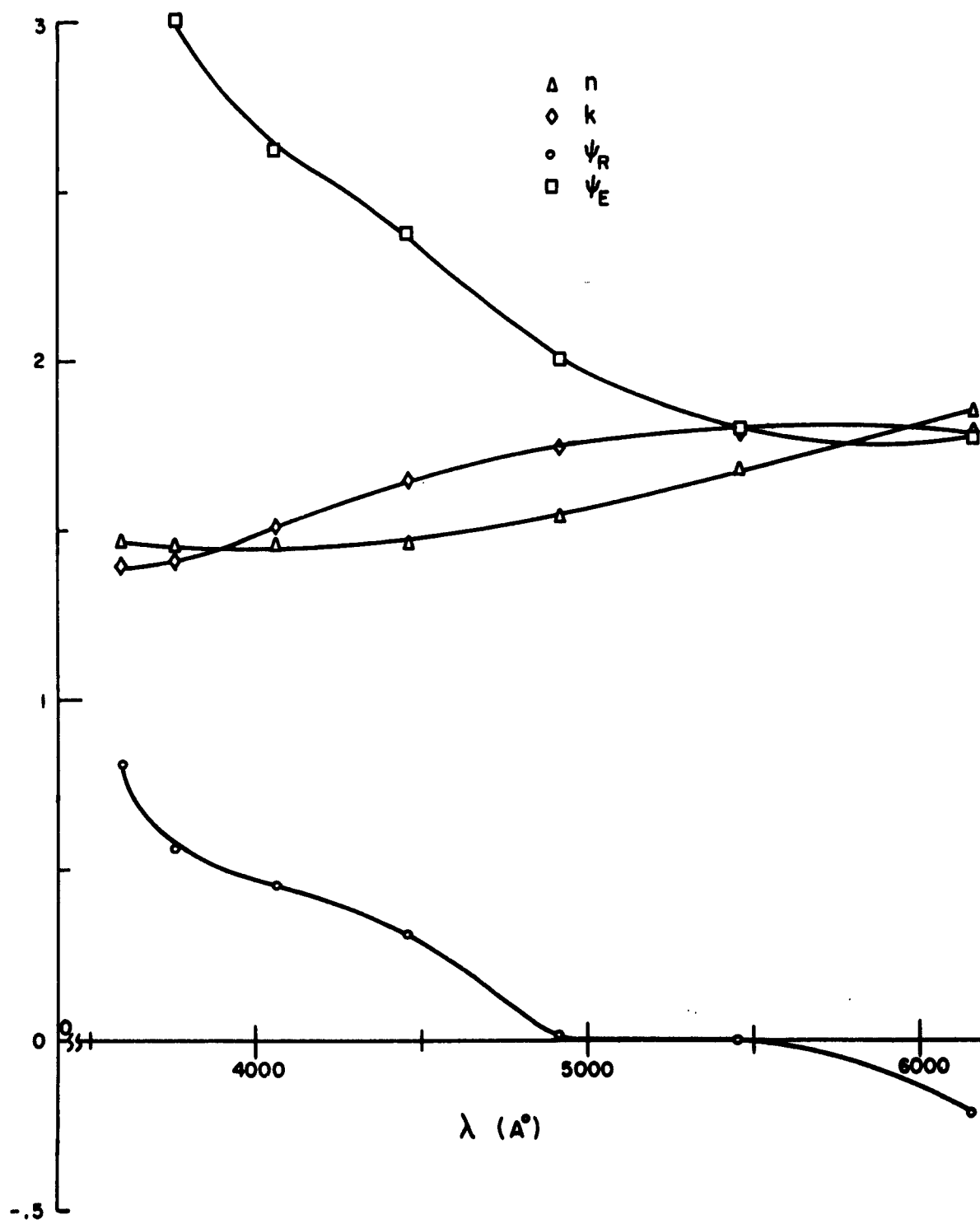


FIG. 2-3 OPTICAL DATA FOR PERMALLOY FILM

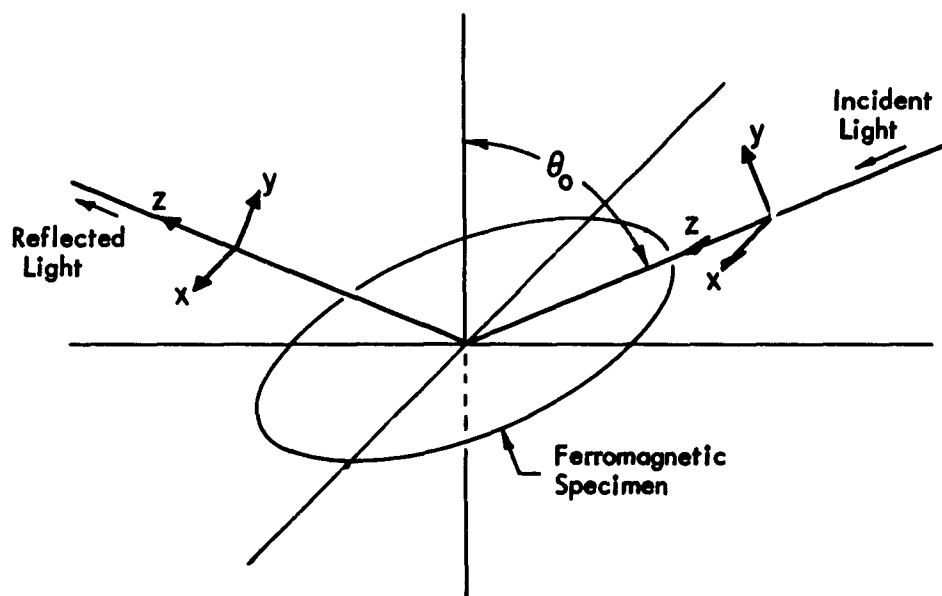


FIG. 2-4 OPTICAL REFERENCE AXES

θ_0 = angle of reflected wave

θ_2 = angle of refracted wave

Q = complex magneto-optic parameter of specimen

δ_x = time phase of \hat{r}_x

δ_y = time phase of \hat{r}_y

δ_k = time phase of \hat{r}_k

In the case of metallic reflection which we are considering,

$$\begin{aligned} n_2 &= n(1 - jk) & N &= \frac{n_2}{n_0} = n(1 - jk) \\ n_0 &= 1 & \cos \theta_2 &\approx 1 \end{aligned}$$

yielding

$$\hat{r}_x = \frac{\cos \theta_0 - n(1 - jk)}{\cos \theta_0 + n(1 - jk)} \quad (\text{II-5a})$$

$$\hat{r}_y = \frac{n(1 - jk) \cos \theta_0 - 1}{n(1 - jk) \cos \theta_0 + 1} \quad (\text{II-5b})$$

$$\hat{r}_k = \frac{-j Q \sin \theta_0 \cos \theta_0}{[n(1 - jk) \cos \theta_0 + 1] [\cos \theta_0 + n(1 - jk)]} \quad (\text{II-5c})$$

The experimental data for the magneto-optic effect is usually given in terms of Ψ_R and Ψ_E where Ψ_R is the space angle of the major axis of the reflected ellipsoidally polarized light with respect to the incident light and Ψ_E is the ellipticity of the reflected light, given by the ratio of the minor axis to the major axis of the ellipse. For our analysis, however, it is much more convenient to work in terms of the magneto-optic reflection coefficient, \hat{r}_k . If we consider incident linearly polarized light of amplitude E_0 and oriented in the y direction, the reflected light from a

magnetized specimen is given by

$$\begin{aligned}\vec{E}_r &= E_o \left[\vec{i}_y \hat{r}_y + \vec{i}_x \hat{r}_k \right] \\ &= E_o \left[\vec{i}_y r_y + \vec{i}_x r_k \cos(\delta_k - \delta_y) + \vec{i}_x j r_k \sin(\delta_k - \delta_y) \right] \exp[j\delta_y]\end{aligned}\quad (\text{II-6})$$

Since $r_k \ll r_y$, Ψ_R and Ψ_E are very closely given by

$$\Psi_R = \frac{r_k}{r_y} \cos(\delta_k - \delta_y) \quad (\text{II-7a})$$

$$\Psi_E = \frac{r_k}{r_y} \sin(\delta_k - \delta_y) \quad (\text{II-7b})$$

From these equations,

$$r_k^2 = (\Psi_R^2 + \Psi_E^2) r_y^2 \quad (\text{II-8a})$$

$$(\delta_k - \delta_y) = \tan^{-1} \frac{\Psi_E}{\Psi_R} \quad (\text{II-8b})$$

Robinson's experimental data for permalloy films can be used with these relationships to compute the reflection coefficients and their phase angles for an angle of incidence of 60° (the angle of incidence used in the magneto-optic apparatus for reasons stated in Chapter IV). It is unnecessary to present here the algebraic computations; the results are shown in Figs. 2-5 and 2-6. No values were computed for $\lambda < 4000 \text{ \AA}$, since the photographic system has a spectral cutoff for wavelengths shorter than 4300 \AA (see Chapter V).

2.2 Monochromatic Analysis

We shall now undertake a fairly exact analysis of the transmission factors for the case of a monochromatic source. This analysis is based

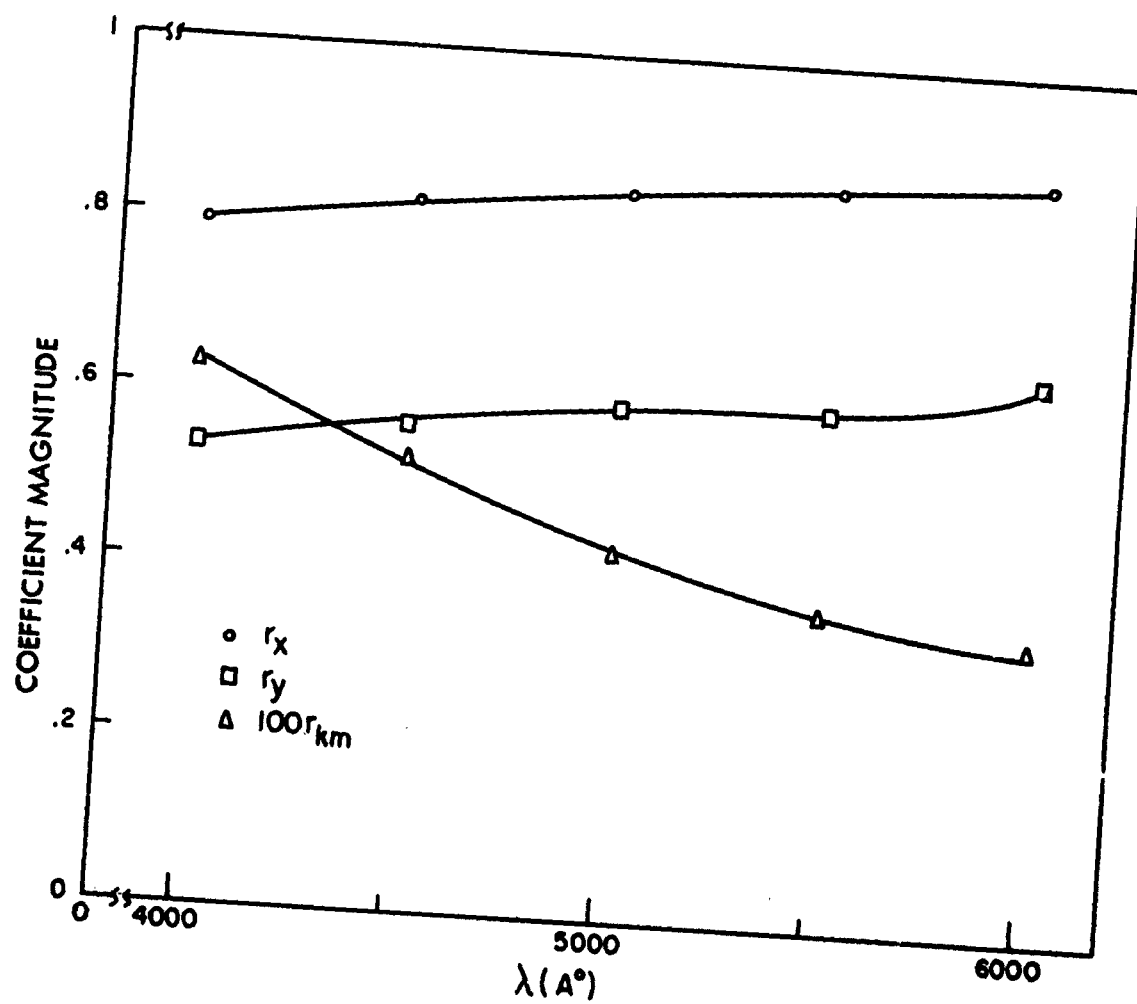


FIG. 2-5 MAGNITUDE OF PERMALLOY REFLECTION COEFFICIENTS

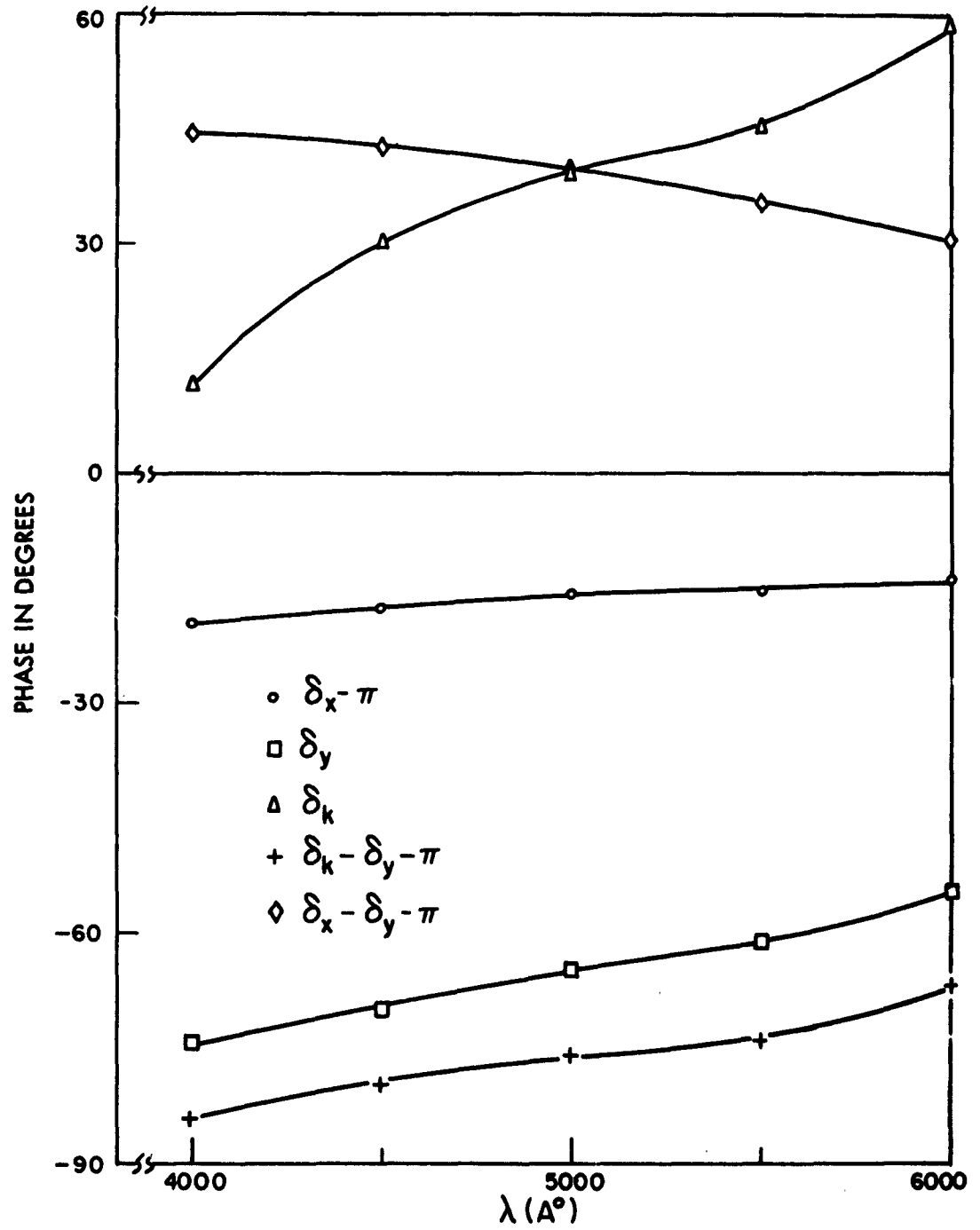


FIG. 2-6 PHASE OF PERMALLOY REFLECTION COEFFICIENTS

on the assumption that the incoming plane of light polarization is very nearly either parallel to or perpendicular to the plane of incidence. For a general analysis using matrix algebra, see Appendix A.

Before we begin the analysis we will define a few characteristics of a polarizer. In Fig. 2-7, we have shown a polarizer with an incident plane wave of random amplitude vector orientation.

In this figure the polarizer is so oriented that the desired transmitted amplitude vector is vertical. Since a polarizer is never perfect, there is an undesired amplitude vector also transmitted; this is shown as a horizontal vector in the figure. We shall refer to the desired vector as the principal component of transmission and to the plane formed by this vector and the optic axis as the principal plane of the polarizer. The corresponding vector and plane of the undesired component are denoted respectively as the minor component and minor plane. If the incident light E_o is unpolarized, it can be regarded as the sum of two waves, $\frac{E_{op}}{\sqrt{2}}$ which lies in the principal plane of the polarizer, and $\frac{E_{om}}{\sqrt{2}}$ which lies in the minor plane. Here

$$\left| E_{op} \right| = \left| E_{om} \right| = \left| E_o \right| \quad (\text{II-9})$$

the subscripts p and m merely being used to distinguish between the two polarization planes. We note that E_{op} and E_{om} are random with respect to one another, i.e., the time average of their product is zero.

We shall denote the principal transmission of the polarizer as t_1 and the minor transmission as t_2 . The ratio of these two transmissions will be referred to as the extinction ratio, R_e , i.e.,

$$R_e = \frac{t_2}{t_1} \quad (\text{II-10})$$

For any polarizer which we shall consider, $R_e \ll 1$.

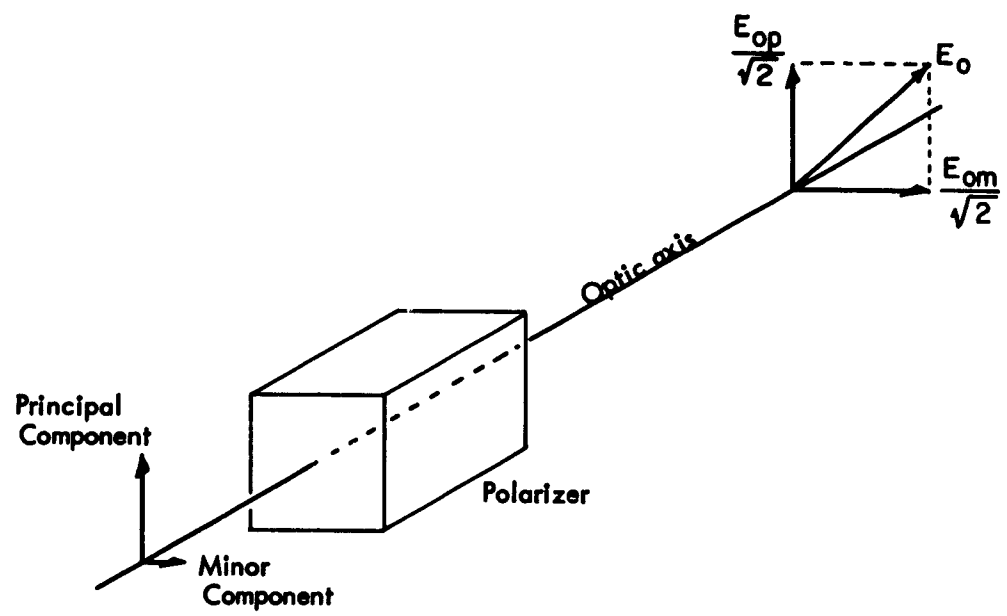


FIG. 2-7 POLARIZER TRANSMISSION

We shall now proceed with our analysis. Assume the initial polarizer in the system so oriented that there is an angle γ between the plane of incidence and the principal plane of the polarizer. Then if the amplitude of the light incident upon the prism is E_o , as mentioned above, the light transmitted by this polarizer is

$$\vec{E}_T = \frac{t_1}{\sqrt{2}} \left[\vec{i}_x (E_{op} \sin \gamma + R_e E_{om} \cos \gamma) + \vec{i}_y (E_{op} \cos \gamma - R_e E_{om} \sin \gamma) \right] \quad (\text{II-11})$$

If we assume γ to be small and neglect second order terms (remembering that $R_e \ll 1$), we can write this as

$$\vec{E}_T = \frac{t_1}{\sqrt{2}} \left[\vec{i}_x (E_{op} \gamma + R_e E_{om}) + \vec{i}_y E_{op} \right] \quad (\text{II-11a})$$

The reflected amplitude wave from the specimen surface can be obtained by substituting the x and y components of Eq. (II-11a) into Eq. (II-3). In vector form, the reflected amplitude wave is

$$\vec{E}_R = \frac{t_1}{\sqrt{2}} \left\{ \vec{i}_x [E_{op} (\gamma \hat{r}_x + \hat{r}_k) + R_e E_{om} \hat{r}_x] + \vec{i}_y E_{op} \hat{r}_y \right\} \quad (\text{II-12})$$

where we have dropped terms containing $\hat{r}_k R_e$ and $\hat{r}_k \gamma$ since they are second order. The vector diagram at this point is shown in Fig. 2-9.

The reflected light then passes through the second polarizer which is so oriented that its minor plane makes an angle ϕ with the plane of incidence, the major plane coinciding with the a-axis shown in Fig. 2-10. If ϕ is small, the light transmitted by this polarizer can be represented by

$$\vec{E}_A = \vec{i}_a t_1 \{ [E_{Rx} + \phi E_{Ry}] + \vec{i}_b R_e [E_{Ry} - \phi E_{Rx}] \} \quad (\text{II-13})$$

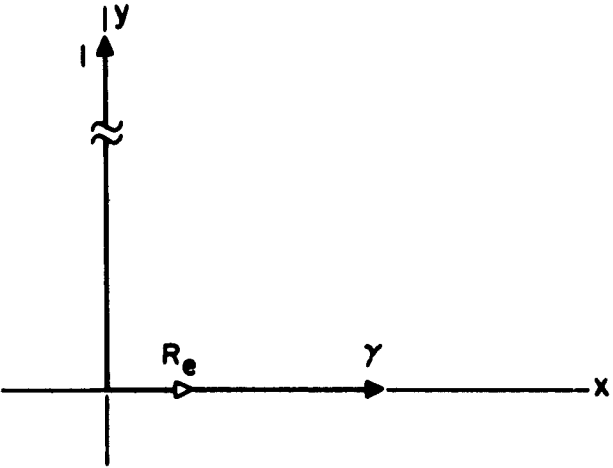


FIG. 2-8 AMPLITUDE VECTORS AFTER FIRST POLARIZER

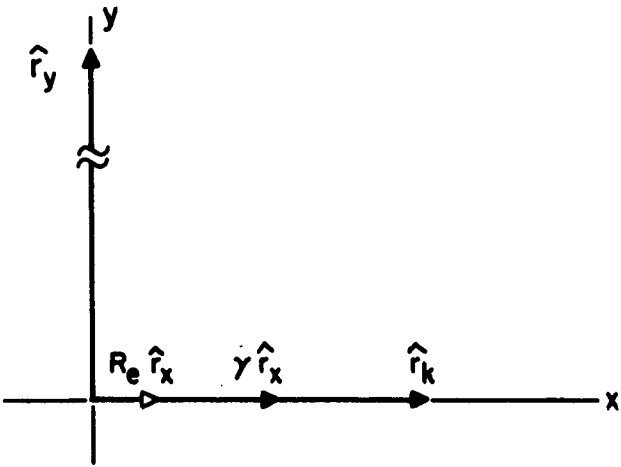


FIG. 2-9 AMPLITUDE VECTORS AFTER REFLECTION

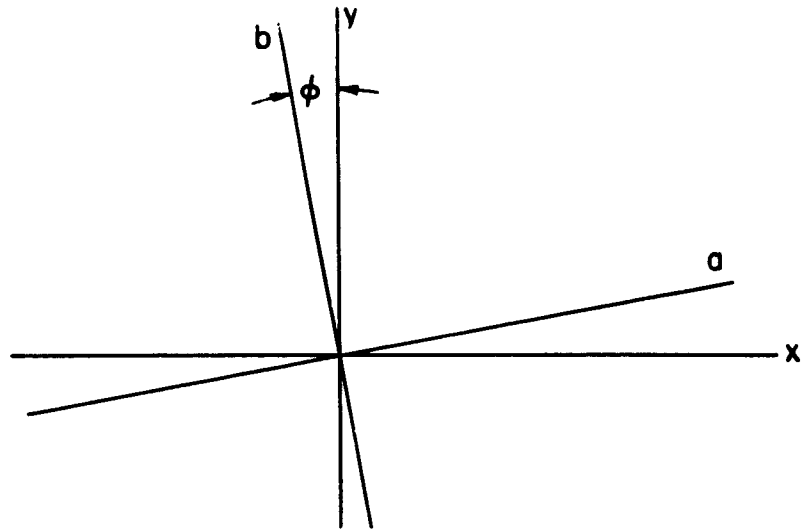


FIG. 2-10 ROTATION OF REFERENCE AXES

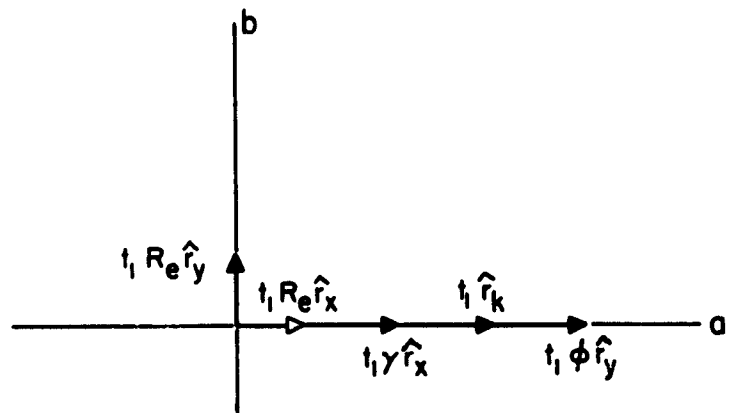


FIG. 2-11 AMPLITUDE VECTORS AFTER SECOND POLARIZER

In this expression E_{Rx} and E_{Ry} are the coefficients of \vec{i}_x and \vec{i}_y respectively in Eq. (II-12). The reference vectors \vec{i}_a and \vec{i}_b , which coincide respectively with the major and minor planes of the second polarizer, have been introduced to simplify subsequent calculations. Continuing, we have, upon substituting the expressions for E_{Rx} and E_{Ry} into Eq. (II-13) and rearranging the terms,

$$\begin{aligned} \vec{E}_A = & \vec{i}_a \frac{t_1^2}{\sqrt{2}} E_{op} [\gamma \hat{r}_x + \hat{r}_k + \phi \hat{r}_y] \\ & + \frac{t_1^2 R_e}{\sqrt{2}} [\vec{i}_a E_{om} \hat{r}_x + \vec{i}_b E_{op} \hat{r}_y] \\ & - \vec{i}_b \frac{t_1^2 R_e \phi}{\sqrt{2}} [E_{op} (\gamma \hat{r}_x + \hat{r}_k) + R_e E_{om} \hat{r}_x] \end{aligned} \quad (II-14)$$

If we examine Eq. (II-14), we note that because of the magnitudes of R_e , \hat{r}_k , γ , and ϕ , the terms in the third line of the equation are much smaller than those in the first two lines. Hence we will drop this third line from further calculations. The vector diagram for the remaining two lines of Eq. (II-14) is shown in Fig. 2-11. Note that the amplitude of two of these vectors are dependent on the orientations of the two polarizers, a third is dependent upon the Kerr amplitude reflection coefficient, while the remaining two are dependent only upon the polarizer characteristics and the ordinary amplitude reflection coefficients \hat{r}_x and \hat{r}_y of the specimen. The three vectors corresponding to E_{op} on the a-axis are coherent with one another, although their time phases differ.

The intensity of the light of which \vec{E}_A is the amplitude vector is given by the time average of the dot product of the amplitude vector and its complex conjugate.

Using Eq. (II-9),

$$\begin{aligned}
 I &= \vec{E}_A \cdot \vec{E}_A^* \\
 &= \frac{t_1^4}{2} E_{op}^2 \left[(\gamma \hat{r}_x + \hat{r}_k + \phi \hat{r}_y) (\gamma \hat{r}_x^* + \hat{r}_k^* + \phi \hat{r}_y^*) + (r_x^2 + r_y^2) R_e^2 \right]
 \end{aligned}
 \tag{II-15}$$

As previously stated, the term $(r_x^2 + r_y^2) R_e^2$ is a function only of the characteristics of the specimen and of the polarizers. Hence, it can be treated as a background noise which we can minimize by a choice of good polarizers but cannot eliminate in the practical situation. In all further calculations, it will be represented by

$$N = (r_x^2 + r_y^2) R_e^2 \tag{II-16a}$$

If we also write

$$P = [\hat{r}_k + \gamma \hat{r}_x + \phi \hat{r}_y] \tag{II-16b}$$

Eq. (II-15) can be written as

$$I = \frac{t_1^4}{2} E_{op}^2 (PP^* + N) \tag{II-17}$$

The transmission from the source to the point under present consideration is then simply

$$T = \frac{t_1^4}{2} (PP^* + N) \tag{II-18}$$

At this point we will introduce the contrast ratio, R_c , which we will define as the ratio of the transmission factor in State II to the transmission

factor in State I, i.e.,

$$R_c = \frac{T_2}{T_1} \quad (\text{II-19})$$

It is possible to manipulate Eq. (II-15) to show that as γ and ϕ are varied the loci of constant contrast on the $\gamma - \phi$ plane are ellipses whose centers are located on a line passing through the origin. An example of such a plot is shown in Fig. 2-12. We now wish to determine the point on a given ellipse for which the transmission T_2 is at a maximum. The determination of this relationship between γ and ϕ could be performed by calculus, but it is more simply done by examining the phases of the terms in P (Eq. II-16b). We will write these terms as two complex quantities.

$$A = (\gamma \hat{r}_x + \phi \hat{r}_y) \quad (\text{II-20a})$$

$$B = \hat{r}_{km} \cos \alpha \quad (\text{II-20b})$$

where we have used Eq. (II-2) in writing Eq. (II-20b). In State I, $B = B_1 = -r_{km}$, while in State II, $B = B_2 = r_{km}$. The three quantities A , B_1 , and B_2 are shown on a complex plane in Fig. 2-13, as well as the quantities P_1 and P_2 (the values of P in States I and II).

Obviously,

$$P_1 = A + B_1 \quad (\text{II-21a})$$

$$P_2 = A + B_2 \quad (\text{II-21b})$$

In this figure we show the loci of P_2 , A , and P_1 as A is varied keeping P_2 constant. It is immediately evident that P_1 is at a minimum when A is in phase with B_2 . The contrast ratio can be written as

$$R_c = \frac{P_2 P_2^* + N}{P_1 P_1^* + N} \quad (\text{II-21c})$$

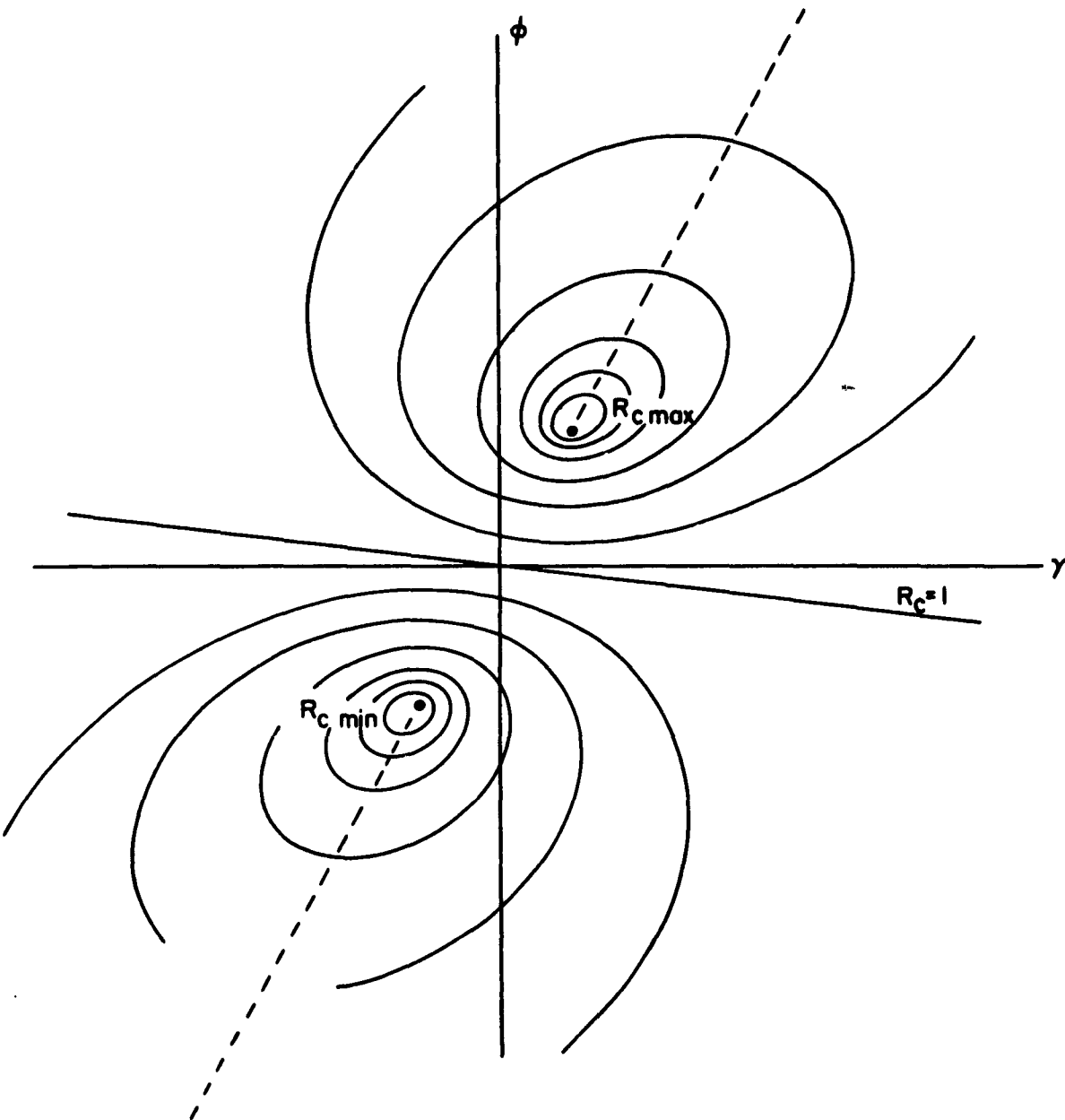


FIG. 2-12 LOCI OF CONSTANT CONTRAST

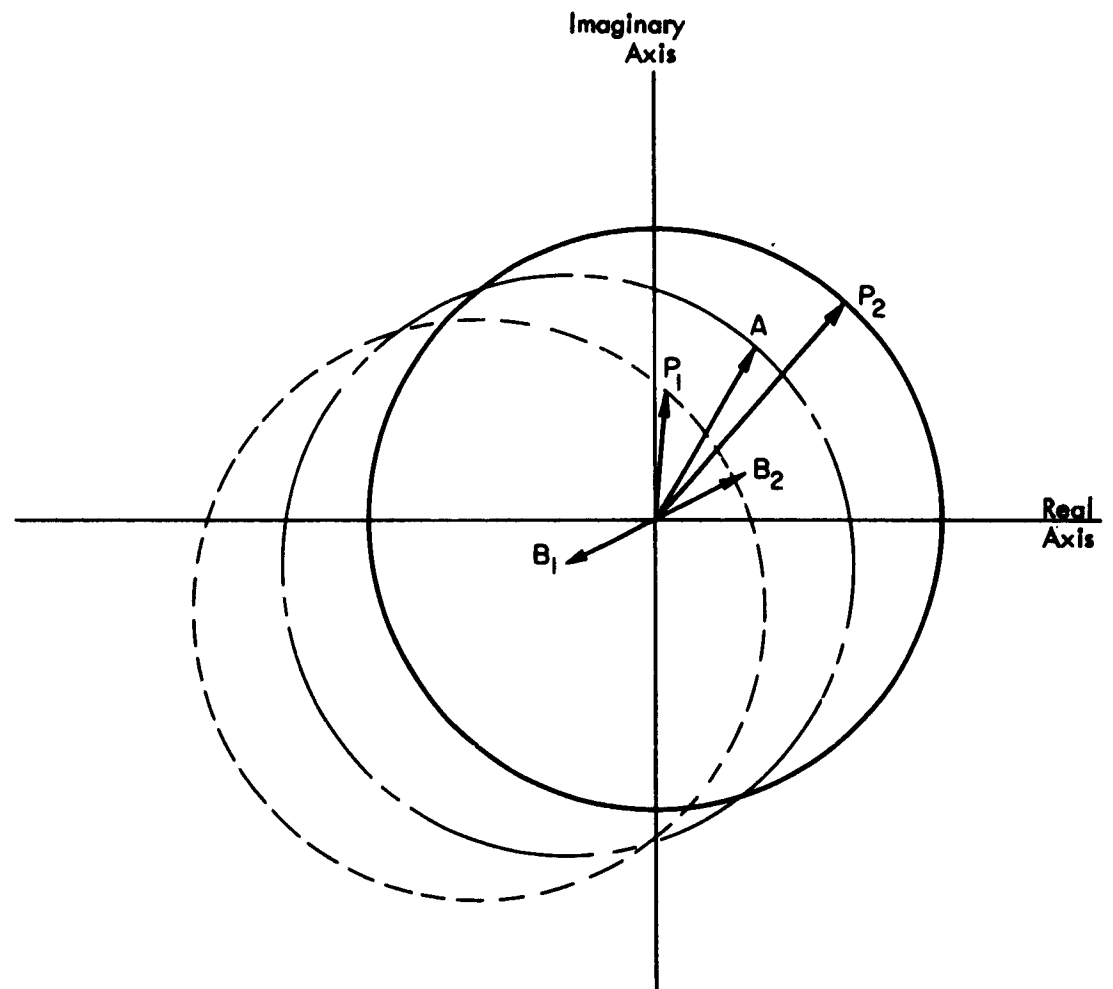


FIG. 2-13 VARIATION OF P-VECTORS

The quantity $P_1 P_1^*$ is always positive; hence R_c is at a maximum for a given value of P_2 when P_1 is at its minimum. The relationship between γ and ϕ for this to occur is given by

$$\gamma r_x \sin(\delta_x - \delta_k) + \phi r_y \sin(\delta_y - \delta_k) = 0 \quad (\text{II-22})$$

from which

$$\phi = -\gamma \frac{r_x}{r_y} \frac{\sin(\delta_k - \delta_x)}{\sin(\delta_k - \delta_y)} \quad (\text{II-23})$$

Substituting this result in Eq. (II-20a)

$$A = \gamma r_x \frac{\sin(\delta_x - \delta_y)}{\sin(\delta_k - \delta_y)} \quad (\text{II-24})$$

We see, then, that A can always be made any value so long as $\delta_y \neq \delta_x$. Although it appears that the value of A is indeterminant when $\delta_y = \delta_k$, this is not actually true, as can be readily seen by evaluating Eqs. (II-22) and (II-20a) for this special case. From Eq. (II-22) we see that γ would be zero, resolving the indeterminacy of Eq. (II-24), and that A in this case would be

$$A = \phi r_y \quad (\text{II-24a})$$

Substituting Eqs. (II-16b) and (II-24) into Eq. (II-18), we find that

$$T = \frac{t_1^4}{2} \left[\left(\gamma r_x \frac{\sin(\delta_x - \delta_y)}{\sin(\delta_k - \delta_y)} + r_{km} \cos \alpha \right)^2 + N \right] \quad (\text{II-25})$$

If we now normalize T to $\frac{t_1^4}{2} r_{km}^2$ and let

$$\Gamma = \frac{\gamma r_x}{r_{km}} \frac{\sin(\delta_x - \delta_y)}{\sin(\delta_k - \delta_y)} \quad (\text{II-26a})$$

$$q^2 R_e^2 = \frac{N}{2 r_{km}} \quad (\text{II-26b})$$

then the normalized transmission factor is

$$T_n = T \left[\frac{2}{t_1^4 r_{km}^2} \right] = (\Gamma + \cos \alpha)^2 + q^2 R_e^2 \quad (\text{II-27})$$

and the normalized transmission factors for States I and II are

$$T_{2n} = (\Gamma + 1)^2 + q^2 R_e^2 \quad (\text{II-27a})$$

$$T_{1n} = (\Gamma - 1)^2 + q^2 R_e^2 \quad (\text{II-27b})$$

The behavior of Eqs. (II-27a) and (II-27b) as a function of Γ are shown in Fig. 2-14, for $R_e^2 q^2 = 0.5$. From this figure we can easily see the general behavior of the contrast ratio R_c as we vary Γ . When $\Gamma = 0$, $R_c = 1$. As we increase Γ , R_c increases, goes through a maximum and then asymptotically approaches unity. If we decrease Γ from zero, R_c decreases, goes through a minimum, and then asymptotically approaches unity. An example of the R_c behavior is also given in Fig. 2-13.

Obviously, for any given value of R_c such that

$$R_{c \min} < R_c < R_{c \max}$$

and for a given value of $R_e^2 q^2$ there are two possible values of T_{2n} . Since we wish to have as high a transmission factor as possible in State II for the

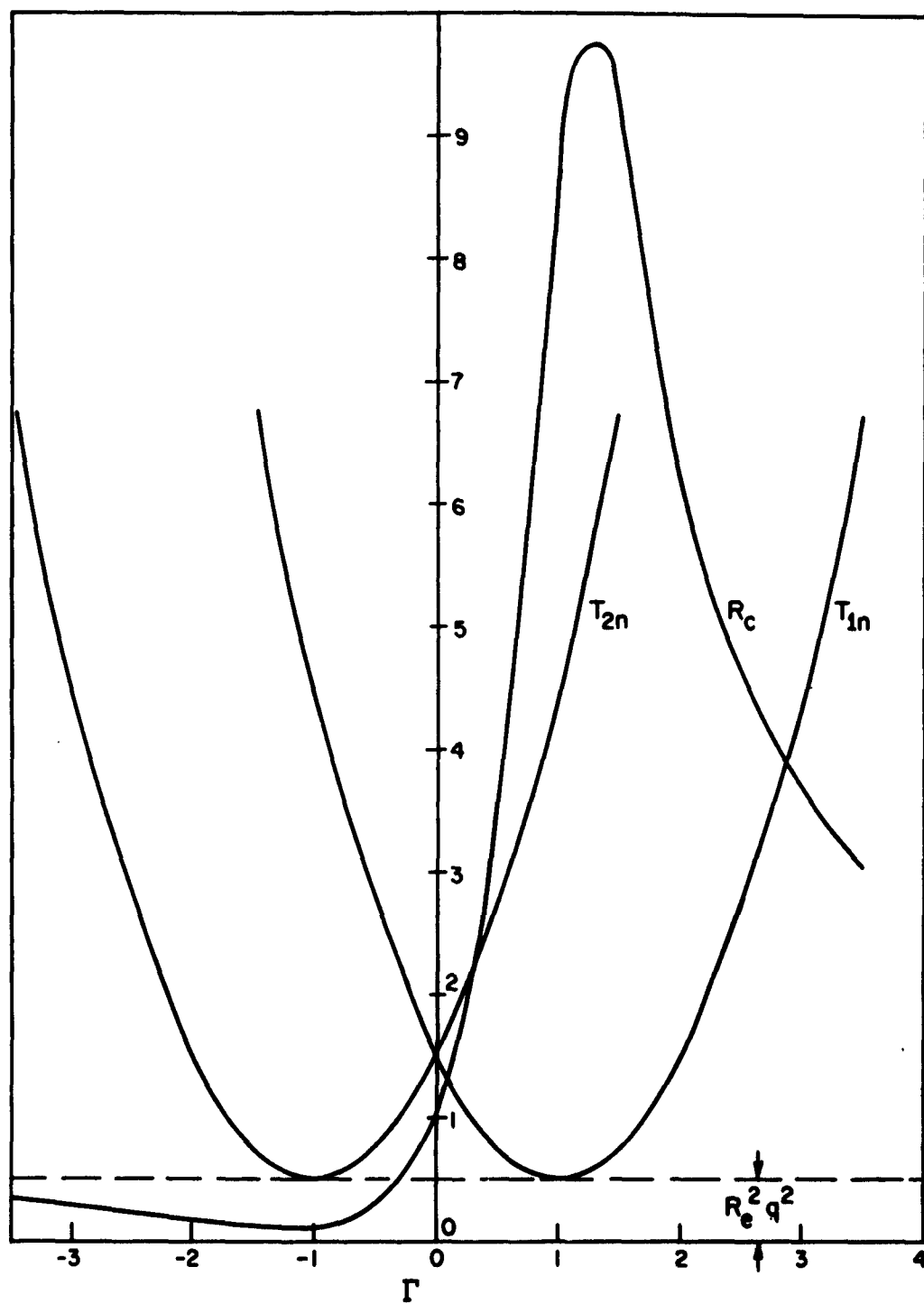


FIG. 2-14 CONTRAST RATIO AND NORMALIZED TRANSMISSION

given R_c value, the system would be operated at the higher of the two values.

The contrast ratio can be written in terms of the normalized functions Γ and $R_e^2 q^2$

$$R_c = \frac{(\Gamma + 1) + R_e^2 q^2}{(\Gamma + 1) - R_e^2 q^2} \quad (\text{II-28})$$

We can maximize Eq. (II-28) with respect to Γ (and hence to γ) by setting $\frac{dR_c}{d\Gamma} = 0$. We find that the condition for the maximum is

$$\Gamma = \sqrt{1 + R_e^2 q^2} \quad (\text{II-29a})$$

and therefore

$$R_{c \max} = 1 + \frac{2}{R_e^2 q^2} \left[1 + \sqrt{1 + R_e^2 q^2} \right] \quad (\text{II-29b})$$

$R_{c \max}$ as a function of $R_e^2 q^2$ is plotted in Fig. 2-15. We note that the smaller the value of $R_e^2 q^2$, the higher the maximum contrast. This is intuitively obvious, since a smaller value of $R_e^2 q^2$ means either a lower background noise or a higher r_{km} , and either of these means a higher maximum contrast ratio.

If we solve Eq. (II-28) for Γ as a function of R_c and $R_e^2 q^2$ and use the result to eliminate Γ from Eq. (II-27a), we find that the normalized State II transmission factor as a function of R_c and $R_e^2 q^2$ is

$$T_{2n} = \left[\frac{4R_c}{R_c - 1} \right] \left[\frac{R_c + 1}{R_c - 1} \right] \left[1 \pm \sqrt{1 - (1 + R_e^2 q^2) \left(\frac{R_c - 1}{R_c + 1} \right)^2} \right] \quad (\text{II-30})$$

If we designate Γ_{\max} as the Γ value at $R_{c \max}$, then the plus sign in Eq. (II-30) applies when $\Gamma > \Gamma_{\max}$, while the minus sign applies for

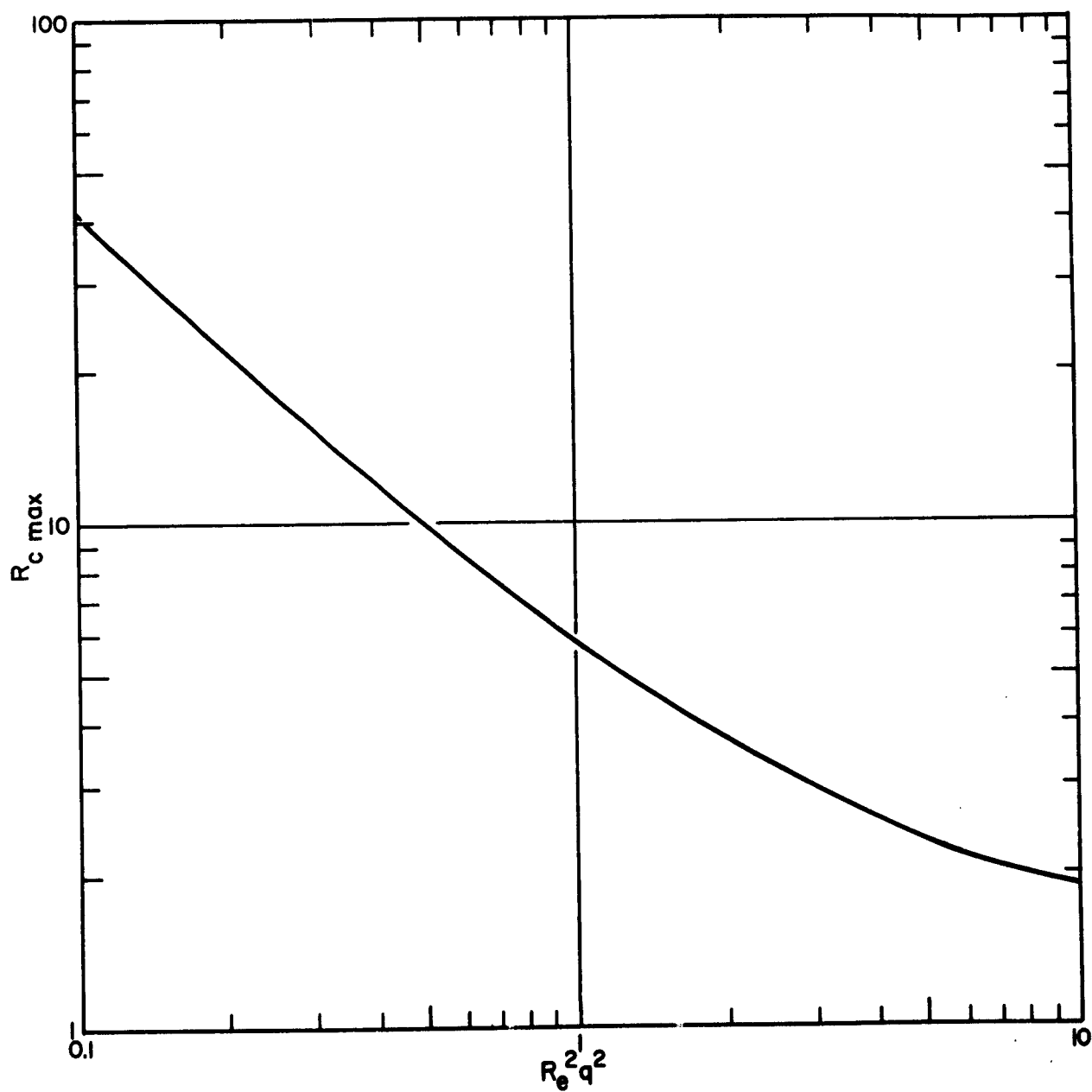


FIG. 2-15 MAXIMUM CONTRAST RATIO (MONOCHROMATIC)

$\Gamma < \Gamma_{\max}$. Examination of Eq. (II-30) reveals that the value of the radical is always less than unity; hence, the plus sign yields the higher T_{2n} value. Eq. (II-30) is plotted as a function of R_c with $R_e^2 q^2$ as a parameter (for the plus sign only) in Fig. 2-16.

It is interesting to note that, if we select some given contrast value at which to operate, decreasing $R_e^2 q^2$ gives only limited dividends in transmission. Suppose, for example, we select $R_c = 5.8$. From Fig. 2-15, we see that the maximum allowable $R_e^2 q^2$ value is unity. From Fig. 2-16, we find that under these circumstances $T_{2n} = 6.83$. As $R_e^2 q^2$ is decreased to zero, the value of T_{2n} increases to 11.8, about a 50 per cent increase.

We also note from Fig. 2-16 that if we are willing to sacrifice contrast ratio, we can gain in T_{2n} transmission. For example, when $R_e^2 q^2 = 1$ and $R_c = R_{c \max} = 5.83$, $T_{2n} = 6.83$. If, however, we are willing to work at a contrast ratio of $R_c = 2$, for this value of $R_e^2 q^2$ we find that $T_{2n} = 23$, almost a four-fold increase over that at maximum contrast ratio.

If we arbitrarily set a minimum working contrast ratio of two, we find from Eq. (II-33) that

$$R_e^2 q^2 \leq 8$$

and therefore

$$\frac{(r_x^2 + r_y^2) R_e^2}{r_{km}^2} \leq 8$$

Then

$$R_e^2 \leq \frac{8 r_{km}^2}{r_x^2 + r_y^2}$$

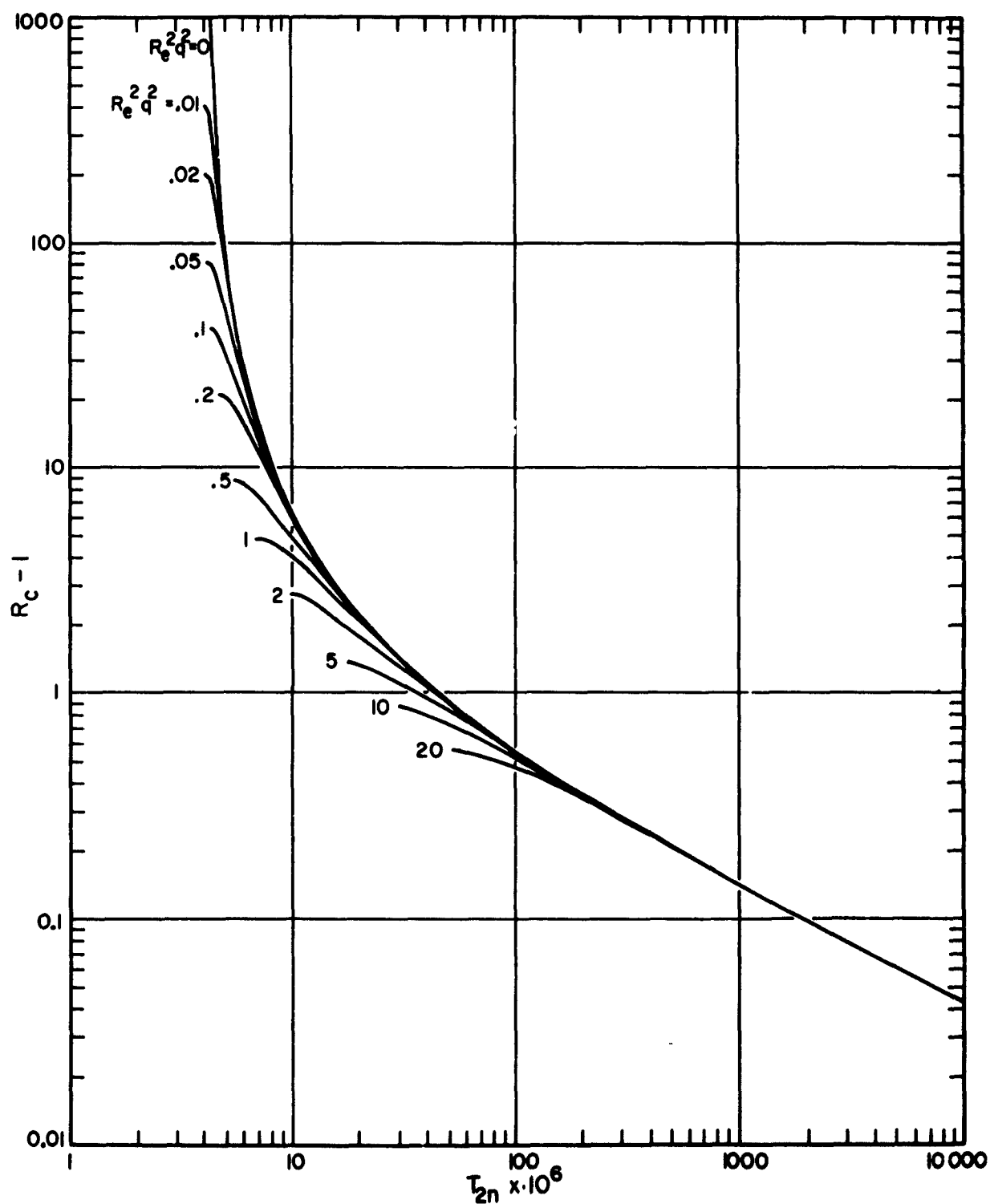


FIG. 2-16 NORMALIZED MONOCHROMATIC TRANSMISSION
VS CONTRAST RATIO

Evaluating this for the extremes encountered according to Fig. 2-4 we find that at 6000 Å

$$R_e^2 \leq .00033$$

and at 4000 Å

$$R_e^2 \leq .000077$$

The t_1^2 and t_2^2 characteristics of a number of available polarizers are shown in Fig. 2-17. The squared extinction ratios for these polarizers at 4300 Å and 6000 Å, computed from this data are listed in Table II-1. As can be seen from this table, the Glan-Thompson prism and the Polaroid HN-22 are the only polarizers which meet the R_e^2 requirements which we have just computed. The Polaroid HN-22, however, has a t_1^2 value varying from 0.35 to 0.56 in the bandwidth stated, as opposed to a t_1^2 value of 0.96 for the Glan-Thompson prism. From Eq. (II-28b) we see that the transmission T_2 is proportional to t_1^4 . This means that use of the Polaroid HN-22 would result in a reduction of T_2 by a factor of 3 to

TABLE II-1

EXTINCTION RATIOS OF POLARIZERS

Polarizer	R_e^2 (4300 Å)	R_e^2 (6000 Å)
Polaroid HN-38	.04	.000375
" HN-32	.002	.000027
" KN-36	.00083	.0000375
" HN-22	.0000154	.0000048
Glan-Thompson Prism	.0000041	.0000041

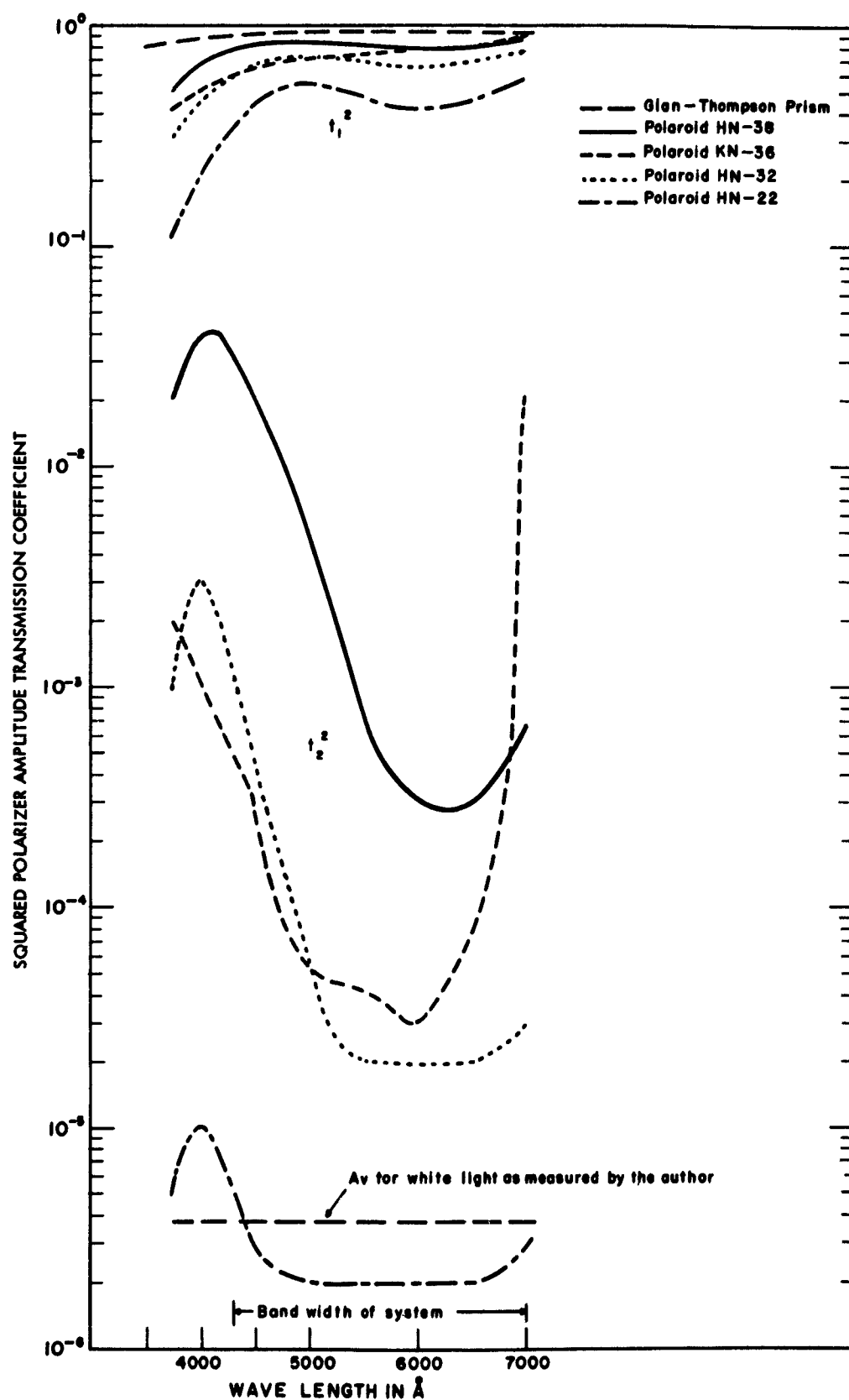


FIG. 2-17 TRANSMISSION CHARACTERISTICS OF POLARIZERS

8.5, depending on the wavelength, over that available with Glan-Thompson prisms. The necessity of operating at as high a T_2 value as possible in addition to the high extinction ratio of Glan-Thompson prisms dictates their use in this apparatus.

Therefore, for $R_e^2 = 4.1 \times 10^{-6}$ we find from Robinson's data that R_{eq}^2 for permalloy films ranges from .0956 to .426 with corresponding values of $R_{c \max}$ from 45 to 13.

2.3 Analysis for white light source

The preceding analysis has dealt with the case of a monochromatic source. The present work requires a very high intensity source for reasons which will become apparent in Chapter III. Such sources are unavailable, except as a white light source with a monochromatic filter. Since such filters inherently lessen the total light energy which can be transmitted through the system -- e.g., an interference filter with a 50 Å bandwidth will pass about 5 per cent of the total visible energy radiated from a white light source -- it is desirable to know the effects of substituting a white light source in place of the monochromatic source. We shall extend the previous analysis, using some simplifying approximations, to the case of a white light source.

If we consider a source of intensity I_0 per unit bandwidth, then the light transmitted over an incremental bandwidth $d\lambda$ is

$$Id\lambda = I_0 T d\lambda \quad (\text{II-31})$$

where T is the monochromatic transmission factor of Eq. (II-18). We will assume that the source has uniform intensity over its spectral range λ_3 to λ_4 . Then the total intensity transmitted is obtained by integrating Eq. (II-31) over the source spectral range, resulting in

$$\begin{aligned} \int_{\lambda_3}^{\lambda_4} Id\lambda &= \int_{\lambda_3}^{\lambda_4} I_0 T d\lambda \\ I(\lambda_4 - \lambda_3) &= I_0 \int_{\lambda_3}^{\lambda_4} T d\lambda \end{aligned} \quad (\text{II-32})$$

However, the transmission T is limited by the system spectral range, λ_1 to λ_2 (assuming that this lies entirely within the range λ_3 to λ_4). Hence the limits on the right side of Eq. (II-32) can be changed to the system limits, yielding after slight manipulation

$$\begin{aligned} T_w &= \frac{I}{I_0} \\ &= \frac{\mathcal{F}}{\lambda_2 - \lambda_1} \int_{\lambda_1}^{\lambda_2} T d\lambda \end{aligned} \quad (\text{II-32a})$$

where \mathcal{F} represents the loss from the system spectral limitation, i.e.,

$$\mathcal{F} = \frac{\lambda_2 - \lambda_1}{\lambda_4 - \lambda_3} \quad (\text{II-32b})$$

and T_w is the transmission factor for a white light source.

Substituting Eqs. (II-16b) and (II-18) into Eq. (II-32a), we have

$$T_w = \frac{t_1^4 \mathcal{F}}{2(\lambda_2 - \lambda_1)} \int_{\lambda_1}^{\lambda_2} \left[(\hat{r}_k + \gamma \hat{r}_x + \phi \hat{r}_y) (\hat{r}_k^* + \gamma \hat{r}_x^* + \phi \hat{r}_y^*) + N \right] d\lambda \quad (\text{II-33})$$

At this point we will introduce notation in the form of a bar over a quantity to represent averaging of the quantity over the spectral bandwidth, i.e.,

$$\bar{A} = \frac{1}{\lambda_2 - \lambda_1} \int_{\lambda_1}^{\lambda_2} A d\lambda$$

Carrying out the integration of Eq. (II-33), we then have

$$\begin{aligned} T_w &= \frac{t_1^4 \mathcal{F}}{2} \left[\overline{r_k^2} + \overline{r_x^2} \gamma^2 + \overline{r_y^2} \phi^2 + 2 \overline{r_k r_x \cos(\delta_k - \delta_x)} \gamma \right. \\ &\quad \left. + 2 \overline{r_k r_y \cos(\delta_k - \delta_y)} \phi + 2 \overline{r_x r_y \cos(\delta_x - \delta_y)} \phi \gamma + (\overline{r_x^2} + \overline{r_y^2}) R_e^2 \right] \end{aligned} \quad (\text{II-34})$$

In this form, the transmission equation is practically useless, since any maximization procedures become quite hopelessly involved. To resolve this dilemma, we will introduce an "average" P-vector similar to that of Eq. (II-14b).

$$\hat{P}_{av} = \bar{r}_{km} \exp[j\bar{\delta}_k] \cos \alpha + \bar{r}_x \exp[j\bar{\delta}_x] \gamma + \bar{r}_y \exp[j\bar{\delta}_y] \phi \quad (\text{II-35})$$

If we now both add and subtract the quantity $\hat{P}_{av} \hat{P}_{av}^*$ to Eq. (II-34) and at the same time normalize the transmission by dividing both sides of the equation by $t_1^4 \bar{r}_{km}^2 / 2$ we have

$$\begin{aligned} T_{wn} = & \frac{\hat{P}_{av} \hat{P}_{av}^*}{\bar{r}_{km}^2} + \frac{\bar{r}_x^2 + \bar{r}_y^2}{\bar{r}_{km}^2} R_e^2 + \left[\frac{\bar{r}_k^2 - \bar{r}_k^2}{\bar{r}_{km}^2} \right] + \left[\frac{\bar{r}_x^2 - \bar{r}_x^2}{\bar{r}_{km}^2} \right] \frac{\gamma^2}{\bar{r}_{km}^2} \\ & + \left[\frac{\bar{r}_y^2 - \bar{r}_y^2}{\bar{r}_{km}^2} \right] \frac{\phi^2}{\bar{r}_{km}^2} + 2 \left[\frac{\bar{r}_k \bar{r}_x \cos(\bar{\delta}_k - \bar{\delta}_x) - \bar{r}_k \bar{r}_x \cos(\bar{\delta}_k - \bar{\delta}_x)}{\bar{r}_{km}} \right] \left(\frac{\gamma}{\bar{r}_{km}} \right) \\ & + 2 \left[\frac{\bar{r}_k \bar{r}_y \cos(\bar{\delta}_k - \bar{\delta}_y) - \bar{r}_k \bar{r}_y \cos(\bar{\delta}_k - \bar{\delta}_y)}{\bar{r}_{km}} \right] \left(\frac{\phi}{\bar{r}_{km}} \right) \\ & + 2 \left[\frac{\bar{r}_x \bar{r}_y \cos(\bar{\delta}_x - \bar{\delta}_y) - \bar{r}_x \bar{r}_y \cos(\bar{\delta}_x - \bar{\delta}_y)}{\bar{r}_{km}} \right] \left(\frac{\phi}{\bar{r}_{km}} \right) \left(\frac{\gamma}{\bar{r}_{km}} \right) \end{aligned} \quad (\text{II-36})$$

Letting

$$q_p^2 = \frac{\bar{r}_x^2 + \bar{r}_y^2}{\bar{r}_k^2} \quad (\text{II-37a})$$

$$q_{km}^2 = \frac{\overline{r_{km}}^2 - \overline{r_{km}}^2}{\overline{r_{km}}^2} \quad (\text{II-37b})$$

$$q_x^2 = \overline{r_x}^2 - \overline{r_x}^2 \quad (\text{II-37c})$$

$$q_y^2 = \overline{r_y}^2 - \overline{r_y}^2 \quad (\text{II-37d})$$

$$q_{kx} = \frac{\overline{r_k r_x \cos(\delta_k - \delta_x)} - \overline{r_k} \overline{r_x} \cos(\overline{\delta_k} - \overline{\delta_x})}{\overline{r_{km}}} \quad (\text{II-37e})$$

$$q_{ky} = \frac{\overline{r_x r_y \cos(\delta_k - \delta_y)} - \overline{r_k} \overline{r_y} \cos(\overline{\delta_k} - \overline{\delta_y})}{\overline{r_{km}}} \quad (\text{II-37f})$$

$$q_{xy} = \overline{r_x r_y \cos(\delta_x - \delta_y)} - \overline{r_x} \overline{r_y} \cos(\overline{\delta_x} - \overline{\delta_y}) \quad (\text{II-37g})$$

we can then write Eq. (II-36) as

$$\begin{aligned} T_{wn} = & \frac{\hat{p}_{av} \hat{p}_{av}^*}{\overline{r_{km}}^2} + R_e^2 q_p^2 + q_{km}^2 \cos^2 \alpha + q_x^2 \left(\frac{\gamma}{\overline{r_{km}}} \right)^2 + q_y^2 \left(\frac{\phi}{\overline{r_{km}}} \right)^2 \\ & + 2 \left[q_{kx} \left(\frac{\gamma}{\overline{r_{km}}} \right) + q_{ky} \left(\frac{\phi}{\overline{r_{km}}} \right) \right] \cos \alpha + 2 q_{xy} \left(\frac{\phi}{\overline{r_{km}}} \right) \left(\frac{\gamma}{\overline{r_{km}}} \right) \end{aligned} \quad (\text{II-38})$$

To maximize the contrast ratio for the general case, as was done in the previous section would be quite difficult. It is possible to derive a general relationship between ϕ and γ for maximization, but the resulting expressions

are so complex that no physical insight can be gained from them. We must therefore resort to some approximations.

It is apparent that all q terms, with the exception of q_p^2 , are a result of the variation of the specimen characteristics as a function of wavelength. Therefore, any q term whose factors are constant over the spectral band-pass of interest will be equal to zero. Examining the amplitude reflection coefficient characteristics in Figs. 2-5 and 2-6, we see that all variations other than r_{km} and δ_k are relatively small. Hence, we can say that q_x^2 , q_y^2 , and q_{xy} are approximately zero. For the other terms, we compute

$$R_e^2 q_p^2 = .2163$$

$$q_{km}^2 = .0380$$

$$q_{kx} = .0165$$

$$q_{ky} = .0259$$

If the quantities $2q_{kx} \left(\frac{\gamma}{r_{km}}\right)$ and $2q_{ky} \left(\frac{\phi}{r_{km}}\right)$ are smaller than $R_e^2 q_p^2$ by a factor of three or four, then they can also be neglected. Suppose we assume that the maximization procedure follows along the same lines as that of the monochromatic case, except that averaged values of amplitude reflection coefficient magnitudes and phases are used. Then we will anticipate the result that

$$\Gamma_w = \frac{\bar{r}_x}{r_{km}} \frac{\sin(\bar{\delta}_x - \bar{\delta}_y)}{\sin(\bar{\delta}_k - \bar{\delta}_y)}$$

and that the transmission equation is similar in form to that of the monochromatic case. If this is valid, then we can use the averaged characteristics

to compute that

$$\Gamma_w = -1.62 \frac{\gamma}{r_{km}}$$

From Fig. 2-14, we see that in operation Γ_w will probably not exceed 5 or 6 and hence $\frac{\gamma}{r_{km}}$ will be less than 3.5. $\frac{\phi}{r_{km}}$ will have the same order of magnitude as $\frac{\gamma}{r_{km}}$. Therefore, if Γ_w is near its maximum value, then

$$\left| 2 \cos \alpha \left[q_{kx} \left(\frac{\gamma}{r_{km}} \right) + q_{ky} \left(\frac{\phi}{r_{km}} \right) \right] \right| \ll (\Gamma_w + \cos \alpha)^2$$

while if Γ_w is near the value for R_c to be at a maximum, then

$$\left| 2 \cos \alpha \left[q_{kx} \left(\frac{\gamma}{r_{km}} \right) + q_{ky} \left(\frac{\phi}{r_{km}} \right) \right] \right| \ll R_e^2 q_p^2$$

and we are thereby justified in dropping the terms containing q_{kx} and q_{ky} .

We can now write the transmission equation for this particular case as

$$T_{wn} = \frac{\hat{P}_{av} \hat{P}_{av}^*}{\bar{r}_{km}^2} + R_e^2 q_p^2 + q_{km}^2 \cos^2 \alpha \quad (\text{II-39})$$

This transmission factor differs from the monochromatic transmission factor T in three respects (other than the normalization).

1. There is a factor \bar{r} present in the normalization representing the spectral limitations of the system.
2. The magnitudes and phases of the amplitude reflection coefficients in the monochromatic case have been replaced by average magnitudes and average phases.
3. The term $q_{km}^2 \cos^2 \alpha$ has been added. In States I and II, this can be treated as an additional noise component, arising from

the variation of the magnitude of \hat{r}_k . For magnetization conditions other than States I and II, this term introduces a small variation in the transmission factor when plotted as a function of γ .

We can now carry out a maximization procedure similar to that in Section 2.2, arriving at the following equations for the optimal transmission using a white light source with an uncoated specimen.

$$T_{wn} = (\Gamma_w + \cos\alpha)^2 + q_w^2 \quad (\text{II-40a})$$

$$\Gamma_w = \gamma \frac{\bar{r}_x}{\bar{r}_{km}} \frac{\sin(\bar{\delta}_x - \bar{\delta}_y)}{\sin(\bar{\delta}_k - \bar{\delta}_y)} \quad (\text{II-40b})$$

$$q_w^2 = q_{km}^2 \cos^2\alpha + R_e^2 q_n^2 \quad (\text{II-40c})$$

As long as we are dealing with the magnetization in State I or State II we can apply the transmission and contrast curves of the previous section to the present case. From Fig. 2-15 we see that the maximum contrast corresponding to the total noise parameter, $R_e^2 q_p^2$, is 17.5.

This contrast value is higher than that estimated from visual observations on films in the magneto-optic apparatus. However, the previous analyses are based on the assumption that the angle of incidence for all light rays is the same, i.e., that our source is ideally collimated. In reality the ideally collimated source cannot be attained; the writer would estimate that there is a spread of 5° to 8° in the angle of incidence already encountered. From the previous analyses we see that any variation in reflection characteristics will contribute to the noise parameters. Since the reflection coefficients are functions of the angle of incidence, as we can see from Eqs. (II-4a) through (II-4c), it is apparent that the spread in angle of incidence will increase the noise level and hence decrease the available maximum contrast. The estimated maximum contrast in the

visual observations is approximately 2 to 4. It seems reasonable that a portion, if not all, of this decrease arises from the spread in angle of incidence.

This belief is supported by Anderson's work³ in observing domains in ferromagnetic thin films. Using a highly collimated light source, he has obtained photographs which exhibit considerably higher contrast than that obtained by the writer. As we shall see in subsequent chapters, the use of a high degree of collimation results in a loss of light energy and hence this desirable feature could not be incorporated into the writer's apparatus.

In discussion of the monochromatic analysis, we noted that with sufficient contrast available, one could trade between contrast and transmission. Under certain circumstances there can be an additional reason for working at an increased transmission. Suppose that q_{km}^2 is much greater than $R_e^2 q_p^2$, e.g., $q_{km}^2 = 1$.

Fig. 2-18 shows the variation in normalized transmission as the angle of the magnetization vector, α , is varied from 0° to 180° for $q_{km}^2 = 1$. In these curves T_{no} is the transmission for no noise (monochromatic light and ideal polarizers), T_n is the monochromatic transmission [Eq. (II-25) plotted at a wavelength $\lambda = 4910 \text{ \AA}$], and T_{wn} is the white light transmission. For both values of Γ given in Fig. 2-18 the curves for T_{no} are proportional to $(\Gamma + \cos\alpha)^2$ and the curves for the monochromatic case, T_n , differ from the ideal T_{no} curve only by a small amount. For a white light source, however, the transmission T_{wn} varies considerably from the ideal T_{no} curve when $\Gamma = 1.5$. From the plot of this curve in Fig. 2-18a we see that it would be impossible to discern any angular difference in the position of the magnetization vector in the range $\alpha = 120^\circ$ to $\alpha = 180^\circ$. If we work at a Γ value of 5, as shown in Fig. 2-17b, the transmission contribution from q_w^2 is small compared with the overall transmission, and the transmission curve differs only slightly from the ideal transmission T_{no} .

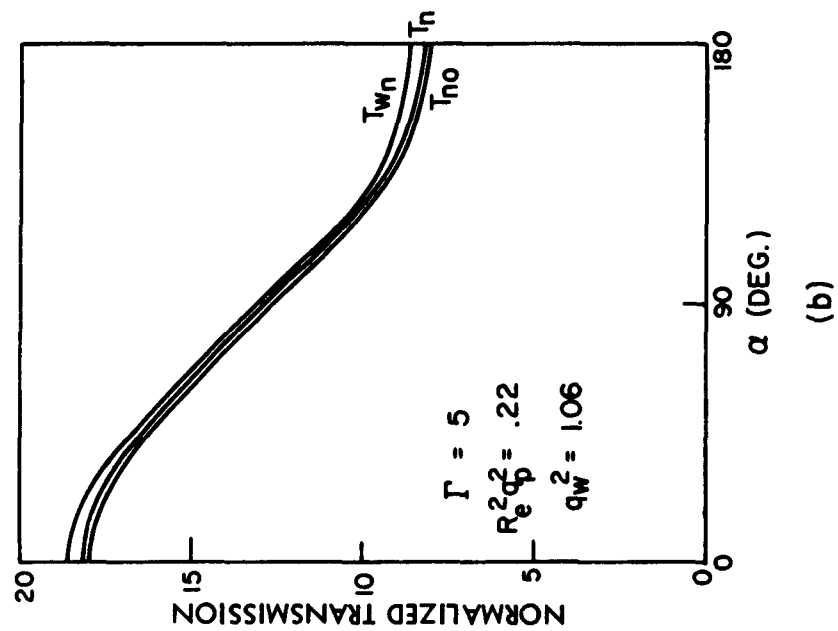
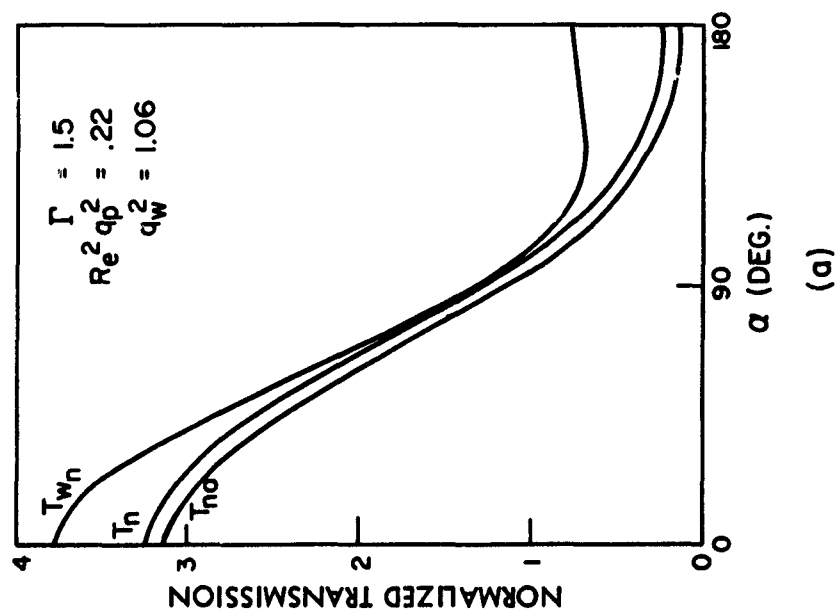


FIG. 2-18 TRANSMISSION VARIATION

It is apparent, then, that the condition of maximum contrast may differ considerably from the most desirable operating point since the characteristics for determining the transmission parameters can vary from specimen to specimen. One can either measure the characteristics of a given specimen and try to compute the necessary adjustments for a magneto-optic apparatus or else use the preceding analyses as a guide and try to determine the optimal apparatus adjustments experimentally. The writer has chosen to do the latter.

2.4 Dielectric Layers on Ferromagnetic Films

If we examine Eqs. (II-27) and (II-40a), we see that the transmission factors are primarily proportional to r_{km}^2 . Obviously, then, any increase in r_{km} will result in an increase in the transmission factors at a given contrast ratio. Such an increase is possible if a thin dielectric layer is evaporated on the surface of the specimen.

All reports which the writer has been able to find on this subject state that there is an increase in the Kerr rotation, Ψ_R , in some cases by as much as a factor of 5 or 6 when the dielectric layer is present⁴. We note from Eq. (II-7a) that such a rotational increase can arise either from an increase in the magnitude of r_{km} or from a decrease in the magnitude of r_y ; as we shall see from the subsequent analysis, both effects can occur. This writer is in disagreement with the argument of these reports that for attaining improved magneto-optic observations the primary objective is to increase Ψ_R . If this increase is caused by a decrease in r_y , the noise parameter q^2 (or q_w^2) will be decreased somewhat, but there will be very little effect in such a case on the total transmission. Since the values of Ψ_R and Ψ_E are both necessary to determine the magnitude of r_{km} , we see that a knowledge of the rotational increase provides only half the necessary data and hence is useless for making any quantitative estimate on the increase in transmission. That some increase is possible with a dielectric

layer is apparent from visual observations of dielectric coated specimens in the magneto-optic apparatus; in comparison to uncoated specimens, a number of coated specimens have exhibited higher contrast and transmission.

The dielectric layer also results in some interesting color effects in the specimens. Again, this is to be expected due to the interference phenomena present. All observations on uncoated specimens involve no color effects whatsoever; the domains in the coated specimens give various color effects depending on the angular setting of the polarizer and analyzer and also upon the thickness of the dielectric layers. One specimen observed shows colors mostly in the blues and violets. Another gives various hues of a rich yellow-brown. The most striking color effects were observed in a specimen in which the domains appeared yellow for one direction of magnetization and purple for the other direction of magnetization. (It is unfortunate that further investigation on this particular specimen was prevented by its accidental destruction.)

We will now proceed to calculate the expressions for the reflection coefficients of a specimen coated with a thin dielectric layer. The only assumption made in the analysis which -- to the writer's knowledge -- has not been experimentally verified is that Eq. (II-4c), the magneto-optic amplitude reflection coefficient, is valid when a dielectric is present at the boundary of the ferromagnetic specimen. (Robinson has verified the validity of this expression for air at the specimen boundary.) We shall see that both the increase in transmission factor and the color effects can be explained from the results of this analysis.

Consider a ferromagnetic specimen coated with a dielectric layer of thickness d as shown in Fig. 2-19. The incoming ray has an amplitude of E_0 . The rays traveling away from the surface in the air are $E_{r(0)}$, $E_{r(1)}$, $E_{r(2)}$, \dots , $E_{r(q-1)}$, $E_{r(q)}$, $E_{r(q+1)}$, \dots , $E_{r(m-1)}$, $E_{r(m)}$, $E_{r(m+1)}$, \dots . We have denoted the air as region 1, the dielectric

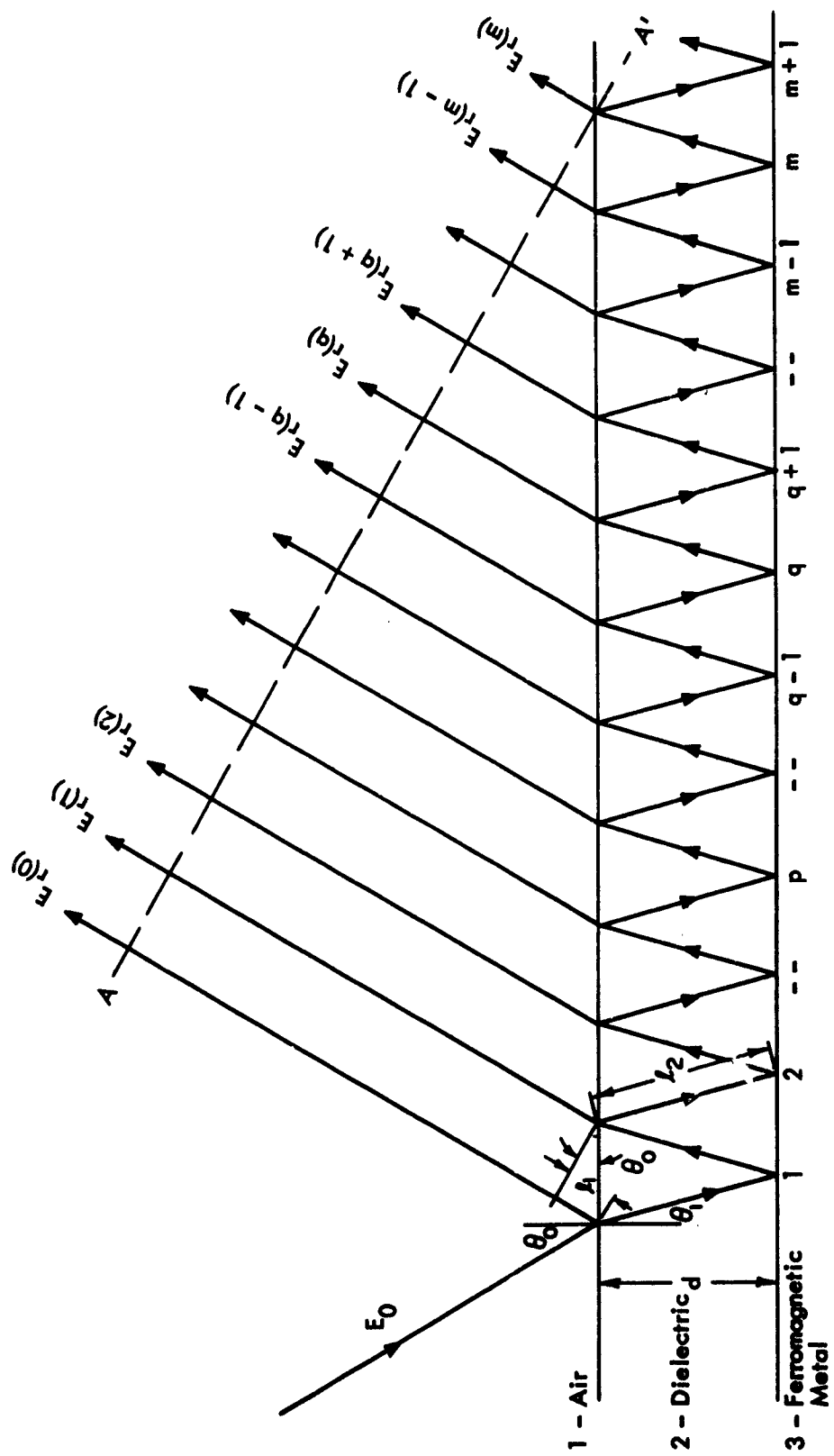


FIG. 2-19 INTERFERENCE RAYS IN DIELECTRIC LAYER

as region 2, and the ferromagnetic metal as region 3. All amplitude transmission and reflection coefficients and their phases have a subscript consisting of two numbers and an x or a y, the numbers denoting the interface, their order denoting the side of the interface upon which light is incident and the letter denoting the polarization. For example, \hat{t}_{21x} denotes transmission across the air-dielectric interface for an x-polarized wave incident on the dielectric side of the interface. The one exception to this notation is the Kerr amplitude reflection coefficient which is written as

$$\hat{r}_k = r_k \exp[i\delta_k]$$

and is defined by Eq. (II-4c). Using standard optical conventions, the relations between the various transmission and reflection coefficients at the air-dielectric interface are as follows:

$$\hat{r}_{12x} = -\hat{r}_{21x} \quad (a)$$

$$\hat{r}_{12y} = -\hat{r}_{21y} \quad (b)$$

$$\hat{t}_{12x} = 1 + \hat{r}_{12x} \quad (c)$$

$$\hat{t}_{21x} = 1 - \hat{r}_{12x} \quad (d)$$

$$\hat{t}_{12y} = \frac{1}{n_1} [1 + \hat{r}_{12y}] \quad (e)$$

$$\hat{t}_{21y} = n_1 [1 - \hat{r}_{12y}] \quad (f)$$

$$\hat{t}_{12x} \hat{t}_{21x} = 1 - r_{12x}^2 \quad (g)$$

$$\hat{t}_{12y} \hat{t}_{21y} = 1 - r_{12y}^2 \quad (h)$$

(II-41)

where n_1 is the index of refraction of the dielectric material. We note here that although we have used complex notation, the phase angles in Eqs. (II-41) are always either zero or π , and therefore the square of any transmission or reflection coefficient at the air-dielectric interface is equal to the square of the coefficient magnitude. To determine the overall reflection coefficients of the coated specimen, we will sum the m rays along the wavefront AA' in Fig. 2-18 and let $m \rightarrow \infty$. We will see that we can then drop the phase term containing m , since it will be common to all reflection coefficients.

We will define the overall amplitude reflection coefficients by means of the matrix equation

$$\begin{bmatrix} \hat{R}_x & \hat{R}_{kx} \\ \hat{R}_{ky} & \hat{R}_y \end{bmatrix} \begin{bmatrix} E_{ox} \\ E_{oy} \end{bmatrix} = \begin{bmatrix} E_{rx} \\ E_{ry} \end{bmatrix} \quad (\text{II-42})$$

The derivations of \hat{R}_x and \hat{R}_y can be found in any advanced optics text⁵, but we will repeat them here in order to avoid any confusion concerning the phase factors involved.

Let E_0 be polarized in the x direction, i.e.,

$$\vec{E}_0 = \vec{i}_x E_{0x}$$

Then, referring to Fig. 2-19, we see that

$$E_{rx(0)} = E_{0x} \hat{r}_{12x} \exp[jm\delta_1] \quad (\text{II-43a})$$

$$E_{rx(q)} = E_{0x} \hat{t}_{12x} (\hat{r}_{23x})^q (\hat{r}_{21x})^{q-1} \hat{t}_{21x} \exp[j\{2q\delta_2 + (m-q)\delta_1\}] \quad (\text{II-43b})$$

where δ_1 and δ_2 are the phase lags along paths l_1 and l_2 respectively. Summing over the wave front AA', and dividing each side of the resulting

equation by E_{0x} ,

$$\hat{R}_x = \hat{r}_{12x} \exp[jm\delta_1] + \sum_{q=1}^m \hat{t}_{12x} (\hat{r}_{23x})^{q-1} \hat{t}_{21x} (-\hat{r}_{12x})^{q-1} \exp[j\{2q\delta_2 + (m-q)\delta_1\}] \quad (\text{II-44})$$

Letting

$$\delta_p = 2\delta_2 - \delta_1 \quad (\text{II-45})$$

we can rewrite Eq. (II-39) as

$$\begin{aligned} \hat{R}_x &= \exp[jm\delta_1] \left[\hat{r}_{12y} \hat{t}_{12x} (-\hat{r}_{12x})^{-1} \hat{t}_{21x} + \sum_{q=0}^m \hat{t}_{12x} (\hat{r}_{23x})^q (-\hat{r}_{12x})^{q-1} \hat{t}_{21x} \exp[jq\delta_p] \right] \\ &= \hat{r}_{12x} \exp[jm\delta_1] \left[1 + \frac{1-\hat{r}_{12x}^2}{\hat{r}_{12x}} - \frac{1-\hat{r}_{12x}^2}{\hat{r}_{12x}} \sum_{q=0}^m (-\hat{r}_{23x} \hat{r}_{12x} \exp[j\delta_p])^q \right] \\ &= \frac{\exp[jm\delta_1]}{\hat{r}_{12x}} \left[1 - (1-\hat{r}_{12x}^2) \sum_{q=0}^m (-\hat{r}_{23x} \hat{r}_{12x} \exp[j\delta_p])^q \right] \quad (\text{II-46}) \end{aligned}$$

It is apparent that as $m \rightarrow \infty$, the series is convergent, since the amplitude coefficients are always less than unity and hence

$$| -\hat{r}_{23x} \hat{r}_{12x} \exp[j\delta_p] | < 1$$

We will take the limit as $m \rightarrow \infty$ but retain the term $\exp[jm\delta_1]$ for the time being. When we have derived R_{ky} , we will see that we can drop this phase factor, since it appears in the same manner in both reflection coefficients. Hence writing the summation in closed form,

$$R_x = \frac{\exp[jm\delta_1]}{\hat{r}_{12x}} \left[1 - \frac{1-\hat{r}_{12x}^2}{1 + \hat{r}_{23x} \hat{r}_{12x} \exp[j\delta_p]} \right] \quad (\text{II-47})$$

The derivative of $|R_x|^2$ is zero when the phase of $\hat{r}_{23x} \hat{r}_{12x} \exp[j\delta_p]$ is zero or an integral multiple of π and changes sign only at those points; hence the maxima and minima must occur at these points also. By looking at the values of $|R_x|^2$ at these points it is relatively simple to show that the maxima always occur at the even multiples of π and the minima at the odd multiples.

For computational purposes and for dealing with phase factors after we derive \hat{R}_{ky} , it is preferably to write Eq. (II-47) in the form

$$\hat{R}_x = \hat{r}_{23x} \exp[j(m\delta_1 + \delta_p)] \frac{1 + \frac{\hat{r}_{12x}}{\hat{r}_{23x}} \exp[-j\delta_p]}{1 + \hat{r}_{12x} \hat{r}_{23x} \exp[j\delta_p]} \quad (\text{II-48})$$

In a similar fashion we can derive

$$\hat{R}_y = \hat{r}_{23y} \exp[j(m\delta_1 + \delta_p)] \frac{1 + \frac{\hat{r}_{12y}}{\hat{r}_{23y}} \exp[-j\delta_p]}{1 + \hat{r}_{12y} \hat{r}_{23y} \exp[j\delta_p]} \quad (\text{II-49})$$

To determine \hat{R}_{kx} , we assume that the incoming radiation is polarized in the y direction, i.e.

$$\vec{E}_o = \hat{y} E_{oy}$$

The contribution to $E_{rx(q)}$ arising from the pth reflection at the metal dielectric interface ($p \leq q$) is

$$E_{rx(q)p} = E_{oy} \hat{t}_{12y} (\hat{r}_{23y} \hat{r}_{21y})^{p-1} \hat{r}_k (\hat{r}_{23x} \hat{r}_{21x})^{q-p} \hat{t}_{21x} \exp[j\{2q\delta_2 + (m-q)\delta_p\}] \quad (\text{II-50})$$

Summing Eq. (II-50) over q and p, and letting $m \rightarrow \infty$, we have

$$\hat{R}_{kx} = \hat{t}_{12y} \hat{t}_{21x} \hat{r}_k \exp[jm\delta_1] \sum_{q=1}^{\infty} \sum_{p=1}^q [-\hat{r}_{23y} \hat{r}_{12y}]^{p-1} [-\hat{r}_{23x} \hat{r}_{12x}]^{q-p} \exp[jq\delta_p] \quad (\text{II-51})$$

If we write out the terms of the double summation in Eq. (II-51), we see that we can sum over all terms for $p = 1$, then for $p = 2$, etc., arriving at

$$\begin{aligned} \hat{R}_{kx} = & \hat{t}_{12y} \hat{t}_{21x} \hat{r}_k \exp[jm\delta_1] \left\{ \exp[j\delta_p] \sum_{q=1}^{\infty} [-\hat{r}_{23x} \hat{r}_{12x} \exp[j\delta_p]]^{q-1} \right. \\ & + [-\hat{r}_{23y} \hat{r}_{12y}] \exp[j2\delta_p] \sum_{q=2}^{\infty} [-\hat{r}_{23x} \hat{r}_{12x} \exp[j\delta_p]]^{q-2} \\ & + [-\hat{r}_{23y} \hat{r}_{12y}]^2 \exp[j3\delta_p] \sum_{q=3}^{\infty} [-\hat{r}_{23x} \hat{r}_{12x} \exp[j\delta_p]]^{q-3} \\ & + \dots \left. \right\} \quad (\text{II-52}) \end{aligned}$$

It is immediately apparent that the summations in Eq. (II-52) are all identical, and that the coefficients of the summations form a power series which is convergent, since all reflection coefficients amplitudes are less than one. Hence we can write (changing the lower summation indexes to zero),

$$\hat{R}_{kx} = \hat{t}_{12y} \hat{t}_{21y} \hat{r}_k \exp[j(m\delta_1 + \delta_p)] \sum_{q=0}^{\infty} \left[-\hat{r}_{23x} \hat{r}_{12x} \exp[j\delta_p] \right]^q \sum_{g=0}^{\infty} \left[-\hat{r}_{23y} \hat{r}_{12y} \exp[j\delta_p] \right]^g \quad (\text{II-53})$$

Again we see that the series are convergent. Writing Eq. (II-53) in closed form, we have

$$\hat{R}_{kx} = \frac{\hat{t}_{12y} \hat{t}_{21x} \hat{r}_k \exp[j(m\delta_1 + \delta_p)]}{(1 + \hat{r}_{12x} \hat{r}_{23x} \exp[j\delta_p])(1 + \hat{r}_{12y} \hat{r}_{23y} \exp[j\delta_p])} \quad (\text{II-54})$$

We can immediately write \hat{R}_{ky} by interchanging the x and y subscripts and by changing the sign of r_k [see Eq. (II-1)]. Hence,

$$\hat{R}_{ky} = \frac{-\hat{t}_{12x} \hat{t}_{21y} \hat{r}_k \exp[j(m\delta_1 + \delta_p)]}{(1 + \hat{r}_{12x} \hat{r}_{23x} \exp[j\delta_p])(1 + \hat{r}_{12y} \hat{r}_{23y} \exp[j\delta_p])} \quad (\text{II-55})$$

Since our observations deal only with the reflection coefficients, we can now drop the factor $\exp[j(m\delta_1 + \delta_p)]$ since it occurs identically in all reflection coefficients.

Using the relations in Eq. (II-41) we can write Eqs. (II-54) and (II-55) as

$$R_{kx} = \frac{\frac{1}{n_1} \hat{r}_k [1 + \hat{r}_{12y}][1 - \hat{r}_{12x}]}{(1 + \hat{r}_{12x} \hat{r}_{23x} \exp[j\delta_p])(1 + \hat{r}_{12y} \hat{r}_{23y} \exp[j\delta_p])} \quad (\text{II-56})$$

$$R_{ky} = \frac{-n_1 \hat{r}_k [1 - \hat{r}_{12y}][1 + \hat{r}_{12x}]}{(1 + \hat{r}_{12x} \hat{r}_{23x} \exp[j\delta_p])(1 + \hat{r}_{12y} \hat{r}_{23y} \exp[j\delta_p])} \quad (\text{II-57})$$

Although the numerators of these last two equations appear to be dissimilar, such is not the case. If we evaluate the numerators, using the Fresnel equations (Eqs. (II-2a) and (II-2b)), we find that the numerator of \hat{R}_{kx} is

$$\frac{4 \hat{r}_k n_1 \cos \theta_o \cos \theta_1}{(n_1 \cos \theta_o + n_o \cos \theta_1)(n_o \cos \theta_o + n_1 \cos \theta_1)}$$

while that of R_{ky} is

$$\frac{-4 \hat{r}_k n_o^2 n_1 \cos \theta_o \cos \theta_1}{(n_1 \cos \theta_o + n_o \cos \theta_1)(n_o \cos \theta_o + n_1 \cos \theta_1)}$$

Since n_o , the refractive index of air, is unity, the numerators are identical except for sign. This latter difference is to be expected from the behavior of the off-diagonal matrix elements in Eq. (II-3).

Hence, we can write the amplitude reflection coefficients for a specimen with a dielectric coating as

$$\hat{R}_x = \hat{r}_{23x} \frac{1 + \frac{\hat{r}_{12x}}{\hat{r}_{23x}} \exp[-j\delta_p]}{1 + \hat{r}_{12x} \hat{r}_{23x} \exp[j\delta_p]} \quad (\text{II-58})$$

$$\hat{R}_y = \hat{r}_{23y} \frac{1 + \frac{\hat{r}_{12y}}{\hat{r}_{23y}} \exp[-j\delta_p]}{1 + \hat{r}_{12x} \hat{r}_{23x} \exp[j\delta_p]} \quad (\text{II-59})$$

$$\begin{aligned} \hat{R}_{kx} = -\hat{R}_{ky} &= \frac{4 \hat{r}_k n_1 \cos \theta_o \cos \theta_1}{(n_1 \cos \theta_o + n_o \cos \theta_1)(n_o \cos \theta_o + n_1 \cos \theta_1)} \\ &\times \frac{1}{(1 + \hat{r}_{12x} \hat{r}_{23x} \exp[j\delta_p])(1 + \hat{r}_{12y} \hat{r}_{23y} \exp[j\delta_p])} \end{aligned} \quad (\text{II-60})$$

From Fig. 2-19, we determine through a simple trigonometric analysis that

$$\delta_p = 2\pi \frac{2dn_1 \cos \theta_1}{\lambda} \quad (\text{II-61})$$

In general, one cannot determine the maxima and minima of Eq. (II-60) as δ_p is varied, because of the difference in phase between \hat{r}_{23x} and \hat{r}_{23y} . In the particular case under discussion, however, when this phase difference is large,

$$\left| \hat{r}_{12y} \hat{r}_{23y} \exp[j\delta_p] \right| < .05$$

whereas when

$$\left| \hat{r}_{12y} \hat{r}_{23y} \exp[j\delta_p] \right| > .05$$

the phase difference is small. Under these conditions, the term $\hat{r}_{12y} \hat{r}_{23y} \exp[j\delta_p]$ has little effect on \hat{R}_{kx} . The magnitudes and phases of the amplitude reflection coefficients are plotted as a function of n_1 in Fig. 2-20, and those for $\hat{r}_{12x} \hat{r}_{23x}$ and $\hat{r}_{12y} \hat{r}_{23y}$ in Fig. 2-21. (δ_{Tx} and δ_{Ty} are the phases of $\hat{r}_{12x} \hat{r}_{23x}$ and $\hat{r}_{12y} \hat{r}_{23y}$.) From these we see that the minima and maxima of \hat{R}_{kx} occur approximately when

$$\delta_{Tx} + \delta_p = n\pi$$

n being odd for the maxima and even for the minima. The magnitude and phase of \hat{R}_{kxn} (normalized to the value of \hat{R}_{kx} when $n_1 = 0$) are plotted in Fig. 2-22 as a function of n_1 . For larger values of n_1 than those plotted, \hat{R}_{kx} asymptotically approaches zero. From this figure, we see that at most the magnitude of \hat{R}_{kx} can be increased by a factor of 1.96 over the magnitude of \hat{r}_k (when the angle of incidence is 60°).

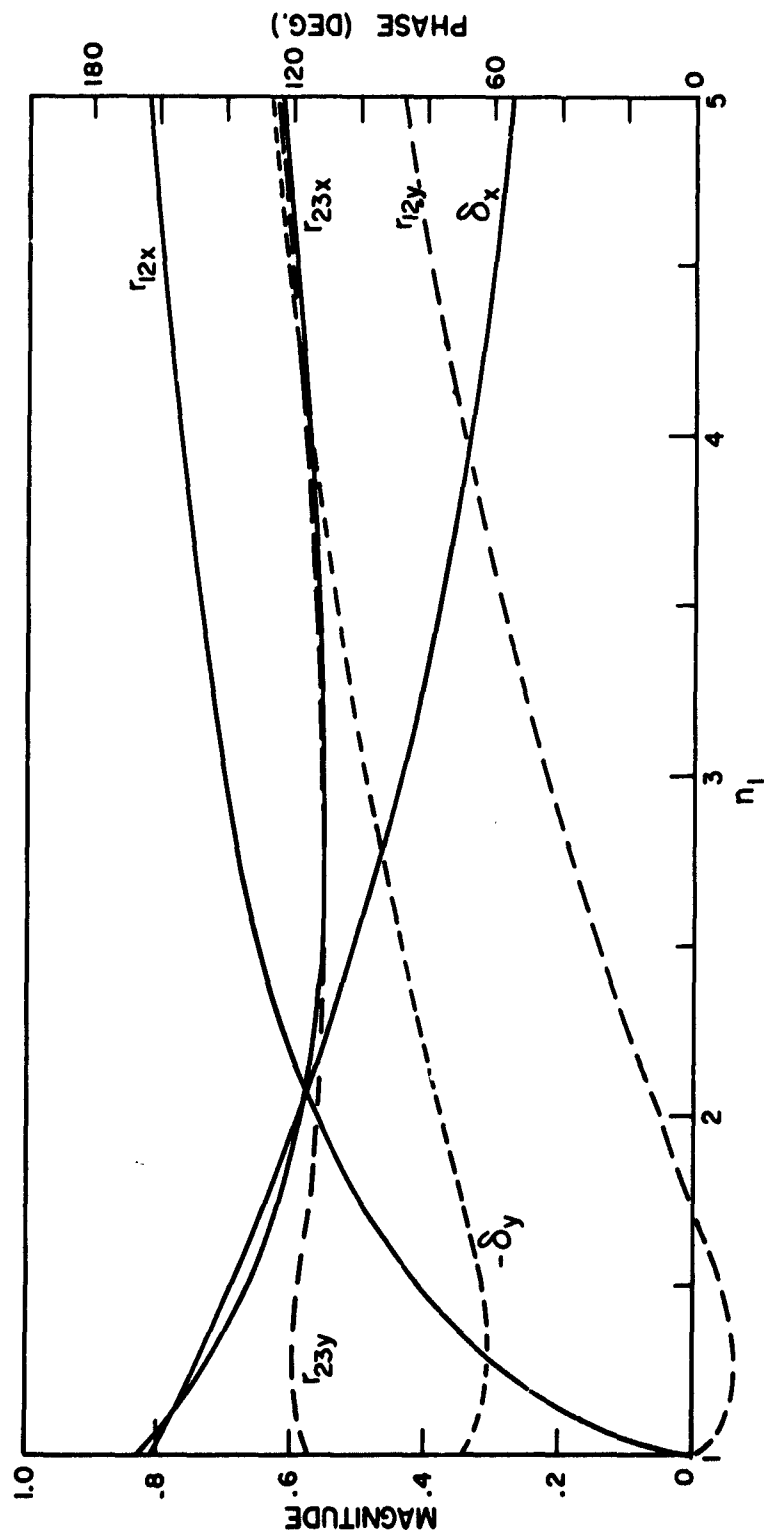


FIG. 2-20 AMPLITUDE REFLECTION COEFFICIENTS

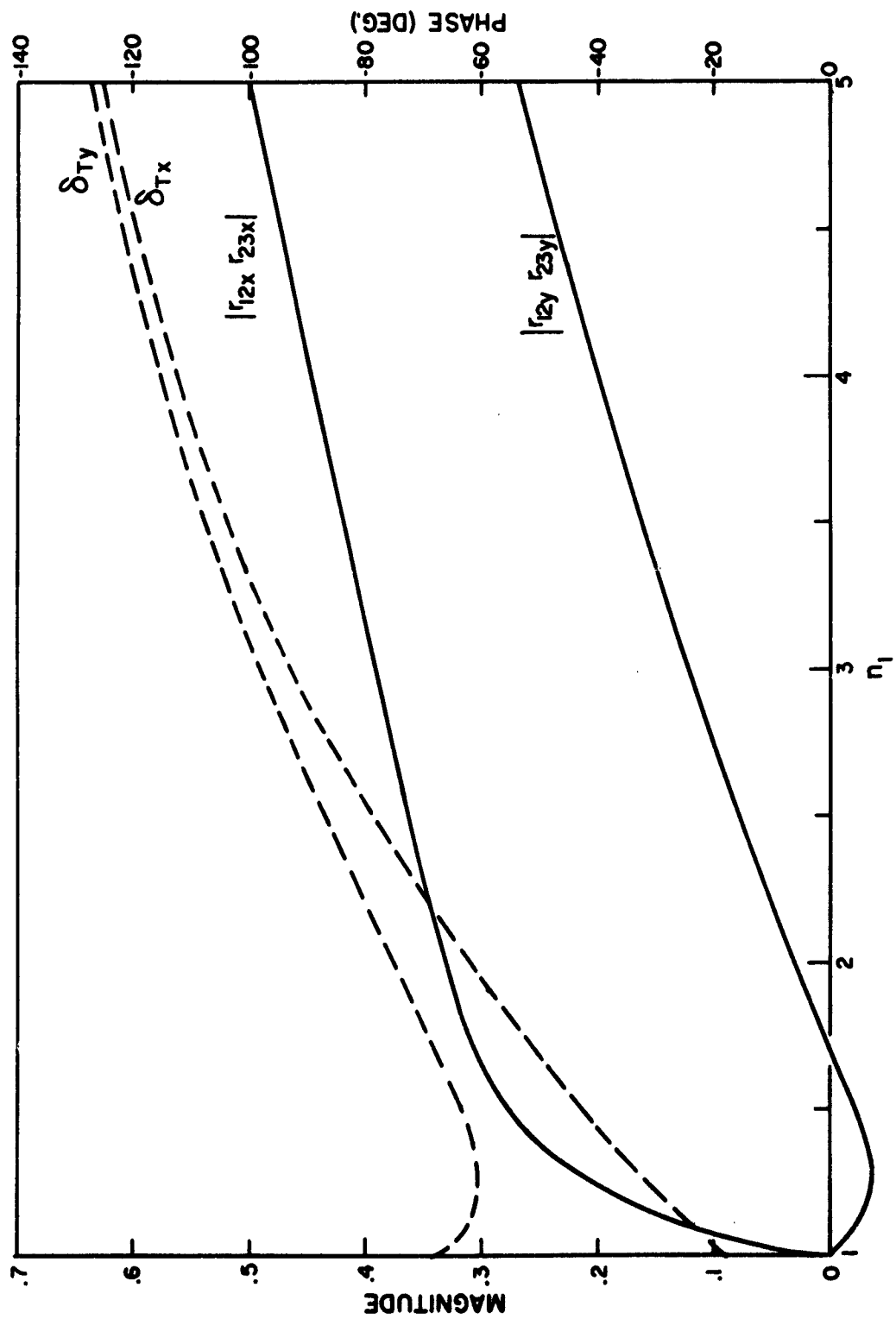


FIG. 2-21 REFLECTION COEFFICIENT PRODUCTS

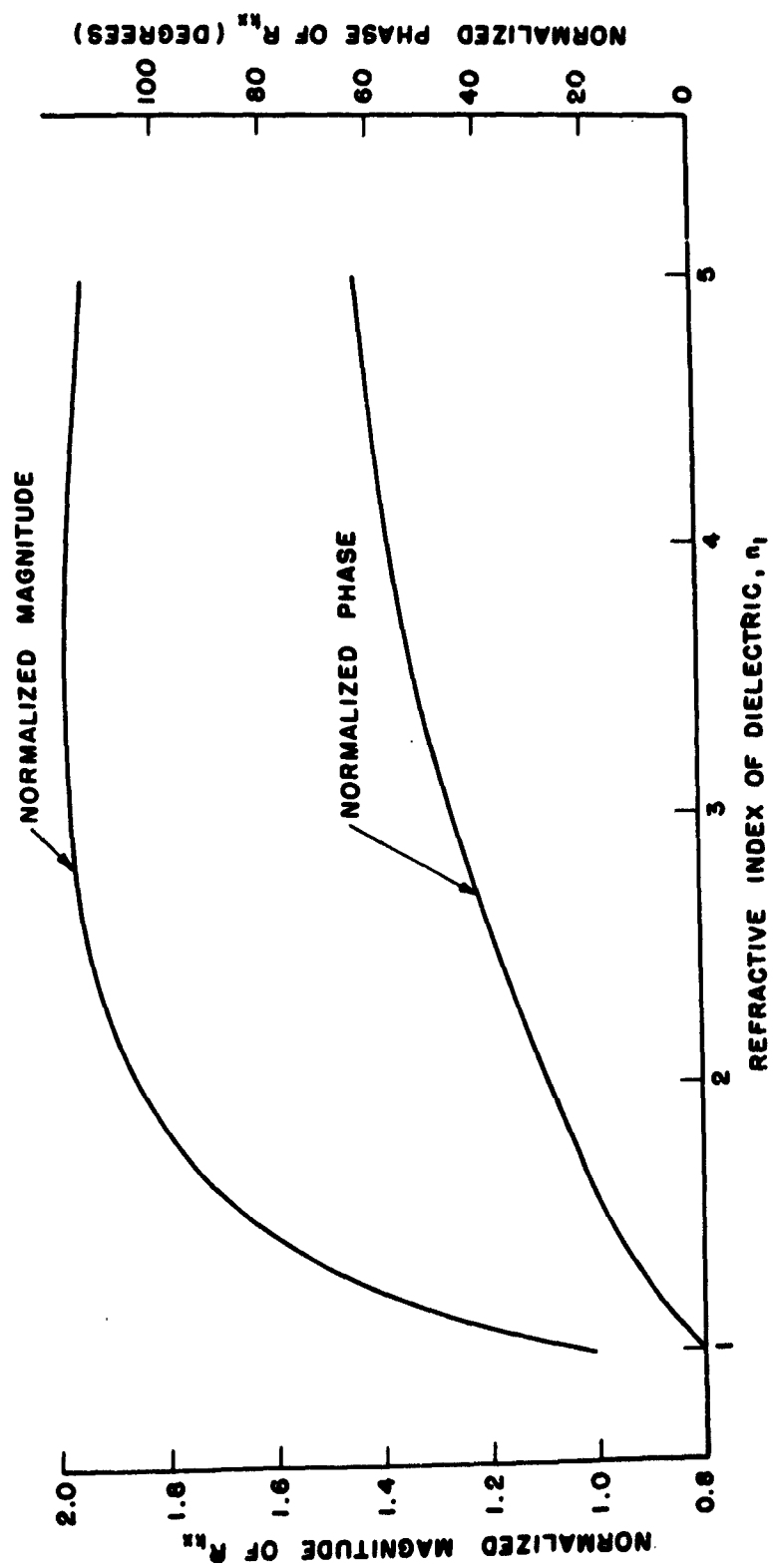


FIG. 2-22 NORMALIZED MAGNITUDE AND PHASE OF R_x

Figs. 2-23 through 2-27 show the behavior of the magnitudes and phases of the coefficients for a number of dielectric refractive indices as δ_p is varied through a range of 2π . Using these curves and those in Fig. 2-5 we can determine the characteristics of a coated specimen as a function of λ : In these figures δ_{\max} is the value of δ_p when R_{kn} is at a minimum.

In Figs. 2-28 and 2-29, the magnitude of \hat{R}_{kx} is shown for a number of values of d for coatings with refractive indices of 1.66 and 2.4. The average magnitudes of \hat{R}_k are summarized in Table II-2. Note that the highest average magnitudes occur for relatively thin dielectric layers (774 Å and 355 Å). For these thicknesses the first maximum of \hat{R}_{kxn} , which has a very broad peak, is centered in the visible spectrum. For the other thicknesses shown, the second maximum, which has a much narrower peak, is centered at various wavelengths from 3000 Å to 7000 Å. The effect of this peak is apparent from examination of the curves. For example, with a refractive index of 1.66 and with the second maximum centered at 4000 Å ($d = 4516$), the variation of \hat{R}_{kxn} combines with the variation of \hat{r}_{km} to yield a very steep curve. On the other hand, if this maximum occurs at 5500 Å ($d = 6210$ Å), the resultant curve is relatively flat. We note from Table II-2 that the average magnitude of \hat{R}_{kx} for both cases is about the same. Finally we note that for the second maximum at 3000 Å we actually have less average magnitude of \hat{R}_{kx} than with an uncoated specimen.

We can now gain some insight into the origin of the color effects mentioned previously. Suppose we have a specimen with a dielectric layer of refractive index 2.4 and a thickness of 4770 Å, so that the second maximum of R_{kx} is centered at 4500 Å (see Fig. 2-29). The specimen parameters, the values of γ and ϕ for a T_1 minimum at 5500 Å, and the values of T_1 and T_2 computed from Eqs. (II-16a), (II-16b), and (II-18) are listed in Table II-3. The transmission factors as a function of wavelength are plotted in Fig. 2-30. We can see from the average transmission values

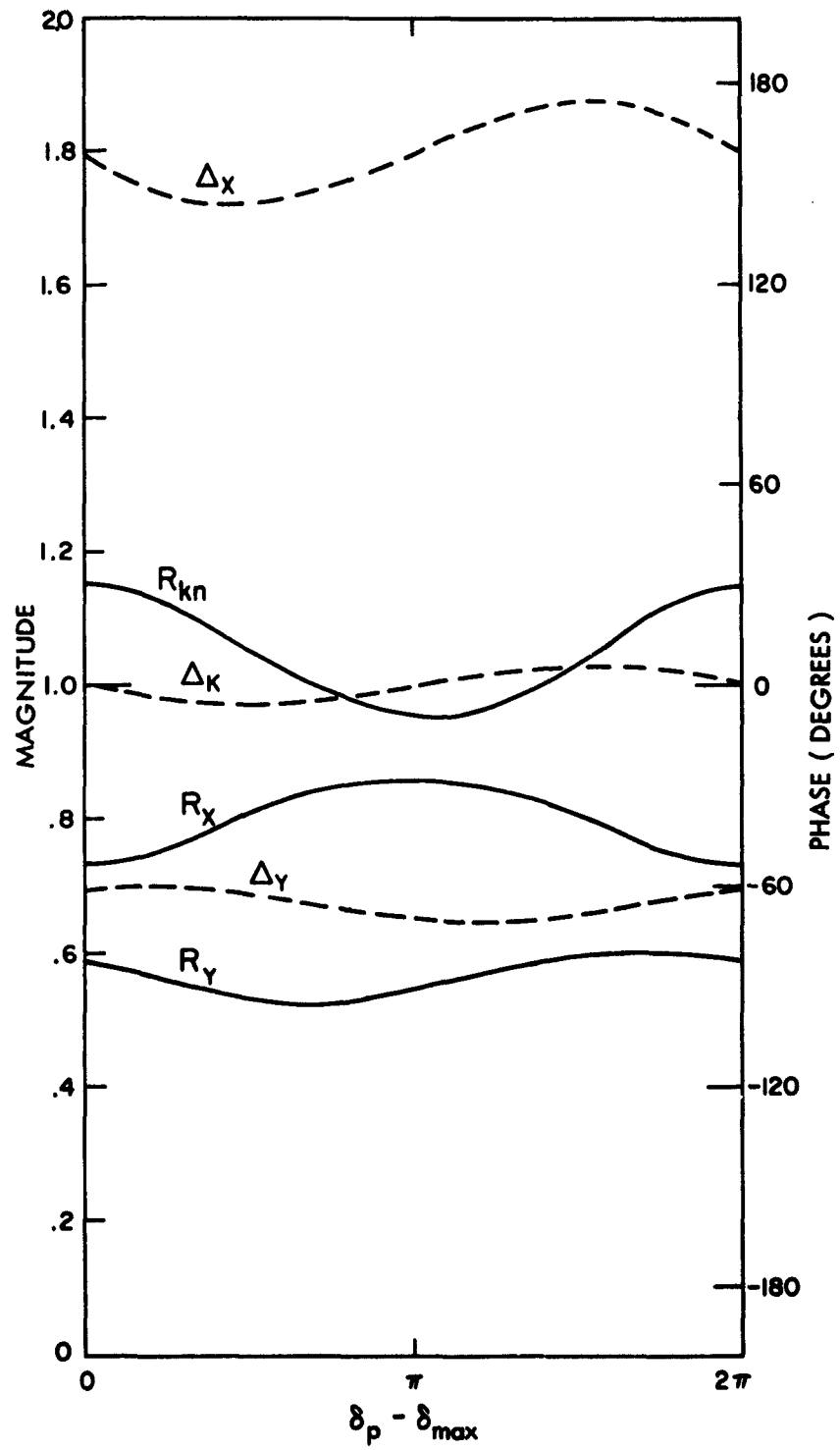


FIG. 2-23 VARIATION OF REFLECTION COEFFICIENTS - $n_1 = 1.065$

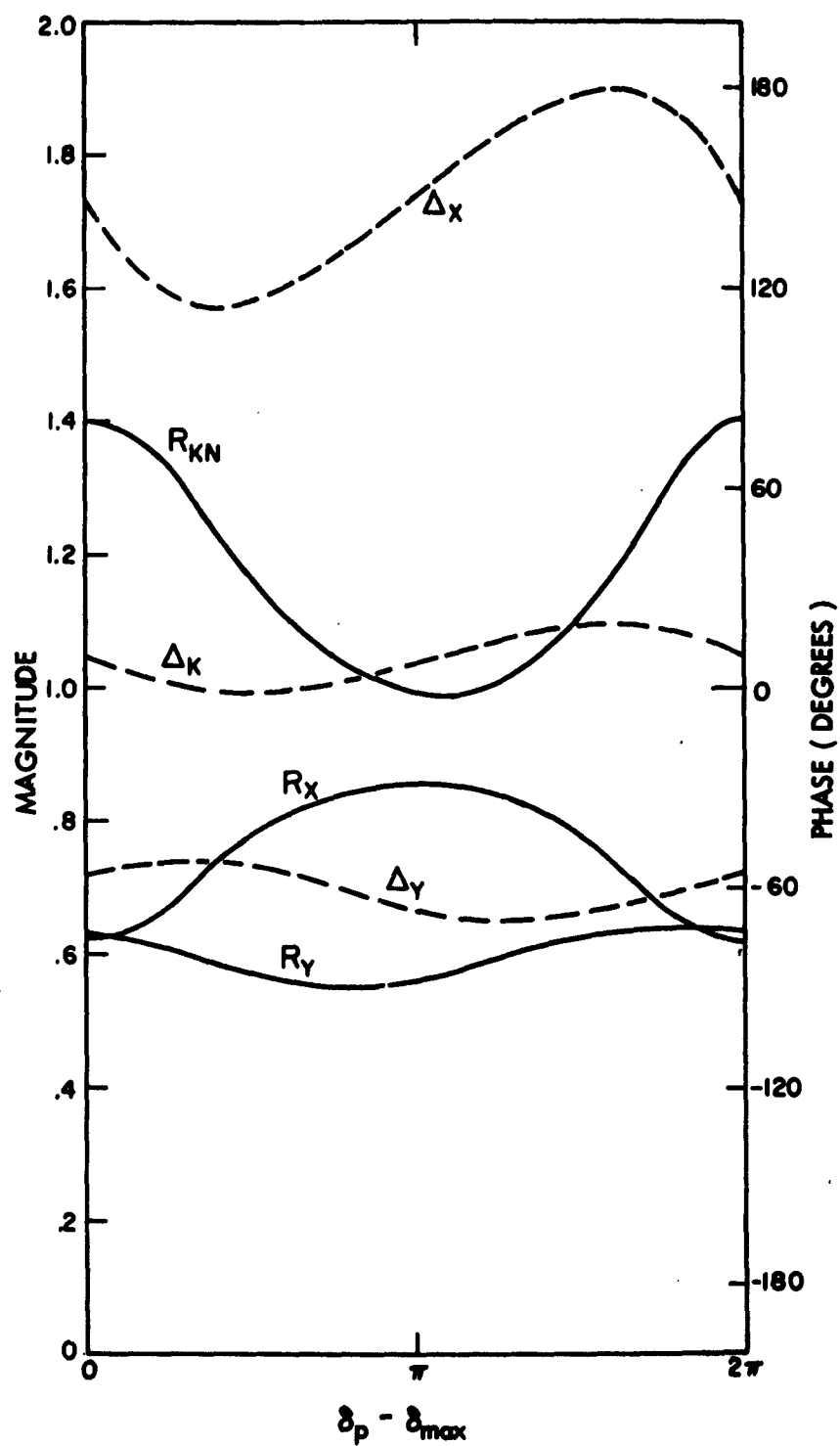


FIG. 2-24 VARIATION OF REFLECTION COEFFICIENTS - $n_1 = 1.23$

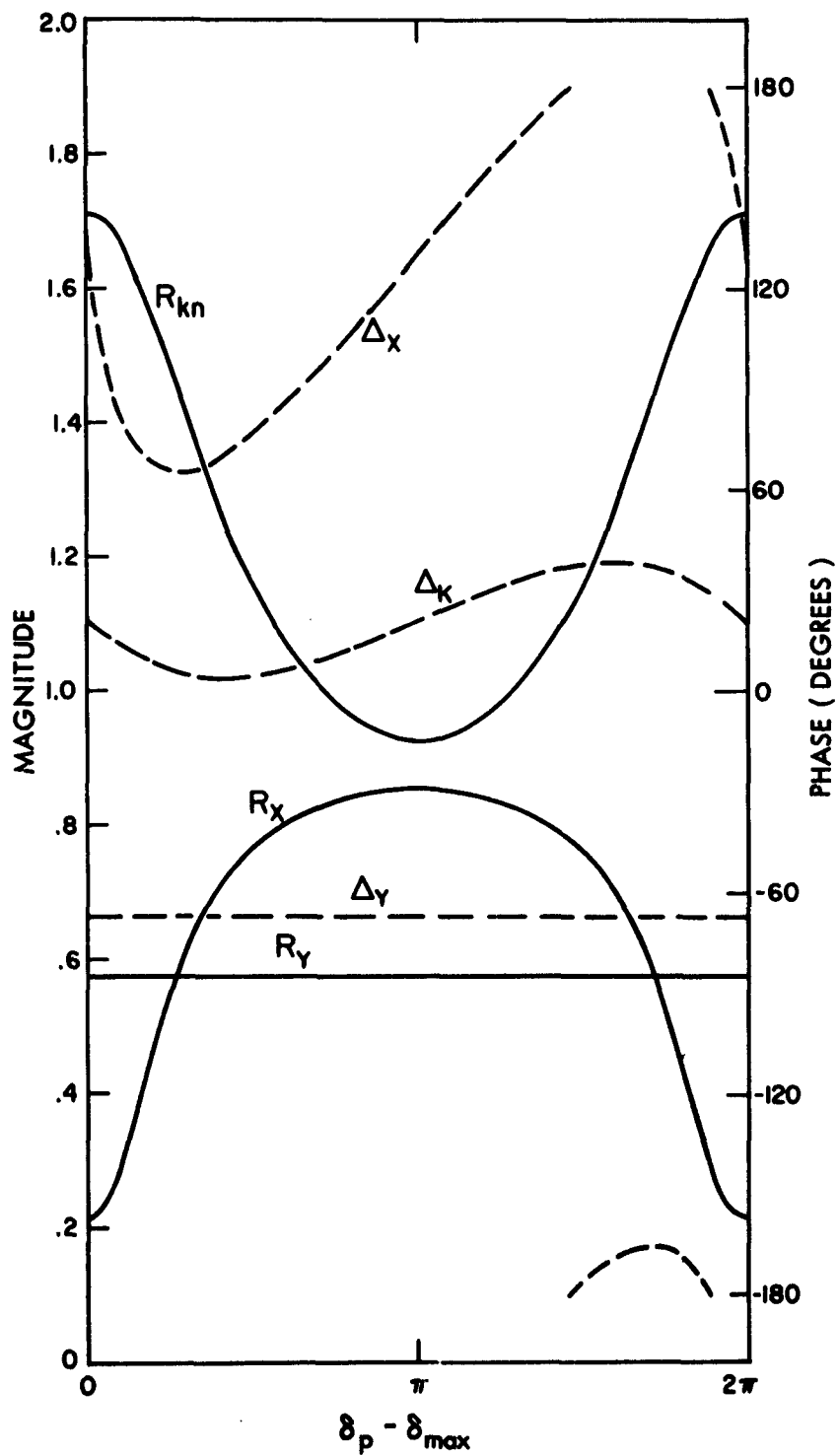


FIG. 2-25 VARIATION OF REFLECTION COEFFICIENTS - $n_1 = 1.66$

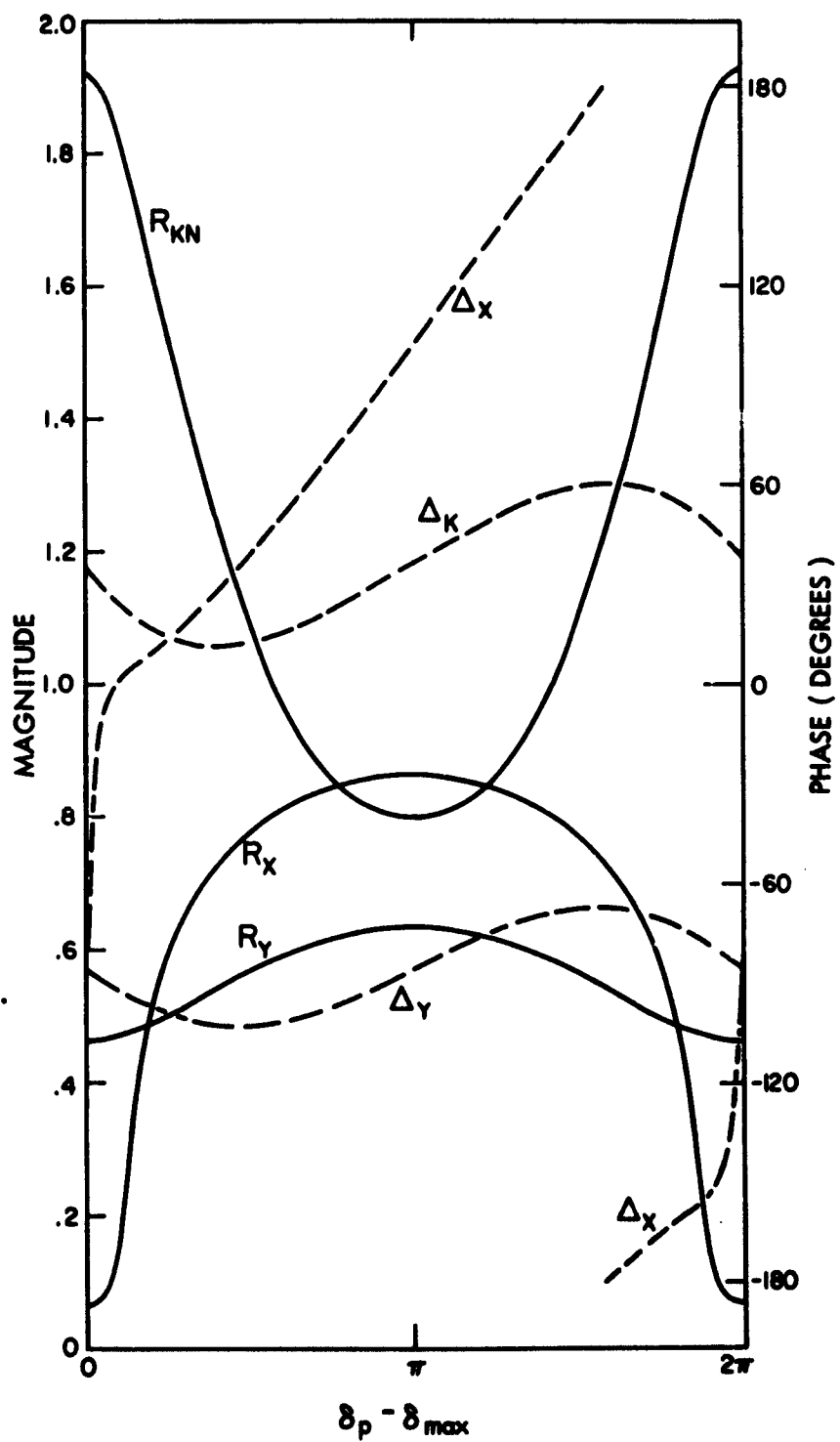


FIG. 2-26 VARIATION OF REFLECTION COEFFICIENTS - $n_1 = 2.40$

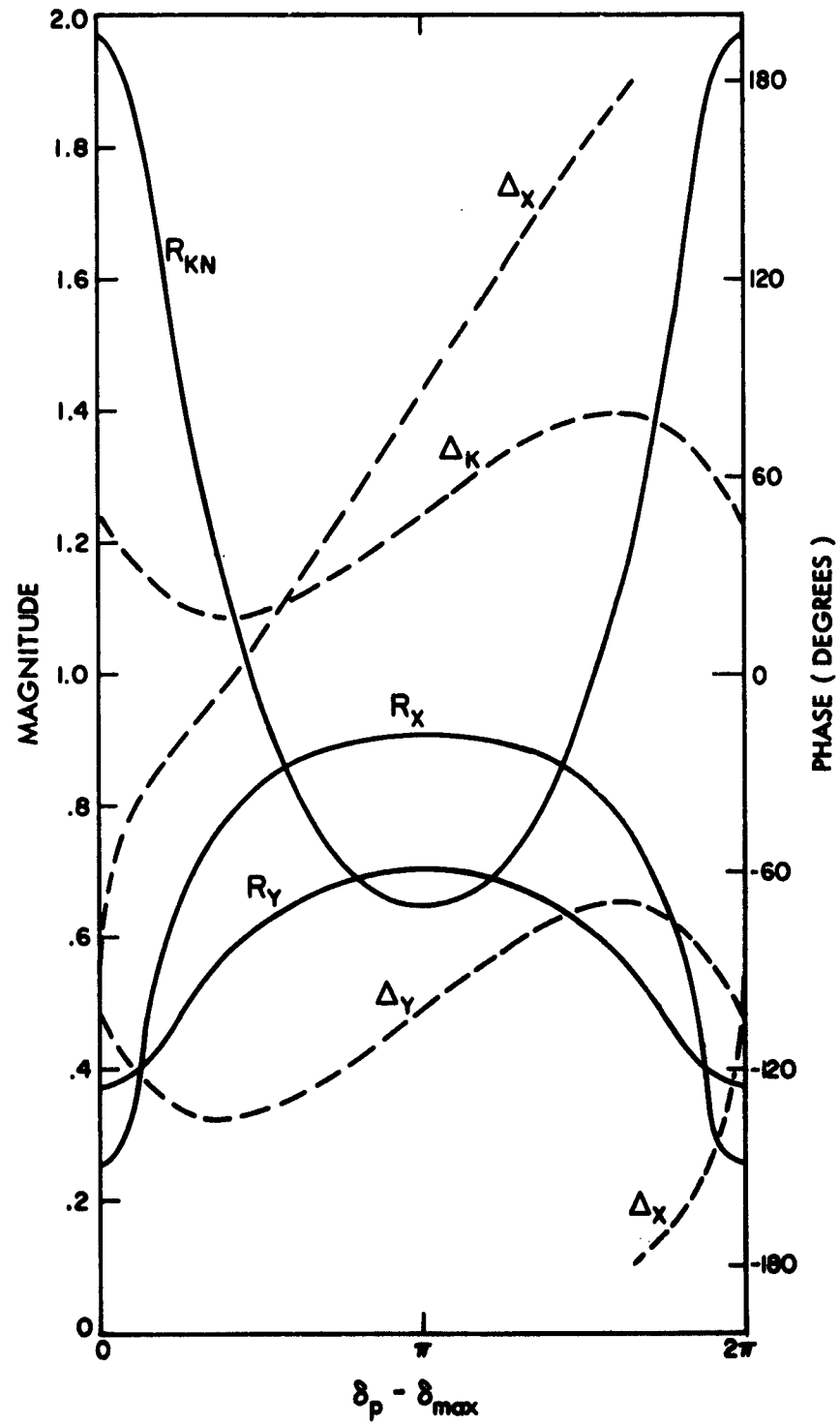


FIG. 2-27 VARIATION OF REFLECTION COEFFICIENTS - $n_1 = 3.14$

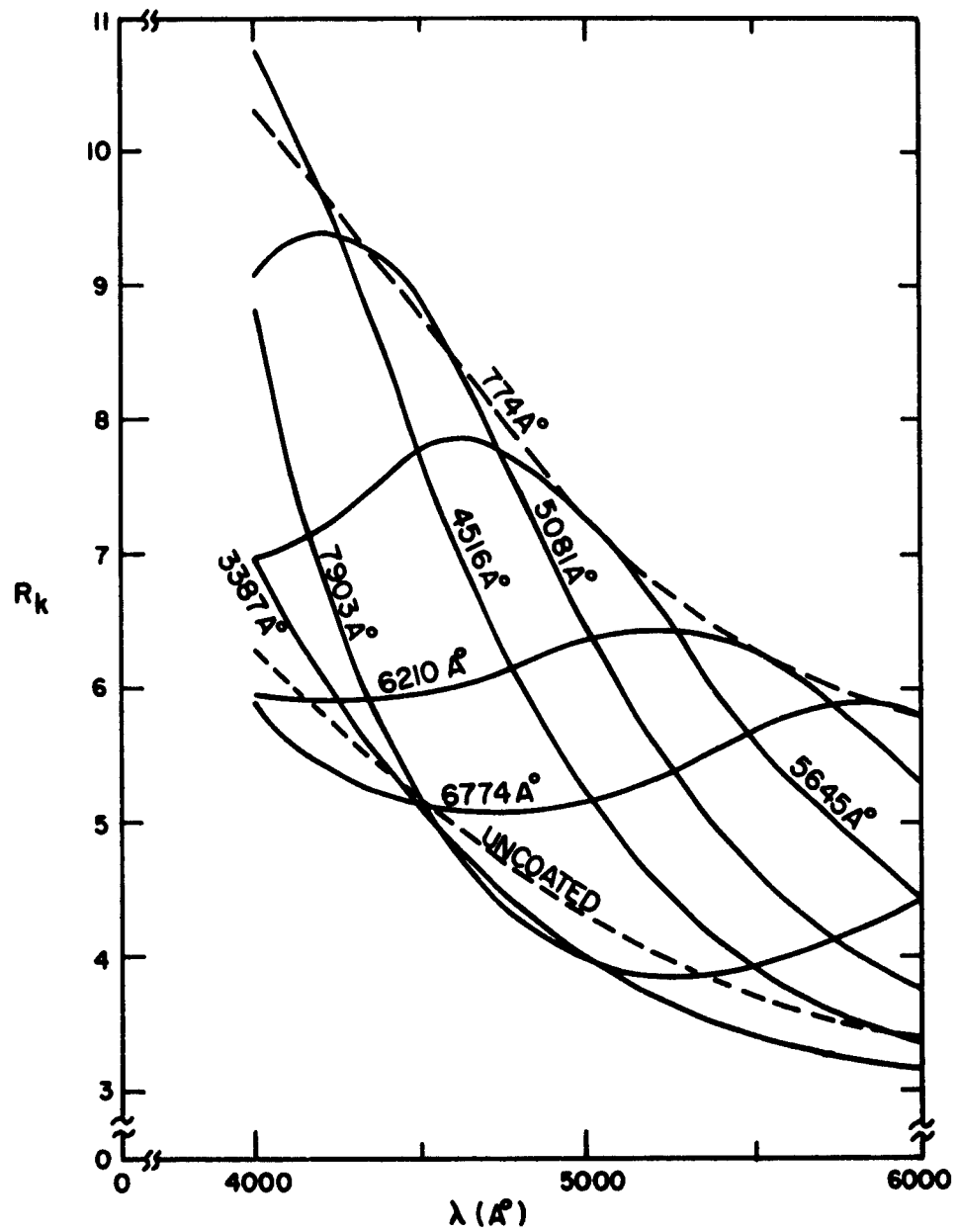


FIG. 2-28 R_k OF PERMALLOY FILM WITH DIELECTRIC LAYER -- $n_1 = 1.66$

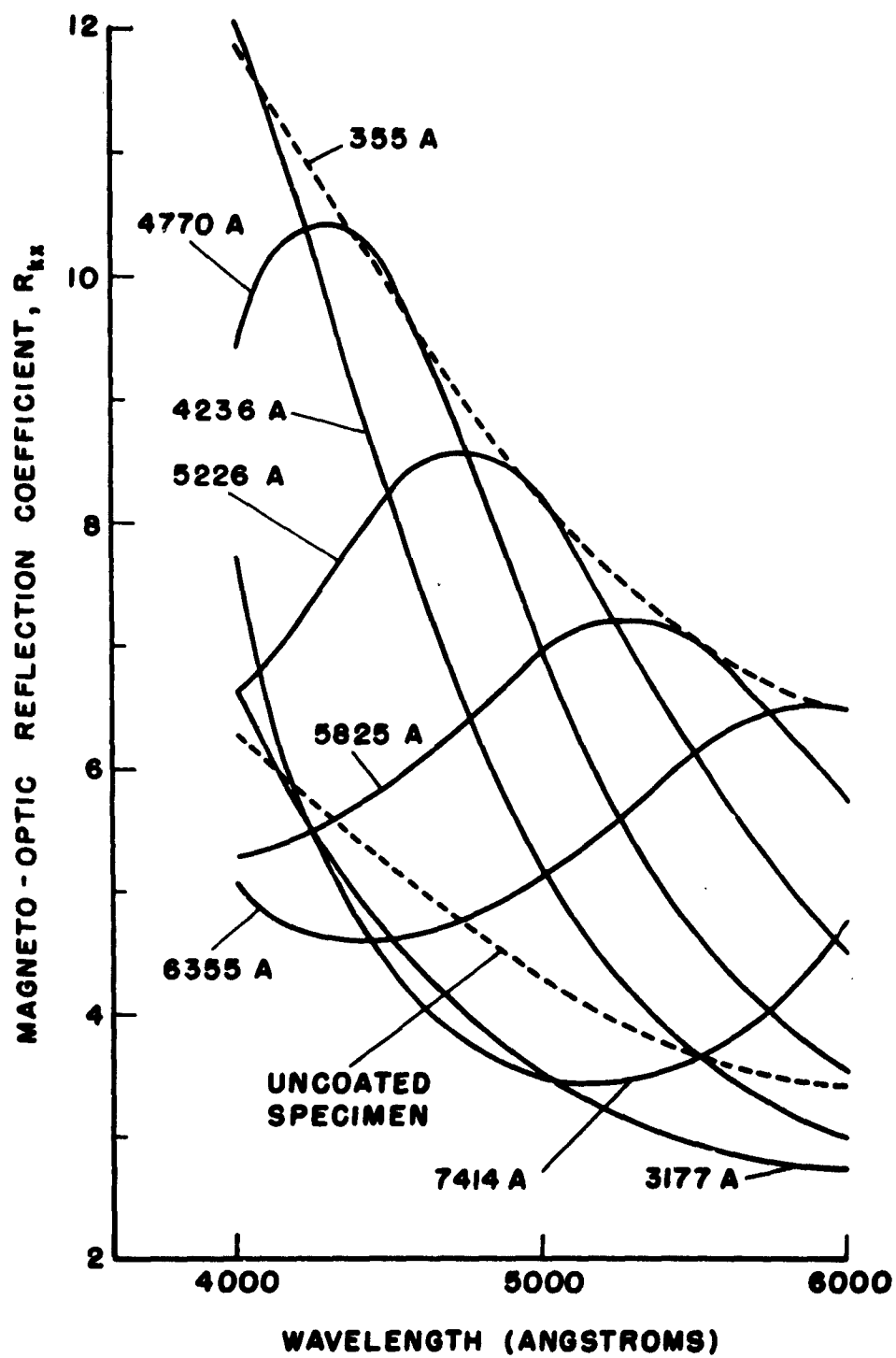


FIG. 2-29 R_k OF PERMALLOY FILM WITH DIELECTRIC LAYER -- $n_1 = 2.40$

d	n_l	$R_e^2 q_p^2$	q_{km}^2	q_x^2	q_y^2	\bar{R}_k	max #	max center
0	--	.216	.038	0	0	4.47		
774 Å	1.66	.029	.035	0	0	7.54	1	5000 A
3387 Å	1.66	.230	.062	.001	0	4.34	2	3000 A
4516 Å	1.66	.095	.218	.036	0	5.93	2	4000 A
5081 Å	1.66	.061	.094	.038	0	6.64	2	4500 A
5645 Å	1.66	.058	.027	.033	0	6.62	2	5000 A
6210 Å	1.66	.077	.002	.052	0	6.06	2	5500 A
6774 Å	1.66	.113	.003	.047	0	5.42	2	6000 A
7903 Å	1.66	.180	.067	.003	0	4.75	2	7000 A
355 Å	2.40	.012	.037	0	0	8.54	1	5000 A
3177 Å	2.40	.301	.081	.003	.008	3.88	2	3000 A
4236 Å	2.40	.084	.218	.053	.003	6.08	2	4000 A
4770 Å	2.40	.045	.120	.065	0	7.08	2	4500 A
5296 Å	2.40	.040	.031	.058	0	7.06	2	5000 A
5825 Å	2.40	.058	.010	.089	0	6.37	2	5500 A
6355 Å	2.40	.107	.018	.078	0	5.38	2	6000 A
7412 Å	2.40	.241	.087	.002	0	4.18	2	7000 A

TABLE II-2

Specimen Parameters

λ	R_k	Δ_k	R_x	Δ_x	R_y	Δ_y	T_2	T_1
4000	.0094	3.5°	.61	16°	.50	-99°	15.6 x 10 ⁻⁶	87.0 x 10 ⁻⁶
4250	.0104	1.0°	.26	4°	.47	-93°	37.5	76.1
4500	.0100	7.0°	.07	-86°	.46	-85°	51.2	51.3
4750	.0086	12.5°	.18	-144°	.47	-78°	49.7	29.0
5000	.0069	16.6°	.52	-162°	.49	-73°	58.1	8.5
5250	.0056	16.5°	.65	-170°	.51	-69°	54.6	8.0
5500	.0047	15.2°	.71	-176°	.54	-68°	50.1	3.6
5250	.0040	9.0°	.76	-186°	.56	-67°	48.2	4.2
6000	.0036	0.2°	.71	-192°	.57	-68°	47.3	6.0

d = 4770 A

$\gamma = -.00691$

$\phi = -.00176$

$t_1 = 1.0$

$T_{w1} = T_{lav} = 28.8 \times 10^{-6}$

$T_{w2} = T_{2av} = 47.6 \times 10^{-6}$

$R_c = 1.65$

TABLE II-3

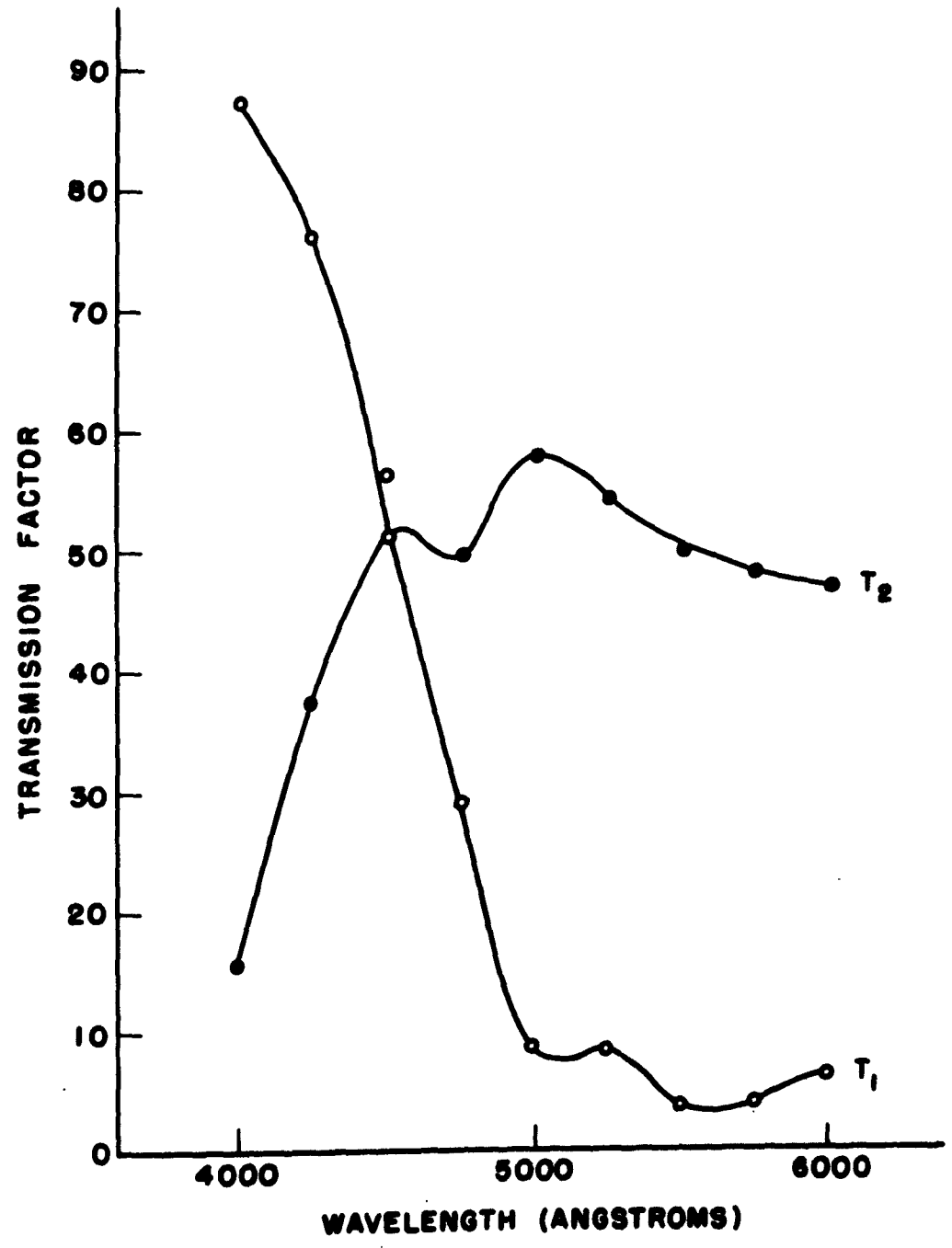


FIG. 2-30 EXAMPLE OF TRANSMISSION FACTORS WHICH YIELD COLOR EFFECTS

given in Table II-3 that the angular settings of the polarizers are probably not optimum, since the contrast ratio for a white light source is quite small, being about 1.65. This is consistent with our previous derivations, which indicated that for a white light source one should adjust the polarizers for a minimum at that value of R_k which is equal to the average value of R_k . To achieve this, we see from Table II-2 and Fig. 2-29 that we should adjust in this case for a T_1 minimum at 4980 \AA ; the computations were done for the 5500 \AA minimum in order to better illustrate the color effects.

The colors which would be observed for the transmission curves in Fig. 2-30 were determined with the aid of a tristimulus diagram⁶. In order to more nearly approximate the transmission curves which would be observed visually, transmission values were estimated for the wavelength range from 6000 \AA to 7000 \AA . According to this determination, in State I the color to the observer would be purple of 75 per cent purity centered at 4000 \AA while that in State II would be yellow of 16 per cent purity centered at 5750 \AA . One notes that it would be relatively easy under such conditions to distinguish between domains, although the overall intensity contrast ratio is only 1.65.

From the parameters listed in Table II-3, one can see the reason for the transmission behavior. In the 5000 \AA to 6000 \AA wavelength range, all parameters are either relatively constant or at the most only slowly varying. Hence the transmission factors T_1 and T_2 vary only slightly over this range. In the range of 4000 \AA to 5000 \AA , however, R_x and Δ_x vary considerably. This means a departure from the T_1 minimum conditions and we see the result in the increase of T_1 in this range. The R_x and Δ_x variations also result in a decrease in the T_2 transmission near 4000 \AA . One would suspect that this is not merely fortuitous, since an unvarying T_2 curve would mean that the specimen in State II would appear white to the observer, and such is not the case. However, to be certain of the transmission factor behavior would require an amount of computation which is beyond the scope of the present project.

To apply a general maximization procedure to the dielectric coated specimen case would be quite difficult, the reason being evident if we refer back to Eq. (II-38).

$$T_{wn} = \frac{P_{av} P_{av}^*}{r_{km}^2} + R_e^2 q_p^2 + q_{km}^2 \cos^2 \alpha + q_x^2 \left(\frac{\gamma}{r_{km}}\right)^2 + q_y^2 \left(\frac{\phi}{r_{km}}\right)^2 + 2 \left[q_{kx} \left(\frac{\gamma}{r_{km}}\right) + q_{ky} \left(\frac{\phi}{r_{km}}\right) \right] + 2 q_{xy} \left(\frac{\phi}{r_{km}}\right) \left(\frac{\gamma}{r_{km}}\right) \quad (II-38)$$

The values of $R_e^2 q_p^2$, q_{km}^2 , q_x^2 and q_y^2 for the various values of d used in Figs. 2-27 and 2-28 have been tabulated in Table II-2. The values of q_{kx} , q_{ky} and q_{xy} were not computed because of the time involved, but the data tabulated is sufficient to indicate the difficulties. We were able to carry out the maximization previously because all terms excepting $R_e^2 q_p^2$ and q_{km}^2 could be neglected. As we see from the data in Table II-2, this cannot be done in the present case, as q_x^2 and q_y^2 are not generally negligible with respect to $R_e^2 q_p^2$ and q_{km}^2 . Moreover, the values of q_{kx} and q_{ky} for the uncoated specimen were comparable in magnitude to q_{km}^2 and the writer suspects that this will also be true in the present case. This means, for example, that for $n_1 = 1.66$ and $d = 5081$ all q terms would be of the same order of magnitude and we would hence have to have numerical values for each maximization.

One case, though, can be treated by our previous analysis, the case when the first R_{kn} maximum lies in the visible spectrum. Since the maximum in this instance is broad, all magnitude and phase characteristics are simply changed by a constant value. Specifically, $R_{kn} > 1$, R_x and R_y are decreased, and the phases are shifted. This means that q_{km}^2 remains the same as for the uncoated specimen case, while all other q values are

decreased; hence, by the same arguments as were used in the uncoated specimen case for a white light source, we need only consider $R_e^2 q_p^2$ and q_{km}^2 , and the results in Eqs. (II-40a) through (II-40c) can be applied. Moreover, as was noted previously, for a given value of n_1 the maximum value of \bar{R}_k occurs in this case.

We can summarize the results of this section as follows:

1. R_{kn} is maximized with a dielectric layer with a refractive index equal to three. In practice, the highest refractive index attainable in a thin dielectric seems to be 2.4, that for zinc sulfide and titanium dioxide. However, this only decreases R_{kn} by about two per cent from its maximum possible value.
2. \bar{R}_k is maximized when the thickness of the layer is such that the first maximum of R_{kn} lies in the visible spectrum. For such a thickness the background noise is decreased over that for the uncoated specimen. Therefore, considerably higher contrast should be available.
3. Because of the broad maximum, there should be little, if any, color effects visible.
4. For any dielectric thickness other than that mentioned immediately above, \bar{R}_k is lessened and the background noise may be increased.
5. For relatively thick dielectric layers (2000 Å or higher) color effects will probably be present.

CHAPTER III

SYSTEM DESIGN

For photographing the switching phenomena described in Chapter I, three photographic systems have been considered:

System I -- a single exposure system with sufficient aperture and light source intensity to record a stage of the switching in one exposure.

System II -- a repetitive system which would strobe any given stage of the magnetic switching and repeatedly photograph it until a sufficiently dense image had been built up on the photographic film.

System III -- a multiple exposure system which would record successive stages of switching during a single switching cycle.

This Chapter will present a description of the completed system, a discussion of the various design decisions which led to the selection of the particular components used, and an estimate of the operating limitations of the apparatus.

The design basis of the apparatus, which we are about to describe, was that of System I, mentioned above; the reasons for the choice will be discussed later in this Chapter. Such a system can be viewed basically as a merging of magneto-optic techniques and ultra high speed photographic techniques. Considerable research has been carried out by a number of people in both of these areas.^{1, 2, 3, 4, 5, 6} In addition to the components shown in Figure 22, the electronic apparatus for applying a pulsed field and synchronizing this field with the shutter and the light source (assuming the use of a flash lamp) is required for conducting studies during the switching of ferromagnetic specimens. A few lenses are also necessary. Since all of these items are, to a greater or lessor extent, fairly commonly known and used, the question arises: Why should the construction of such an apparatus involve any

special difficulties? The answer lies in a consideration of the surface brightness of available light sources, the transmission factor of the system, the exposure duration required, and the light sensitivity of available photographic emulsions.

Initially, in this Chapter, we will present a description of the completed system, following which the major design factors and problems will be discussed. Some numerical estimates on the operating limits of the system will be made. The more specific aspects of the design problems will be treated in ensuing chapters.

3.1 The Magneto-optic Photographic System

The completed system is shown in Figure 3-1. Figure 3-2 is a schematic of the optical portion of the apparatus, while Figure 3-3 is a block diagram of the electronic instrumentation.

For dynamic exposure (referring to Figure 3-2), high-intensity short-duration light pulses are focused by the flash lamp lens through a Glan-Thompson prism onto the specimen. The light reflected from the specimen is collected by the object lens and passes through a second Glan-Thompson prism, the analyzer for observing the magnetic configuration of the specimen. Shuttering is accomplished by a Kerr electro-optical shutter (a nitrobenzene cell) oriented at 45° with respect to the principal plane of the analyzer. This analyzer and the third Glan-Thompson prism, which is oriented at 90° with respect to the principal plane of the analyzer, are the polarizers required for the shuttering action of the Kerr electro-optical unit. After passing through the shutter, the light is focused by the camera lens onto the photographic film. The object lens is so positioned that it images the center of the specimen at infinity, and the camera lens is hence focused for an object whose center is at infinity; the reasons for this will be discussed in the following chapter. All Glan-Thompson prisms are mounted in precision rotary tables to facilitate accurate angular positioning and ease of adjustment of their polarizing axes.

In Figure 3-4 we see the specimen holder and the magnetic field coils. The specimen holder is merely a length of polystyrene mounted



FIG. 3-1a COMPLETED MAGNETO-OPTIC PHOTOGRAPHIC APPARATUS

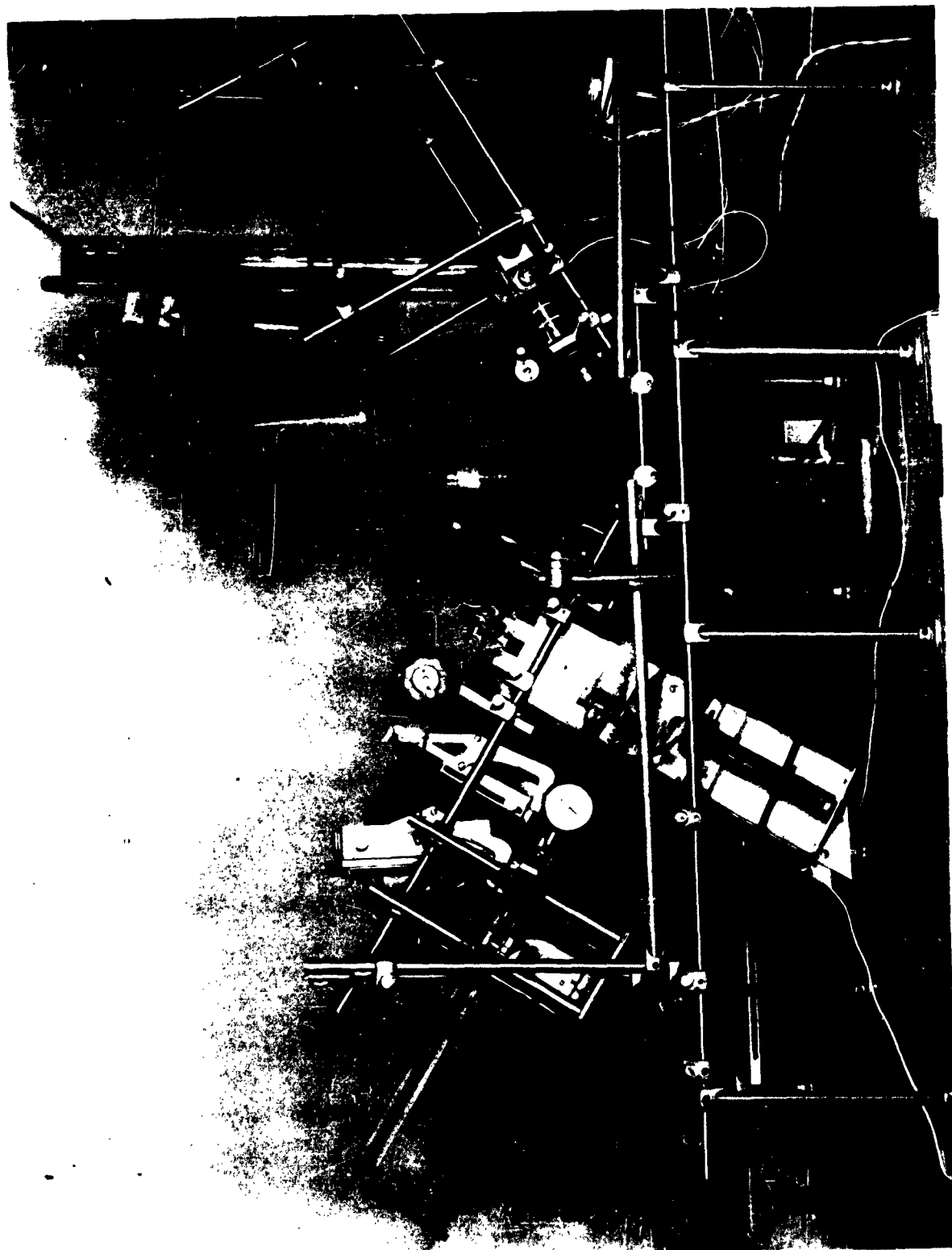


FIG. 3-1b COMPLETED MAGNETO-OPTIC PHOTOGRAPHIC APPARATUS - OPTICAL SECTION

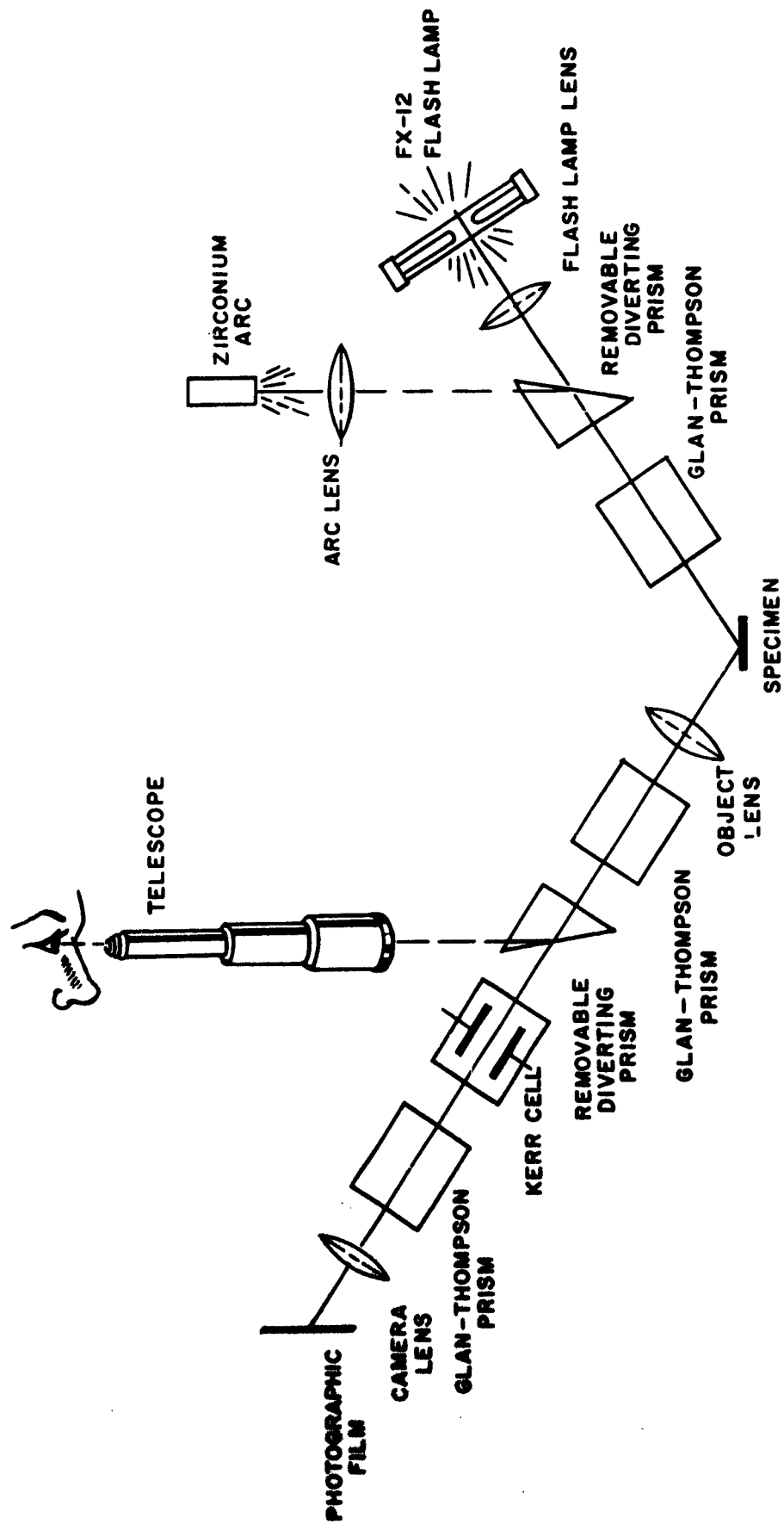


FIG. 3-2 OPTICAL SCHEMATIC

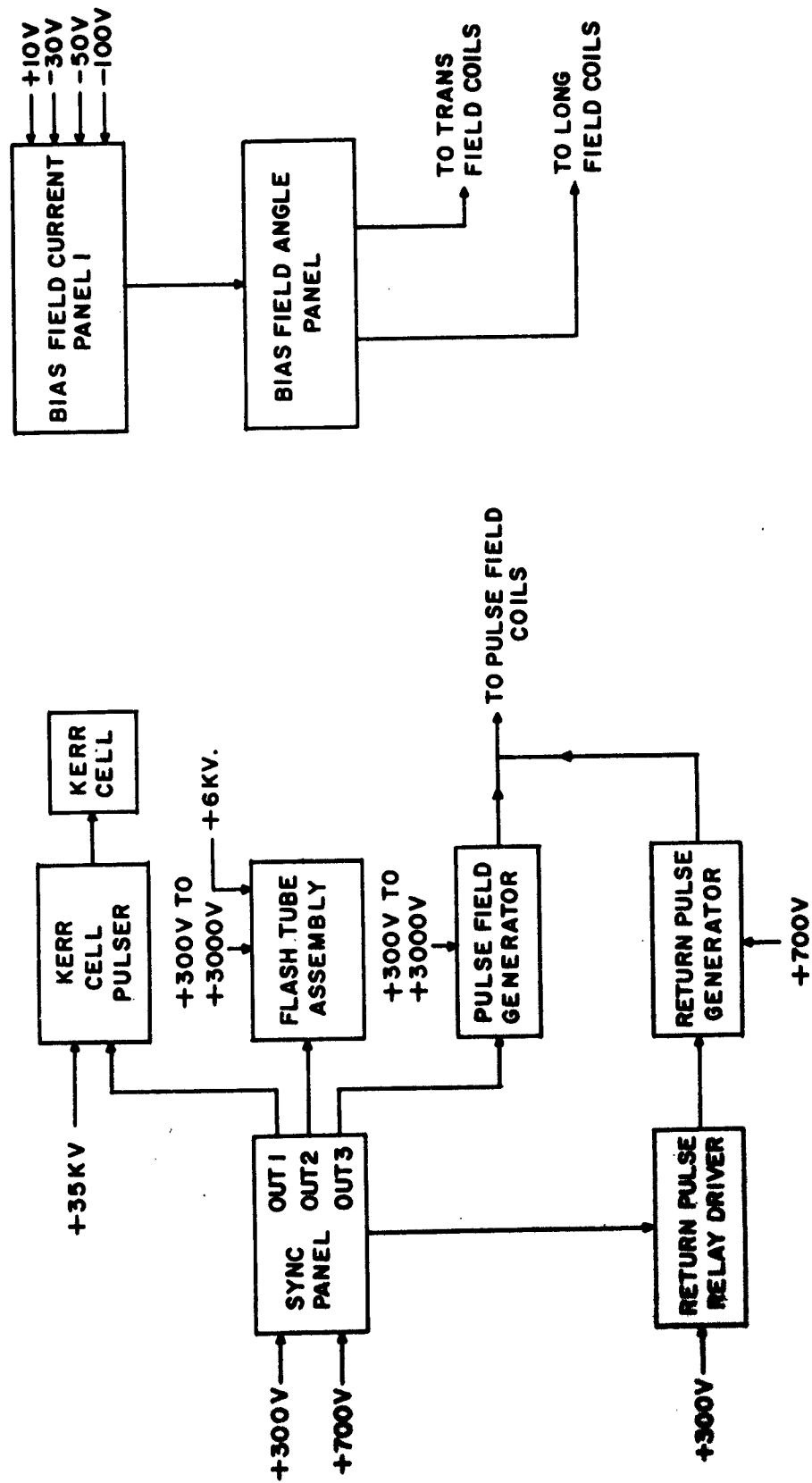


FIG. 3-3 ELECTRONIC INSTRUMENTATION BLOCK DIAGRAM

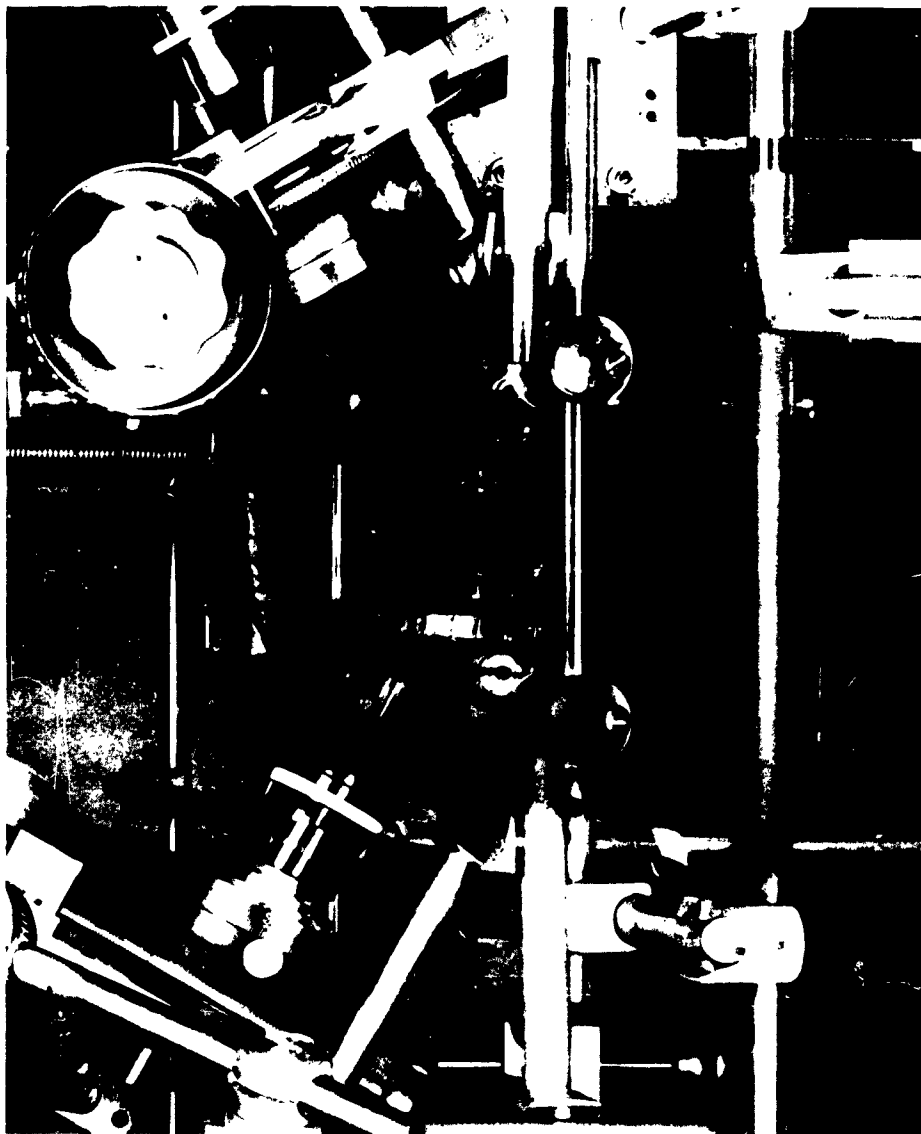


FIG. 3-4 SPECIMEN HOLDER AND FIELD COILS

at its lower end in two ball bearings to facilitate rotary positioning of the specimen. All magnetic fields are generated from Helmholtz coil pairs. The two large Helmholtz pairs supply longitudinal and transverse bias fields; the two small pairs (each coil consisting of a single silverplated brass ring) provide either a longitudinal or a transverse pulsed field for switching the specimen. All apparatus in the vicinity of the specimen is painted with flat black paint.

The voltage pulse for the shutter, the current pulse for the pulsed field coils, and the trigger pulse for the flash lamp are all supplied by hydrogen thyratron pulse generators. Synchronization of these pulse generators is accomplished by a pulse distribution panel incorporating variable and tapped delay lines. Current for the bias field coils is supplied by a regulated supply which is so designed that it can be used for visual observation of quasi-static switching.

For static observations a telescope and a zirconium arc lamp with a condensing lens are included in the apparatus. These are introduced into the optical path, as shown, by means of removable diverting prisms.

3.2 Choice of System

At the beginning of this Chapter, three possible systems were described. The multiple exposure system (System III) was considered unfeasible from consideration of cost and time required. With such a system, in order to obtain meaningful data about film switching of 1 μ sec duration, a framing rate on the order of 20,000,000 exposures per second would be required; commercial cameras with such a framing rate are not available. At one point an electric optical multiple exposure unit was designed. This setup would use a Kerr electro-optic cell followed by a Wollaston prism to switch light from one path to another; a number of such units cascaded in a standard relay tree circuit would have a framing rate limited only by the switching speed of the circuitry energizing the Kerr cells. However, for 2^k exposures, $2^k - 1$ prisms and Kerr cells would be required, and for any useful number of exposures the cost of the prisms and developing the Kerr cell units was considered prohibitive; also, an undue amount of development time would be involved.

If the magnetic configurations of the film at a given stage of the switching cycle were the same from cycle to cycle, System II would be quite adequate for the desired results. Unfortunately, the few indications available are to the contrary. Barkhausen effects⁷ and switching studies⁸ for materials other than thin films indicate that switching is non-repetitive; there is no reason to believe that the case would be any different with thin films. A number of remanent states of a thin film are shown in Figure 3-5. (These photographs were taken at an early stage of the work when the optics would not give satisfactory focusing). These states are on the same point of a highly saturated hysteresis loop and were successively photographed upon complete traversals of the loop. The lower photograph is an effective superposition of twenty such states; it is obvious that the magnetic configuration does not repeat from cycle to cycle in this case. The observations of Conger *et al.*⁹ on thin film switching indicate that while some areas of a film may switch repetitively, others may not. Moore¹⁰ states that he has observed repetitive switching but that adjustment of operating conditions is very critical to obtain this behavior.

None of these objections apply to System I. Many of the basic ideas of this system are quite straightforward, albeit one may expect difficulties in employing them. Since this system seems to be feasible, we shall now examine the reasons for the choice of the major components involved.

3.3 Light Source

Four types of light sources are available when high intensity sources are required: xenon flash lamps, spark gaps, exploding wires, and argon bombs. Of these the xenon lamp is the most desirable in the present application. Spark gaps can be designed for short duration¹¹ (which would eliminate the need for a shutter in the system if the intensity was sufficient) or for high intensity, but not both. Exploding wires¹² have yielded total outputs as high as 2×10^8 candle power; the surface brightness of such a source is not mentioned, and, as we shall see later, surface brightness is far more important for our purposes than total



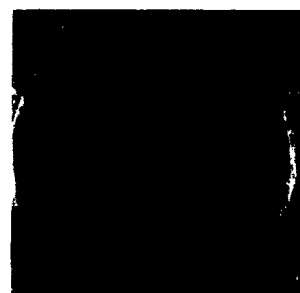
72.4 PER CENT DARK



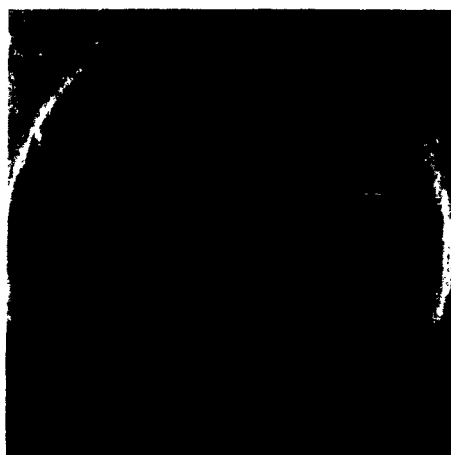
78.5 PER CENT DARK



80.6 PER CENT DARK



81.4 PER CENT DARK



20 REMANENT STATES SUPERIMPOSED

FIG. 3-5 REMANENT STATES

output since we can only utilize a small area of the source. Both spark gaps and exploding wires have fair amounts of jitter and for this reason were dropped from consideration. The light from an argon bomb is generated by a shock wave traveling through argon gas, the shock wave arising from an explosive charge. This source has long duration, eliminating synchronization problems, but has the disadvantage of being dangerous and likely to blow up the entire apparatus as well as being exceedingly inconvenient to use. Hence xenon lamps were chosen as the light source; they are easily synchronized, have high intensities, and are available in a wide variety of shapes and sizes. The particular lamp selected for this work is an Edgerton, Germeshausen and Grier type FX-12 lamp.¹³ This device can be operated at a peak surface brightness of 4×10^{11} candles/meter² with a total peak output of 3,000,000 horizontal candle power and a duration of 2 microseconds. Its small size (1.2 mm x 6.4 mm) makes it readily adaptable to the optical system, as we shall see later.

3.4 Shutter

From the data of Olson and Pohm we have seen that switching times as short as 8×10^{-8} seconds are of interest. To make any pretense at stopping the motion at these speeds requires an exposure duration of 5 to 10 mμ sec. at the most. Such short exposures are only obtainable with a Kerr electro-optical shutter, an image-converter shutter, or possibly a solid state electro-optical shutter based on the electro-optical behavior of ammonium or potassium dihydrogen phosphate. Magneto-optic shutters were considered, but it was decided that it would be difficult, if not impossible, to operate them in this range. The solid state shutter requires the use of highly collimated light; in addition, the only data available on its high speed behavior concerns its use in a wave guide at a frequency of 3,000 mc¹⁴ and considerable experimentation might be required to attain successful operation. The image-converter shutter, developed by RCA,¹⁵ was not commercially available at the time this work was started; it has the advantage of having a certain amount of light amplification, but the disadvantages of critical shuttering voltage for proper operation and poor resolution relative to that of the electro-optical shutters.

The only drawbacks of the Kerr electro-optical shutter are that (1)

extremely high voltages are required for use with wide aperture shutters and (2) the active element is nitrobenzene, an organic liquid which is toxic and which stops all wave lengths shorter than 4300 Å. Despite these factors, in view of the fact that this type of shutter has been used extensively in the fractional μ sec. region, the decision was made to incorporate a shutter of this type. Two commercial Kerr cells are available. Investigation of these units revealed that one of them has an intolerable amount of jitter and that both use undesirable polarizers for this particular application; also, the cost of both units was prohibitive. Since one of these units seems to be exceedingly well designed, having wide aperture and low jitter, the writer decided to construct a similar unit making modifications where desirable.

3.5 Photographic Film Sensitivity

Initial investigations on the requirements of the problem indicated that photographic emulsion speed would be of considerable importance towards obtaining results. High-speed emulsions, of course, mean some sacrificing of resolution, but high resolution is of no value if there is not sufficient light energy to form a photographic image. The optical system has an input aperture limitation, since the variation of angle of incidence of light on the specimen must be only a few degrees. This means that for a given specimen and a given exposure duration the total light energy available for forming an image on the photographic film is constant. By changing the camera lens focal length (See Figure 3-2), the image size can be varied and the light energy per unit area in the image can be matched to the film speed. Under such circumstances, optimum results are obtained with a photographic emulsion that has a high speed-to-granularity ratio. There are certain limitations to this; for example, one should not choose an emulsion with an ASA rating of 1 just because the speed-to-granularity ratio of that emulsion is high.

The initial choice of film was Kodak Royal-X Pan film. This film can be rated at ASA 1600 and has a fairly flat response over the visible spectrum. An example of a 10 millimicrosecond exposure of a specimen taken with this film is shown in Figure 3-6. As is apparent from the



FIG. 3-6 10 μ SEC EXPOSURE -- ROYAL-X PAN FILM



FIG. 3-7 10 μ SEC EXPOSURE -- DOUBLE-X FILM

photograph, the film is quite grainy, obscuring the domain detail.

A later choice of film was Eastman Double-X Cine Film. This emulsion is somewhat slower than Royal-X Pan but has a higher speed-to-granularity ratio. Figure 3-7 is a 10 millimicrosecond exposure under the same magnification conditions as Figure 3-6. The density of the image on the Double-X film is less than the image on the Royal-X Pan film, but the granularity of the former is far less than that of the latter.

ASA ratings are somewhat meaningless when working at the toe of the log density-log exposure curve of an emulsion. A rough estimate would be that the films mentioned can be used somewhere in the range of ASA speeds from 1000 to 5000.

3.6 Pulsed Magnetic Field

Some characteristics of parallel plate transmission lines and single-turn Helmholtz coil pairs were investigated to determine their relative merits for providing a pulsed magnetic field.

A parallel plate transmission line has the immediate advantage that, when properly terminated, it presents a resistive load to the driving source, a desirable feature in high speed pulse work. The field-current relationship in such a line of width w is given approximately by

$$H = 1.26 \frac{I}{w} \quad (\text{III-1})$$

where H is in oersteds, I is in amperes, w is in cm. If we desire that a minimum field of 10 oersteds is being generated by a source current of 30 amperes, a plate width equal to or less than 4.75 cm will provide the necessary field. If we assume for this width, a plate separation on one centimeter, the field on a one-centimeter diameter specimen centered within the line will be uniform to about 3 per cent.

Since we wish to be able to apply pulsed fields both along and transverse to the optic axis, two sets of parallel plate lines would have to be used. In each case the top plate intersects the optic axis in the system and viewing holes would therefore have to be cut in the plates. It is also desirable to be able to rotate the specimen for optimum positioning; this would mean either a specimen holder of increased complexity

over that which is actually being used or holes cut in the bottom plates of the lines to allow the use of a specimen holder mounted underneath the line and projecting into the pulsed field space. All such holes tend to distort the magnetoc field and to introduce higher modes other than the simple TEM mode which is present in the ideal parallel plate transmission line.

Curves for inductance and field per unit current as a function of coil diameter are shown in Figure 3-8 for a Helmholtz coil consisting of two single loops of wire. A Helmholtz coil approximately 2" in diameter meets the field-current requirements and has an inductance, for a wire diameter of about 0.1", of 0.2. microhenries. As we shall see shortly, this amount of inductance will have little effect, considering the current pulse source impedance. The Helmholtz coils also present no problems in viewing or in the use of a specimen holder. An analysis of the field in the center plane of this coil shows that for a specimen 1 cm in diameter the field over the specimen varies about one per cent in the direction of the coil axis and about 2.2 per cent at right angles to the coil axis. These factors seem to justify the choice of Helmholtz coils over parallel plate transmission lines for use in the apparatus.

A delay line pulse generator was considered the best circuit for generating the pulse field current. For millimicrosecond rise time, three switching devices can be used in such a pulse generator: hydrogen thyratrons, mercury-wetted contact relays, and spark gaps. The mercury relay has an extremely rapid rise time (less than a millimicrosecond in the proper circuit configuration) but neither it nor a spark gap can be synchronized for the system operation required. Hydrogen thyratrons, as we shall see later, can be operated with minimum rise times of 15 to 30 μsec . They are easily synchronized and, with careful circuit design, jitter can be reduced to about 2 μsec . The thyatron presents an impedance which must be taken into account in the pulse generator design, and it can supply a pulse of only one polarity, unless a pulse transformer is used (which in this case is undesirable). The specimen must be switched in both directions, but the system need be synchronized to only one direction of switching for study. Therefore,

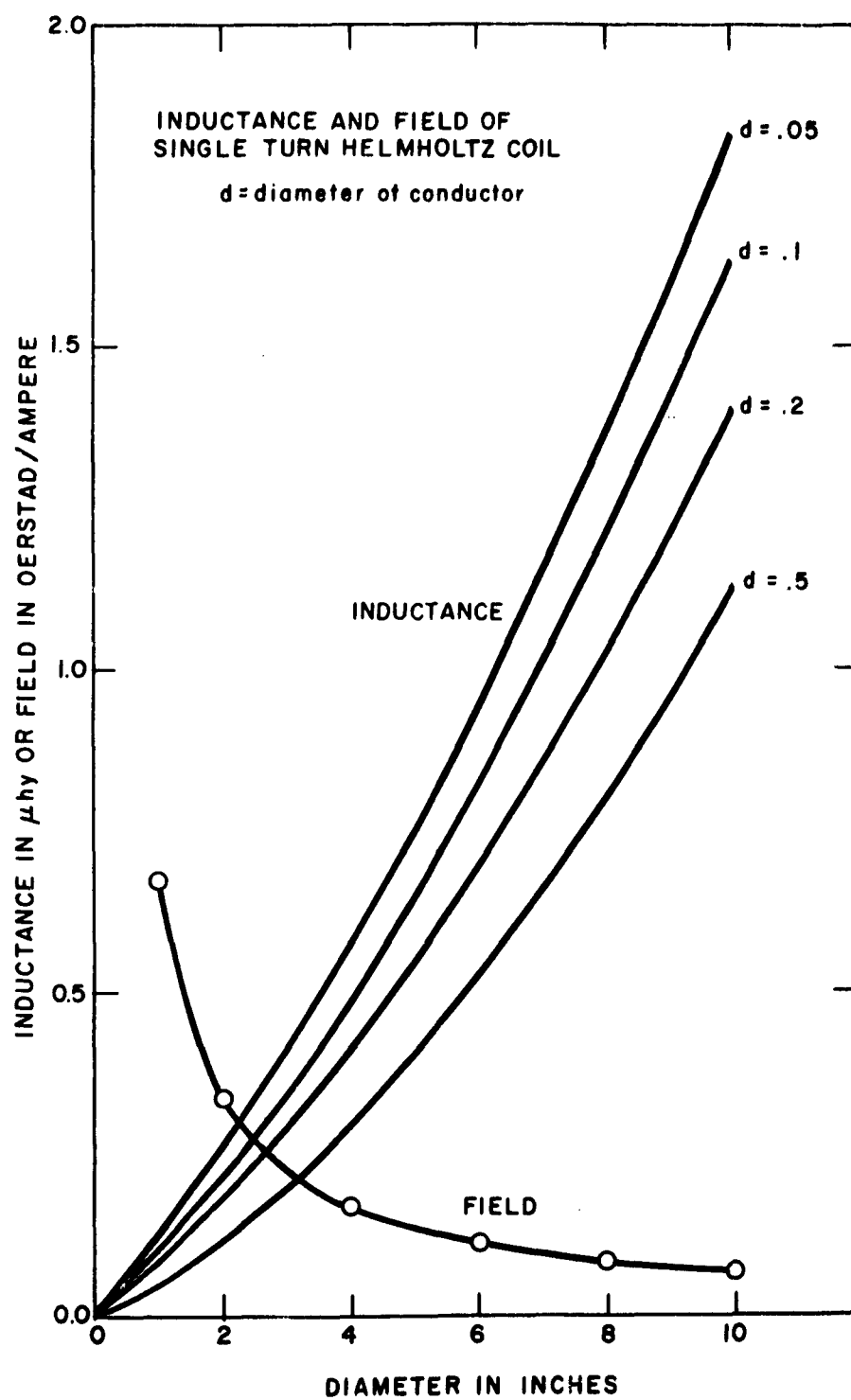


FIG. 3-8

rather than use two sets of Helmholtz coils for a switching field, and two thyatron pulse generators, a single Helmholtz coil is used, with a hydrogen thyatron pulse generator supplying a current pulse of one polarity synchronized to the system and a mercury relay pulse generator supplying an unsynchronized pulse of opposite polarity which restores the magnetization of the specimen to its original state at some later time.

3.7 Estimated Operating Limits

We shall now attempt to estimate some limits on the minimum exposure time at which the system can be operated. To do this we need to know the surface brightness of the light source, the solid angle which the optical system subtends with respect to an elemental source area, the transmission factor of the optical system (including the magneto-optic transmission factor), the ratio of a differential area of the photographic image to a differential source area, and the speed of the photographic film. For this estimate, we shall make use of the results of subsequent chapters as well as those of Chapter II. The reader is requested to bear with the writer in this advance use of results.

In Chapter IV we will point out that for maximum illumination of the specimen, the source should be imaged on the specimen. This means that the light per unit area on the specimen is

$$I_2 = B \Omega \frac{dA_1}{dA_2} \quad (\text{III-2})$$

where B = surface brightness of source in candles/ m^2
 Ω = effective source solid angle in steradians
 dA_1 = elemental source area
 dA_2 = elemental specimen area corresponding to
 dA_1
 I_2 = lumens/ m^2 on specimen

If all light reflected from the specimen arrives at the photographic film, then

$$I_3 = I_2 \frac{dA_2}{dA_3} = I_2 M_{2A} \quad (\text{III-3})$$

where dA_3 = elemental film area corresponding to dA_2

M_{2A} = area magnification (see Section 4)

I_2 = lumens/m² on photographic film.

Now $\frac{dA_3}{dA_2}$ is the area magnification of the specimen image on the photographic film, while $\frac{dA_1}{dA_2}$ is the area magnification of the source

image of the specimen multiplied by the cosine of the angle between the specimen normal and the optic axis. Formulas for computing these are given in Chapter IV; If we know the photographic film speed, the minimum exposure time required is simply

$$t = \frac{1}{SI_3} \quad (\text{III-4})$$

where t = minimum exposure time in sec.

S = ASA film speed rating in meter²/lumen sec.

Thus far, we have assumed no transmission losses. If we represent the overall system transmission factor as T_0 , then from the preceding equations we have

$$t = \frac{M_{2A}}{BST_0} \left(\frac{dA_2}{dA_1} \right) \quad (\text{III-5})$$

As was stated in Section 3.3, the FX-12 flashlamp can be operated at a peak surface brightness of 4×10^{11} candles/meter. Analysis of the optical system indicates that the effective solid angle of the source will probably be between 0.11 and 0.24 steradians. The system value for $\frac{dA_2}{dA_1}$ is 32. Ordinarily we prefer to operate with the value of

$\frac{dA_3}{dA_2}$ no greater than unity, which means the photographic image of

the same physical size as the specimen. Experimental tests show that we can decrease $\frac{dA_3}{dA_2}$ to 167 and still make out large domain configurations, although the resolution decreases because of film grain.

The optical transmission factor is the result of the reflection losses from the lens elements and the Kerr cell, the transmission loss in the Kerr cell due to the nitrobenzene spectral cutoff, the t_1 transmission of the Glan-Thompson prism following the Kerr cell, and the State II transmission discussed in Chapter II. The lenses used in this system are all high-quality coated lenses. Their reflection losses should vary somewhere between 2 per cent and 5 per cent, for each lens element. All lenses shown in Fig. 3-2 in the optical path from the flash source to the photographic film are compound lens assemblies, each having three lens elements. If we regard the Kerr cell reflection loss as being about the same as the lens element losses, then we have ten such losses in the system. Assuming the losses to be identical for each element and denoting each loss as r , the total contribution to the system optical transmission factor is

$$T_L = (1 - r)^{10} \quad (\text{III-6})$$

The transmission factor for spectral limitation was denoted as F in Eq. (II-32b); experimentally, the writer has determined its value as approximately 0.85.

We shall write the product of the magneto-optic transmission factor (determined in Chapter II) and that of the third Glan-Thompson prism as

$$T_m = 1/2 t_1^2 \overline{r_{km}}^6 T_{2n} \quad (\text{III-7})$$

where t_1^2 = prism transmission factor

$\overline{r_{km}}^2$ = squared average value of Kerr amplitude reflection coefficient

T_{2n} = normalized magneto-optic transmission factor.

Our estimate shall be made for two cases, that of an uncoated specimen and that of an optimally dielectric coated specimen as determined in Chapter II. We shall assume that operation is at a contrast ratio value of two, at which value for any specimen with a usable $R_e^2 q_p^2$ value will have a T_{2n} transmission factor of about 45 (see Fig. 2-15). T_0 is the product of all transmission factors and is

$$T_0 = 1/2(1 - r)^{10} F_{t_1}^{6-\frac{2}{r}} T_{2n} \quad (\text{III-8})$$

The speed at which we can use the emulsions discussed in Section 3.5 is in question. It may well be that this can be used at an ASA rating of 5000. The work of Castle et al. shows that the rating of the film might be reduced by a factor of 2 or 3 at short exposure durations due to reciprocity-law failure. We shall assume, therefore, in our estimates that the film rating is somewhere between 1000 and 5000.

Values for the various factors and the resultant evaluation of exposure time from Eq. (II-4) are summarized in Table III.

If we desire to use a $10\text{m}\mu\text{sec}$ exposure duration, we see that at unity area magnification (M_{2A}), we are very unlikely to get results with an uncoated specimen and possibly not with an optimally coated specimen either. With an area magnification of 0.162, we have a fair chance of getting a photograph of an uncoated specimen and an excellent chance of getting a photograph of an optimally coated specimen.

	<u>Uncoated Specimen</u>			<u>Optimally Coated Specimen</u>			
M_{2A}	1	1	0.167	0.167	1	0.167	0.167
Ω	0.11	0.24	0.11	0.24	0.11	0.11	0.24 steradians
B	4	4	4	4	4	4	4×10^{11} candles/m ²
$\frac{dA_2}{dA_1}$	32	32	32	32	32	32	
S	1000	5000	1000	5000	1000	1000	5000 m ² /lumen sec
t_1^2	0.96	0.96	0.96	0.96	0.96	0.96	0.96
\mathcal{F}	0.85	0.85	0.85	0.85	0.85	0.85	0.85
\bar{F}_k	4.47	4.47	4.47	4.47	8.54	8.54	8.54×10^{-3}
T_{2n}	45	45	45	45	45	45	45
r	0.05	0.02	0.05	0.02	0.05	0.05	0.02
t	358	26.1	59.6	4.34	98	7.14	1.194 msec

Estimated Minimum Exposure Durations

TABLE III

CHAPTER IV

OPTICAL APPARATUS

Optical systems for viewing the longitudinal Kerr magneto-optic effect are described in a number of references.^{1, 2, 3} Most of these consist of a collimated source of light which is polarized, reflected from the specimen, passed through an analyzer, and imaged on a photographic film by a lens which may be placed either before or after the analyzer. The angle of incidence is usually 60° , this angle being selected because the data and theory indicate that the Kerr rotation (Ψ_R of Chapter II) maximizes in the vicinity of this angle. The plane of the photographic film is usually shown tilted with respect to the optic axis, but the angle is not specified.

This chapter will present the requirements of an optical system tailored to our specific project, some of the major problems encountered, and analysis whose results can be used to minimize the inherent distortion in the system, and a discussion of the specific optical system which was finally used. Some minor items which facilitate the operation of the system will also be mentioned.

4.1 Requirements of Optical System

Ideally, we would like a system operating with collimated light, having no light losses, and focusing a non-distorted image of as large a size as possible on the photographic film. None of these qualifications can actually be realized. Highly collimated light from physical sources inherently results in low light intensity. The aperture at best is limited by the size of the specimen. A large image reduces the energy per unit area on the photographic film, and some distortion is inherent except under special conditions because the specimen plane is not perpendicular to optic axis.

Let us define the cone angle of light in the following manner. If a piece of black paper containing a pinhole intercepts the path of the light normal to the direction of propagation, the light emerging from the pinhole will be divergent, having a conical shape of some sort. The solid angle of this divergent light is the cone angle of the light at the pinhole.

It is apparent from the above definition that we can have zero cone angle only for a point source. Such a source is nonexistent in the physical world. For any given source the cone angle at any point is simply the solid angle subtended by the source at the point. If we have such a source sending light into an optical system we can find the cone angle at any point in the optical system in the following manner. We determine the location and size of the image of the source as seen from the point under consideration. The cone angle is then that solid angle which is subtended by the visible portion of the source. We emphasize the word "visible" since part of this image may be obscured because of aperture limitations.

We now wish to define two other terms commonly used in photometry. Illuminance is the total flux per unit area incident on a surface. Brightness is the total flux per unit projected area per unit solid angle emitted from or incident upon a given surface, provided that the surface has the properties of a Lambert radiator.⁴ By projected area, we mean the projection of the surface area onto a plane normal to the direction of light propagation. Thus a source with a surface brightness of one candle per unit area will emit one lumen per unit projected area per unit solid angle. Our definition of brightness is slightly different from that found in the optical texts,⁵ but the writer believes it to be more concise. The fact that the apparent area of the surface as seen by an observer is the projected area gives rise to the so-called cosine distribution of flux emitted from a Lambert surface source.

We shall show in Section 4.5 that at any point in an optical system, neglecting reflection and transmission losses, the brightness, (as we have defined it) is equal to the brightness of the source. The projected area dA_p of a differential specimen area dA_s is approximately

$$dA_p = dA_s \cos \theta \quad (IV-1)$$

where

θ = angle of incidence

provided that the incoming light rays are within a few degrees of being parallel. From the definitions and discussion above we see that the illuminance I and the brightness B are related by

$$I = B\Omega_c \cos \theta \quad (\text{IV-2})$$

Hence we see that for a given surface brightness and for a given angle of incidence

$$\frac{I}{\Omega_c} = \text{constant} \quad (\text{IV-3})$$

What we wish to point out here is that when one tries to collimate with a given source, the resulting illumination is specified only by the surface brightness of the source and the cone angle desired. Introduction of additional lenses only serves to lower this illumination through reflection losses and aperture restrictions.

At a later point in this chapter, we will show (1) that certain restrictions on aperture and physical location of optical elements limit the maximum value of collimation angle and (2) that if we try to maximize the total light passing through the system the light falling on a differential area of the specimen will have a solid angle of about 0.01 steradian. This will be referred to as quasi-collimated light since the light rays are close to being parallel, and we will continue to use Eq. (IV-2) as a basis in our design discussion. These were the reasons, then, for the choice of the FX-12 flash lamp -- small size and higher surface brightness than other available xenon flash tubes.

A second consideration of the system is that the light aperture should be kept as large as possible. However, the choice of specimen size immediately begins to impose aperture limits. The specimens range up to one centimeter in diameter and, since they behave as a specular reflecting

surface, act as an aperture stop part way through the system.

Since we plan to use quasi-collimated light, it should be possible to design the system so that any increase in cross-sectional area of the prisms beyond a certain point would be useless. (This must be kept in mind, because the price of a Glan-Thompson prism is roughly proportional to its volume.) The prisms used have a working cross-sectional area of about 16 mm. by 17 mm. This size causes some aperture limitation; further discussion of this can be found in Section 4.6.

An obvious requirement of the apparatus is that the resulting photographs be well focused and as free from distortion as possible. If the optic axis was normal to the specimen surface, this requirement would present no problem -- one would simply use high quality lenses and exercise care in focusing the photographic image on the film. However, in this apparatus the optic axis makes an angle of 60° with the normal to the specimen. We shall show that this introduces image distortion which can be minimized by proper optical design.

4.2 Initial Optical Experimentation

Some initial experiments were conducted in order to try to get some well-defined static photographs of the magnetic configuration of ferromagnetic films and to determine some of the effects of the optical components being used. The light source for this work was a 150-watt Sylvania zirconium arc lamp followed by a 38 mm Hastings triplet lens. For photographing the images, a 4 x 5 Busch Pressman camera was modified so that the photographic film would be tilted 60° from its normal position in the camera. A small telescope was made and installed along with a removable diverting prism to allow changing the optical path from the camera to the telescope. For all optical setups tried, visual observation through the telescope looked quite good. Definition of domains was excellent, particularly for some specimens which were coated with silicon

monoxide layers (thickness not known).

The visual observations showed that commercial achromatic lenses are sufficiently strain-free so as to introduce no birefringence problems if placed before the analyzer. Numerous arrangements of optical elements were tried in efforts to obtain well-focused photographs of the magnetic configuration of the specimen. All such photographs showed poor focusing.

The variation of index of refraction of the Glan-Thompson prisms was suspected to be causing an achromatic aberration of the image. Following a suggestion by Hardy⁶, the following lens setup was tried. A lens of 100 mm focal length was placed so that the center point of the specimen coincided with the focal point of this lens. The camera, which had a lens of 175 mm focal length, was focused at infinity. Under these conditions the specimen is imaged by the first lens at infinity, and therefore the length of the prism is only a negligible portion of the effective optical path seen by the camera lens. The linear magnification of the image for this arrangement (to a first approximation) is the ratio of the focal lengths of the two lenses, in this case 1.75.

Some improvements were noted with this arrangement. The center of the specimen image could be well focused, but the edges were badly blurred. The appearance of the photographs indicated that the photographic film did not coincide in space with the specimen image. Since the optical system has a fairly wide aperture and therefore little depth of field, such coincidence is necessary for good focusing.

These results indicated that a complete analysis of a lens system with a tilted object was in order, since no such analysis could be found in the standard references. The ensuing sections deal with single lens and two-lens systems (single lens and two-lens referring simply to the number of lenses between the specimen and the photographic film).

4.3 Single Lens Analysis

Initially, we wish to show that if a plane object is imaged by a simple lens or a series of simple lenses the image is also a plane. Consider the simple lens and plane object (viewed edgewise) shown in Fig. 4-1. The lines O_1 and A_1 (shown as points since we are looking at them end on) in the object are imaged respectively as lines O_2 and A_2 in the image. From simple lens theory and obvious geometry we have

$$\frac{1}{k_1 F} + \frac{1}{k_2 F} = \frac{1}{F} \quad (\text{IV-5})$$

$$\frac{1}{k_1 F + l_1 \sin \theta_1} + \frac{1}{k_2 F - x_2} = \frac{1}{F} \quad (\text{IV-6})$$

$$\frac{y_2}{y_1} = \frac{k_2 F - x_2}{k_1 F + l_1 \sin \theta_1} \quad (\text{IV-7})$$

$$\frac{x_2}{y_2} = \tan \theta_2 \quad (\text{IV-8})$$

where

F = focal length of lens

$k_1 F$ = object distance on optic axis

$k_2 F$ = image distance on optic axis

l_1 = distance between lines O_1 and A_1

From Eq. (IV-5) we get

$$k_2 = \frac{k_1}{k_1 - 1} \quad (\text{IV-9})$$

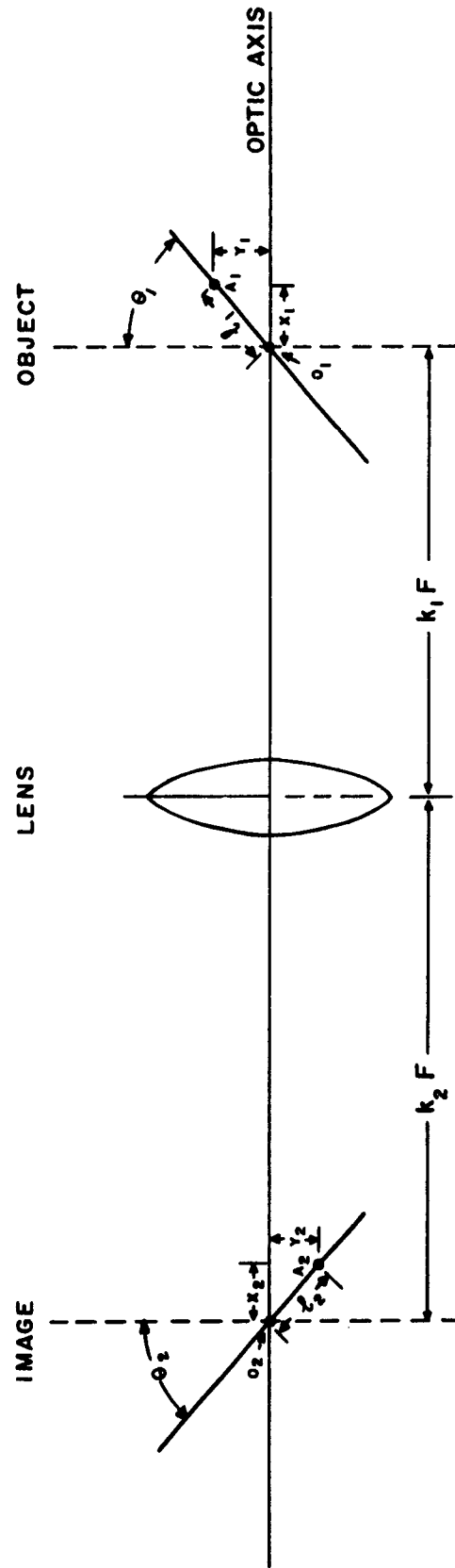


FIG. 4-1 SINGLE LENS ANALYSIS

Substituting Eq. (IV-9) into Eq. (IV-6) and solving for x_2 yields

$$x_2 = \frac{F l_1 \sin \theta_1}{(k_1 - 1) [(k_1 - 1) F + l_1 \sin \theta_1]} \quad (\text{IV-10})$$

Substituting Eq. (IV-10) into Eq. (IV-7) and solving for y_2 yields

$$y_2 = \frac{l_1 \cos \theta_1 F}{(k_1 - 1) F + l_1 \sin \theta_1} \quad (\text{IV-11})$$

Using these relations with Eq. (IV-8), we get

$$\tan \theta_2 = \frac{\tan \theta_1}{(k_1 - 1)} \quad (\text{IV-12})$$

Eq. (IV-12) is dependent only upon k_1 and θ_1 ; hence, we see that the image of a plane object is indeed a plane in the case of a single lens.

If now a second lens is placed after the first lens, the plane image in the present case is a plane object for the second lens and the process repeats itself.

The area magnification can be easily computed by considering the ratio of a differential area $\underline{dA_2}$ on the image to the corresponding differential area $\underline{dA_1}$ on the object

$$M_{1A} = \frac{dA_2}{dA_1} \quad (\text{IV-13})$$

$$= \frac{dl_2}{dl_1} \quad \frac{dz_2}{dz_1} \quad (\text{IV-14})$$

where z_1 and z_2 are perpendicular to the plane of Fig. 4-1.

We see from an examination of the figure and from consideration of Eq. (IV-11) that

$$z_2 = z_1 \frac{1}{(k_1 - 1) + \frac{l_1}{F} \sin \theta_1} \quad (\text{IV-15})$$

and also from (IV-11) that

$$l_2 = \frac{\cos \theta_1}{\cos \theta_2} l_1 \frac{1}{(k_1 - 1) + \frac{l_1}{F} \sin \theta_1} \quad (\text{IV-16})$$

Differentiating these two equations and substituting the results into Eq. (IV-14) yields

$$M_{1A} = \frac{\cos \theta_1}{\cos \theta_2} \frac{(k_1 - 1)}{\left[(k_1 - 1) + \frac{l_1}{F} \sin \theta_1 \right]^3} \quad (\text{IV-17})$$

We reiterate that M_{1A} is the magnification of a differential area on the object and should not be confused with the overall magnification of the object. From Eqs. (IV-15) and (IV-16), we see that (contrary to statements in the literature²) the l -magnification differs from the z -magnification by a factor $\frac{\cos \theta_1}{\cos \theta_2}$ and that both suffer some distortion from the presence of the $\frac{l_1}{F} \sin \theta_1$ term. An illustration of this distortion is given in Fig. 4-2.

4.4 Two-Lens Analysis

Now consider the two-lens system shown in Fig. 4-3. We wish to find k_2' , θ_3 , and M_A in terms of the parameters F_1 , F_2 , d , k_1 , θ_1 , and l_1 . By setting up the dimensions as shown in the figure, we can disregard the fact that the two principal planes of a given lens do not necessarily coincide.

From our previous results and from Fig. 4-3 we can immediately write the following relations

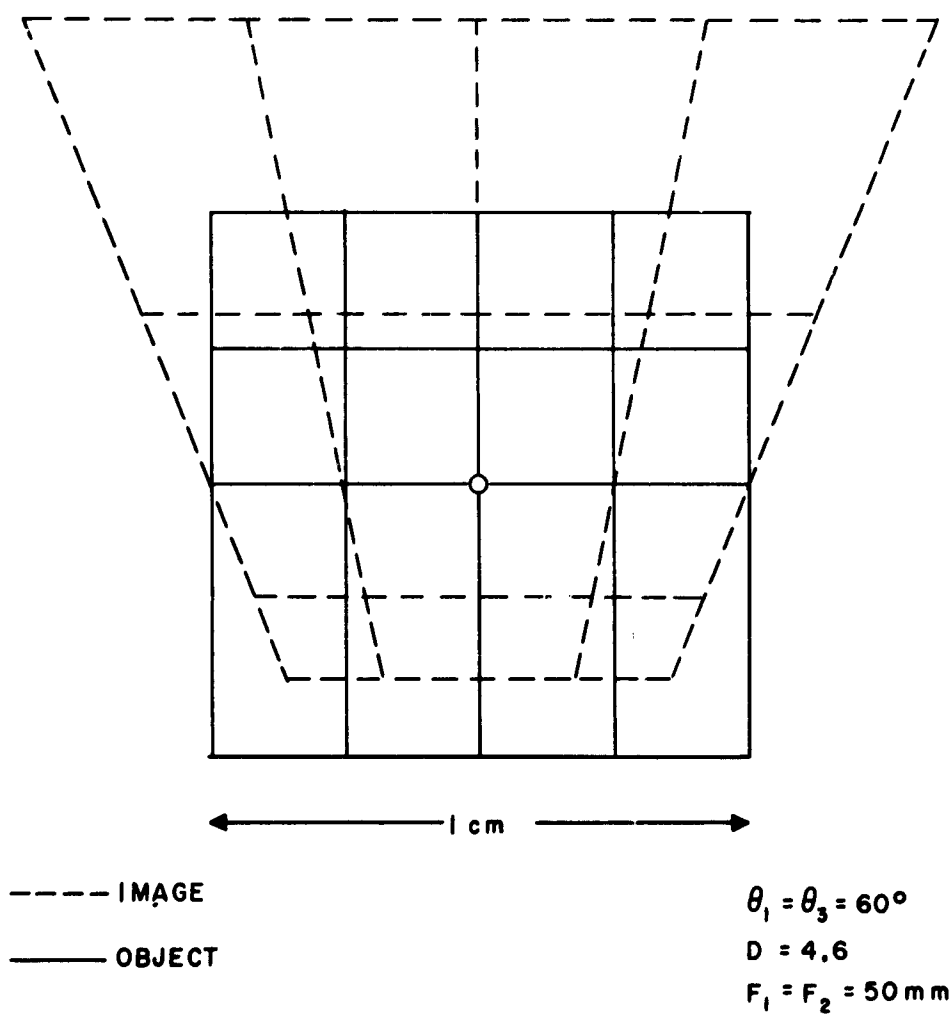


FIG. 4-2 IMAGE AREA DISTORTION

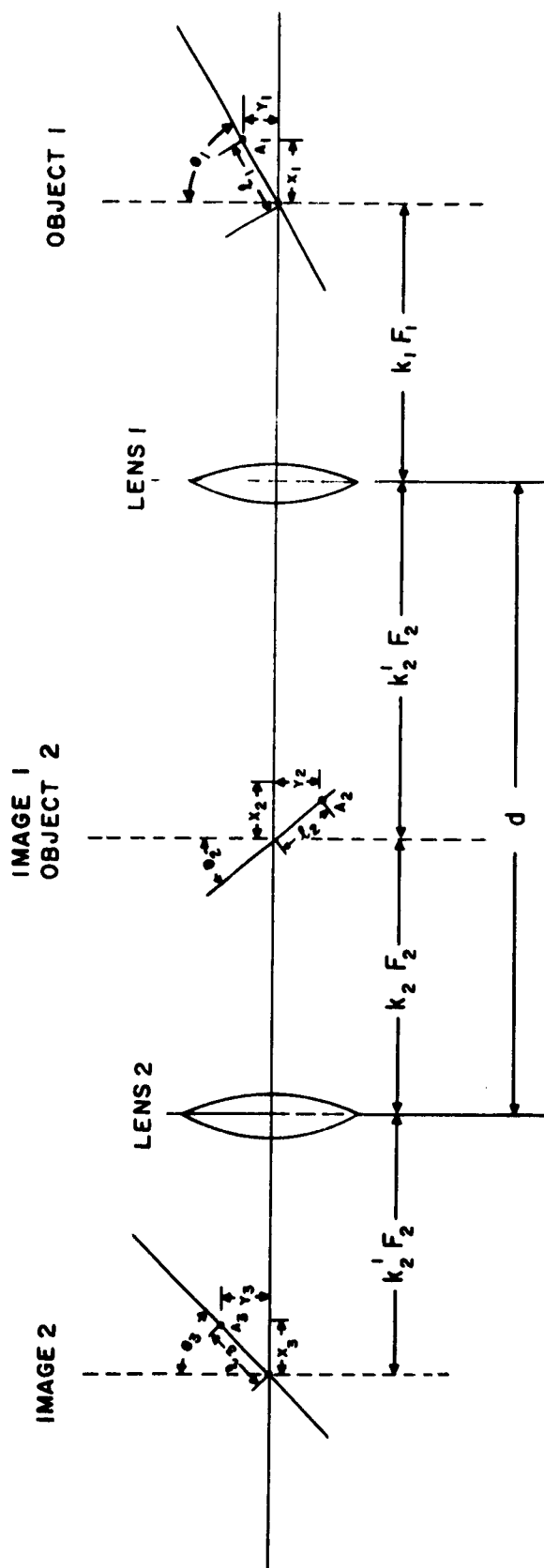


FIG. 4-3 TWO LENS ANALYSIS

$$k_1' = \frac{k_1}{k_1 - 1} \quad (\text{IV-18a})$$

$$k_2' = \frac{k_2}{k_2 - 1} \quad (\text{IV-18b})$$

$$k_2 F_2 + k_1' F_1 = d \quad (\text{IV-19})$$

$$\tan \theta_2 = \frac{\tan \theta_1}{k_1 - 1} \quad (\text{IV-20a})$$

$$\tan \theta_3 = \frac{\tan \theta_2}{k_2 - 1} \quad (\text{IV-20b})$$

$$z_2 = z_1 \frac{1}{(k_1 - 1) + \frac{l_1}{F_1} \sin \theta_1} \quad (\text{IV-21a})$$

$$z_3 = z_2 \frac{1}{(k_2 - 1) + \frac{l_2}{F_2} \sin \theta_2} \quad (\text{IV-21b})$$

$$l_2 = l_1 \frac{\cos \theta_1}{\cos \theta_2} \frac{1}{(k_1 - 1) + \frac{l_1}{F_1} \sin \theta_1} \quad (\text{IV-22a})$$

$$l_3 = l_2 \frac{\cos \theta_2}{\cos \theta_3} \frac{1}{(k_2 - 1) + \frac{l_2}{F_2} \sin \theta_2} \quad (\text{IV-22b})$$

where

F_1 = focal length of lens 1

F_2 = focal length of lens 2

$k_1 F_1$ = object distance on optic axis for lens 1

$k_2 F_2$ = object distance on optic axis for lens 2

$k_1' F_1$ = image distance on optic axis for lens 1

$k_2' F_2$ = image distance on optic axis for lens 2

d = distance between principal planes of lens 1 and lens 2

Solution of Eqs. (IV-18a), (IV-20b), and (IV-19) yields

$$k_2' = \frac{1 - (k_1 - 1) \left[D + \frac{F_2}{F_1} \right]}{1 - (k_1 - 1) D} \quad (\text{IV-23})$$

where

$$D = \frac{d - F_1 - F_2}{F_1} \quad (\text{IV-23a})$$

Solving for θ_3 we find that

$$\theta_3 = \tan^{-1} \frac{\frac{F_2}{F_1} \tan \theta_1}{(k_1 - 1) D - 1} \quad (\text{IV-24})$$

For z_3 and l_3 we find that

$$z_3 = \frac{\frac{F_2}{F_1} z_1}{D \left[k_1 - 1 + \frac{l_1}{F_1} \sin \theta_1 \right] - 1} \quad (\text{IV-25})$$

$$l_3 = \frac{\frac{F_2}{F_1} \frac{\cos \theta_1}{\cos \theta_3} l_1}{D \left[k_1 - 1 + \frac{l_1}{F_1} \sin \theta_1 \right] - 1} \quad (\text{IV-26})$$

As before, the area magnification can be defined as

$$M_{2A} = \frac{d\ell_3}{d\ell_1} \frac{dz_3}{dz_1} \quad (\text{IV-27})$$

Differentiating Eqs. (IV-25) and (IV-26) and substituting the results into Eq. (IV-27)

$$M_{2A} = \left(\frac{F_2}{F_1} \right)^2 \frac{\cos \theta_1}{\cos \theta_3} \frac{D(k_1 - 1) - 1}{[D(k_1 - 1 + \frac{\ell_1}{F_1} \sin \theta_1) - 1]^3} \quad (\text{IV-28})$$

For the more conventional case treated in ordinary optics texts, in which $\theta_1 = 0$, we see that the linear and area magnifications are uniform, being

$$\frac{z_3}{z_1} = \frac{\ell_3}{\ell_1} = \frac{F_2}{F_1} \left[\frac{1}{D(k_1 - 1) - 1} \right] \quad (\text{IV-29})$$

$$M_{2A} = \left(\frac{F_2}{F_1} \right)^2 \left[\frac{1}{D(k_1 - 1) - 1} \right]^2 \quad (\text{IV-30})$$

In the case of the tilted image, this is not true; as in the single lens case the ℓ -magnification differs from the z -magnification by the factor $\frac{\cos \theta_1}{\cos \theta_3}$, and the image is distorted because of the presence of the $\frac{\ell_1}{F_1} \sin \theta_1$ term. The distortion in this instance, however, can be reduced if the magnitude of D is kept small or can be made zero; hence, D is denoted as the distortion parameter.

For our purposes, the two-lens case is completely specified by Eqs. (IV-23), (IV-23a), (IV-24), and (IV-28). Of these, Eq. (IV-23) is

not too interesting, since it merely indicates the location of the image along the optic axis, and this can be found approximately by focusing on a ground glass plate or, more accurately, by taking a series of test photographs with the film at various positions along the optic axis. The other equations mentioned are far more interesting since they indicate the source of the focusing and distortion problems.

The area magnification, Eq. (IV-28), concerns us not only because it is the source of image distortion as shown in Fig. 4-2, but also because the image intensity (for a uniformly illuminated magnetically saturated specimen) is proportional to the inverse of this magnification. The initial reason for operating at a value of k_1 equal to unity was to avoid chromatic aberration; we find in actual operation that there is not very much choice in the matter. The image intensity varies as

$$\left[D(k_1 - 1 + \frac{\lambda_1}{F_1} \sin \theta_1) - 1 \right]^3$$

over the image surface. We see that the variation can be minimized by (1) minimizing the magnitude of D , (2) making F_1 as large as possible, or (3) making k_1 as large as possible.

If we examine Eq. (IV-23a), we see that D is zero when

$$d = F_1 + F_2 \tag{IV-31}$$

Because of the prisms and the electro-optical shutter which must be between the two lenses, the minimum value of d is about 425 mm. If, for the condition of Eq. (IV-31), $F_1 = F_2$, giving unity area magnification, then $F_1 = 212$ mm. If $F_1 = 2F_2$, giving an area magnification of about 0.167, then $F_1 = 284$ mm. An aperture study of both cases indicates that the stop aperture will be severely limited for the cross-sectional area of the prisms and shutter being used.

A study of the aperture of the system including the initial polarizer indicates that the best aperture is obtained when (see Section 4.5)

$$F_1 \approx 100 \text{ mm}$$

and

$$1.0 \leq k_1 \leq 1.4$$

This, combined with the minimization of chromatic aberration when $k_1 = 1$, leads to the choice of that value for k_1 .

Eq. (IV-29) is plotted in Fig. 4-4 for $k_1 = 1$ with D as a parameter. In this figure M_{2A} is normalized to its value at $l_1 = 0$. Note that the abscissa is the magnitude of $\frac{l_1}{F_1}$; curves in the upper half of the figure are for positive values of l_1 , while those in the lower half are for negative values of l_1 . For the values

$$d = 425 \text{ mm}$$

$$F_1 = 100 \text{ mm}$$

$$F_2 = 100 \text{ mm}$$

we find that

$$D = 2.25$$

$$M_{2A}(l_1 = 0) = 1$$

From Fig. 4-4, we find that for a specimen one centimeter in diameter the area magnification over the surface varies from 0.78 to 1.32. This amount of variation is more than we would desire but still tolerable. An earlier lens setup (the results of which led to the analysis of the area magnification) used focal lengths of 50 mm for supposed unity magnification. This resulted in a value of D of 6.5 and a variation of M_{2A} from approxi-

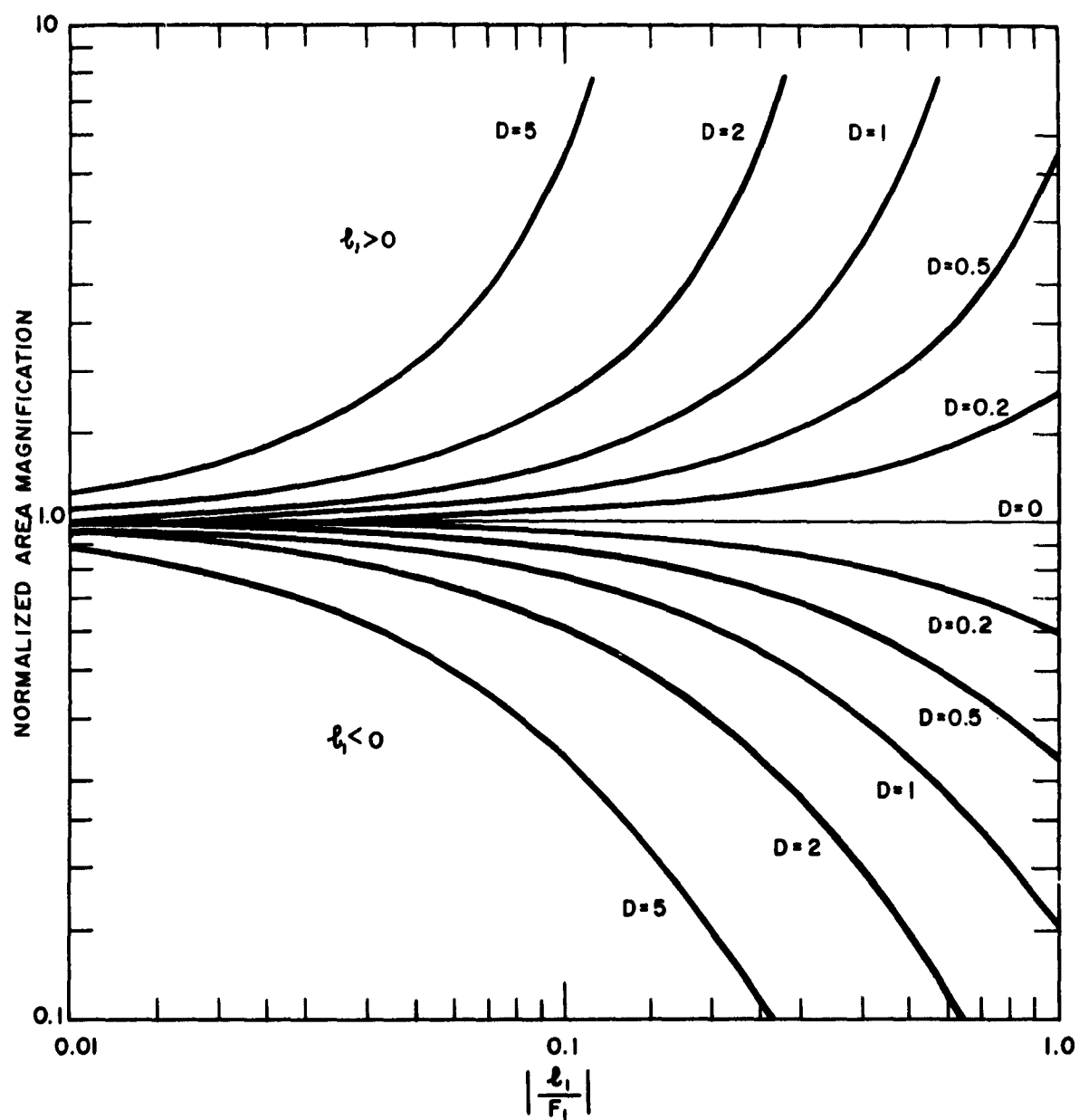


FIG. 4-4 VARIATION IN AREA MAGNIFICATION

mately 0.27 to 9.0 over a one centimeter specimen. Such a variation was immediately apparent in the photographic results, both as image distortion and as intensity variation. A photograph of a specimen of 0.5 cm diameter taken under these conditions is shown in Fig. 4-5.

When observed visually, the domains are approximately parallel.

Examination of Eq. (IV-29) indicates that the variation of θ_3 was the major cause of earlier focusing problems. There seems to be a tacit assumption in the literature that $\theta_3 = \theta_1$ (or that $\theta_2 = \theta_1$ in the single lens case), and the initial work was based on this assumption. That this is not true is apparent from Fig. 4-6. Here, θ_3 is plotted as a function of k_1 for four combinations of F_1 and F_2 and for $\theta_1 = 60^\circ$. We note that in the vicinity of $k_1 = 1$, the variation of θ_3 is close to its maximum, a fact which was not realized in the initial work. With the first two-lens system used, corresponding to curve II in Fig. 4-5, θ_3 is 60° when k_1 is unity. However, if k_1 is 1.1 (corresponding to an error of 5 mm), θ_3 is about 72° . With a wide aperture and little depth of field, it is impossible to obtain a well-focused photograph if the photographic film surface angle is in error by as much as 10° .

To verify this behavior, lenses of focal length $F_1 = 100$ mm and $F_2 = 50$ mm were installed in the apparatus. Beforehand, the principal planes of the 100 mm lens were accurately located so that k_1 could be set to unity. To allow variation of the angle of the photographic film, a modified Graflex Graphic II view camera was installed in the apparatus. These modifications were as follows:

1. The camera backing was modified to allow the photographic film film to be tilted by as much as 70° from its normal position.
2. A shorter bellows was made and installed because the original bellows was too bulky.
3. A large aperture shutter was installed.



**FIG. 4-5 SPECIMEN PHOTOGRAPH SHOWING AREA
DISTORTION AND INTENSITY VARIATION**

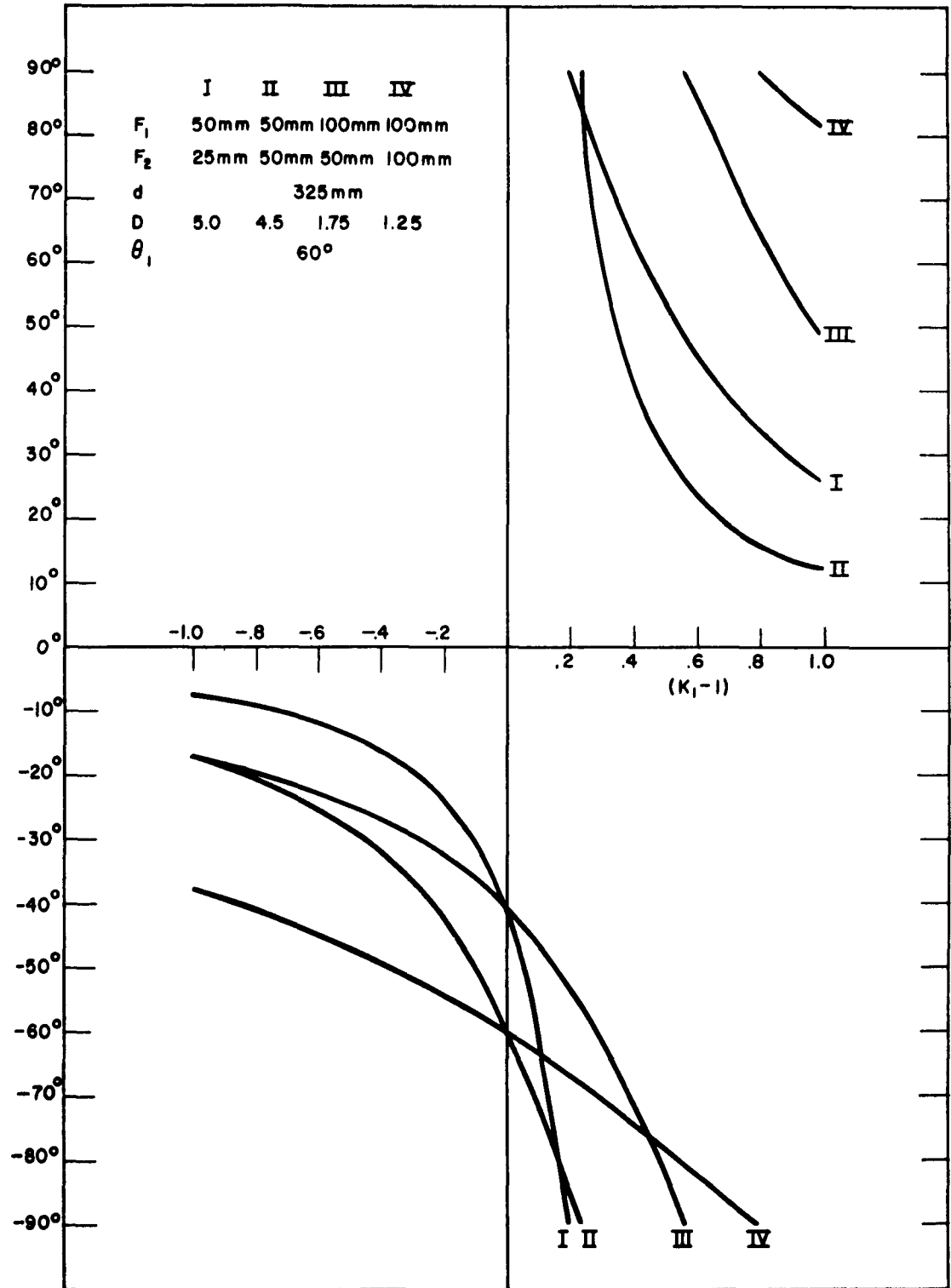


FIG. 4-6 VARIATION OF IMAGE ANGLE

4. Provision was made for mounting short focal length lenses inside the camera.
5. A dial indicator was mounted on the camera to accurately measure the position of the photographic film along the optic axis.

When the system was adjusted according to the equations which we have just discussed, the resulting photographs were reasonably well focused. Some focusing variation was still noticed and was traced to buckling of the film in the film holders. To remedy this, special film holders were made by cementing stainless steel strips onto glass plates. These plates were then used in ordinary photographic plate holders. A second technique was to modify a roll film holder so that the film surface in it could be held to close tolerance. Although this roll film holder was designed to accommodate size 120 roll film (the only roll film available with Royal-X Pan emulsion), it was easily adapted for the 35 mm Double-X Cine film by making special spools to hold 35 mm film.

4.5 Brightness

Consider two differential areas dA_1 and dA_2 separated by a distance r as shown in Fig. 4-7. The normals to these surfaces make angles θ_1 and θ_2 with the line connecting the areas. Then the total flux falling on dA_2 is

$$F_2 = \left[B_1 \cos \theta_1 dA_1 \right] \left[\frac{dA_2 \cos \theta_2}{r^2} \right] \quad (\text{IV-32})$$

where B_1 = surface brightness at dA_1 .

Remembering that we are defining brightness as the flux per unit projected area per unit solid angle, we can write the brightness of

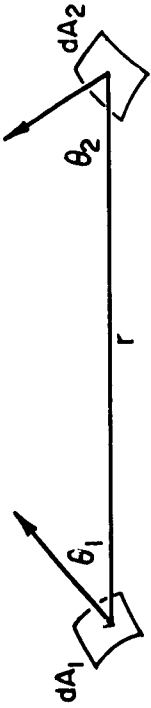


FIG. 4-7 BRIGHTNESS DERIVATION

dA_2 as

$$B_2 = \frac{F_2}{\left[dA_2 \cos \theta_2 \right] \left[\frac{dA_1 \cos \theta_1}{r^2} \right]} \quad (\text{IV-33})$$

Upon comparing Eqs. (IV-32) and (IV-33), it is immediately apparent that

$$B_1 = B_2 \quad (\text{IV-34})$$

If we have lossless lenses present, Eq. (IV-34) is still true. That this is so is apparent when we remember that the brightness of the image formed by a lens system is equal to the brightness of the object under consideration⁷. In any such lens system, the source for the light arriving at any given point in the system can be regarded as the image of the source seen from that given point. Hence we can make the statement that for a differential source of brightness B_1 , the brightness at every point in the system is B_1 . This statement holds for all points of the system, even those points where there is no light flux.

This may seem odd, that there can be brightness when there is no light flux, but in a formal sense it is quite true. Suppose we slowly pass a shutter in front of dA_1 in Fig. 4-7. Examining Eqs. (IV-32) and (IV-33), we see that the numerator and denominator of Eq. (IV-33) go to zero at the same rate, and hence B_2 remains constant, even when flux from dA_1 is completely blocked from dA_2 .

The differential illuminance on dA_2 is

$$\begin{aligned} dE_2 &= \frac{B_1 (dA_2 \cos \theta_2) (d\Omega_2)}{dA_2} \\ &= B_1 \cos \theta_2 d\Omega_2 \end{aligned} \quad (\text{IV-35})$$

where $d\Omega_2$ is the solid angle subtended by dA_1 .
 The illuminance at dA_2 is obtained by integrating over the solid angle subtended by A_1'

$$E_2 = \int B_1 \cos \theta_2 d\Omega_2 \quad (\text{IV-36})$$

where A_1' is the source image as seen from dA_2 .

One must remember, however, in dealing with A_1' that all aperture limitations must be observed. Figure 4-8 shows a source S focused by a lens F into an image S' . At first one might imagine that the image S' could be "seen" from point P , but this is not the case. To be able to see any point in an image of this sort, the line connecting the point P and the image point under consideration must not intersect any of the aperture stops between the image and the source. Note that Eq. (IV-36) is perfectly general, applying to a surface emitter of any size and shape, having uniform or non-uniform brightness. This equation is quite useful in practice, since it provides a relatively simple means for determining the illuminance at any point in a lossless lens system. For our purposes, we shall make two assumptions: first, that the brightness B_1 is constant over the source and second that θ_2 is approximately constant. This latter assumption automatically restricts Ω_2 to a relatively small solid angle. Equation (IV-36) can now be rewritten as

$$E_2 = B_1 \cos \theta_2 \Omega_2 \quad (\text{IV-37})$$

This equation is proof of the statement made in Chapter III: that, for a given source brightness, specifying the divergence angle of the light at a given point automatically specifies the illuminance.

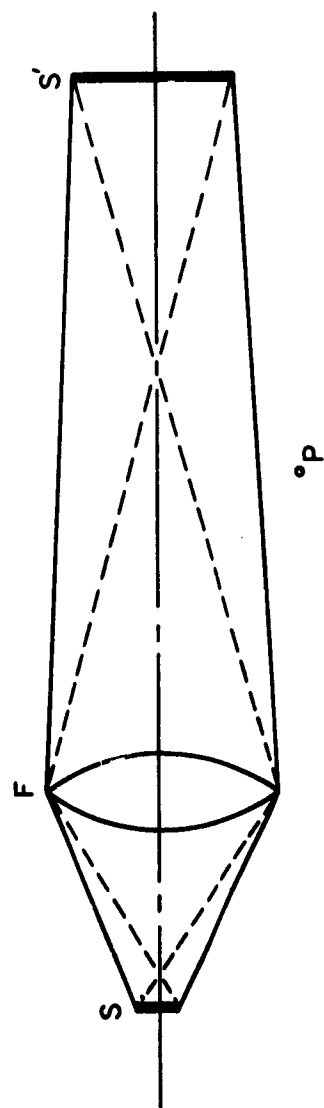


FIG. 4-8 APERTURE LIMITATION OF SOURCE IMAGE

4.6 Aperture and Field of View

It would be desirable to have an optical system in which the aperture and field of view were limited only by the source and specimen size. This is impossible because of the presence of the polarizers and Kerr cell and because there are limits on the aperture ratings of lenses. In the design computation for the lens requirements, impossible lens specifications arose time and again. For example, a lens with a rating of $f/0.065$ is a physical impossibility. The input aperture and field of view of the system shown in Fig. 4-9 were analyzed for a number of values of object lens focal length F_1 . For simplicity, the specimen was assumed to be perpendicular to the optic axis; this approximation has negligible effect on the analysis. Since the analysis was done graphically, the drawing was done as if light were passing through the specimen instead of being reflected from it.

Consider a point P on the specimen. If the light passing through this point has a small cone angle, we can consider its direction as that of the ray in the center of the cone, which we will call the principal ray. Now consider the circle in the specimen plane whose center is the optic axis O and which passes through P . Let the plane determined by OP and the principal ray be called the radial plane and that determined by the tangent to the circle at P and the principal ray be called the tangential plane. The angle of the cone of light in the radial plane is the radial angle ω_r , while that in the tangential plane is the tangential angle ω_t . As the distance OP is increased from zero, ω_r decreases much more rapidly than ω_t . Hence to a first approximation, we can consider that the cone angle of light passing through P varies as ω_r .

To analyze the system for a given value of F_1 , the image (as seen from the specimen) of all optical elements to the right of the object lens were constructed. The value of ω_r was then determined graphically for various locations of P . Although light rays from the source may

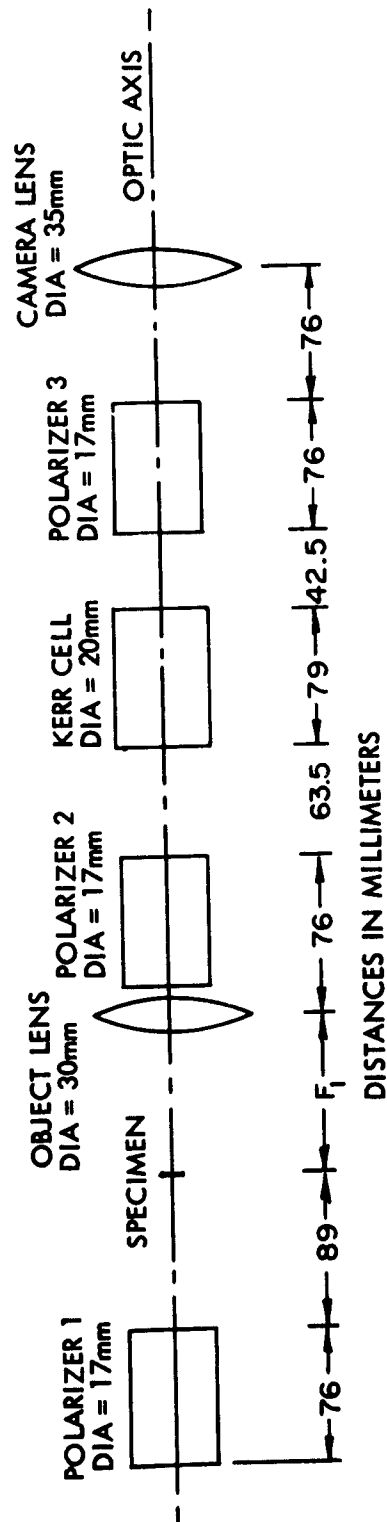


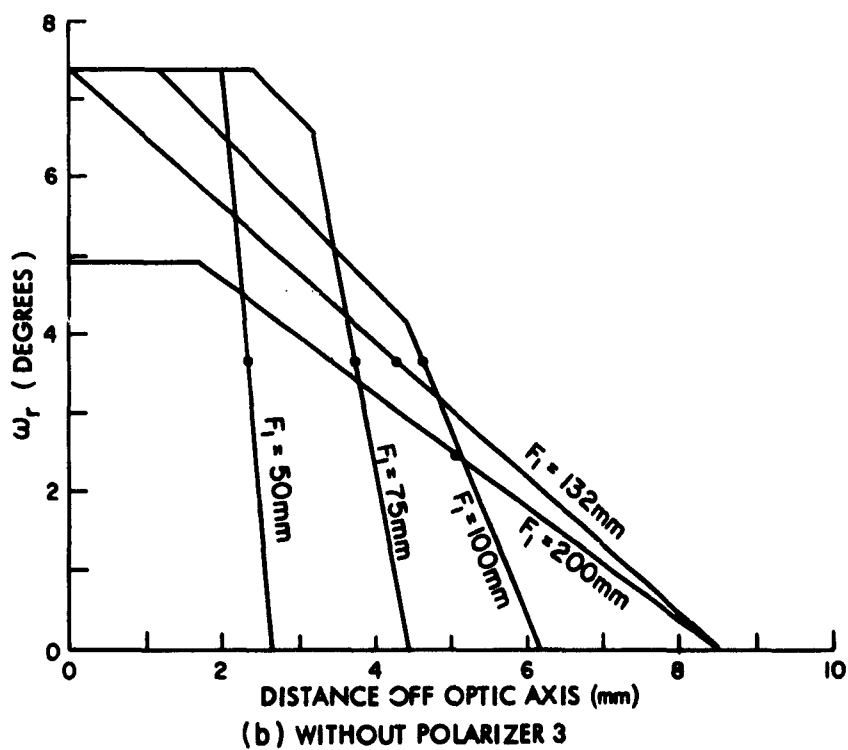
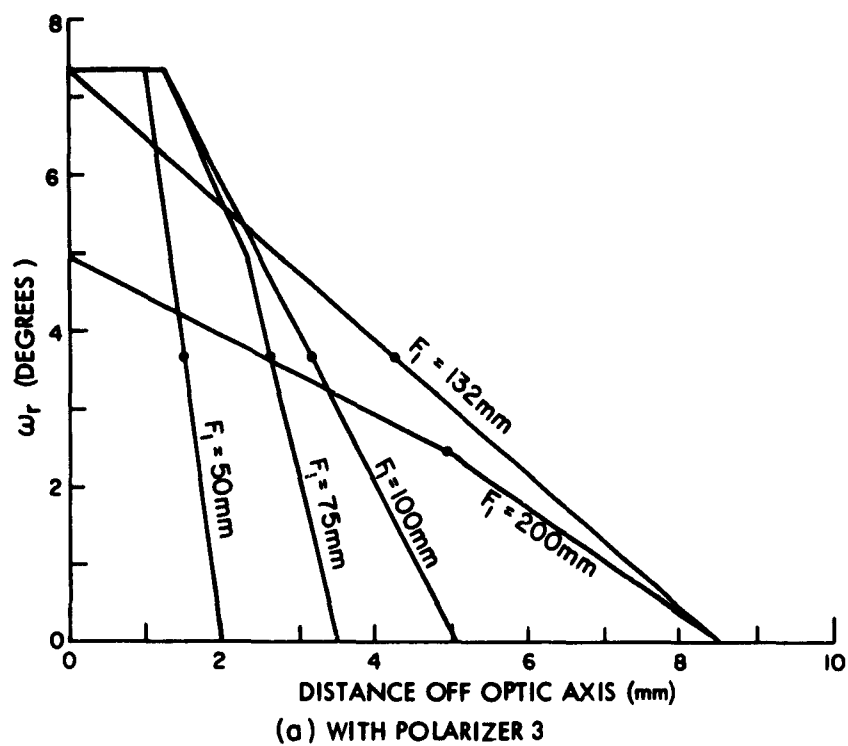
FIG. 4-9 APERTURE ANALYSIS

arrive at P over a wider angle than ω_r , only those lying within ω_r can reach the photographic film.

For $OP = 0$, the value of ω_r was 7.3° for focal lengths from 50 mm to 132 mm, decreasing at larger values of F_1 . This decrease was caused by aperture limitation from polarizer 3.

Curves of ω_r as a function of OP for various values of F_1 are shown in Fig. 4-10a. Note the breaks in the curves as the various apertures take effect. From Section 4.5, we remember that the illuminance is proportional to the cone angle Ω_c and hence in our present approximation to ω_r . If we denote the field of view as being limited by the halfvalue points of ω_r , we can immediately determine the field of view for the various focal lengths. The field of view limits are shown as circles on the curves of Fig. 4-10a. As we increase F_1 from 50 to 132 mm, the field of view increases. At $F_1 = 200$ mm, we have a still wider field of view, but the maximum value of ω_r has decreased. For the best photographic results we would like to have as large a field of view as possible and to have ω_r remain at its maximum for as large a value of OP as possible. These conditions are best met by the curve for $F_1 = 100$ mm, giving a field of view of about 6.5 mm.

The primary source of aperture and field of view limitation in all cases was polarizer 3. In Fig. 4-10b are plotted aperture curves in which this prism was disregarded in the analysis. It is immediately apparent that use of a larger prism would yield an improvement in the field of view. However, a prism of the required size (30 mm x 30 mm cross section) is quite expensive, and it was felt that such an expenditure was not warranted at the present stages of experimental work.

FIG. 4-10 VARIATION OF ω_r

CHAPTER V

THE ELECTRO-OPTICAL SHUTTER

The nitrobenzene electro-optical shutter, commonly known as a Kerr cell shutter, consists of a nitrobenzene cell positioned between two crossed polarizers. The nitrobenzene cell is simply a container for the nitrobenzene, with transparent faces to allow the passage of light through the cell and with electrodes immersed in the nitrobenzene so that an electric field can be applied at right angles to the optical path. Briefly, the cell operates as follows: when no field is applied the liquid is isotropic, and linearly polarized light from the input polarizer is blocked by the output polarizer. When an electric field is applied, the nitrobenzene becomes birefringent; the field is oriented at an angle of 45° to the linearly polarized light passing through the cell. The light can then be regarded as two vectors, one parallel to the field and the other perpendicular to the field, traveling at different velocities through the liquid. If the electric field is such, for a cell of given length, that the phase lag between the two vectors is 180° upon emerging from the cell, then the linearly polarized light resulting from the recombination of these vectors makes an angle of 90° with the original polarized light and hence passes through the second polarizer. (See Appendix B for a more detailed discussion.)

In order to design a Kerr cell shutter, we must know something of the characteristics of nitrobenzene. We will present a short summary of these characteristics followed by a discussion of the design of the nitrobenzene cell. Finally we will examine the design of the high voltage pulse generator which energizes the cell and consider some of the problems encountered in constructing the shutter unit.

5.1 Nitrobenzene Characteristics

Nitrobenzene is a pale, straw-colored organic liquid which has a pleasant odor but is quite toxic. Its electrical and optical characteristics are as follows:

Refractive index:	1.553
Transmission:	100 per cent from 8500 Å to 4600 Å 96 per cent at 4500 Å 2 per cent from 4200 Å to 2000 Å
Dielectric Constant:	36 from d.c. to 4 m.c. 27 at 6 m.c. 24 at 8 m.c. 22 from 10 to 15 m.c.
Resistivity, Commercial:	10^6 Ohm centimeters
Purified:	10^{20} Ohm centimeters
Dielectric Strength, Commercial:	4500 v/cm
Purified:	150,000 v/cm
Kerr Constant:	500×10^{-7} at 5000 Å 400×10^{-7} at 5800 Å 300×10^{-7} at 6500 Å

The Kerr constant is defined as

$$K = \frac{n_y - n_x}{\lambda} \quad (V-1)$$

where

n_x and n_y are refractive indices parallel and perpendicular to the applied field

E = applied fields (esu)

K = Kerr constant (electrostatic units)

λ = wave length of incident light in centimeters

The time phase angle between the slow and fast waves through the energized nitrobenzene is given by

$$\delta = 2\pi LKE^2 \quad (V-2)$$

where

δ = phase angle in radians

L = length of light path in centimeters

E = energizing electric field

The value of the Kerr constant is subject to some question. The literature indicates wide variation of this constant depending upon the purity of the nitrobenzene. Zarum, et al.² report that for short pulse operation the impurities do not seem to affect the Kerr characteristics, although the extent of these impurities is not mentioned. The impurities are apparently ionic in nature; in dc operation they collect at the electrodes and thereby reduce the electric field throughout the rest of the liquid. No data seems to be available on the migration time of these impurities, although Zarum estimates times of about one msec. It was felt that as pure a grade of nitrobenzene as possible should be used, and considerable effort was put forth in an attempt to obtain fairly high-purity nitrobenzene according to a procedure given by Whyte³, who reported purities on the order of 10^{12} ohm-centimeters. (No data has been found indicating how to attain purities of 10^{20} ohm-centimeters.) The purification procedure yielded nitrobenzene whose resistivity was measured to be between 10^8 and 10^9 ohm-centimeters; Whyte's value of 10^{12} could not be reached. In practice, the nitrobenzene purified by the writer gave quite satisfactory results.

5.2 Kerr Cell Design

For the nitrobenzene cell to give optimal behavior when energized, δ must equal π ; hence, from Eq. (V-2) we can derive (though we have

made some changes in units)

$$V = \frac{.212 d}{\sqrt{KL}} \quad (V-3)$$

where

V = cell voltage in KV

d is the electrode separation in centimeters

K is the Kerr constant in ESU

L is the effective optical path through the energized nitrobenzene

Computations to determine the Kerr constant of nitrobenzene using the dimensions and operating voltage of two commercial cells^{4, 5} indicate that the value is on the order of 500×10^{-7} (ESU). Using this value in Eq. (V-3), we have the following simple cell design equation

$$V = \frac{30d}{\sqrt{L}} \quad (V-4)$$

As was mentioned in Chapter II, the shutter was designed in a similar manner to that of a commercial unit⁵. The pulser for this commercial unit will operate in the range of 30 to 40 Kv. A plate separation, d, of 2 cm was used so as not to obstruct any light from the input polarizer (which is also the analyzer for the magneto-optic effect observations). Using electrodes 3 cm long, resulting in an effective L of about 3.4 cm, we find from Eq. (V-4) that the required operating voltage to open the shutter is 32.5 Kv.

A sketch of the nitrobenzene cell is shown in Figure 5-1. The ends of the cylinder in which the electrodes are mounted are ground flat and parallel within .001 inch, and optical flats (coated to minimize reflection losses) are cemented to the ends of the cylinder. A number of cements which would

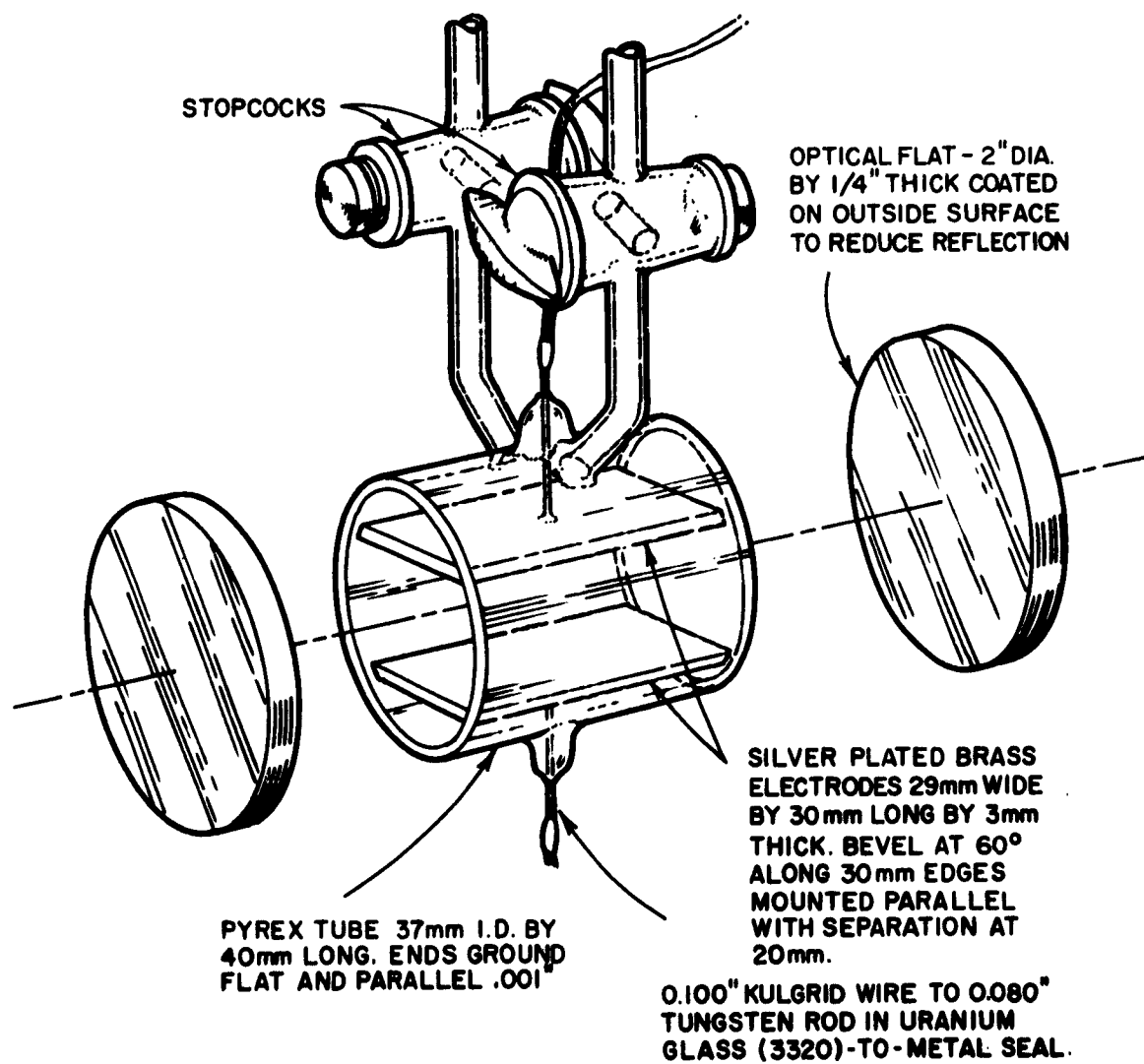


FIG. 5-1 NITROBENZENE CELL DESIGN

adhere to glass were tested for their resistance to nitrobenzene; the only one which proved successful was a commercial epoxy resin (trade name, Epoxypatch). The cell is filled to the level of the stopcocks with nitrobenzene; one of the stopcocks is left open to avoid any problems which might be encountered from thermal expansion of the nitrobenzene.

5.3 High Voltage Pulse Generator

A simplified schematic of the pulse generator used to operate the Kerr cell is shown in Figure 5-2; this design, although not original with the writer, is rather unique in its operation.

In the initial steady state, the center conductor of the coaxial delay line is maintained at ground potential by the terminating resistor R_0 . The outer conductor is charged to V through the charging resistor. The delay line in the unit is wound in a tight coil so that when the switch, S_1 , is closed, all points of the outside conductor are grounded simultaneously. Since no current can flow at the Kerr cell end of the line, except for a small momentary charging current to the Kerr cell capacity, the potential across the delay line remains unchanged at that point, and a voltage V is applied to the Kerr cell. At the terminated end of the line we have the conventional behavior of a delay line pulse generator; a voltage $\frac{V}{2}$ appears across the terminating resistance, and a wave front of magnitude $\frac{V}{2}$ begins to travel down the delay line. At time T , the instant at which this wave front (assuming it to be an ideal step function) arrives at the Kerr cell end of the line, it is reflected with a reflection coefficient of +1, and the voltage across the Kerr cell drops to zero, since the line at that point is now discharged. The wave then travels back down the line and is absorbed in the terminating resistor. The switch, S_1 , opens, and the line recharges to its initial state through the charging resistor.

For this application, this pulse generator has the advantage that it supplies an output pulse equal to the potential to which the line has been

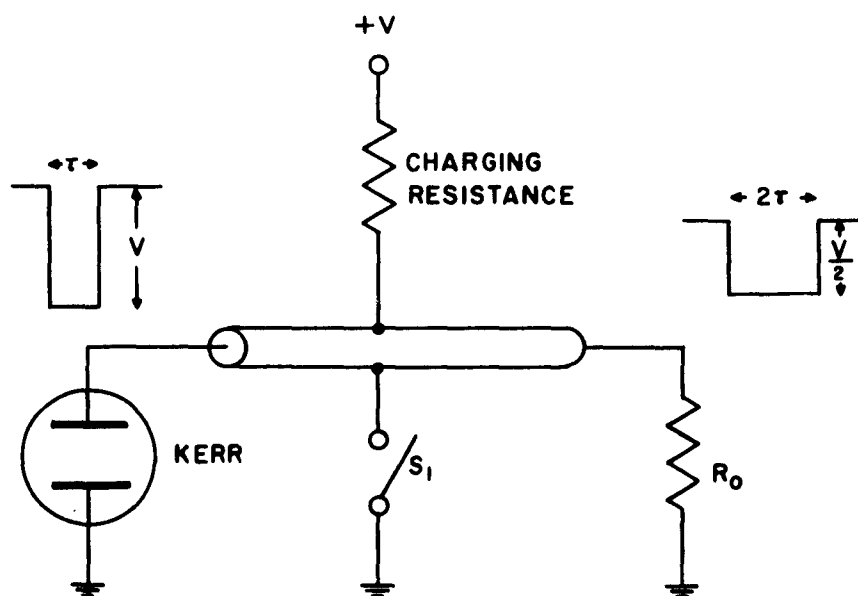


FIG. 5-2 SIMPLIFIED PULSE GENERATOR

charged, whereas most other delay line pulse generators have a pulse amplitude of only half the line voltage; this is extremely desirable when trying to generate pulses of several kilovolts in amplitude. True, such a pulse source cannot be loaded to any extent; however, as long as the time constant determined by the capacity of the Kerr cell and the characteristic impedance of the line is small compared to the risetime of the switching device used, no ill effects will be observed. In this particular case the cell capacity is about $20 \mu\mu f$ and the line impedance is 50 ohms, resulting in a time constant of about one millimicrosecond, which is much less than the rise time of the switch.

In actual practice the rise time of the switch is not instantaneous but is some value t_r and must be taken into account when computing the required transmission line length. Assume that the rise time of the switch is linear and let the switch be triggered at time t_0 . At time t_r , the potential across the Kerr cell has changed by V while that at the termination resistor has changed by $\frac{V}{2}$. The potential distribution along the line is that shown at $t = t_r$ in Figure 5-3. Note that a ramp of magnitude $\frac{V}{2}$ is propagating along the transmission line. This ramp causes the line potential at the Kerr cell to begin decreasing at $t = \tau$. The resulting pulse applied to the Kerr cell has a rise and fall time of t_r and a flat top of length $\tau - t_r$. Referring to the cell transmission characteristic in Appendix B, we see that if we consider the exposure duration of the shutter to be measured between the half amplitude values of light transmission the effective exposure duration is

$$\begin{aligned} t_e &= \tau - t_r + 2(.293 t_r) \\ &= \tau - .414 t_r \end{aligned} \tag{V-5}$$

This must be taken into account for accurate computation of transmission line length when τ is comparable in magnitude to t_r .

The switch for the pulse generator is a modified 6587 hydrogen thyatron. This tube is manufactured with a four-pin base; the hydrogen

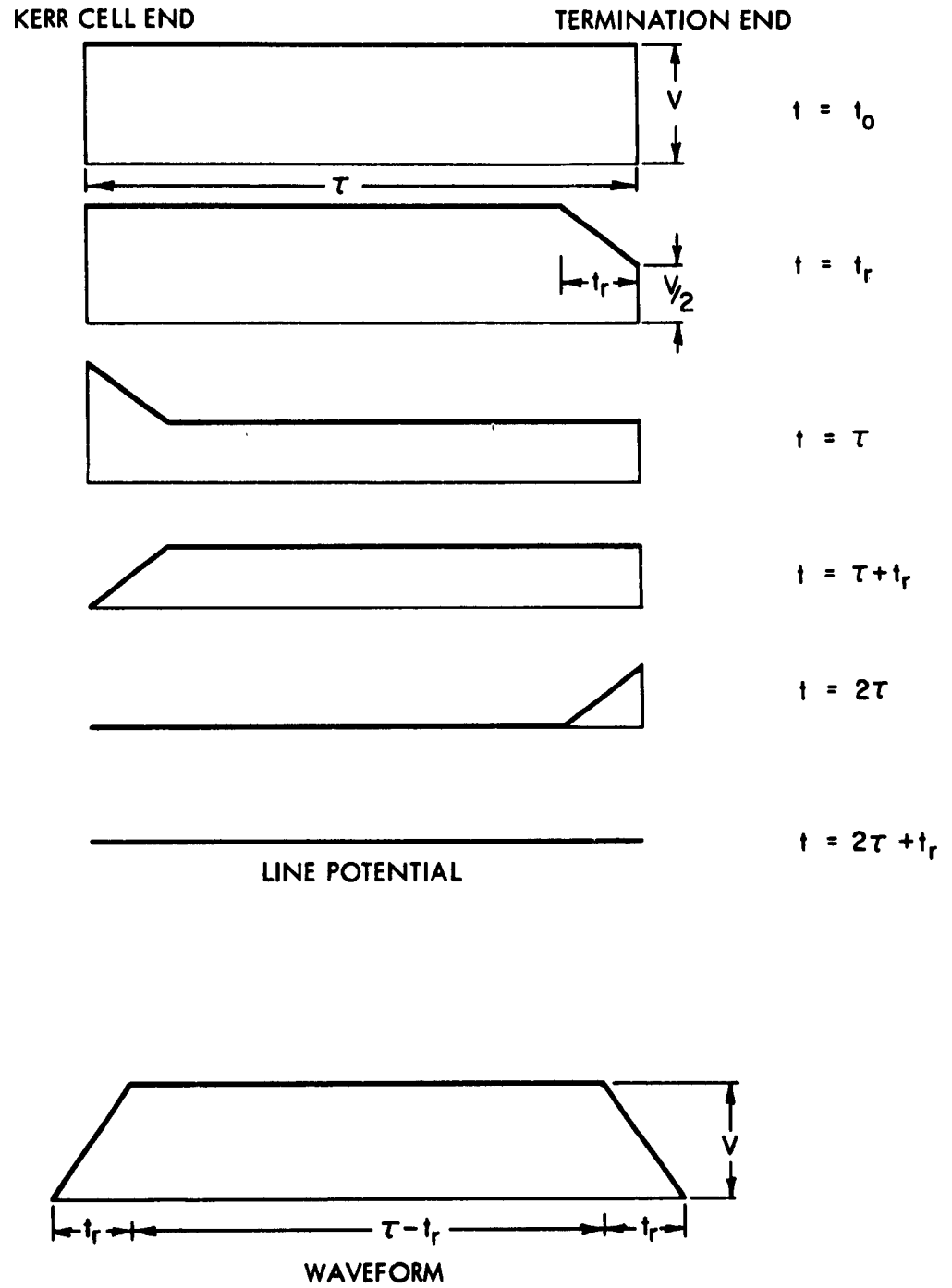


FIG. 5-3 LINE POTENTIAL DISTRIBUTIONS AND PULSE WAVEFORM

reservoir is connected inside the tube base in parallel with the filament leads. The base of the tube was removed and a seven-pin base substituted. The cathode leads were connected to four of these pins to minimize inductance effects. The hydrogen reservoir was brought out on a separate lead so that it could be varied during operation, since rise time and holdoff voltage both change as the hydrogen pressure is varied. (See Appendix C) The 6587 is normally rated at an anode voltage of about 20 Kv, but Zarum reports operation as high as 40 Kv⁵, and the writer's experience bears this out.

Because of the rapid rise times and short pulse durations involved, the entire shutter unit was designed to be as compact as possible; a photograph of the unit is shown in Figure 5-4 and a close-up of the Kerr cell module with the terminating resistors in Figure 5-5. As is apparent from the photographs, the design of the unit was such as to minimize inductance effects in the circuit.

The delay line is a length of RG-58/u coaxial cable with the outside vinyl jacket removed. The line is wound in a tight spiral on a metal post which is mounted on the anode of the thyatron. The ends of the inner conductor are attached to contacts mounted in a polystyrene bracket which mate with two contacts in the Kerr cell module. Although normally rated at 1200 volts rms, the sections of cable used were tested to 40 Kv and showed no signs of breakdown; Zarum reports that selected sections of this cable can withstand 50 Kv.

Three delay lines were constructed, giving pulse lengths of 10 μ sec, 35 μ sec, and 85 μ sec. The longer lines, having a larger diameter when wound in a coil, introduced arc-over problems between the lines and the frame of the shutter assembly; to prevent this, lucite shields were placed between the delay line and the frame, and the delay lines were encased in a lucite shell which was then filled with a high-voltage transformer oil. A photograph of the 10 μ sec delay line assembly is shown in Figure 5-6.

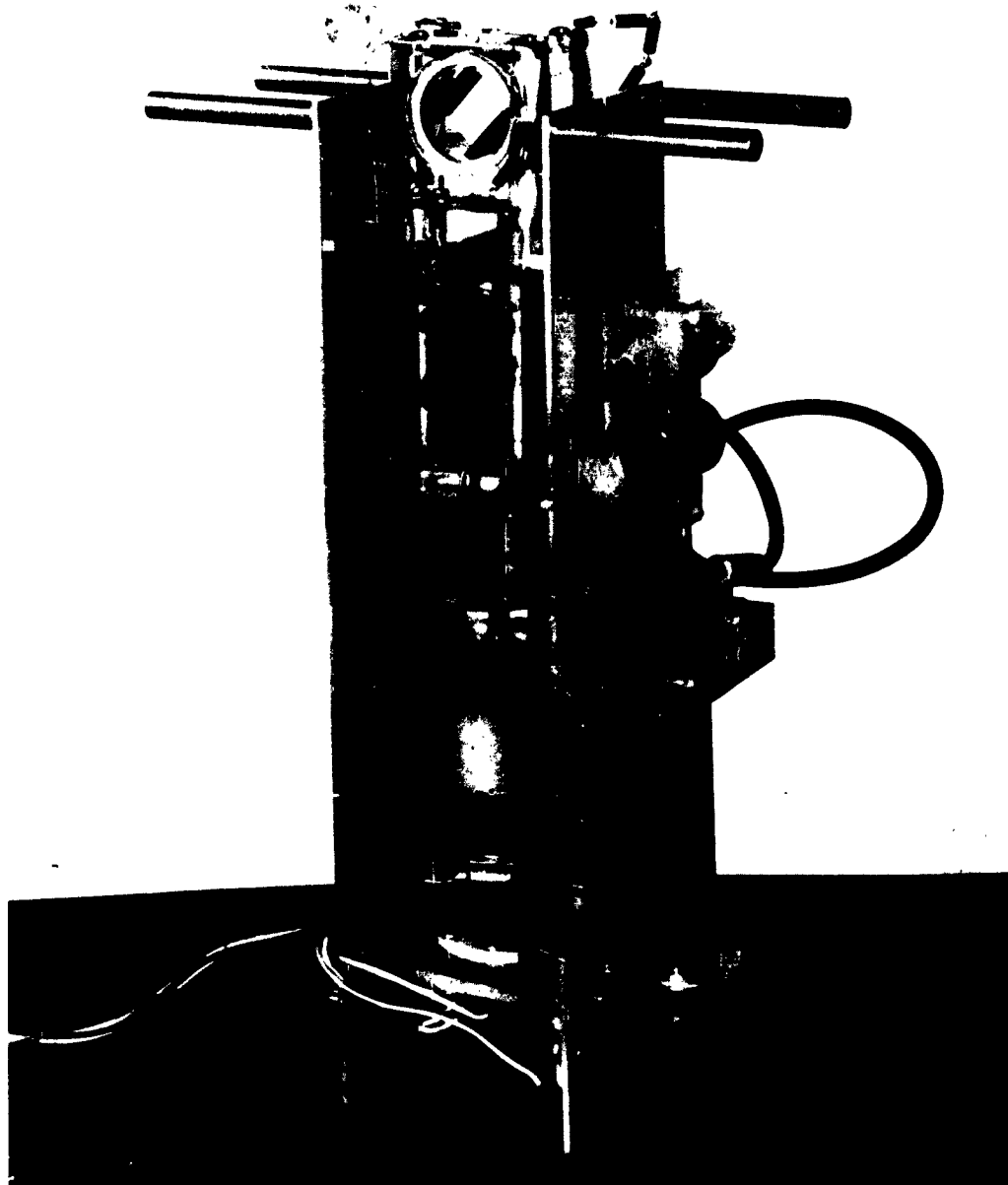


FIG. 5-4 ELECTRO-OPTICAL SHUTTER UNIT

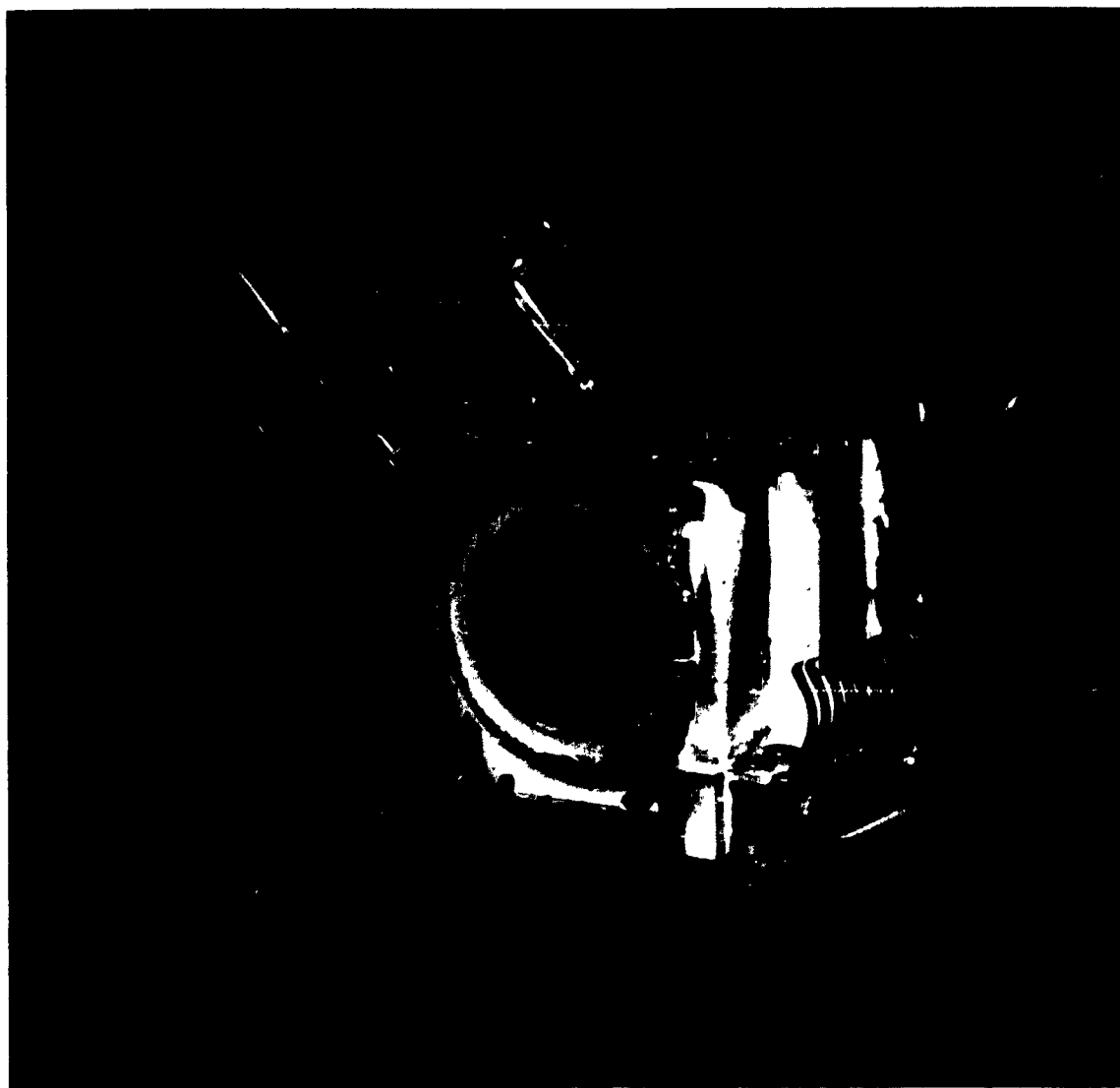


FIG. 5-5 KERR CELL MODULE

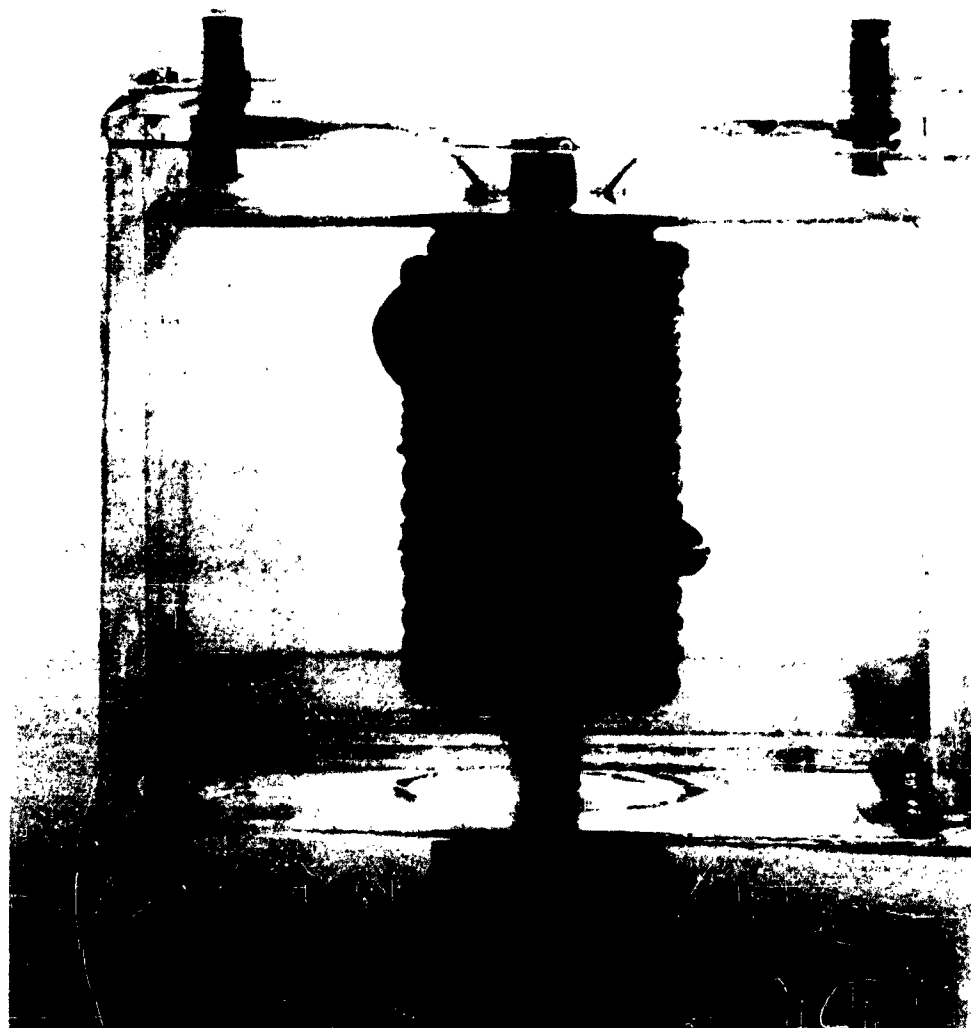


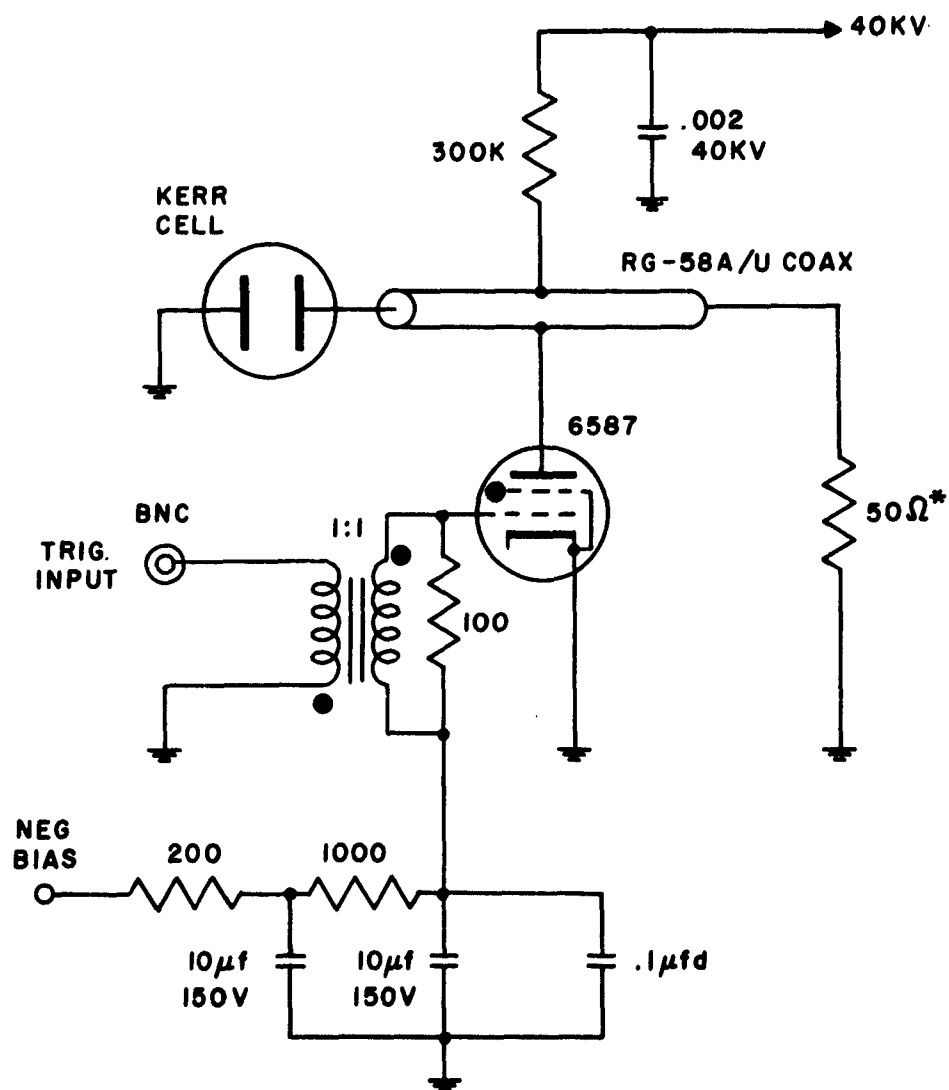
FIG. 5-6 10 μ SEC DELAY LINE ASSEMBLY

Initial attempts to view the wave form of the voltage pulse were unsuccessful because high fields generated when the thyatron was triggered blanked out the oscilloscope. After several attempts to trace this difficulty (including putting the entire shutter assembly inside a copper box), the fields were found to be generated by a 5-foot length of cable connecting the thyatron anode to the high voltage supply. A 40 Kv RC decoupling network was installed to remedy this problem. A second difficulty was suppression of corona and arcing from the anode cap. Several anode connectors of various geometries were made to try to lower the electric field at the anode cap below the corona point. The final solution was to encapsulate the entire lower portion of the cap in General Electric RTV-60 silicone rubber compound. Another compound, RTV-11 compound, was used at one place in the Kerr cell module to suppress arcing (see Fig. 5-5).

The complete circuit of the pulse generator is shown in Figure 5-7. A negative grid-biasing network was included to aid in attaining the 35-Kv thyatron holdoff voltage.

The voltage wave forms supplied to the Kerr cell are shown in Figure 5-8, along with the resulting light transmission wave forms. Light transmission for the 10 μ sec line could not be observed because of the risetime limitations of the measuring apparatus. The voltage wave forms were viewed directly on plates of a Tektronix 545 oscilloscope. The average pulse jitter seemed to be about 4 μ sec, the extreme being about 8 μ sec; triggering jitter contributed about 2 μ sec to this. The light transmission wave forms were viewed with a 929 phototube operated at 500 volts into a 90 ohm load, and observed on a Tektronix 545 Oscilloscope with a type 54K preamplifier; the oscilloscope with this preamplifier has a vertical risetime of 12 μ sec.

The light transmission maximized for a shuttering supply of 42 Kv. This is higher than the design figure; the writer believes that the values



* NOTE: SERIES - PARALLEL COMBINATION OF EIGHTEEN 100 OHM $\frac{1}{2}$ WATT RESISTORS, SIX PARALLEL UNITS OF THREE SERIES CONNECTED RESISTORS

FIG. 5-7 HIGH VOLTAGE PULSE GENERATOR CIRCUIT

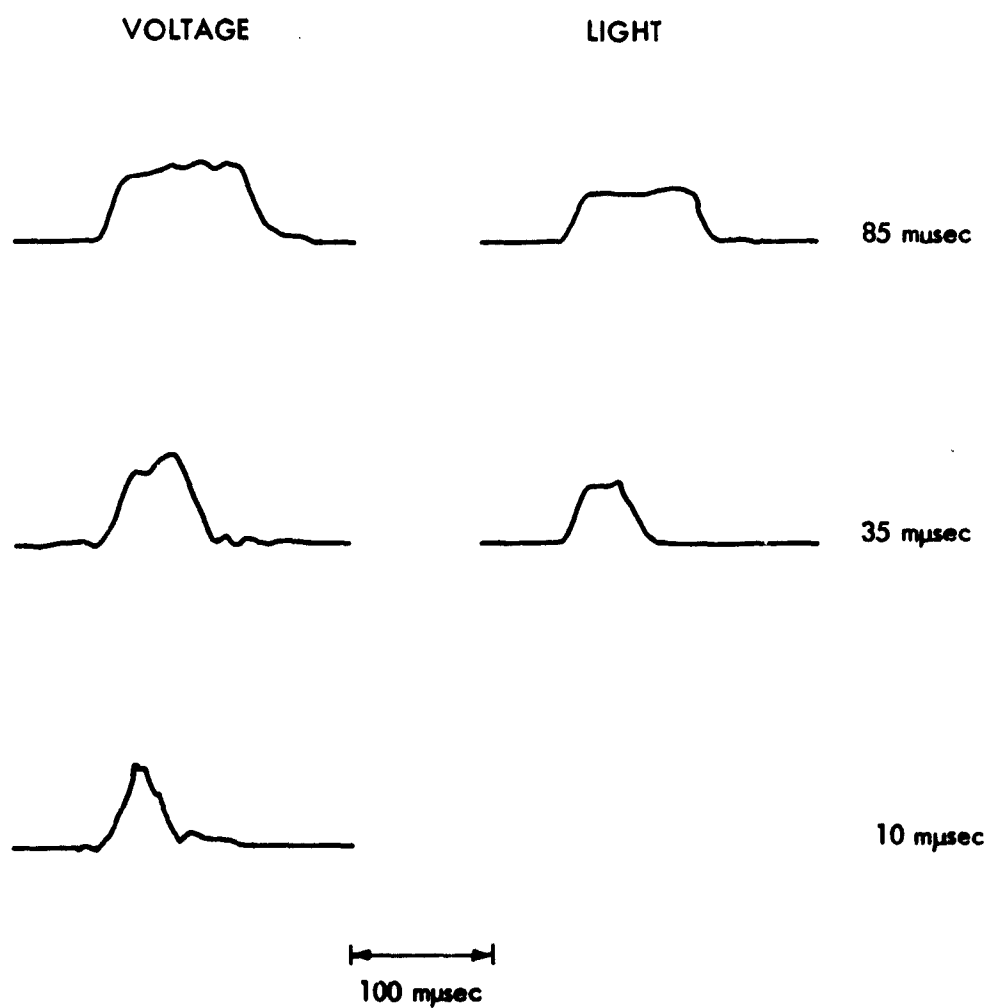


FIG. 5-8 VOLTAGE PULSE AND LIGHT TRANSMISSION WAVEFORMS

of Kerr constant given in Section 5.1 are low frequency values and that the Kerr constant at the high frequencies being used is in the vicinity of 300×10^{-7} . No data seems to be available in the literature concerning the high frequency behavior of this constant.

CHAPTER VI

ELECTRONIC INSTRUMENTATION

The instrumentation for this project, aside from the shutter discussed in the previous chapter, consists of the following items:

1. A delay line pulse generator driving one of two single-turn Helmholtz coils to provide the pulsed magnetic field.
2. A flash tube with a hydrogen thyratron triggering circuit.
3. A synchronizing panel to generate the proper triggers for the shutter, the flash tube, and the field pulse generator.
4. A static field generator to allow static observations of specimens and biasing during pulsed studies.
5. Miscellaneous items, e.g., power supplies, et cetera.

6.1 Pulsed Magnetic Field Apparatus

To apply a pulsed magnetic field to the specimen, two sets of single-turn Helmholtz coils are used. To avoid confusion between these, the coils generating an H field perpendicular to the plane of incidence will be denoted as the transverse coils, while the coils generating a field parallel to the plane of incidence will be denoted as the longitudinal coils. In view of the data of Olson and Pohm, it was felt that a maximum pulsed field of about 10 oerstads would be adequate for the studies being considered. As was mentioned in Chapter II, Helmholtz pairs of about 2 inches in diameter will have a sufficiently uniform field, inductance of about 2 microhenries, and a field generating capability of about .33 oerstads/amp. Therefore, a pulse generator capable of supplying a maximum of about 30 amperes will meet these requirements. The source impedance of such a pulse generator should be greater than 40 ohms so that the L/R time constant will be less than the rise time of the switch, in this case the hydrogen thyratron.

For the Helmholtz coils to see a source impedance of 40 ohms would mean a delay line impedance of 20 ohms; the line charging voltage for the numbers mentioned would have to be 1200 volts. It is impractical to use coaxial delay lines in a case such as this since the pulses being considered may be as long as 10 microseconds, which would require several hundred feet of coaxial cable. A 3C45 hydrogen thyratron was chosen for the switch; this thyratron has a peak current capability of 40 amperes and is rated at 3000 volts. Because of this voltage rating, the line impedance was chosen to be 50 ohms, which for proper termination would then result in a maximum current of 30 amperes.

The pulse field Helmholtz coils were constructed from brass rings having a 1/8" square cross section. Since one Helmholtz pair had to fit inside the other, with their axes at right angles, the diameters were slightly different. The specific characteristics of the coils used are as follows:

Longitudinal coils	2.14" mean diameter	0.21 μ hy	0.325 oer/amp
Transverse coils	2.375 mean diameter	0.22 μ hy	0.28 oer/amp

The artificial delay lines used for pulse forming were Guillemin "Type E" networks¹. This line is most easily described as a long solenoid of diameter d with taps at distances $4/3 d$ along the entire solenoid. Lumped capacities are connected from these taps to a ground bus parallel to the solenoid. If the total inductance is L_0 and the total capacity is C_0 , then the characteristic impedance of the line is $\sqrt{L_0/C_0}$ and the time length of the pulse is $2\sqrt{L_0/C_0}$.

Four lines were constructed so as to generate pulses of 0.3 microseconds, 1 microsecond, 3 microseconds, and 10 microseconds. Each line had about 20 sections, so that the ripple frequency from the top of the pulse would be high with respect to the specimen switching time. The lines were encased in lucite tubes to afford high voltage protection; two of these lines, with their protecting tubes removed, are shown in Fig. 6-1.



FIG. 6-1 ARTIFICIAL DELAY LINES

The capacity at the input section of each line was adjusted to obtain the best compromise between pulse risetime and pulse overshoot. Two additional delay lines were made from RG-8/u coaxial cable to provide pulses of 75 μsec and 150 μsec duration. Although these pulse lengths are too short for the photographic studies for which the apparatus has been designed, they are still useful for studying domain propagation and rotational thresholds. This will be discussed more fully in Chapter VII.

Since the use of a hydrogen thyatron permits only one polarity pulse in the field coil, a second pulse generator using a mercury-wetted contact relay as a switch was built to provide the pulses to the specimen between pulses from the hydrogen thyatron generator. A schematic of both pulse generators is shown in Fig. 6-2. The hydrogen thyatron will operate from 300 volts minimum to 3000 volts maximum; this means that for a given terminating resistor the current amplitude has a 10 to 1 range as the supply voltage is varied. In order to obtain lower currents a shunting resistor can be inserted in the circuit and the values of R_{T1} and R_{T1}' are so adjusted as to properly terminate the line.

Photographs of the current wave forms from the various lines are shown in Fig. 6-3. The risetime in all these pulses is about 25 μsec . The fall time is much slower, but is of no importance since we assume that the film will switch completely during the pulse. The peak-to-peak ripple amplitude is approximately 4 per cent of the current amplitude. We note that the risetime at higher current amplitudes is somewhat faster than that at lower amplitudes, thus bearing out the comments on this in Appendix C.

6.2 Flash Lamp Circuitry

The FX-12 flash tube is designed to provide a high peak light output from a small area (1.2 mm x 6 mm) with a duration of 1 to 2 microseconds. The tube normally operates from the discharge of a capacitor charged

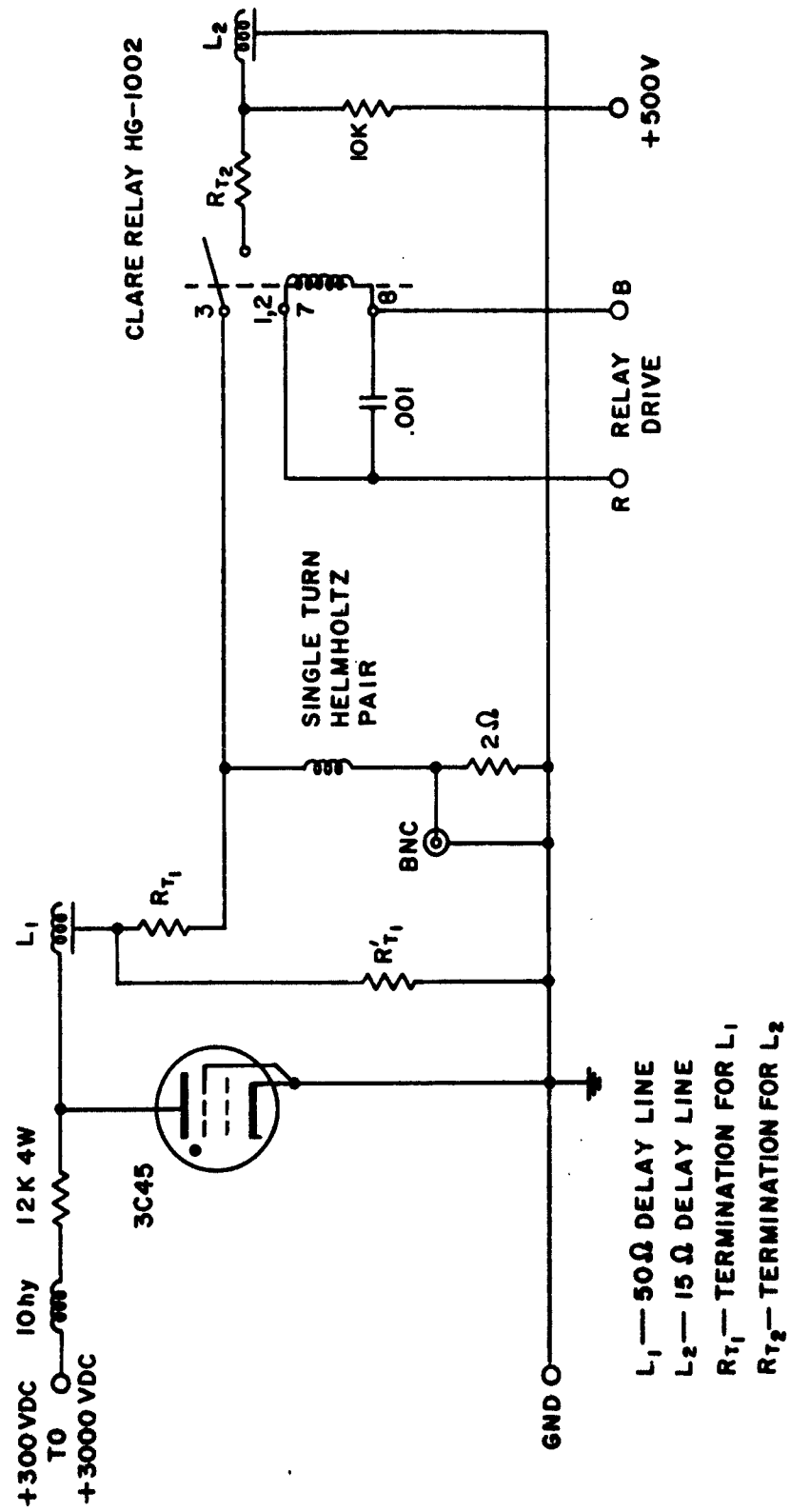


FIG. 6-2 FIELD PULSE GENERATOR CIRCUIT

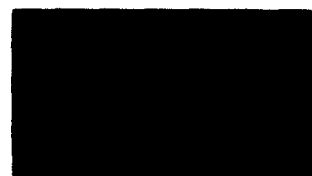
150 m μ SEC PULSE300 m μ SEC PULSE1 μ SEC PULSE3 μ SEC PULSE10 μ SEC PULSE

FIG. 6-3 PULSE GENERATOR CURRENT WAVEFORMS

initially anywhere from 400 volts, the minimum starting voltage for the lamp in trigger operations, to 4000 volts, the self-flash voltage of the lamp. The recommended energy input to the lamp is one joule, resulting in a peak output of 2,000,000 horizontal candle-power. The lamp can be operated with an energy input as high as 10 joules, although this results in a shorter operating lifetime. The manufacturer states that "the spectral output of this lamp shows a continuous spread of energy over the entire visual region with broad superimposed lines of xenon." When this lamp is flashed, the light appears to be bluish-white, indicating that some of the stronger xenon lines are probably in the wave length region less than 4300 \AA and therefore will not be transmitted by our system because of the nitrobenzene spectral cutoff.

An initial experiment was conducted to see if the peak output of this flash lamp could be increased by operating it at excessive voltages in series with a 5C22 hydrogen thyratron for a switch. The capacitor used was rated at 0.03 ufd at 10,000 volts. With an operating voltage of 10,000 volts, the peak output was measured in the following manner. The flash lamp was placed beside a General Radio Type 1532-B Strobolume and a 929 phototube was placed 10 feet away from both units. The 929 phototube was operated at 500 volts into a 90-ohm load; the wave form was observed on a Tektronix 545 oscilloscope. The Strobolume, whose peak output is 10 megacandle-power, was used as a standard against which to measure the output of the FX-12 unit.

The peak output of the FX-12 unit, for 10,000 volt operation, was one megacandle-power with a duration of one microsecond as measured at the $1/3$ intensity points (the standard reference for measuring flash duration). The unit was unreliable in its triggering, showing jitter of several microseconds, and occasionally refusing to flash at all. The efficiency of the circuit was also quite low because of the high impedance of the 5C22 relative to the FX-12 impedance. Therefore, the circuitry was changed to a more conventional type of trigger operation.

The initial flash lamp circuitry discharged a one microfarad capacitor into the lamp. The flash lamp was mounted in open fuse clips; the trigger electrode consisted of one and one-half turns of fine wire wrapped around the discharge area of the lamp. This arrangement presented two problems. The high energy of the discharge often caused the lamp to explode. Also the peak discharge current was sufficiently high (estimated somewhere between 1000 and 8000 amperes) so as to generate an appreciable magnetic field in the vicinity of the specimen, which was about 12 inches from the lamp.

The explosion problem was eliminated by decreasing the discharge capacitance to 0.5 microfarad. To reduce the magnetic field, the lamp was completely enclosed (with the exception of a hole to allow emission of light) in a cylindrical brass housing with walls 0.125" thick.

At this point a new problem arose. Although the FX-12 flash lamp is rated at a holdoff voltage of 4000 volts it seemed impossible to attain this operation, as the lamp tended to self-fire in the vicinity of 2200 volts. Tests by the manufacturer indicated that the lamps themselves were not at fault. Some experimental investigation revealed that the trigger electrode was the source of difficulty. In the brass housing, the trigger electrode is half of a brass ring mounted at the midpoint of the lamp. This electrode was connected through a 680 Ω resistor to ground. In operation one electrode of the flash lamp is connected to ground while the other is connected through a charging network to the supply voltage (see Fig. 6-4). If the trigger electrode is not present, the quiescent electric field in the tube is approximately V/d , where V is the voltage across the flash lamp and d is the separation of the flash lamp electrodes. The trigger electrode in the configuration mentioned above introduced a ground potential near the midpoint of the lamp. This effectively doubled the quiescent electric field, thereby halving the holdoff voltage.

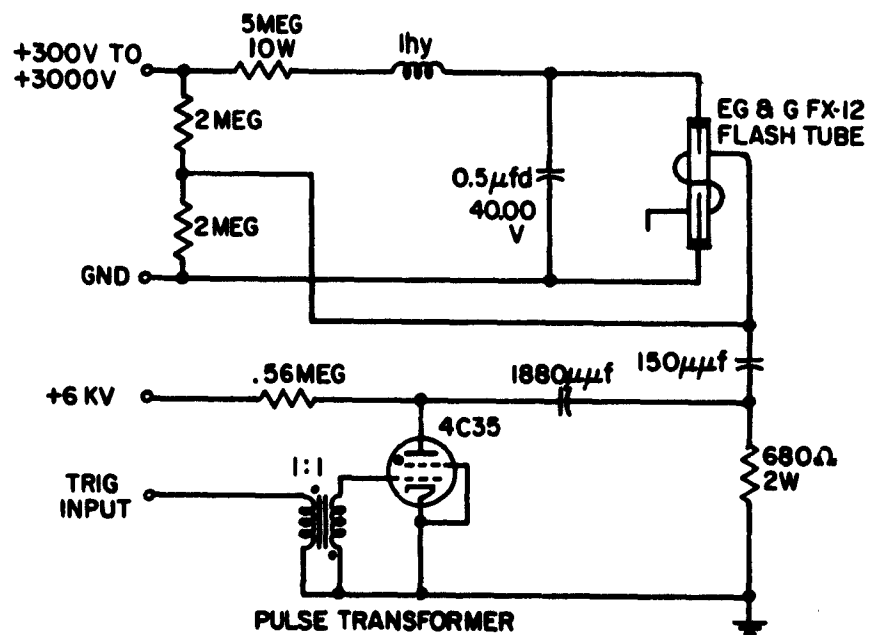


FIG. 6-4 FLASH LAMP CIRCUITRY

Holdoff voltage was improved by using a small trigger electrode at a farther distance from the flash lamp and by maintaining the potential of this electrode midway between the supply voltage and ground. As can be seen from the circuit in Fig. 6-4, the latter was accomplished by a d-c isolation capacitor and a simple voltage divider. These changes enabled operation of the flash lamp at 3000 v; supposedly, it should be possible to operate at higher potentials, but the writer has been unable to attain such operation.

The light output of this unit as a function of lamp voltage is shown in Fig. 6-5; the measurement technique to determine this output was the same as that described previously. These curves correspond closely to the data in the literature.² The delay from the time of pulse input to the 4C35 to the peak light output of the FX-12 is 0.5 microseconds, output jitter is about 20 μsec . This amount of jitter causes no problems, since the light output remains at its peak value for about 400 μsec .

6.3 Synchronization Circuitry

Operation of the flash tube trigger generator, the pulse field generator, and the shutter require fast rise pulses of 400 to 500 volts peak amplitude. The pulse to trigger each unit must be independently variable in time so that the units can be properly synchronized for operation of the apparatus; these pulses must also be quite free from jitter. In Fig. 6-6 is shown the pulse distribution circuit for generating and delaying the pulses which trigger the hydrogen thyratrons. The pulse generator circuits are given in Fig. 6-7.

The switching elements for these generators are Shockley 4-layer diodes; a sample characteristic of a 4-layer diode is given in Fig. 6-8. As can be seen from the characteristic curve, the 4-layer diode is a non-linear high resistance until the voltage across it approaches the firing value V_d , with a corresponding current I_d . At the current I_d , the slope

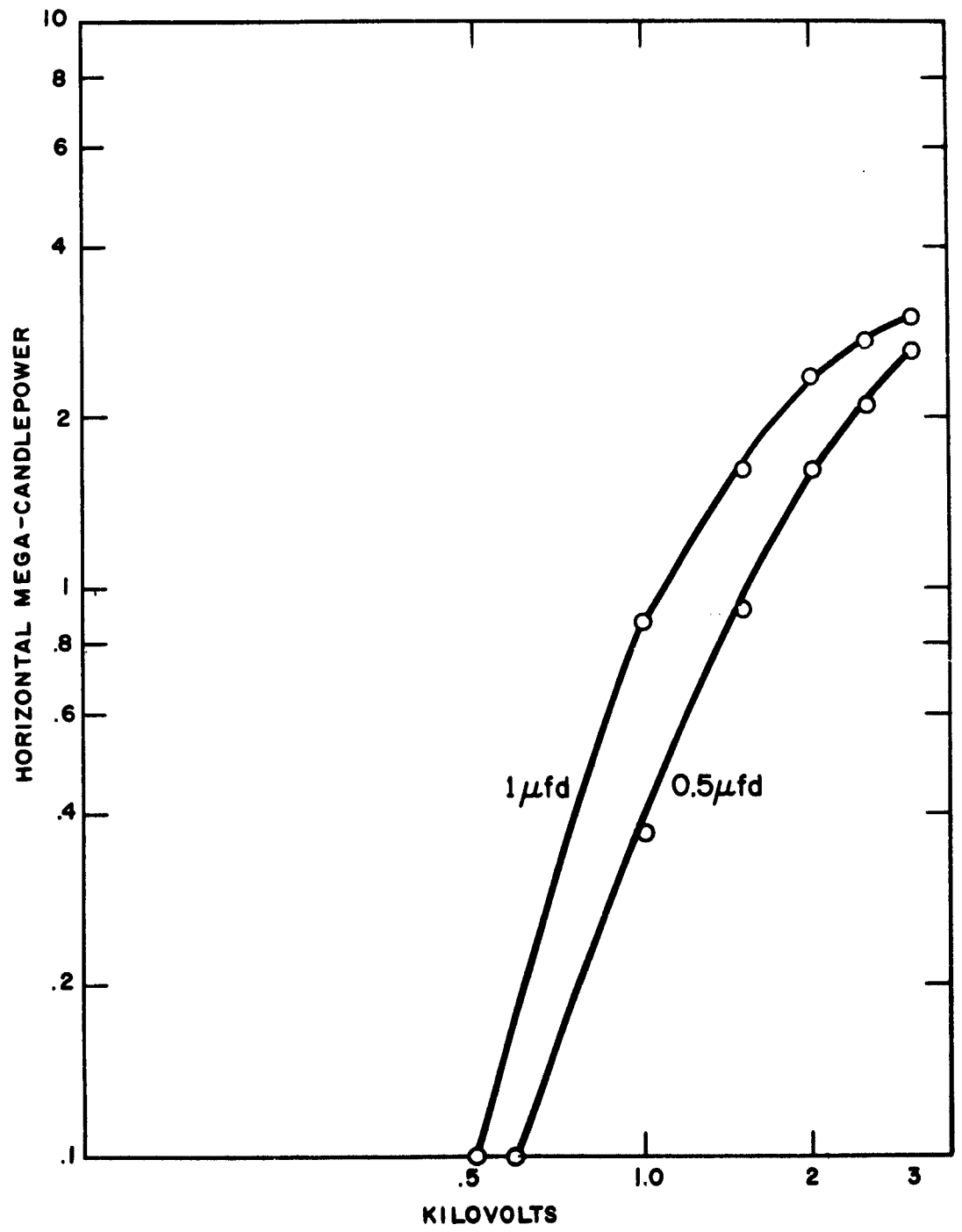


FIG. 6-5 FLASH LAMP OUTPUT

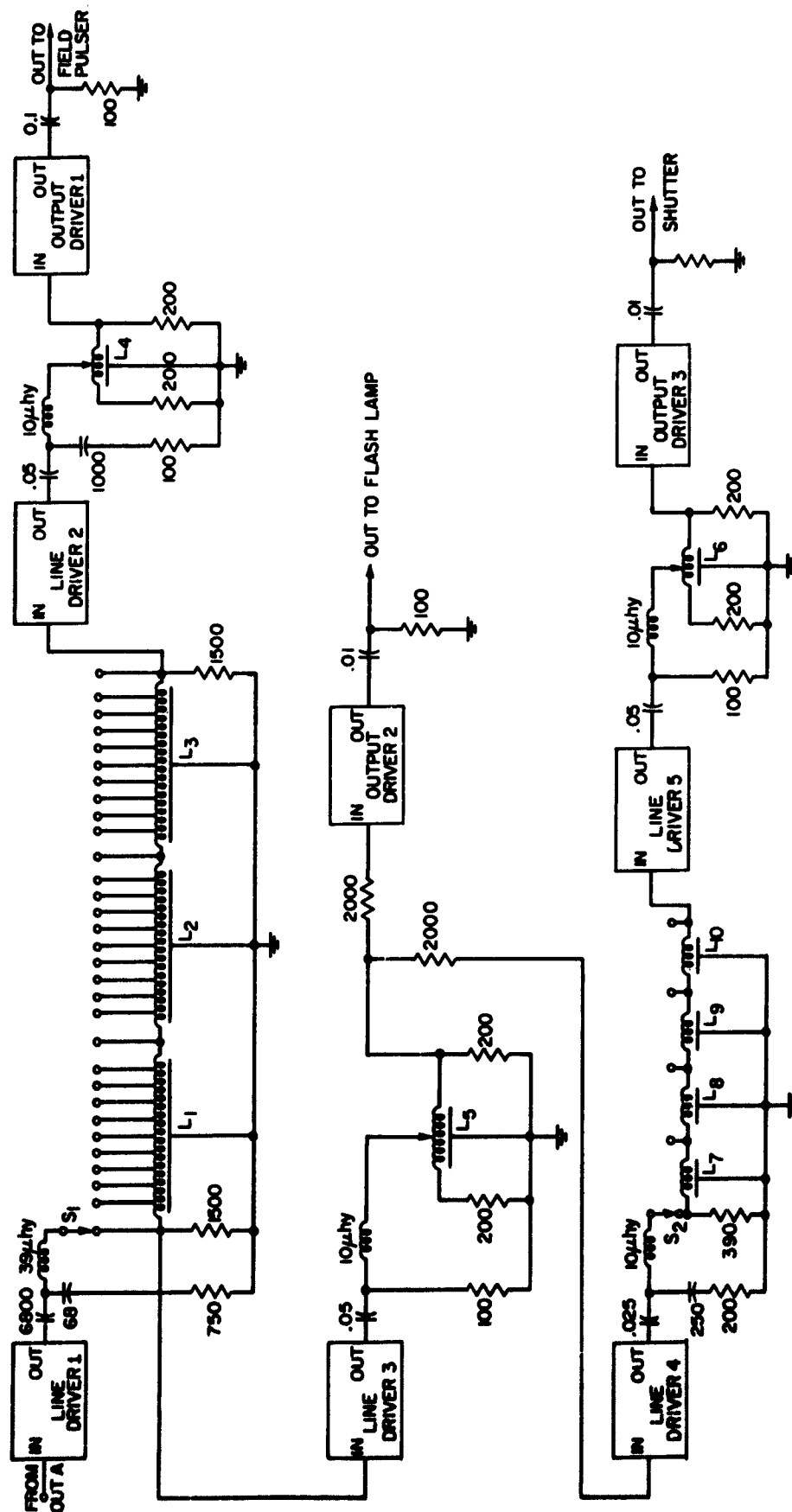


FIG. 6-6 PULSE DISTRIBUTION CIRCUIT

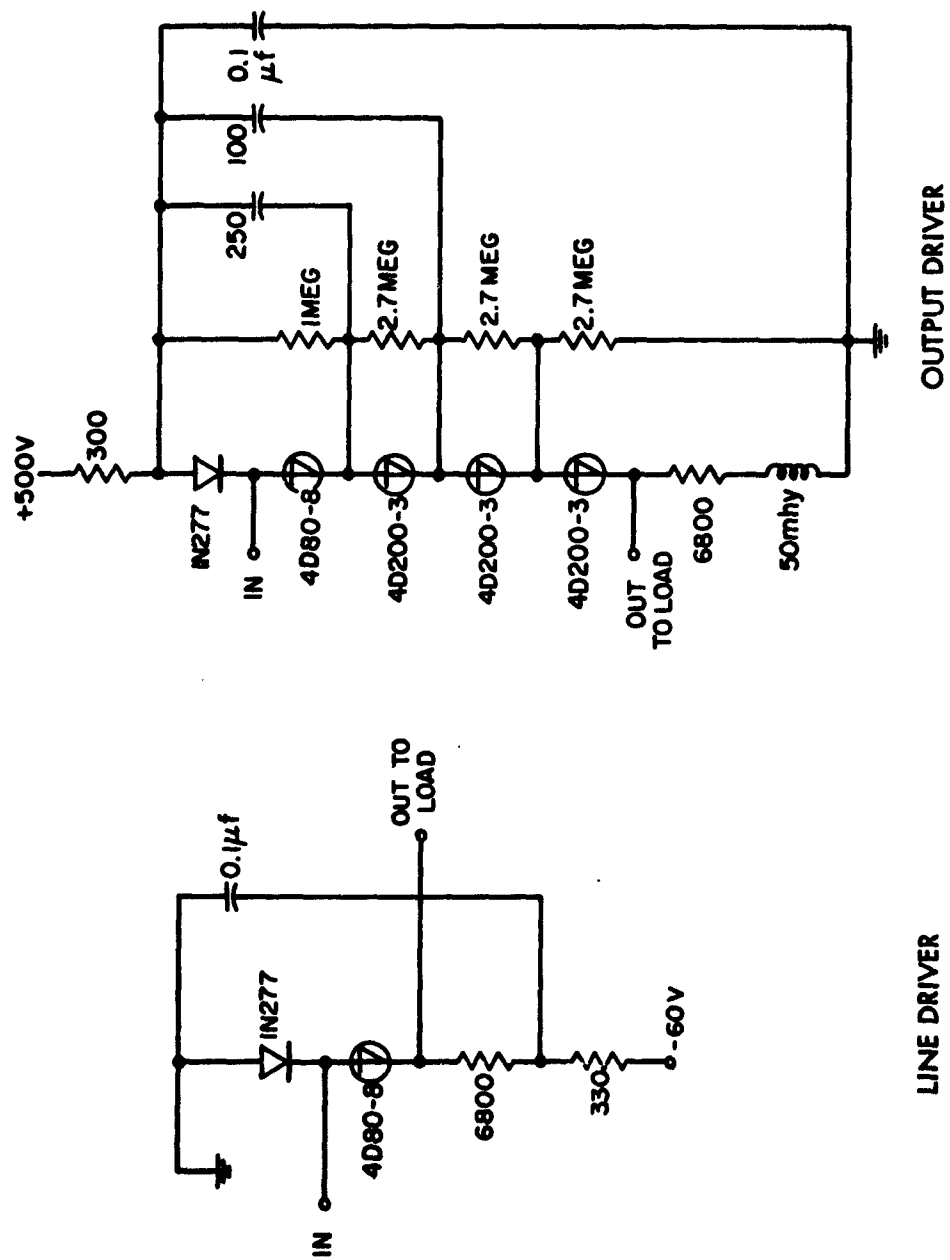


FIG. 6-7 PULSE GENERATOR CIRCUITS

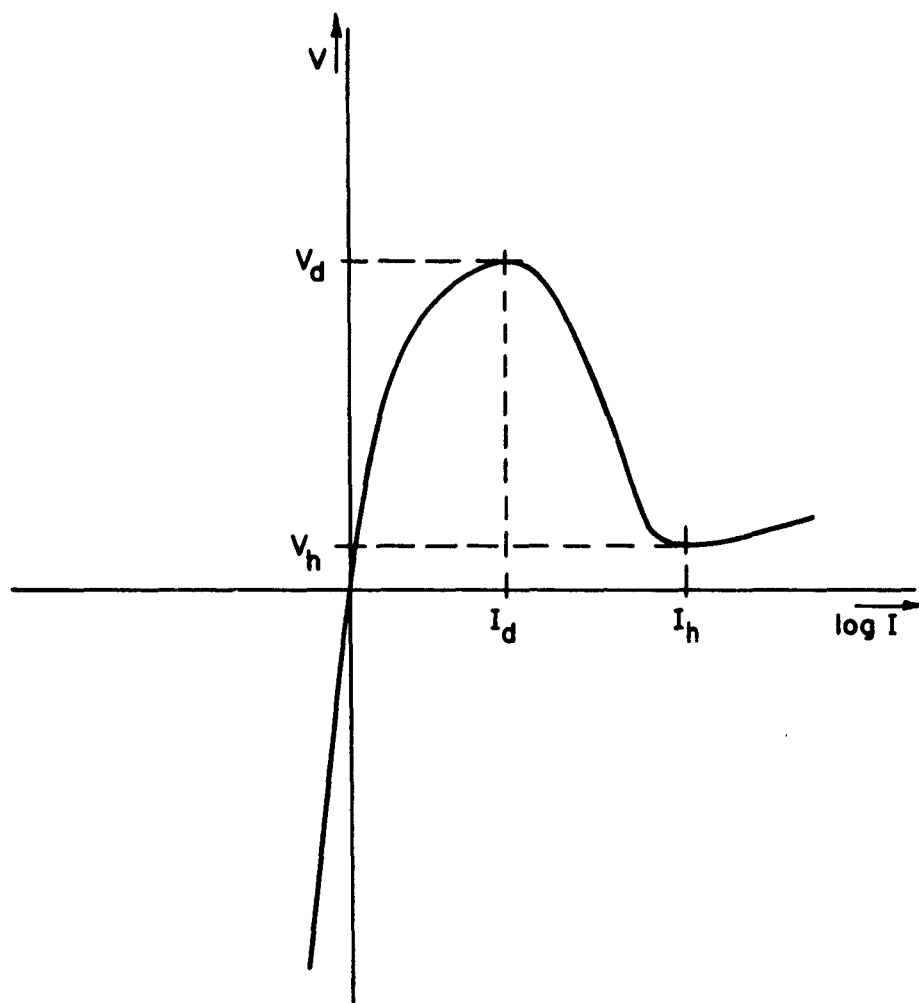


FIG. 6-8 4-LAYER DIODE CHARACTERISTIC

of the curve is zero; at higher values this slope becomes negative. The voltage decreases until it reaches a minimum value V_h , whereupon the curve resumes a slight positive slope, referred to as the holding state. A 4-layer diode in the holding state will remain so until the current is decreased below the holding current value I_h^* ; when this decrease occurs, the diode turns off and requires a few microseconds to recover. Switching time in properly designed circuits is about 20 μsec . Although the diodes used have maximum pulse current ratings of 2 amperes, operation at pulse currents as high as 6 amperes showed no signs of deterioration.

Operation of the pulse generator is quite simple. Consider the line driver circuit shown in Fig. 6-7. The quiescent voltage across the 4D80-8 is 60 volts. A positive input pulse reverse biases the IN277 coupling diode, and this input pulse voltage is added to the quiescent voltage across the 4D80-8. When the total voltage reaches V_d , the 4D80-8 becomes a negative resistance. Current is drawn from the external load (a pulse forming circuit), and the IN277 is switched to forward conduction. The load discharges, forming a pulse in the process, and the 4D80-8 turns off. The circuit then recharges and awaits the next input pulse.

If higher pulse voltages are required, the diodes can be connected in series, as shown in the output driver circuit, to increase the overall hold-off voltage. A voltage divider must be incorporated to be certain that the quiescent voltage across any one diode does not exceed its firing voltage. Small capacitors connected from the first one or two diodes to ground insure reliable triggering. Note that the 4-layer diode at the input end of the output driver has a lower firing voltage than the other diodes in the circuit. This is to allow more reliable triggering from a 60 volt pulse. By use of this technique of increasing firing voltage along the series string of diodes, it is quite possible to build a pulse generator capable of delivering

*The diode type number gives the specifications on V_0 and I_h . For example, a 4D80-8 diode has a nominal firing voltage V_d of 80 volts and a nominal holding current of 8 ma.

a 2000 volt 5 ampere pulse which can be reliably triggered with a three or four volt pulse.

Other advantages of the use of the 4-layer diode circuitry are that the circuits have the same input and output polarity, they can be designed for either polarity operation, and they require negligible quiescent current. (At 1000 cps repetition rate, the distribution pulse generators require a total current of about 30 ma.)

The pulse distribution circuit, then, is simply several tapped variable delay lines driven by the pulse generators just described. All lines are terminated at both ends and driven at their taps; this minimizes reflection problems and gives more uniform delay. The lines L_1 , L_2 , and L_3 have a total delay of 3 microseconds tapped every 0.1 microsecond. By taking outputs from both ends of the line, the relative time between these outputs can be varied by 6 microseconds. Of this, only 4.0 microseconds can be used for dynamic studies because of other delays in the system. Lines L_4 , L_5 , and L_6 are General Radio 314-S86 Variable Delay Lines, having a delay of 0.5 microseconds with a resolution of 0.4 μsec . A tapped line with a total delay of 1.2 microseconds is made of L_7 , L_8 , L_9 , and L_{10} .

In operation, L_6 and the line comprised of L_7 , L_8 , L_9 , and L_{10} are set so that the shutter pulse is centered at the peak of the flash lamp output. L_4 is used for initial zero adjustment between the shutter pulse and the pulsed magnetic field. L_1 , L_2 , L_3 , and L_5 are then varied to change the position of the shutter pulse (and hence the flash lamp peak also) with respect to the pulsed magnetic field.

Output A of the clock circuit shown in Fig. 6-9 initiates the pulse distribution circuit. This circuit consists of two capacitor charging and discharging circuits operated by the 4-layer diodes and transistors T_1 through T_6 and of a flip flop operated by transistors T_7 and T_8 . To follow the circuit operation, assume that the flip flop has just switched

so that T_1 , T_4 , T_6 , and T_8 are on, while T_2 , T_3 , T_5 , and T_7 are off. The capacitor selected by S_{3a} has been discharged for the previous half cycle, while that selected by S_{3b} has just been discharged by the firing of D_2 . T_1 supplies a constant current (determined by the 50 K potentiometer) to the capacitor at S_{3a} , resulting in a negative voltage ramp across D_1 . When D_1 reaches its firing voltage, it discharges the capacitor at S_{3a} . The leading edge of this discharge is coupled to the flip flop and switches it to its opposite state. All transistor conduction states reverse, and the processes are repeated on the opposite sides of the circuit. The circuit as designed will operate from .05 cps to 50 cps with the 40 uf capacitors and from 2 cps to 2000 cps with the 1 uf capacitors.

For single cycle push button operation, S_1 is closed, clamping the capacitor charging ramp so that D_2 cannot fire. When the push button S_2 is depressed, the circuit behaves in the same fashion as if D_2 had fired and continues operation until the capacitor charging ramp is again clamped by the diode at S_1 .

Output B is used to drive the circuit of Fig. 6-10, which in turn drives the restoring pulse generator relay.

6.4 Static Field Circuitry

Two sets of Helmholtz coils, one 6.5" in diameter and the other 4.5" in diameter, were wound to provide static fields for biasing and static observations. The coils were designed to have 500 turns and 722 turns respectively, which would have resulted in identical fields for the same current through each set of coils. Through an error, the number of turns was reversed, i.e., the larger coils were wound with 500 turns and the smaller coils with 722 turns. Compensation for this error was accomplished in the resistance networks of the bias angle panel, which will be described shortly.

The current for the Helmholtz coils is supplied by the static field supply shown in Fig. 6-11. This supply can be used either as a constant voltage regulated supply, capable of supplying 2 amperes at 50 volts output, or as a wave form generator to switch the specimens for quasi-static observations. For biasing operation, one or the other of the microswitches is operated, connecting the DT80 transistor in the desired polarity to the Helmholtz coils. The Clare relay is also actuated, allowing a fixed current to flow into the feedback amplifier comprised of the 904A, the 4DJ1A21, and the 2N144 transistors. A second feedback amplifier, with the DT80 transistor output, is designed as a dc voltage amplifier with a very low impedance output. The voltage output is then determined by the input level selected by the helipot.

For quasi-static observations the microswitches are alternately closed by an eccentric cam on a variable speed motor, thus reversing the current to the Helmholtz coils each half cycle. The Clare relay opens wherever either microswitch is operating. The current in the first feedback amplifier jumps to some given value when the Clare relay is open and then slowly rises to its quiescent value, the rate of rise being determined by the RC networks; the time constants for these networks can be varied in five steps from one second to 100 seconds. The voltage driving the Helmholtz coils follows this wave form; hence the circuit can be adjusted so that upon reversal of the field the current in the Helmholtz coils generates a field just below the coercive force of the film after which the field slowly increases, enabling observation of the domain changes.

The output from the static field supply is connected to the Helmholtz coils through the bias angle panel shown in Fig. 6-12. This panel provides for direct connection of the static field supply to one set of coils, and also for connection of the supply to both coils through resistance networks selected by the rotary selector. The values of these resistance networks are such that the angular position of the magnetic field in the plane of the

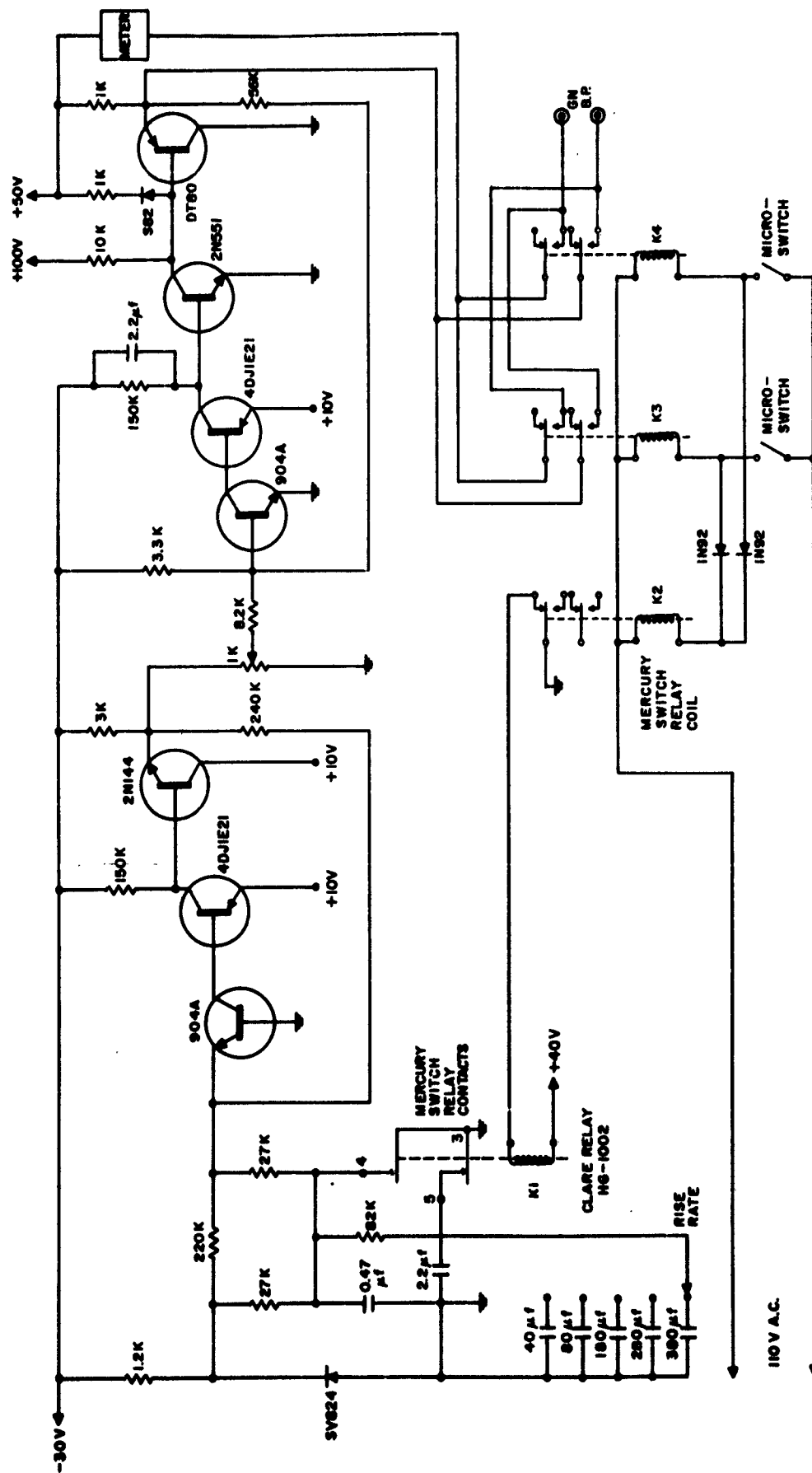


FIG. 6-11 STATIC FIELD SUPPLY

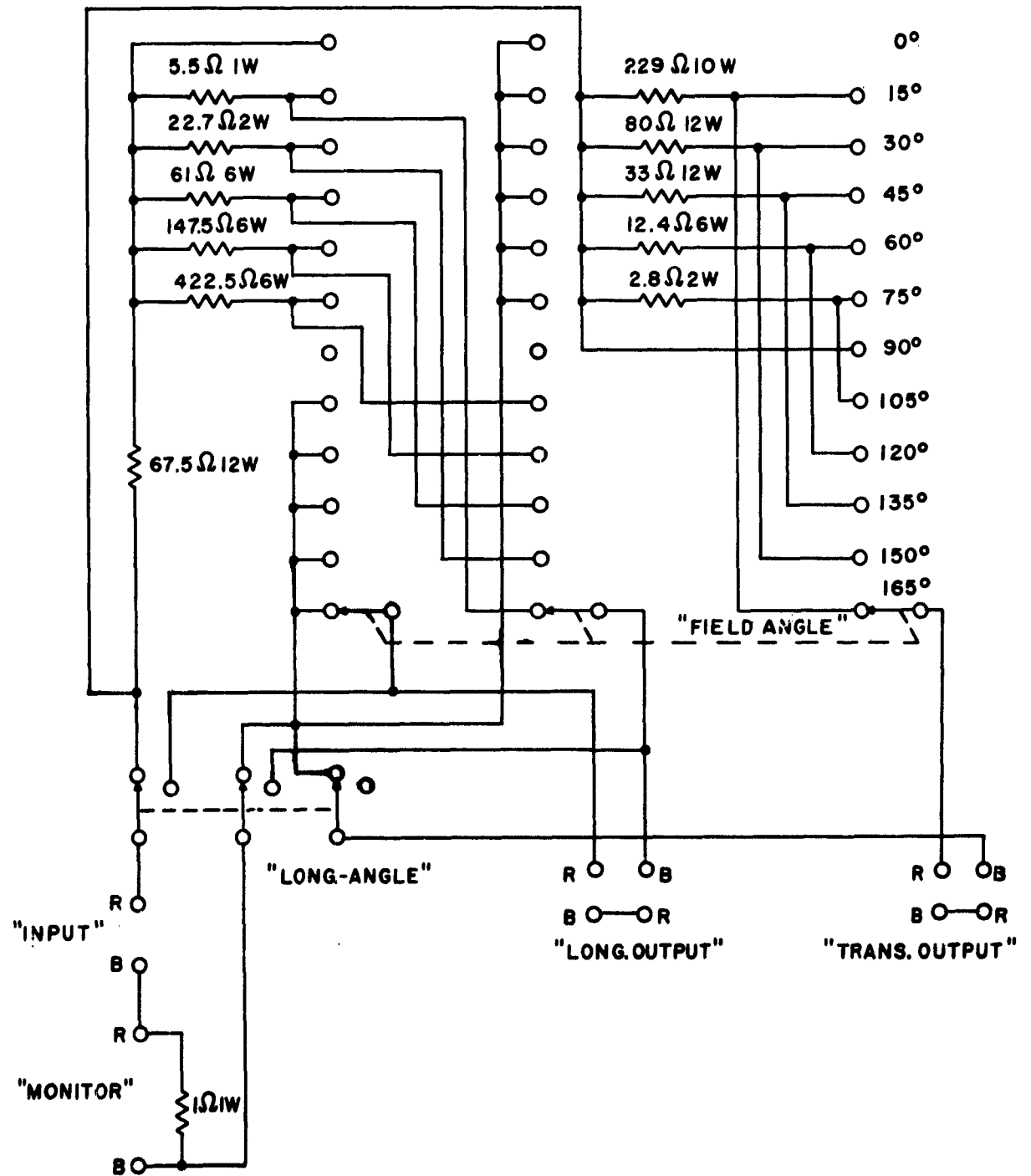


FIG. 6-12 BIAS ANGLE PANEL

specimen advances 15° for each step of the rotary selector, being variable from zero through 165° . This covers all twenty-four 15° increments, since the current to the bias angle panel can be reversed in the static field supply. For direct connection to the coils the maximum field available is 60 oerstads; for setting the field at an angle the maximum field available is 30 oerstads.

6.5 Miscellaneous Circuitry

Two regulated high voltage supplies were designed and constructed to power the flash lamp and the field pulse generator. The feedback loops from these supplies were analyzed and the poles adjusted to allow a high loop gain with stable operation. Output ripple is about 0.1 per cent of the output voltage. These supplies will regulate at outputs from 300 volts to 3200 volts; available output current is 300 mills up to 2500 volts output, which drops to 140 mills at 3200 volts output. The load regulation of the supply was not measured, but changing the load current from zero to 300 mills caused a change in output voltage just barely detectable on the output voltmeter. The schematic for these power supplies is shown in Fig. 6-13.

Power for the hydrogen thyratron filaments and the 6587 hydrogen reservoir were supplied by the simple circuit shown in Fig. 6-14.

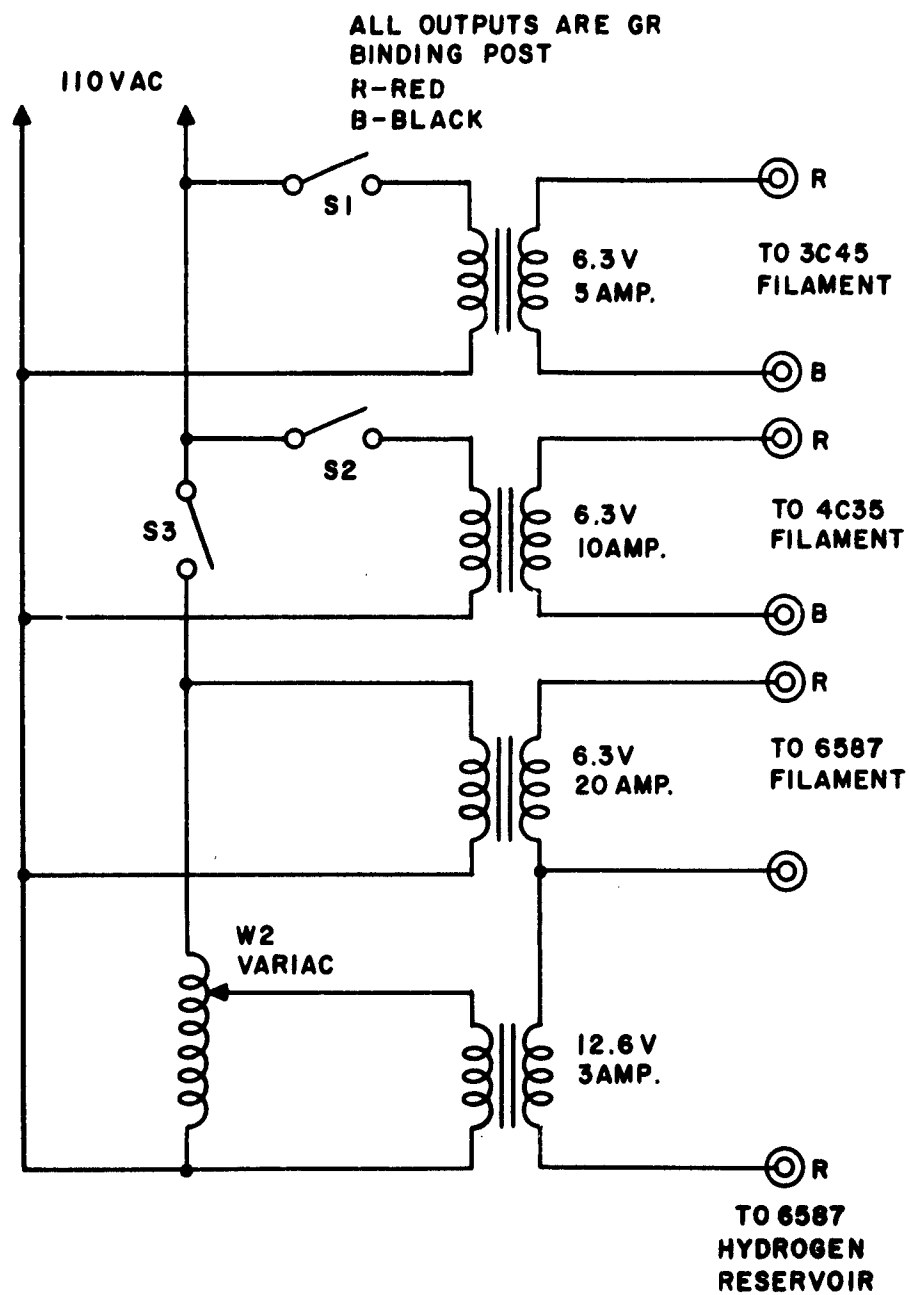


FIG. 6-14 THYRATRON HEATER POWER PANEL

CHAPTER VII

EXPERIMENTAL RESULTS

The apparatus described in the previous chapters has been used to photograph the reversal of thin ferromagnetic film specimens and to visually observe the remanent states of specimens after the application of short duration magnetic field pulses. As quite often happens when an involved apparatus of this sort is constructed, many problems arise which, if foreseen, would have resulted in a considerable difference in the design of the apparatus. In this final chapter we discuss some examples of the various experimental results and the problems encountered in obtaining these results. Improvements which could be made are noted; the chapter concludes with some suggestions toward further research which could be conducted with this instrument.

7.1 High Speed Photographs

Originally, the author had planned to take single exposure photographs of specimen reversal for various magnitudes of longitudinal switching field and transverse bias field. Because of problems encountered which will be discussed in the next section, it became necessary to take triple exposure photographs instead. To take such photographs the following procedure was employed. The time delay from the pulse distribution panel was set so that the electro-optical shutter would open at a given time following the application of the pulsed magnetic field. The specimen was saturated with a magnetic field of .50 oersteds. Following the removal of this field the system was triggered, switching the specimen and exposing the photographic film. The specimen was then reset to its original state with the 50 oersted field and the system was triggered again. This process was repeated a third time. During this time the photographic film was not advanced, resulting in a triple exposure on the film. To

obtain a time sequence of specimen reversal, the procedure was repeated for various delay settings of the pulse distribution panel.

The camera lens used for the photographs in this section has a focal length of 38 mm. This results in a smaller image on the photographic film than was originally intended with an accompanying increase in graininess in the photographs in this section. Although in the author's mind this is undesirable, it became necessary because of the experimental problems which we will discuss later.

The specimen used in the examples which we will show was a thin film of eighty-three per cent nickel and seventeen per cent iron. Specimen diameter was 0.375 inch; thickness was approximately 1000 Angstroms. A quarter-wave coating of zinc sulfide was evaporated on top of the specimen in accordance with the discussion in Chapter II.

The anisotropy axis of the specimen was supposedly parallel to the sides of the square glass specimen substrate. The specimen was positioned in the apparatus so that the switching field would be applied parallel to the side of the substrate. From the switching observed, it became apparent that the anisotropy axis was a few degrees off from its assumed position. From the data of Olsen and Pohm¹, it is apparent that as the transverse field is increased, the switching time should decrease (see Fig. 1-2). This was not the case. For example, the following switching times were noted for a longitudinal switching field of 2.8 oersteds.

Transverse field	Switching time
0 oer.	2.5 μ sec.
.39 oer.	4.5 μ sec.
.70 oer.	3.5 μ sec.

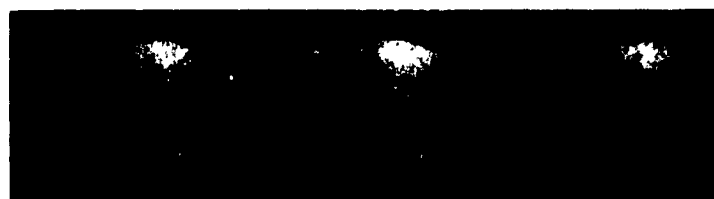
In Figs. 7-1 through 7-5, we have shown some examples of photographic sequences during switching. Fig. 7-6 shows sketches of the progression of the switching sequence illustrated in Fig. 7-1. The number underneath



500

1000

1500



2000

2500

3000



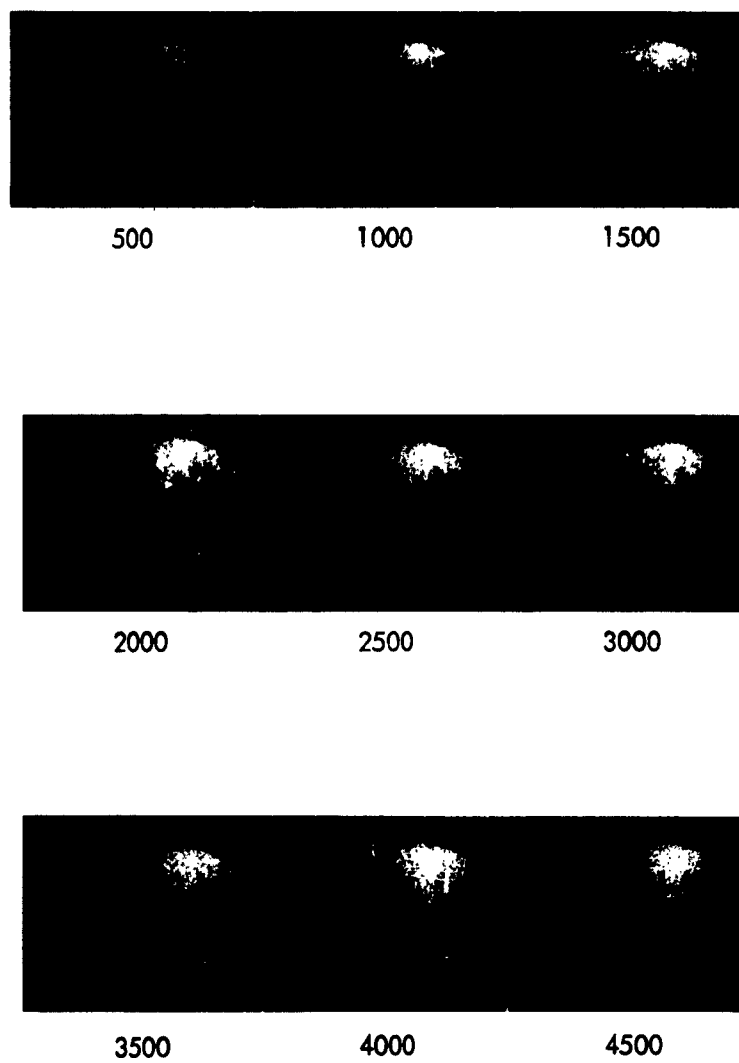
3500

4000

4500

$\uparrow H_L = 2.2$
 $\longrightarrow H_T = .39$

FIG. 7-1 SWITCHING SEQUENCE 1



$H_L = 2.6$
 $H_T = .39$

FIG. 7-2 SWITCHING SEQUENCE 2

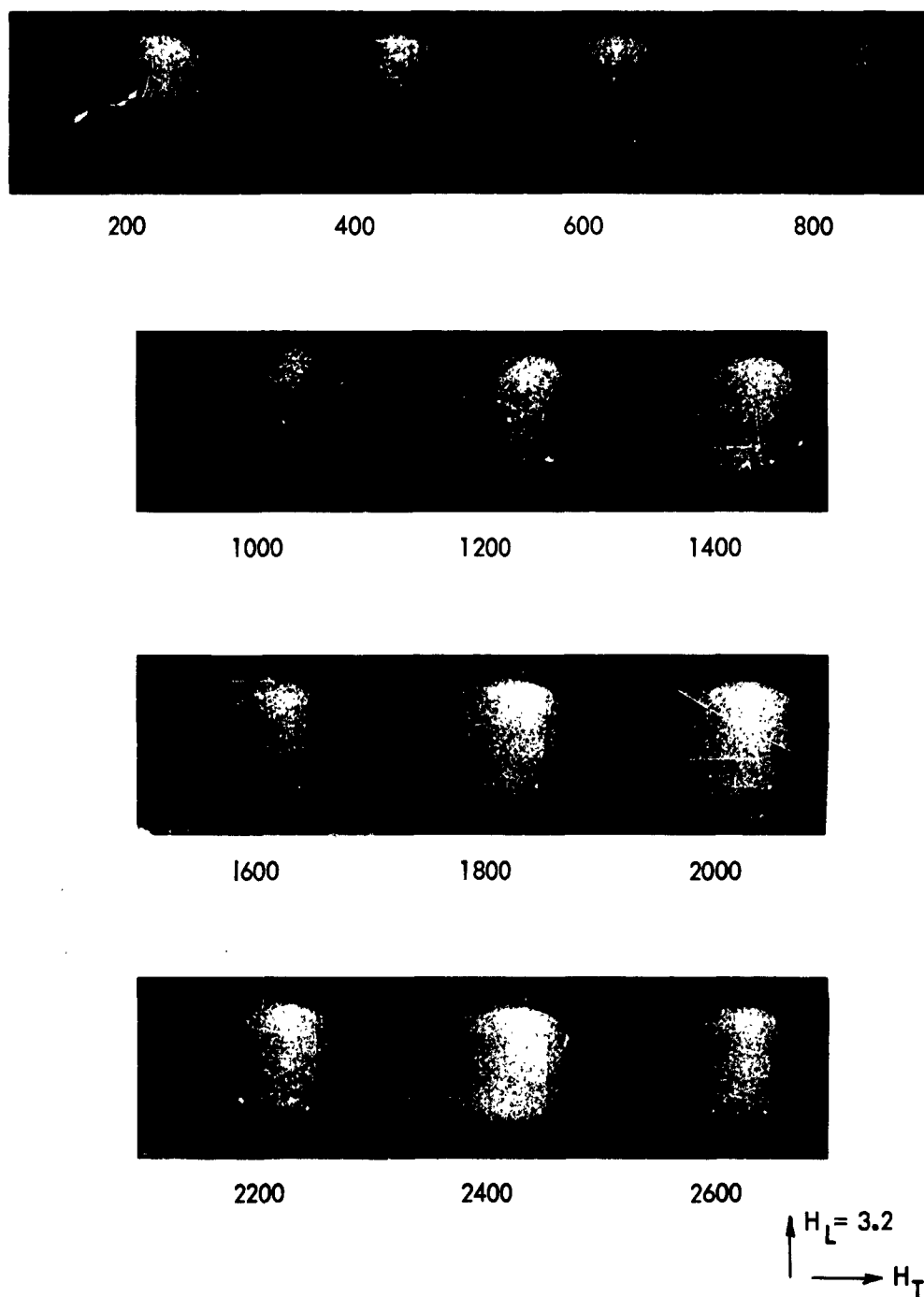


FIG. 7-3 SWITCHING SEQUENCE 3

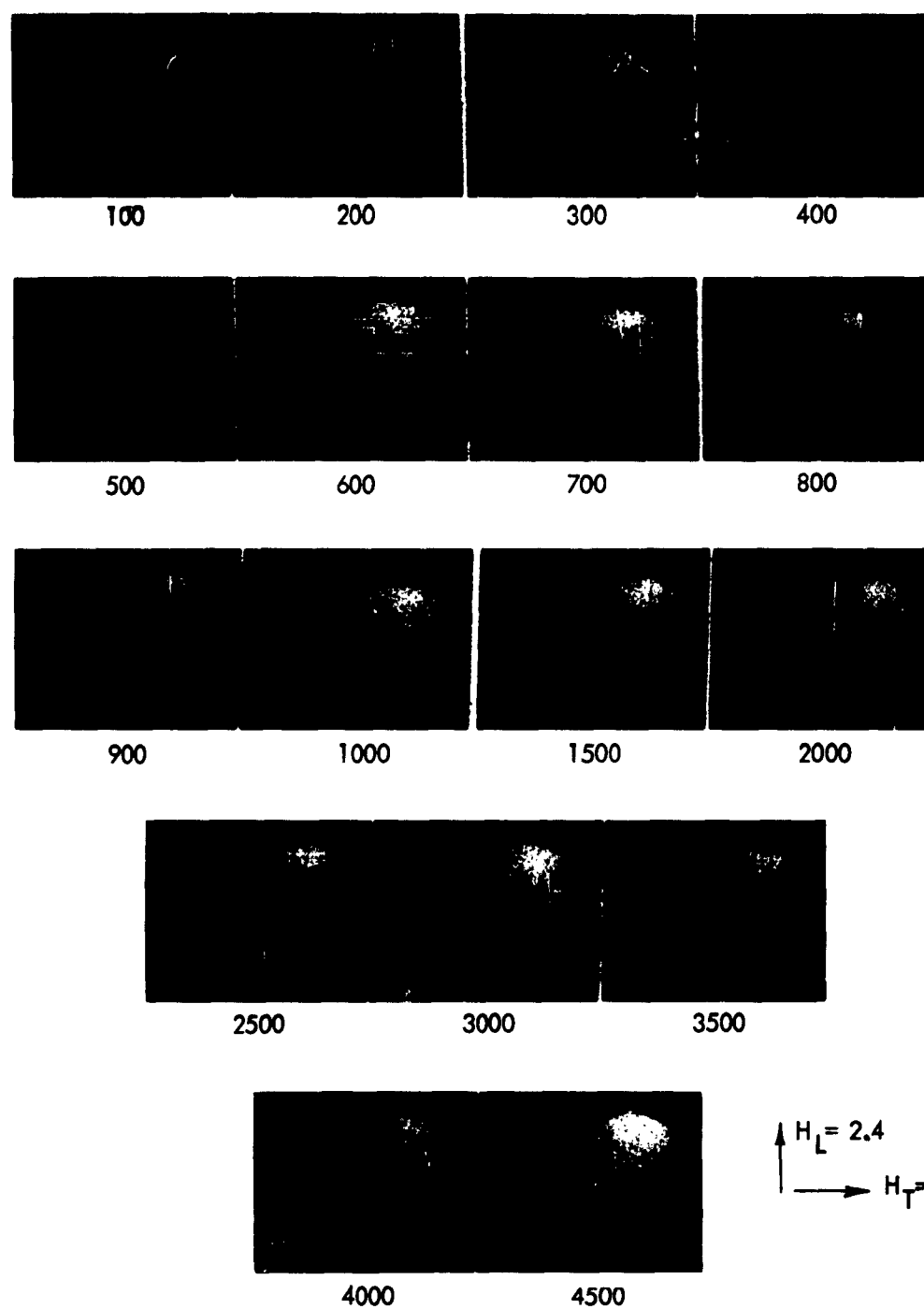


FIG. 7-4 SWITCHING SEQUENCE 4

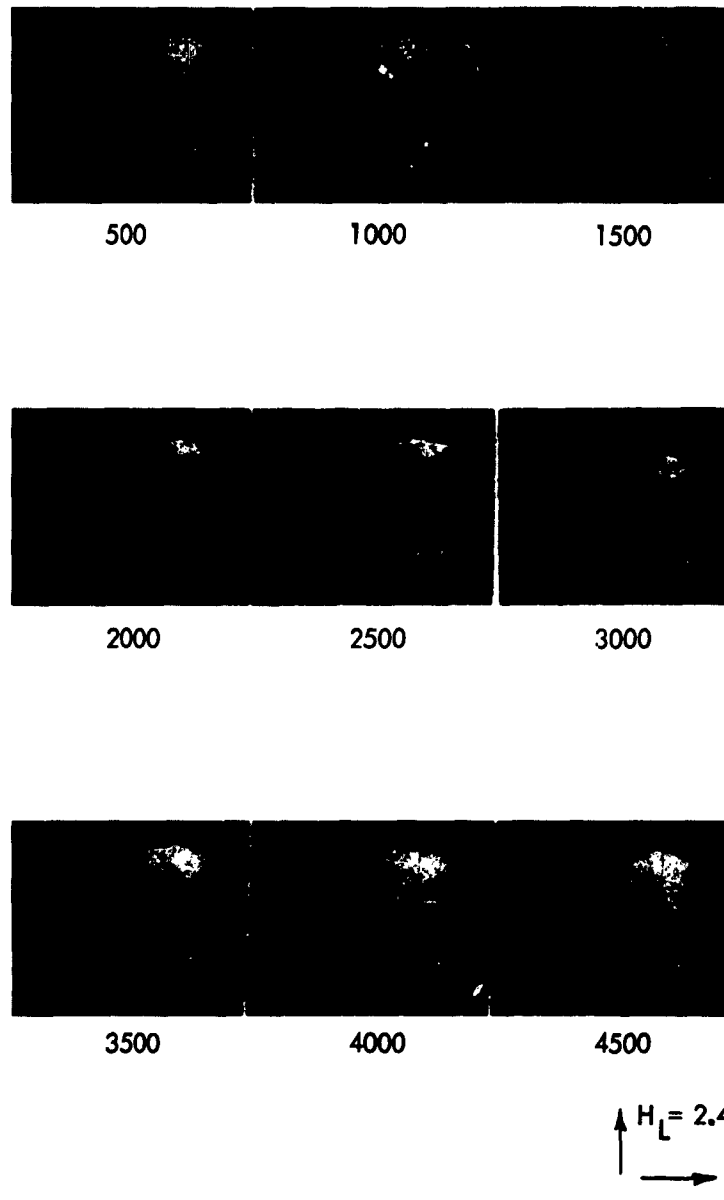
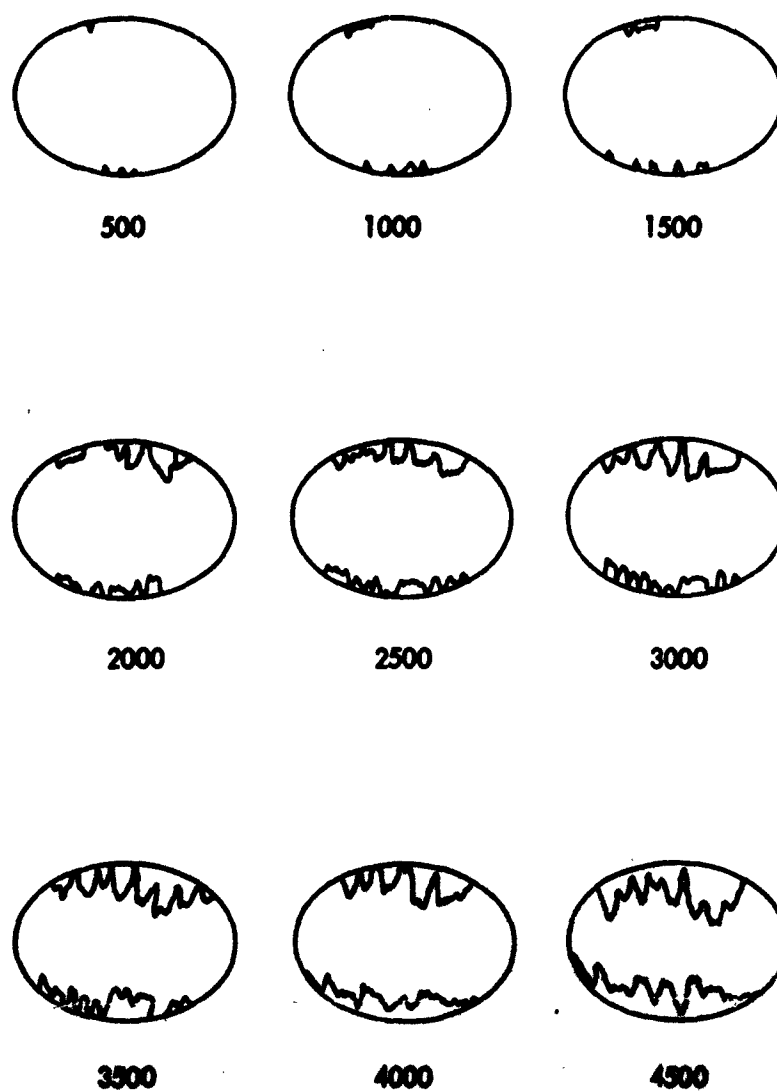


FIG. 7-5 SWITCHING SEQUENCE 5

**FIG. 7-4 SKETCH OF SWITCHING SEQUENCE 1**

each photograph indicates the time elapsed in millimicroseconds from the application of the switching field. The magnitudes of the longitudinal switching field H_L and the transverse bias field H_T are also given in each figure.

In Fig. 7-1 the specimen has reversed approximately twenty per cent in 4500 μsec , the maximum delay available from the pulse distribution panel. One can see the beginning of domain propagation at the top and bottom of the specimen. In Fig. 7-2 we see that a higher switching field increases the rate of domain propagation and also increases the number of domains initially nucleated, in accordance with the hypothesis of Conger and Essig². Note in this specimen that a domain nucleation occurs just slightly to the left of center in the specimen. The domain is barely visible at 1500 μsec , increases to a noticeable size at 2000 μsec and is merging with the domains propagating from the top of the specimen at 2500 μsec . In Fig. 7-3 we have again increased the longitudinal switching field. Whereas before we could see the entire reversal process, here we can see very little. At the bottom of the photographs labeled 400, 600, and 800, domain propagation is observable, but at the top of the specimen we can tell almost nothing of what is going on. That this latter must have reversed is apparent from the photograph at 1600 μsec . Here we see a small domain on the left which shrinks with increasing time. Note again the appearance of the small center domain at 600 μsec .

This inability to determine the reversal may arise from (1) the fact that the domain structure is too fine to be resolved in these photographs, (2) the possibility that there is a rotational process occurring, or (3) the possibility that the reversal process is not repeatable at this switching speed and hence the triple exposure is causing blurring of the photograph. In Fig. 7-4 we see the same situation again, although under a different set of field conditions. Domain propagation at the bottom of the specimen is observed while at the top it is not. Note at 900 μsec that a large domain

has formed in the upper right portion of the specimen, although we cannot determine the process by which this formation occurred.

In Fig. 7-5, we see that the application of a large transverse bias field (.70 oersted) drastically affects the direction of domain propagation. The propagation is at an angle of twenty or thirty degrees away from the anisotropy axis.

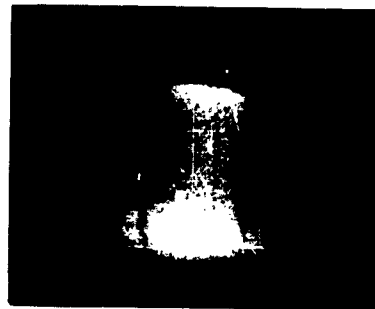
7.2 Experimental problems

As we have stated several times (perhaps to the point of monotony), the original intent in this project was to take single exposure photographs of 10 μ sec duration. In Fig. 7-7 are photographs of a single, a double, and a quadruple exposure taken with 10 μ sec exposure duration. In this case the electro-optical shutter was operating at 40,000 volts and the flash lamp at 2700 volts. The exposures were of the specimen mentioned and were taken with the specimen in a static condition. The Eastman Double-X film which was used to take the photographs was developed for thirty minutes in Ethol UFG Developer at a temperature of 24°C. As is obvious from the photographs, even the single exposure has better quality than the triple exposures in the switching sequences which we have shown. At a later time, for some reason unknown to the author, it proved impossible to duplicate these results.

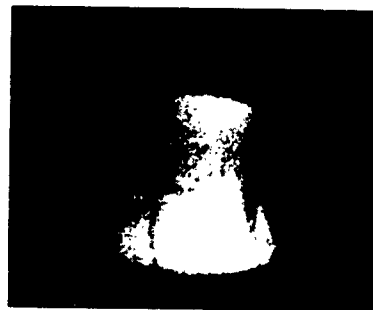
The writer believes that this deterioration in performance quality is very likely due to changes in the optical alignment of the system. The rod lattice supports which serve as an optical bench are quite useful in initial experimental work because of the flexibility of the structure. However, the clamps do not hold well and it is quite tedious and time consuming to realign the optical apparatus. It has been the writer's experience that small changes in optical alignment can cause considerable changes in viewing quality. In addition, it requires only a few minutes of tilt in the plane of the specimen to cause a change in the observed specimen reflection.



SINGLE EXPOSURE



DOUBLE EXPOSURE



QUADRUPLE EXPOSURE

FIG. 7-7 TEST PHOTOGRAPHS

Considerable difficulties were encountered in the operation of the flash lamp. The electrode configuration mentioned in Chapter VI helped somewhat on the holdoff characteristics of the lamp, but still did not enable lamp operation above 2700 volts. The lamps are not precision manufactured; consequently, every time a lamp was replaced, the position of the discharge area with respect to the flash lamp lens would be altered, necessitating a realignment of lamp assembly. The angle of incidence would then be changed, requiring a readjustment of the polarizers in order to maintain good contrast. The lamp voltage also decreased slightly during operation; the end result was that the lamp was operated at 2400 volts, at which voltage its light output is about two-thirds of its maximum possible output.

Operation of the electro-optical shutter in excess of its initial design voltage caused corona problems which in turn increased the tendency of arcing from the thyatron anode cap. As this became progressively worse, it became necessary to reduce the shutter voltage to 38,000 volts, causing a ten per cent decrease in light transmission.

These were the major contributive factors which led to the use of the triple exposure technique. Their correction would require that a major portion of the optical apparatus be rebuilt, but time did not allow such a remedy.

7.3 Visual Observation with Short Pulses

Using field pulses of short duration (75 μ sec, 150 μ sec, and 300 μ sec), some interesting specimen behavior was observed by visually observing the specimen through the telescope. Illumination in this case was provided by the zirconium arc source. Observations were made at various pulse repetition rates.

With rapid pulse sequences, one observes reversal which appears to be domain propagation in slow motion. For low field amplitudes, domain nucleation occurs only at the edges of the specimen.

At the lowest amplitudes at which reversal occurred in one particular specimen, the initial nucleation occurred at a total of eight points on the specimen boundary. As the amplitude is increased, the number of nucleation points increased also, until the reversal consisted of two fronts advancing towards each other in a manner similar to that illustrated in Fig. 7-2. Increasing the amplitude still further caused nucleation to occur at points other than on the specimen boundary.

At this stage, reversal was occurring so rapidly that the pulse rate had to be decreased to the point that continuous motion was no longer apparent. It was now observed that a single pulse on an initially saturated specimen could cause very small domains to appear throughout the entire specimen, very similar to the appearance of pepper scattered on a piece of paper. The field threshold for this nucleation to appear could be determined to within about four per cent.

Further experiments with varying pulse lengths showed that the field threshold decreased as the pulse length was increased. This dependence leads the writer to conclude that these nucleations occur at regions of low H_K (anisotropy field). If they arose from imperfections, it seems that there should be threshold dependence only on pulse field amplitude. Consider, however, the rotational process which would occur in a region of low H_K . When a step function magnetic field of sufficient magnitude is applied, the low H_K region begins to rotate. The rotational process also occurs in the surrounding area, but the low H_K region progresses at a faster rate. If the pulse field is removed at a time when the low H_K region has rotated by less than 90 degrees, then the magnetization vector collapses to its original state. If the field is removed when the rotation is greater than 90 degrees, the magnetization vector will try to realign itself with the anisotropy field, resulting in the formation of a reversed domain in the low H_K region. The verification of this hypothesis obviously requires further experimental work.

7.4 Apparatus Improvements

By this time, the reader has probably gathered that there are many improvements which could be made over the present system. The following is a listing of the major improvements which the author would incorporate in a rebuilding of this apparatus.

1. Optical component mounting. The entire optical system should be mounted on a rigid heavy-duty optical bench. The design of this bench should be such that the various optical components could be easily removed from and replaced on the bench without requiring any optical aligning. It would be desirable to include some means for easily varying the angle of incidence.
2. Flash lamp. The flash lamp should be mounted in a housing which will prevent radiation of magnetic fields and allow positioning of the lamp with respect to the flash lamp lens. A trigger electrode configuration should be determined which will allow the lamp to be operated at its maximum holdoff voltage.
3. Electro-optical shutter. The shutter should be redesigned to operate at 30,000 to 35,000 volts. This should alleviate the arc-over problems which are presently being encountered.
4. Shielding. All high current and high voltage units should be more adequately shielded to prevent false triggering. This has been only an occasional problem but should be guarded against.
5. Camera. It would be extremely convenient to build a special camera for the system. Such a camera would have automatic film advance and a solenoid operated shutter and would be designed to maintain the film plane position within .001 inch. Some means for accurately and easily setting the angle of the film plane should be included.

6. System transmission measurement. At present it is necessary to take a large number of photographs at various polarizer settings to determine the best polarizer adjustments for photographic work. This procedure could be minimized, and possibly eliminated, by providing a modulated light source and a photo multiplier detector which could be used to measure system transmission and contrast ratio. This arrangement could also be used to make direct measurements of the value of r_k .
7. Revision of optics. Preliminary examination has indicated that the lens arrangement between the specimen and the photographic film can be revised to obtain an increased field of view. The revised setup would use the present polarizers but would require four lenses rather than the present two. Sufficient flexibility of design would be available to allow the distortion parameter to be reduced to zero (see Section 4.4).

7.5 Summary and Conclusions

The present work has demonstrated the feasibility of making thin ferro-magnetic film reversal studies by a combination of magneto-optic and high-speed photographic techniques. Problems in the present apparatus prevent the full illustration of the possibilities of this study technique, but the writer believes that an apparatus capable of single exposure photographs of ten or twenty millimicroseconds duration is quite practical.

The ramifications of this work indicate several interesting experimental projects which could be undertaken. The threshold observations mentioned in Section 7.3 could be extended to a study under varying conditions of transverse bias field, longitudinal switching field, and pulse duration. If the "pepper patterns" observed are indeed the result of a rotational process, the experimental observations coupled with an analysis of the rotation of a low H_K region in a specimen in response to a step field should prove quite fruitful toward understanding the onset of the nonhomogeneous rotational mode.

System transmission measuring apparatus can be used to directly determine the magnitude of r_k , the magneto-optic reflection coefficient magnitude. Whether or not the phase of the reflection coefficient can be as easily determined is not yet known. If the phase can be measured, studies of dielectric coatings of various thicknesses and indices of refraction could be undertaken, yield experimental proof of the validity (or nonvalidity) of the dielectric coating analysis presented in Section 2.4.

Other possibilities for experimental studies have been mentioned in Chapter I, and the reader may have considered experiments during the perusal of this thesis. The writer believes that the Kerr magneto-optic effect, although a small effect in itself, provides a useful technique for the investigation of thin ferromagnetic film reversal.

Appendix A

ALTERNATIVE TRANSMISSION DERIVATION

In Section 2.2, we derived the transmission equation (Eq. II-18) using a space vector notation. The derivation can be carried out equally well using matrix notation. The technique of Section 2.2 lends itself to the pictorial vector diagrams incorporated which tend to give some physical insight as to what is happening. The matrix notation, on the other hand, shows the mathematical transformation from stage to stage more clearly and is also more compact. For completeness, the derivation in matrix form is presented here.

We can consider that there are three sets of planar coordinates involved in the transmission analysis. Let us denote unit space vectors, all of which are perpendicular to the z-axis, as follows:

- \vec{i}_p lies in the principal plane of the first polarizer
- \vec{i}_m lies in the minor plane of the first polarizer
- \vec{i}_y lies in the plane of incidence
- \vec{i}_x is perpendicular to the plane of incidence
- \vec{i}_a lies in the principal plane of the second polarizer
- \vec{i}_b lies in the minor plane of the second polarizer

All of these unit vectors are perpendicular to the z-axis (optic axis). From Section 2.2, we see that \vec{i}_p and \vec{i}_y form an angle γ , and that \vec{i}_x and \vec{i}_a form an angle ϕ .

Assume that the light emerging from the first polarizer is

$$\begin{bmatrix} t_1 & \frac{E_{op}}{\sqrt{2}} \\ t_2 & \frac{E_{om}}{\sqrt{2}} \end{bmatrix} \quad (M-1)$$

Referring to our unit vector notations above, we see that this matrix represents the p-q coordinate system. To rotate to the x-y coordinate system, we premultiply by the coordinate transformation matrix

$$\begin{bmatrix} \sin \gamma & \cos \gamma \\ \cos \gamma & -\sin \gamma \end{bmatrix} \quad (M-2)$$

The process of reflection from the specimen is referenced to the x-y coordinates, so we now premultiply by the amplitude reflection coefficient matrix

$$\begin{bmatrix} \hat{r}_x & \hat{r}_k \\ -\hat{r}_k & \hat{r}_y \end{bmatrix} \quad (M-3)$$

and then by the coordinate transformation matrix

$$\begin{bmatrix} \cos \phi & \sin \phi \\ -\sin \phi & \cos \phi \end{bmatrix} \quad (M-4)$$

to get to the a-b coordinate system in which the second polarizer is referenced. For transmission through this polarizer we simply premultiply by the transmission matrix for the polarizer

$$\begin{bmatrix} t_1 & 0 \\ 0 & t_2 \end{bmatrix} \quad (M-5)$$

Representing the output from this polarizer as

$$\begin{bmatrix} E_{oa} \\ E_{ob} \end{bmatrix} \quad (M-6)$$

the total matrix representation for the transmission is

$$\begin{bmatrix} E_{oa} \\ E_{ob} \end{bmatrix} = \begin{bmatrix} t_1 & 0 \\ 0 & t_2 \end{bmatrix} \begin{bmatrix} \cos \phi & \sin \phi \\ -\sin \phi & \cos \phi \end{bmatrix} \begin{bmatrix} \hat{r}_x & \hat{r}_k \\ -\hat{r}_k & \hat{r}_y \end{bmatrix} \begin{bmatrix} \sin \gamma & \cos \gamma \\ \cos \gamma & -\sin \gamma \end{bmatrix} \begin{bmatrix} t_1 & 0 \\ 0 & t_2 \end{bmatrix} \begin{bmatrix} \frac{E_{op}}{\sqrt{2}} \\ \frac{E_{om}}{\sqrt{2}} \end{bmatrix} \quad (A-1)$$

where we have recognized that matrix (M-1) can be written as

$$\begin{bmatrix} t_1 & \frac{E_{op}}{\sqrt{2}} \\ t_2 & \frac{E_{om}}{\sqrt{2}} \end{bmatrix} = \begin{bmatrix} t_1 & 0 \\ 0 & t_2 \end{bmatrix} \begin{bmatrix} \frac{E_{op}}{\sqrt{2}} \\ \frac{E_{om}}{\sqrt{2}} \end{bmatrix} \quad (A-2)$$

Carrying out the multiplication of the 2 x 2 matrices, we have

$$\begin{bmatrix} E_{oa} \\ E_{ob} \end{bmatrix} = \begin{bmatrix} a_{11} & a_{12} \\ a_{21} & a_{22} \end{bmatrix} \begin{bmatrix} \frac{E_{op}}{\sqrt{2}} \\ \frac{E_{om}}{\sqrt{2}} \end{bmatrix} \quad (A-3)$$

where

$$a_{11} = t_1^2 (\hat{r}_x \sin \gamma \cos \phi + \hat{r}_k \cos \gamma \cos \phi - \hat{r}_k \sin \gamma \sin \phi + \hat{r}_y \cos \gamma \sin \phi) \quad (A-3a)$$

$$a_{21} = t_1 t_2 (-\hat{r}_x \sin \gamma \sin \phi - \hat{r}_k \cos \gamma \sin \phi - \hat{r}_k \sin \gamma \cos \phi + \hat{r}_y \cos \gamma \cos \phi) \quad (A-3b)$$

$$a_{12} = t_1 t_2 (\hat{r}_x \cos \gamma \cos \phi - \hat{r}_k \sin \gamma \cos \phi - \hat{r}_k \cos \gamma \sin \phi - \hat{r}_y \sin \gamma \sin \phi) \quad (A-3c)$$

$$a_{22} = t_2^2 (-\hat{r}_x \cos \gamma \sin \phi + \hat{r}_k \sin \gamma \sin \phi - \hat{r}_k \cos \gamma \cos \phi - \hat{r}_y \sin \gamma \cos \phi) \quad (A-3d)$$

The transmitted intensity is given by

$$I = \begin{bmatrix} E_{oa}^* & E_{ob}^* \end{bmatrix} \begin{bmatrix} E_{oa} \\ E_{ob} \end{bmatrix} \quad (A-4)$$

which, multiplying out Eq. (A-3) and substituting into Eq. (A-4), is

$$I = \left[\left(\frac{E_{op}^{a11}}{\sqrt{2}} + \frac{E_{om}^{a12}}{\sqrt{2}} \right) \left(\frac{E_{op}^{a21}}{\sqrt{2}} + \frac{E_{om}^{a22}}{\sqrt{2}} \right) \right] \begin{bmatrix} \left(\frac{E_{op}^{a11}}{\sqrt{2}} + \frac{E_{om}^{a12}}{\sqrt{2}} \right) \\ \left(\frac{E_{op}^{a21}}{\sqrt{2}} + \frac{E_{om}^{a22}}{\sqrt{2}} \right) \end{bmatrix} \quad (A-5)$$

where the bar represents the time averaging process.

Remembering from Section 2.2 that

$$\left| E_{op} \right| = \left| E_{om} \right| = \left| E_o \right| \quad (\text{II-9})$$

and that the time average of $E_{op} E_{om}$ is zero, we carry out the multiplication in Eq. (A-5) and divide each side by E_o^2 to get

$$T = 1/2 (a_{11} a_{11}^* + a_{12} a_{12}^* + a_{21} a_{21}^* + a_{22} a_{22}^*) \quad (\text{A-6})$$

Thus far the derivation is exact, but the present result is too cumbersome to be of any use. Therefore, we shall examine the matrix coefficients of Eq. (A-3) and see what we can discard. We know from previous discussion in Section 2.2 that

$$\begin{aligned} t_1 &\gg t_2 \\ r_x &\gg r_k \\ r_y &\gg r_k \end{aligned} \quad (\text{A-7})$$

Immediately we see that $a_{22} \ll a_{11}$, and therefore a_{22} can be dropped from further consideration. If we perform the multiplications indicated in Eq. (II-10) and compare terms, we find that all terms containing \hat{P}_k in Eqs. (A-3b) and (A-3c) are negligible. Finally, if we restrict γ and ϕ to small angles (say less than 10°), the three terms containing $\sin \gamma \sin \phi$ can also be neglected. Letting

$$\begin{aligned} \sin \gamma &\approx \gamma \\ \sin \phi &\approx \phi, \quad \cos \gamma \approx \cos \phi \approx 1 \end{aligned} \quad (\text{A-8})$$

we can now write

$$T = \frac{t_1^4}{2} [PP^* + (r_x^2 + r_y^2) R_e^2] \quad (\text{II-18})$$

where

$$P = \hat{P}_x \gamma + \hat{P}_y \phi + \hat{P}_k$$

Appendix B

KERR CELL TRANSMISSION

Assume a nitrobenzene cell with a polarizer on either side. The principal plane of the input polarizer is positioned at an angle θ with respect to the direction of the electric field in the Kerr cell. The output polarizer is positioned at an angle $\theta + \frac{\pi}{2}$ so that when the cell is unenergized the passage of light through the assembly is blocked by the crossed polarizers.

Let the light from the input polarizer entering the cell have amplitude E_0 . Letting the applied field in the cell be in the x direction and the direction perpendicular to both the x direction and the optical path be the y direction, the amplitude vector of the light entering the cell can be written as

$$\vec{E}_1 = E_0 \left[\vec{i}_x \cos \theta + \vec{i}_y \sin \theta \right] \quad (\text{B-1})$$

The x and y components of the light emerging from the cell have a phase difference of

$$\delta = 2\pi L K E^2 \quad (\text{V-2})$$

where

L is the optical path through the energized nitrobenzene

K is the Kerr constant

D is the electric field applied to the nitrobenzene

This difference is introduced by the difference in indices of refraction in the x and y directions caused by the electric field. Hence the E-vector of light emerging from the cell is

$$\vec{E}_2 = E_0 \left[\vec{i}_x \cos \theta + \vec{i}_y \exp[-j\delta] \sin \theta \right] \quad (\text{B-2})$$

The amplitude of the E-vector emerging from the output polarizer is then

$$\begin{aligned}
 E_3 &= \vec{E}_2 \left[\vec{i}_x \cos \left(\theta + \frac{\pi}{2} \right) + \vec{i}_y \sin \left(\theta + \frac{\pi}{2} \right) \right] \\
 &= E_0 \left[\vec{i}_x \cos \theta + \vec{i}_y \sin \theta \exp[-j\delta] \right] \cdot \left[-\vec{i}_x \sin \theta + \vec{i}_y \cos \theta \right] \\
 &= E_0 \sin 2\theta \left[\frac{\exp[-j\delta] - 1}{2} \right] \\
 &= jE_0 \exp[-j\frac{\delta}{2}] \sin 2\theta \sin \frac{\delta}{2}
 \end{aligned} \tag{B-3}$$

and the intensity is

$$\begin{aligned}
 I &= E_3 E_3^* \\
 &= E_0^2 \sin^2 2\theta \sin^2 \frac{\delta}{2}
 \end{aligned} \tag{B-4}$$

Substituting Eq. (V-2) in Eq. (B-4) and recognizing that the input intensity is simply E_0^2 , the transmission of the Kerr cell is

$$T = \sin^2 2\theta \sin^2 (\pi L K E^2) \tag{B-5}$$

This transmission maximizes for $\theta = 45^\circ$ and for $L K E^2 = \frac{n}{2}$, where n is any odd integer. A plot of this curve for $\theta = 45^\circ$ and for $L K E^2$ varying from 0 to 1 is given in Fig. B-1.

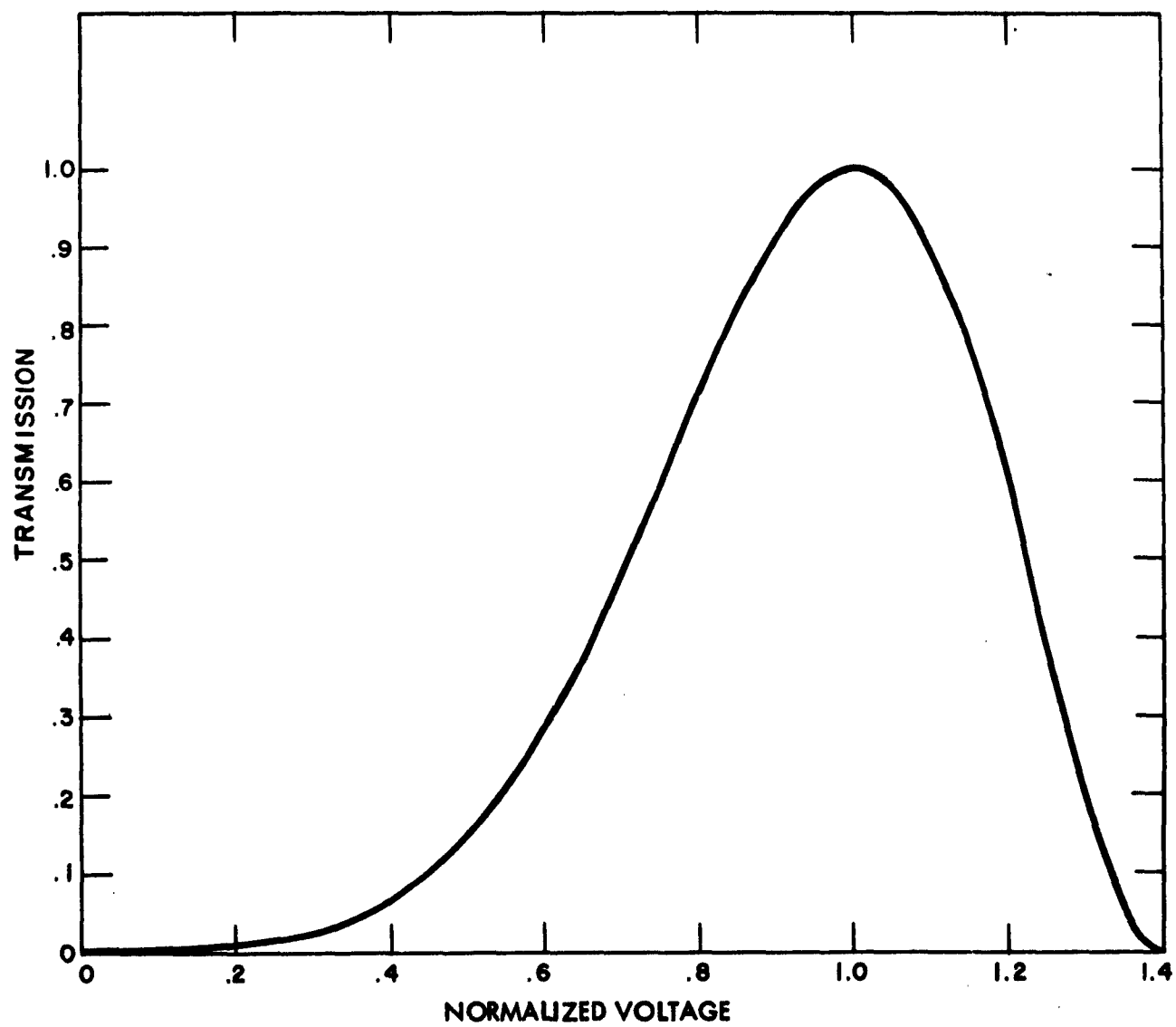


FIG. B-1 KERR CELL TRANSMISSION

Appendix C

HYDROGEN THYRATRON CONSIDERATIONS

High currents, high voltages, or both must be switched in three major items in the electronic instrumentation -- the field pulse generator, the electro-optical shutter, and the flash lamp trigger. The field pulse generator supplies current pulses up to 40 amperes in amplitude with a source impedance at about 80 ohms, requiring a switch which will hold off about 3 Kv. The electro-optical shutter operates in the vicinity of 35 Kv switching a current of 350 amperes into a 100 ohm load. The flash lamp requires a triggering pulse of about 2 Kv; however, because of the desirability of reliable triggering and low jitter, a 6 Kv pulse is used.

In addition, sharp rise times and close synchronization are necessary. Ideally, all switches should have an operating time of about 5 μ sec and jitter of less than this; practically, this is not quite attainable.

The only devices which readily meet the voltage and current requirements are spark gaps and hydrogen thyratrons. Spark gaps can be designed for excellent rise times¹; however, at high voltages they require pressurizing (which is a nuisance), they require fairly high triggering voltages proportional to their holdoff voltage, and the amount of jitter can be quite large.

Hydrogen thyratrons are slightly more limited regarding rise time. The literature indicates a minimum rise time of 10 to 12 μ sec for a 5C22² and about 15 to 20 μ sec for a 4C35³. The writer has attained rise times of about 25 μ sec with 3C45 thyratrons. On the other hand, a variety of hydrogen thyratrons are commercially available for meeting various current and voltage requirements, the triggering voltages (200 to 500 volts) are relatively small in comparison to the holdoff voltages, and the jitter is between 2 and 10 μ sec (depending on the thyatron and its operating conditions).

Martin and Goldberg³ conducted an extensive study of the characteristics of the 4C35 thyatron. A few of their results which are pertinent to the present work are mentioned here. While these results are specifically stated for the 4C35 hydrogen thyatron, the ideas concerned can be generally applied to other hydrogen thyatrons.

Although rated at a maximum holdoff voltage of 8 Kv, the dc breakdown voltage of the average 4C35 is in excess of 25 Kv. The voltage drop across the tube after breakdown is nominally 60 to 120 volts, varying inversely as the filament voltage; this variation is apparently related to the voltage drop across the cathode coating.

The rise time depends to a large extent upon the applied grid voltage and the tube pressure. A plot of rise time constant versus grid voltage for a 4C35 operating at an anode voltage of 3 Kv is shown in Fig. C-1. The time constant varies inversely as the square of the hydrogen pressure; the normal 4C35 pressure is 500 microns. Wood, et al.² have also indicated an inverse relationship between rise time constant and anode voltage.

Jitter is largely a function of the applied grid voltage. Variation of anode delay (i. e., the time between the application of the grid voltage and the beginning of the anode drop) as a function of grid voltage is also shown in Fig. C-1. From this we can deduce that jitter can be minimized by triggering pulses of sharp rise time and high amplitude. An interesting point in the 4C35 study is that, operating at an anode potential of 3 Kv, breakdown begins to occur almost precisely 36 μ sec after a grid current of 49 ma is reached; this is independent of the applied grid voltage.

The writer's experience has been as follows: With a 1258 miniature hydrogen thyatron, jitter can be reduced to about 2 μ sec; with a 3C45 the jitter is about 3 to 4 μ sec; operating a 6587 at excessive anode voltages, the jitter is as much as 30 μ sec with a grid voltage of 150 volts, but drops to 8 μ sec when the grid voltage is increased to 450 volts.

Cobine⁴ states that for mercury vapor thyatrons the holdoff voltage increases for decreasing pressure. Although the same is probably true for hydrogen thyatrons, no data has been found indicating the magnitude of the effect.

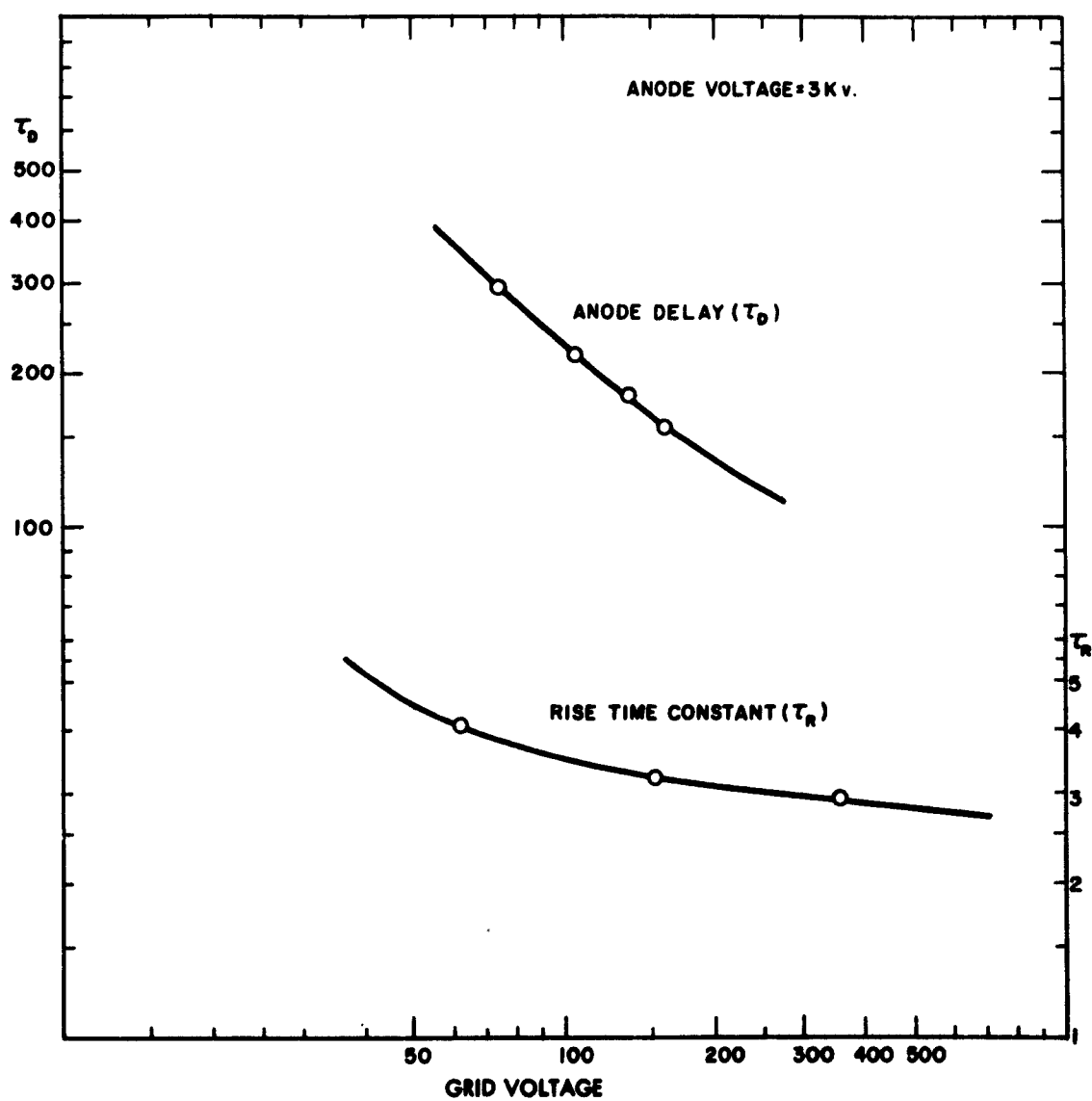


FIG. C-1 4C35 RISE TIME CONSTANT AND ANODE DELAY

BIBLIOGRAPHY*

Chapter I

1. J. I. Raffel, "Operating Characteristics of a Thin Film Memory, " Jour. Appl. Phys., 30 (supplement), 605 (1959).
2. M. S. Blois, Jr., "Preparation of Thin Magnetic Films and Their Properties, " Jour. Appl. Phys., 26, 975 (1955).
3. C. P. Olson and A. V. Pohm, "Flux Reversal in Thin Films of 82 Per Cent Ni, 18 Per Cent Fe, " Jour. Appl. Phys., 29, 274 (1958).
4. D. O. Smith, "Static and Dynamic Behaviour of Thin Permalloy Films, " Jour. Appl. Phys., 29, 264 (1958).
5. F. B. Humphrey and E. M. Gyorgy, "Flux Reversal in Soft Ferromagnetics, " Jour. Appl. Phys., 30, 935 (1959).
6. E. M. Gyorgy, "Rotational Model of Flux Reversal in Square Loop Ferrites, " Jour. Appl. Phys., 28, 1011 (1957).
7. R. L. Conger and F. C. Essig, "Resonance and Reversal Phenomena in Ferromagnetic Films, " Phys. Rev., 104, 915 (1956).
8. F. B. Humphrey, "Transverse Flux Change in Soft Ferromagnetics, " Jour. Appl. Phys., 29, 284 (1958).
9. P. C. Archibald, R. L. Conger, R. W. Sharp, and J. L. Tomlinson, "High Speed Magneto-Optical Measurements on Films, " Rev. Sci. Inst., 31, 653 (1960).
10. R. L. Conger and F. C. Essig, "Magnetization Reversal in Thin Films at Low Fields, " Jour. Appl. Phys., 28, 855 (1957).
11. D. O. Smith, Lincoln Laboratory - private communication.
12. R. Kikuchi, "On the Minimum of Magnetization Reversal Time, " Jour. Appl. Phys., 27, 1352 (1956).

* Since the bibliography is organized by chapters, designations in brackets following an op. cit. indicate the chapter and reference number for the entire reference information.

13. D. O. Smith, "Magnetization Reversal in Thin Films," Phys. Rev., 104, 1280 (1956).
14. H. J. Williams, F. G. Foster, and A. Wood, "Observations of Magnetic Domains by the Kerr Effect," Phys. Rev., 82, 119 (1951).
15. C. A. Fowler and E. M. Fryer, "Magnetic Domains by the Longitudinal Kerr Effect," Phys. Rev., 94, 52 (1954).
16. C. A. Fowler and E. M. Fryer, "Magnetic Domains in Thin Films of Nickel-Iron," Phys. Rev., 100, 746 (1955).
17. C. A. Fowler and E. M. Fryer, "Magnetic Domains in Thin Films by the Faraday Effect," Phys. Rev., 104, 552 (1956).
18. C. A. Fowler, E. M. Fryer, and D. Treves, "Domain Structures in Iron Whiskers as Observed by the Kerr Method," Sixth Annual Conference on Magnetism and Magnet Materials, New York, November, 1960.
19. D. R. Callaby, "Determination of the Directions of Magnetization in Polycrystalline Ferrites," Sixth Annual Conference on Magnetism and Magnetic Materials, New York, November 1960.
20. R. W. Olman and E. N. Mitchell, "Slow Domain Wall Motion in Homogeneous Vacuum-Deposited Iron Nickel Films," Jour. Appl. Phys., 30 (supplement), 2585 (1959).
21. B. W. Roberts and C. P. Bean, "Large Magnetic Kerr Rotation in Bi-Mn Alloy," Phys. Rev., 96, 1494 (1954).
22. H. J. Williams, R. C. Sherwood, F. G. Foster, and E. M. Kelley, "Magnetic Writing on Thin Films of MnBi," Phys. Rev., 28, 1181 (1957).
23. L. Kleinrock, Optical Data Processing with Thin Magnetic Films, S. M. Thesis, Massachusetts Institute of Technology (May, 1958).
24. W. Heinrich, "The Magnification of the Magneto-Optic Kerr Rotation by Means of Evaporated Layers," Sitzungsberichten der Bayerischen Akademik der Wissenschaften, Mathematisch-Naturwissenschaftliche Klasse, p. 133 (1956).
25. E. W. Lee, "A Study of Ferromagnetic Domains in Perminvar Possessing a Rectangular Hysteresis Loop," International Conference on Magnetism, Grenoble, France (1958).

26. G. H. Moore, "The Demonstration of Magnetic Domain Dynamics by Means of the Longitudinal Kerr Effect," NOLC Technical Memo, No. 42-5 (August, 1957).

Chapter II

1. C. C. Robinson, The Longitudinal Kerr Magneto-Optic Effect in Ferromagnetic Thin Films, Ph.D. Thesis, Massachusetts Institute of Technology (September, 1960).
2. C. C. Robinson, op. cit., p. 56.
3. A. H. Anderson, "Paired Thick Films," Information Processing, Quarterly Progress Report, June, 1960, Lincoln Laboratory Publication.
4. J. Kranz and W. Drechsel, "Über die Beobachtung von Weißschen Bereichen in polykristallinem Material durch die vergrößerte magneto-optische Kerndrehung," Zeit. Phys., 150, 632-639 (1958).
5. A. Vasicek, Optics of Thin Films (New York: Interscience Publishers, Inc., 1960), p. 311.
6. D. B. Judd, "Color Vision and Colorimetry," in E. U. Condon and H. Odishaw (eds.), Handbook of Physics (New York: McGraw-Hill Book Company, Inc., 1958), p. 6-64.

Chapter III

1. C. A. Fowler and E. M. Fryer, op. cit. [I, 16; I, 17; I, 18].
2. H. J. Williams, F. G. Foster, and A. Wood, op. cit. [I, 14].
3. B. W. Roberts and C. P. Bean, op. cit. [I, 21].
4. G. H. Moore, op. cit. [I, 26].
5. R. F. Saxe and R. A. Chippendale, "Millimicrosecond Exposures by Image Tubes," Brit. Jour. Appl. Phys., 6, 336 (1955).
6. A. M. Zarem, F. R. Marshall, and S. M. Hauser, "Millimicrosecond Kerr Cell Camera Shutter," Rev. Sci. Instr., 29, 1041 (1958).

7. R. M. Bozorth, Ferromagnetism (New York: D. Van Nostrand Company, Inc., 1951), p. 532.
8. C. P. Bean and D. S. Rodbell, "Kinetics of Magnetization in Some Square Loop Magnetic Tapes," Jour. Appl. Phys., 26, 124 (1955).
9. P. C. Archibald, et al., op. cit. [I, 9].
10. G. H. Moore, NOLC - private communication.
11. K. W. Cooper, Jr., An Investigation of Spark Discharge Phenomena in the Millimicrosecond Region, S.M. Thesis, Department of Electrical Engineering, Massachusetts Institute of Technology (1959).
12. D. A. Spencer, Progress in Photography, 1951-1954 (New York: The Focal Press, 1955), p. 210.
13. H. F. Edgerton and P. Y. Cathou, "Xenon Flash Tube of Small Size," Rev. Sci. Instr., 27, 821 (1956).
14. R. McDunna, Baird Atomic, Inc. - private communication.
15. R. G. Stoudenheimer and J. C. Moore, "An Image-Converter Tube for High-Speed Photographic Shutter Service," RCA Review, 18, 322 (1957).
16. J. Castle, W. Woodbury, and W. A. Shelton, "Reciprocity-Law Failure at Very Short Exposure Times," Third International Congress on High-Speed Photography (New York: Academic Press, Inc., 1957), p. 219.

Chapter IV

1. C. A. Fowler, E. M. Fryer, and J. R. Stevens, "Magnetic Domains in Evaporated Thin Films of Nickel-Iron," Phys. Rev., 104, 645 (1956).
2. H. Y. Fon, "Induced Double Refraction on Thin Films," in K. Lark-Horovitz and V. A. Johnson (eds.), Methods of Experimental Physics, Vol. 6, Part B (New York: Academic Press, 1959), p. 278.
3. G. H. Moore, op. cit. [I, 26].
4. M. Born and E. Wolf, Principles of Optics (London: Pergamon Press, 1959), p. 181.

5. F. A. Jenkins and H. E. White, Fundamentals of Optics, 3rd Ed. (New York: McGraw-Hill Book Company, Inc., 1957), p. 109.
6. A. C. Hardy, Massachusetts Institute of Technology - private communication.
7. M. Born and E. Wolf, op. cit., p. 187.

Chapter V

1. A. M. Zarem, B. R. Poole, and F. R. Marshall, "An Electro-Optical Shutter for Photographic Purposes," Inyokern, U.S. NOTS (May, 1948), NavOrd Report No. 1016.
2. A. M. Zarem and F. R. Marshall, "A Multiple Kerr Cell Camera," Rev. Sci. Instr., 21, 514 (1950).
3. H. J. White, "The Technique of Kerr Cells," Rev. Sci. Instr., 6, 22 (1935).
4. J. A. Hull, "Millimicrosecond, Wide-Aperture Electro-Optical Shutter," Research Report, Research and Advanced Development Division, Avco, Wilmington, Massachusetts.
5. A. M. Zarem, F. R. Marshall, and S. M. Hauser, op. cit. [III, 6].

Chapter VI

1. E. A. Guillemin, "A Historical Account of the Development of a Design Procedure for Pulse Forming Networks," Colloquium on Pulse Forming Networks, Radiation Lab Report 692, March 14, 1945.
2. H. F. Edgerton, op. cit. [III, 13].

Chapter VII

1. C. P. Olson and A. V. Pohm, op. cit. [I, 3].
2. Conger and Essig, op. cit. [I, 10].

Appendix C

1. G. A. Theophanis, "Millimicrosecond Triggering of High Voltage Spark Gaps," Rev. Sci. Instr., 31, No. 4, 427 (1960).
2. J. B. Woodward and E. M. Williams, "The Initial Conduction Interval in High-Speed Thyratrons," Jour. Appl. Phys., 23, 722 (1952).
3. K. J. Germeshausen, et al., "Research Study on Hydrogen Thyratrons," U.S. Army Signal Corps Contract No. DA36-039-SC-15372 (June, 1953).
4. J. D. Cobine, Gaseous Conductors (New York: McGraw-Hill Book Company, Inc., 1941), p. 452.